The Measurement of the Production Cross Section Ratio of Identified Hadrons and the Calibration of the Magnetic Distortion in RICH1 at LHCb

Andrea Contu
St Anne's College, Oxford





Thesis submitted in partial fulfilment of the requirements for the degree of Doctor of Philosophy at the University of Oxford

Trinity Term, 2012

The Measurement of the Production Cross Section Ratio of Identified Hadrons and the Calibration of the Magnetic Distortion in RICH1 at LHCb

Andrea Contu
St Anne's College, Oxford

Thesis submitted in partial fulfilment of the requirements for the degree of Doctor of Philosophy at the University of Oxford.

Trinity Term, 2012

Abstract

Physics measurements at the LHC rely on the simulation of the proton-proton interaction to estimate detector performance and physics backgrounds. Therefore, a good understanding of all the processes involved is crucial to the final precision of any measurement. Monte Carlo event generators try to provide a realistic description of the proton-proton collision by combining the theoretical models describing different stages of the interaction process. Within this framework, the baryon number transport and the hadronisation mechanism are currently described by phenomenological models that need input from experimental data. This thesis investigates these subjects in the unique kinematic region covered by the LHCb detector.

The production cross section ratios of identified hadrons (protons, kaons and pions) have been measured as a function of pseudorapidity and transverse momentum both at $\sqrt{\mathbf{s}} = 0.9\,\text{TeV}$ and $\sqrt{\mathbf{s}} = 7\,\text{TeV}$ collisions using $320\,\mu\text{b}^{-1}$ and $1.8\,\text{nb}^{-1}$ of data respectively. The measurements are then compared to the predictions from several tunings of the PYTHIA Monte Carlo generator. In general, current models do not give a satisfactory description of the hadronisation and tend to underestimate the transport of the baryon number into the final state.

Critical to this analysis is the particle identification provided by the LHCb Ring Imaging Cherenkov (RICH) system. To ensure high performance, a proper calibration of the RICH photon detectors response is necessary. A system for the calibration of the magnetic distortion induced by the LHCb dipole magnet onto the photon detectors is described. The system currently provides calibration parameters used in the LHCb event reconstruction software and introduces a critical improvement to the overall particle identification performance.

Preface

The LHCb experiment at the Large Hadron Collider (LHC) is designed to study heavy-flavour physics. The LHC's large $b\bar{b}$ and $c\bar{c}$ production cross-sections at the TeV scale provide unprecedented statistical power to investigate CP-violating processes and rare decays in the B and D sectors. Studies of hadronic interactions, precision tests of the Standard Model (SM) and searches for New Physics (NP) effects, well beyond the mass scales directly accessible at the LHC, can also be performed.

Physics analyses at the LHC often rely on Monte Carlo (MC) simulations of the proton-proton interaction to unfold the acceptance and efficiency of the detector from the physics measurement and background estimations. The final reliability and precision of the result is clearly dependent on the modelling of the proton-proton (pp) interactions. MC generators usually divide the problem into two distinct components: the "hard interaction" and "soft interaction" parts. Heavy particles are usually produced in the "hard" part where the two incoming partons interact at energies in which a perturbative approach to Quantum Chromodynamics (QCD) allows for theoretical calculations to be performed. The "soft" part accounts for low momentum-transfer processes and quark hadronisation into colourless final states. Since such processes fall into the non-perturbative regime of QCD, where perturbative calculations become unpractical, theoretical predictions are usually obtained through a phenomenological approach. The two parts must be combined in a consistent way into a realistic description of the pp collision. Feedback is required from the experimental data in order to check performance and refine the MC model in case of discrepancies, or when a new energy regimes or new kinematic regions are explored.

The main topics of this thesis are the measurement of the prompt hadron production ratios of identified particles, such as protons, kaons and pions, in "minimum bias" events and the calibration of the magnetic distortion inside the photon detectors of the LHCb Ring Imaging Cherenkov (RICH) detectors, which is vital for the particle identification performance.

Chapter 1 introduces the concepts of *minimum bias* events, *baryon number transport (BNT)* and *hadronisation*. Strategies to access these quantities, such as the measurement of prompt hadron productions ratios, are discussed.

Chapter 2 provides an overview of the LHCb experiment. Although all general aspects of the LHCb experiment are covered, particular emphasis is given to the experiment's two RICH detectors. In order to distinguish efficiently between different particle species, the LHCb RICH system is required to provide excellent particle identification (PID) over a wide kinematic range. A detailed description of the photon detectors used, the Hybrid Photon Detectors (HPDs), is given.

Chapter 3 describes the Magnetic Distortion Calibration System (MDCS) currently operating in RICH1. The hardware employed, the analysis of the calibration data and the extraction of the correction parameters, developed by the author, are outlined. The calibration of the magnetic distortions in the HPDs is vital for the RICH reconstruction and greatly improves the RICH system performance.

The measurement of the hadron production ratios is the central physics study of the thesis. Chapter 4 presents the analysis strategy while Chapter 5 is focused on the estimation of the systematic uncertainties and final results.

Finally, conclusions are drawn in Chapter 6.

The work described in Chapters 3-5 is largely due to the author.

Acknowledgements

I wish to thank Regione Sardegna for funding my three years studentship. I am also grateful to STFC, St Anne's College, the Institute of Physics (IOP) and the Oxford Particle Physics Department.

During my PhD I had the privilege to work with many people within the LHCb collaboration. Moreover, my friends and family supported me in any way they could throughout these years. I wish to thanks them all. The following people, however, I am particularly indebted to:

Firstly, Neville Harnew and Guy Wilkinson, my supervisors, for their encouragement, direction and comprehension. Also, for making the final result what it is.

Malcolm John, which has guided me through the hardware studies developed in Chapter 3.

Andrew Powell, to whom I owe countless beers, which helped me in any way and at any time he could.

All my colleagues in the Oxford LHCb group, in particular Sneha Malde, Chris Thomas and Paolo Gandini for all their help and the interesting discussions during coffee breaks.

The Oxford secretaries Sue Geddes, Kim Proudfoot and Laura Neavy for all their assistance in the administrative side of my DPhil.

All the students and post-docs in the Oxford sub-department of Particle Physics.

The Oxford “Honeybadgers” for the glorious performance at the Bubble-Chamber tournament and the St John’s MCR football team.

All the members of the LHCb RICH group for their unconditioned support during my LTA at CERN.

Paolo, Nicola, Francesco, Francesca, Marianna, Riccardo, Giamba, known as “the exiled”, for fearlessly spreading Sardinian genes and expertise all over the world.

Valerio, Tony and Alice for finding the time for a pizza even with very short notice.

A special thank to Dorothea for all her love, support, patience and for constantly reminding me that there is something else beyond the screen of my laptop.

Finally, to my parents and family, for their tireless efforts, without whose encouragement and support I would not be where I am today.

Contents

Abstract **i**

Preface **ii**

Acknowledgements **iv**

1 High energy pp collisions in the forward region **1**

1.1 Quantum Chromodynamics 2

1.2 Regge Theory for Strong Interacting Particles 4

1.3 High Energy *pp* Interactions 6

1.4 Hadronisation 9

1.4.1 String Fragmentation 9

1.4.2 Cluster Fragmentation 13

1.5 Baryon Number Transport 14

1.6 Prompt Hadron Production Ratios 17

2 The LHCb experiment **19**

2.1 Introduction 19

2.2 The LHC 19

2.3 The LHCb Detector Overview 21

2.3.1 Tracking System 22

2.3.1.1 VELO 23

2.3.1.2 Dipole Magnet 27

2.3.1.3 TT 28

2.3.1.4 Inner Tracker 28
2.3.1.5 Outer Tracker 29
2.3.2 Track Reconstruction 30
2.3.3 Calorimeters 32
2.3.3.1 Scintillator Pad and Pre-Shower detector 33
2.3.3.2 Electromagnetic Calorimeter 33
2.3.3.3 Hadronic Calorimeter 34
2.3.4 Muon System 34
2.3.5 Trigger 36
2.3.5.1 Level-0 Trigger 36
2.3.5.2 High Level Trigger 38
2.3.5.3 Trigger Strategies in First Data 39
2.4 The LHCb RICH System 40
2.4.1 Cherenkov Radiation 40
2.4.2 The LHCb RICH Layout 42
2.4.2.1 Number of Detected Photons and Momentum Coverage 43
2.4.2.2 Resolution on the Cherenkov Angle Measurement . . . 45
2.4.3 The RICH Hybrid Photon Detectors 46
2.4.3.1 Photocathode 47
2.4.3.2 Photoelectron Focusing 47
2.4.3.3 Silicon Pixel Sensor 48
2.4.3.4 RICH Pattern Recognition 49
2.5 LHCb Detector Performance 51
2.5.1 Tracking Performance 51
2.5.2 Energy Resolution 53
2.5.3 Particle Identification Performance 54

3 The Magnetic Distortion Calibration System in RICH1 56
3.1 Introduction 56
3.2 Magnetic Field Shielding in RICH1 57

3.3 MDCS System Design 60
3.3.1 Hardware Description 60
3.3.1.1 Light Bar 62
3.3.1.2 Motion Control 63
3.3.2 Light Bar Operation 65
3.4 Data Processing 66
3.4.1 Peak Finder 67
3.4.2 Sources of Background 68
3.5 Pattern Cleaning 70
3.5.1 Peak Properties 71
3.5.2 Likelihood Determination 73
3.5.3 Cleaning Performance 75
3.6 Calibration Parameter Extraction 76
3.6.1 Distortion, Magnification and Refraction 77
3.6.2 Effects of the Magnetic Field 80
3.6.3 Parameter Fitting 82
3.7 Performance on MDCS Data 84
3.7.1 Spatial Resolution 84
3.7.2 Magnification Estimation 85
3.7.3 Correction Stability 87
3.8 Performance on Collision Data 89

4 Hadron Ratios - Analysis Strategy **95**

4.1 Introduction 95
4.2 Promptness Definition 96
4.3 Data Samples and Binning 96
4.4 Selection 98
4.4.1 Event Selection 98
4.4.2 Track Selection 99
4.4.2.1 Track Clones 103

4.5 Raw Ratios Observed and Corrections Needed 103
4.6 RICH Calibration Samples and Results 104
4.6.1 Selection of RICH Calibration Modes 106
4.6.2 Background Subtraction Technique 107
4.6.3 Binning and PID Efficiency Determination 109
4.6.4 PID Efficiencies Re-Weighting 110
4.6.4.1 Approximations in the Re-Weighting Procedure 112
4.6.4.2 Choice of Cell Sub-Division in Momentum and Track Multiplicity 114
4.6.4.3 Comparison of Results with MC Truth after Re-Weighting 118
4.6.5 Contamination Corrections 128
4.6.6 Results and Purities 129
4.7 Material Interactions and Reconstruction Efficiency 130
4.8 Monte Carlo Validation Study 132

5 Hadron Ratios - Systematic Uncertainties and Results 145
5.1 Introduction 145
5.2 Systematic Uncertainties 145
5.2.1 PID 145
5.2.2 Detector Description in MC 146
5.2.3 Material Interaction Cross Sections 147
5.2.4 Ghost Tracks 148
5.2.5 Tracking Asymmetries 151
5.2.6 Non-Prompt Contamination 151
5.2.7 Summary 152
5.3 Robustness Tests 154
5.3.1 Magnet Polarity 154
5.3.2 Clone Tracks 154
5.3.3 Diffractive Events Contribution 154
5.3.4 Correlations 155

5.4 Translating the Results from Pseudo-Rapidity to Rapidity 156
5.5 Results 158
5.5.1 Baryon Number Transport in the $\bar{p}/p$ Ratio. 161

6 Conclusions **170**

A PID Efficiency Tables for Hadron Ratios **172**

B Fake Track Rates Tables **193**

C Non-Prompt Rates Tables **200**

D Pseudorapidity to Rapidity Translation Tables **204**

E Uncertainties Tables for the Hadron Ratios **209**

List of Figures

1.1 Chew-Frautschi diagrams [1] showing N and Δ Regge trajectories. . . . 5

1.2 Regge exchange diagrams illustrating: (a) exchange of a ρ meson trajectory in pion-nucleon charge exchange, (b) Pomeron exchange in elastic $\pi - p$ scattering and (c) neutron exchange in backward $\pi^+ p$ scattering. 6

1.3 Sketch of the string fragmentation process in the centre of mass frame of two receding quarks, $q_0\bar{q}_0$. The hatched area shows where the field is non-vanishing. $q_i\bar{q}_i$ pairs are produced in the same space-time point (x_i, t_i). Nearby vertices are related by mass constraints. 11

1.4 A colour field is stretched between a quark q and an antiquark $\bar{q}$. If virtual $q\bar{q}$ pairs are produced, the colour field can be changed from $r\bar{r}$ to $g\bar{g}$ or $b\bar{b}$. If a second pair is produced inside such a region the colour field can break and a baryon-antibaryon pair can be produced. 12

1.5 Scheme of hadronisation according to the cluster fragmentation scheme. 13

1.6 Three valence quarks located at x_1, x_2 and x_3 joined to the string junction in x. 16

1.7 $\bar{p}/p$ ratio in the central rapidity as a function of Δy as measured by several experiments. 17

1.8 Theoretical predictions for the $\bar{p}/p$ production ratio from MC simulations using different PYTHIA tunings. The plots on the right focus on the LHCb pseudorapidity region. 18

2.1 Layout of the CERN accelerator complex. Before reaching the LHC protons are injected from the linear accelerator (LINAC2) into the PS Booster, then the Proton Synchrotron (PS), followed by the Super Proton Synchrotron (SPS). 20

2.2 Schematic of the LHCb detector shown in the magnet non-bending plane. The right-handed coordinate system used has the z axis along the beam direction, the y axis vertically upwards and the x axis pointing towards the centre of the LHC ring. 21

2.3 Layout of the Vertex Locator. The sensor modules are positioned in the very inner region, very close (8 mm) to the beams. 24

2.4 Design of the VELO sensor positions in the xz plane (top) for the fully closed position and in the xy plane for the fully closed (left bottom) and open (right bottom) positions. 25

2.5 The VELO r- ϕ-sensors. 25

2.6 Photograph of the LHCb dipole magnet. As shown, the proton-proton interaction region lies behind the magnet. 27

2.7 Layout of one of the TT layers. The different readout sectors are shown with different shadings. 28

2.8 (a) Layout of one of the IT layers and (b) exploded view of a two-sensor module of the IT. 29

2.9 Layout of the Outer Tracker (light blue) together with the beam pipe (brown), the TT and the IT (purple). 30

2.10 Classification of the different track types reconstructed by the LHCb tracking algorithms. 31

2.11 Segmentation of the calorimeter system. Only a quarter of the detector front face is shown. 32

2.12 Schematic view of the muon system. 35

2.13 Muon system detection technologies. 35

2.14 Overview of the data processing flow through the LHCb trigger system. 36

2.15 L0 schematic view. 37

2.16 Example of RICH performance for Monte-Carlo-simulated $B_s^0 \to D_s K$ events. 40

2.17 Huygens construction of the light emitted by a particle travelling faster than c in a medium. A coherent wave front is generated at a specific angle θ_{CK} to the particle's trajectory. 41

2.18 RICH detectors layout. 43

2.19 Cherenkov angle as a function of momentum for protons, kaons and pions in the three RICH radiators. 45

2.20 (a) photograph and (b) schematic of an HPD. 47

2.21 HPD photocathode quantum efficiency as a function of the photon wavelength. 48

2.22 Sketch of an LHCb pixel. LHCb pixels are square super-pixels formed by the logic OR of eight ALICE pixels. 49

2.23 Simulated event display for a typical event in (a) RICH1 and (b) RICH2. Fitted rings are superimposed. 50

2.24 Primary vertex resolution in 2011 data in the (a) x and (b) y direction at $\sqrt{\mathbf{s}} = 7\,\mathrm{TeV}$ as a function of the number of tracks used to fit the vertex. Data results (in black) are compared with simulation (in red). . 52

2.25 Primary vertex resolution in 2011 data in the z direction at $\sqrt{\mathbf{s}} = 7\,\mathrm{TeV}$ as a function of the number of tracks used to fit the vertex. Data results (in black) are compared with simulations (in red). 52

2.26 Impact parameter resolution in 2011 data in the (a) x and (b) y direction at $\sqrt{\mathbf{s}} = 7\,\mathrm{TeV}$. Data results (in black) are compared with simulation (in red). 53

2.27 Efficiency for long tracks in 2011 data as a function of (a) momentum and (b) pseudo-rapidity at $\sqrt{\mathbf{s}} = 7\,\mathrm{TeV}$. Data results (in black) are compared with simulation (in red). 53

2.28 Energy resolution of the LHCb calorimeter system. 54

2.29 LHCb PID performance for long tracks in 2011 data. The efficiency to correctly identify (a) kaons and (b) protons are shown by the red data points and the corresponding pion misidentification probability by the black data points. 55
2.30 Muon identification efficiency as measured from 2010 data taken at $\sqrt{s} =$ 7 TeV . Data points (red) are compared to MC simulations (blue). . . . 55

3.1 HPD layout showing the distortion introduced on the photoelectron trajectories due to a magnetic field. 57
3.2 Magnetic shielding of the HPD boxes in RICH1. 58
3.3 Distortion introduced on an HPD image from a cross-shaped pattern without any shielding due to an external magnetic field of 3 mT (a) parallel and (b) perpendicular to the HPD tube axis. 59
3.4 Mu-metal cylindrical shields surround the HPDs and extend 20 mm outwards towards the gas radiator. 59
3.5 Scheme of the MDCS hardware for one of the HPD planes. 61
3.6 The MDCS system, shown here in projection, located inside the photon funnel. 61
3.7 A MDCS PCB module with a 5x28 matrix of LEDs. 62
3.8 An exploded view of an LED PCB module. Light is emitted from LED array L into the collimator unit, encountering first part B having short small-diameter holes followed by longer larger-diameter holes, and then part A having the same short small-diameter holes. Light emerges upwards toward the HPD panel (not shown). 63
3.9 View of the photon funnel and LED modules mounted on the carbon-fibre bar during a test. 64
3.10 A screenshot of MDCS PVSS control panel. 65
3.11 Number of illuminated HPDs in the upper box as a function on the calibration step (magnet polarity down). 66

3.12 A typical HPD pixel hit map caused by a single position of LED light. The peak-finding algorithm uses a search window of 7x7 LHCb pixels that is moved (A), a peak candidate is formed when its position on the silicon sensor is centred around the hit cluster(B). The black dot marks the centre of a two-dimensional Gaussian fit, and the cross marks the position of the arithmetic mean, for comparison. 67
3.13 Fitted peak positions on the upper HPD plane (magnet polarity down) before cleaning. 68
3.14 Hit maps of an HPD affected by (a) IFB and (b) having noisy pixels. . 69
3.15 Total internal reflection in the HPD quartz window caused by LED light illuminating the edge of the window. 70
3.16 The hit structure caused by total refraction of LED light inside the quartz window. 70
3.17 Integrated number of peaks per HPD in the upper box (magnet polarity down). The difference between “all peaks”, “single peaks” and “cleaned peaks” are explained in Section 3.5. 71
3.18 Single peak positions on the HPD upper box (magnet polarity down). . 72
3.19 Distributions from the HPD upper box of the variables used to build the peak-finding likelihood (magnet polarity down). IFB-affected and noisy HPDs are not included. 73
3.20 Fits to the distributions of the variables used to build the likelihood from the HPD upper box (magnet polarity down). 74
3.21 Delta Log Likelihood distribution from the HPD upper box (magnet polarity down). 75
3.22 The cleaned final pattern, with $DLL > 0$, from the upper box (magnet polarity down). 76
3.23 Distribution of fitted $\sigma = \sqrt{\sigma_1^2 + \sigma_2^2}$ of the cleaned peaks. Magnet on data are in red, magnet off in blue. 77

3.24 Distribution of the ratio between the orthogonal widths of the 2-dimensional Gaussian used to fit the peaks. 77
3.25 Single LED photon intensity per 25 ns. 78
3.26 Distortion of the peak patterns extrapolated to the HPD quartz window with no magnetic correction applied. 81
3.27 Reconstructed peak positions (red) at the exterior of the quartz window without distortion correction. The expected grid patterns from two LED modules are superimposed. 83
3.28 ΔR and $\Delta\phi$ data points as a function of radial position. 84
3.29 Reconstructed peak positions (red) at the quartz window after correction. Expected grid patterns from two LED modules are superimposed. 85
3.30 Distribution of the radial parameters (Eq. 3.6) for the HPDs in the upper box. 86
3.31 Distribution of the axial parameters (Eq. 3.6) for the HPDs in the upper box. 86
3.32 Comparison of leading axial parameters for different magnet conditions. The axial correction has opposite sign for the two boxes. 87
3.33 Resolution of MDCS data before and after correction in the x and y directions. 88
3.34 Two dimensional maps of the magnification coefficients of each HPD in the upper panel with magnet off. 89
3.35 Leading correction terms for scans taken at different times for the upper box, column 1 and magnet polarity down. The data points taken in 5/11 corresponds to an HPD HV of 15 kV. 90
3.36 Correction to the magnification law for different scans. The data are taken for the upper box, column 1, HPD 5 and magnet polarity down. . 91
3.37 Resolution of the Cherenkov angle in hadronic b decays (2011 data). The fit is only performed for (b), The full width half maximum, relative to the range shown in the plots, is shown for comparison. 92

3.38 Resolution on the Cherenkov angle for photons reflected by individual spherical-flat mirror pairs (2011 data). 93

3.39 Resolution on the Cherenkov angle in 2011 data for individual HPDs in the lower panel for photons reflected by a particular spherical-flat mirror pair (spherical mirror 2, flat mirror 13). 94

3.40 Resolution on the Cherenkov angle in 2011 data for individual HPDs in the lower panel for photons reflected by a particular spherical-flat mirror pair (spherical mirror 2, flat mirror 12). 94

4.1 Identification efficiency on protons and corresponding retention factor on a minimal track sample, $p_T < 0.8\,\mathrm{GeV}/c$ and $2.5 \leq \eta < 3.0$. The DLL working points before (cross) and after (star) the optimisation are shown. 101

4.2 Distribution of d (see text) in the proton sample for $0.8 \leq p_T < 1.2\,\mathrm{GeV}/c$ at $\sqrt{\mathbf{s}} = 0.9\,\mathrm{TeV}$. 104

4.3 Raw antiparticle/particle ratios at $\sqrt{\mathbf{s}} = 0.9\,\mathrm{TeV}$ and magnet polarity down. 105

4.4 Raw ratios of different particle species at $\sqrt{\mathbf{s}} = 0.9\,\mathrm{TeV}$ and magnet polarity down. 105

4.5 Raw antiparticle/particle ratios at $\sqrt{\mathbf{s}} = 7\,\mathrm{TeV}$ and magnet polarity down. 105

4.6 Raw ratios of different particle species at $\sqrt{\mathbf{s}} = 7\,\mathrm{TeV}$ and magnet polarity down. 106

4.7 Invariant mass distributions reconstructed from the magnet down $\sqrt{s} = 7\,\mathrm{TeV}$ data in the analysis bin for which the positive final-state particle has $p_T \geq 1.2$ GeV and $3.5 \leq \eta < 4.0$ for (a) $K^0_S \to \pi^+\pi^-$, (b) $\Lambda^0 \to p\pi^-$ and (c) $\phi \to K^+K^-$. The results of unbinned maximum likelihood fits to the data are superimposed. 107

4.8 Distribution of $DLL(p-K)$ vs. $DLL(p-\pi)$ for particles from the RICH calibration samples with $p_{\mathrm{T}} > 1.2$ GeV/c and $3.5 < \eta \leq 4.0$. The dotted boxes represent the regions in which protons are selected in the DLL space. 111

4.9 Momentum distributions for different particle species in MC at $\sqrt{\mathbf{s}} = 0.9\,\mathrm{TeV}$ and $p_T < 0.8\,\mathrm{GeV/c}$, for a minimal track sample. If no DLL cut is applied, the momentum shape is dominated by pions. 113

4.10 Weighted distributions for protons in MC for $\sqrt{\mathbf{s}} = 0.9\,\mathrm{TeV}$, $0.8 < p_T < 1.2\,\mathrm{GeV/c}$ and $3.5 < \eta < 4$. Weighted protons from Λ decay in the calibration sample (red) are compared to true protons (green), unweighted calibration sample (blue) and all tracks (black). 116

4.11 Weighted distributions for protons in MC for $\sqrt{\mathbf{s}} = 7\,\mathrm{TeV}$, $0.8 < p_T < 1.2\,\mathrm{GeV/c}$ and $3.5 < \eta < 4$. Weighted protons from Λ decay in the calibration sample (red) are compared to true protons (green), unweighted calibration sample (blue) and all tracks (black). 117

4.12 MC truth PID efficiency of protons in the minimal track sample as a function of the estimated efficiency from the RICH calibration samples, also in MC. Data points are from negative and positive protons and both magnet polarities at $\sqrt{\mathbf{s}} = 0.9\,\mathrm{TeV}$. The dotted lines represent the gradient fit performed for each p_T bin while the blue line for which MC Truth = MC Calib is shown as a reference. 119

4.13 MC truth PID efficiency of kaons in the minimal track sample as a function of the estimated efficiency from the RICH calibration samples, also in MC. Data points are from negative and positive kaons and both magnet polarities at $\sqrt{\mathbf{s}} = 0.9\,\mathrm{TeV}$. The dotted lines represent the gradient fit performed for each p_T bin while the blue line for which MC Truth = MC Calib is shown as a reference. 119

4.14 MC truth PID efficiency of pions in the minimal track sample as a function of the estimated efficiency from the RICH calibration samples, also in MC. Data points are from negative and positive pions and both magnet polarities at $\sqrt{\mathbf{s}} = 0.9\,\mathrm{TeV}$. The dotted lines represent the gradient fit performed for each p_T bin while the blue line for which MC Truth = MC Calib is shown as a reference. 120

4.15 MC truth PID efficiency of protons in the minimal track sample as a function of the estimated efficiency from the RICH calibration samples, also in MC. Data points are from negative and positive protons and both magnet polarities at $\sqrt{\mathbf{s}} = 7\,\mathrm{TeV}$. The dotted lines represent the gradient fit performed for each p_T bin while the blue line for which MC Truth = MC Calib is shown as a reference. 120

4.16 MC truth PID efficiency of kaons in the minimal track sample as a function of the estimated efficiency from the RICH calibration samples, also in MC. Data points are from negative and positive kaons and both magnet polarities at $\sqrt{\mathbf{s}} = 7\,\mathrm{TeV}$. The dotted lines represent the gradient fit performed for each p_T bin while the blue line for which MC Truth = MC Calib is shown as a reference. 121

4.17 MC truth PID efficiency of pions in the minimal track sample as a function of the estimated efficiency from the RICH calibration samples, also in MC. Data points are from negative and positive pions and both magnet polarities at $\sqrt{\mathbf{s}} = 7\,\mathrm{TeV}$. The dotted lines represent the gradient fit performed for each p_T bin while the blue line for which MC Truth = MC Calib is shown as a reference. 121

4.18 Comparison of unweighted (black) and weighted efficiencies (empty marker) from the MC calibration sample with MC truth values (solid marker). Plots are for an average of protons and antiprotons at $\sqrt{\mathbf{s}} = 0.9\,\mathrm{TeV}$. . 122

4.19 Comparison of unweighted (black) and weighted efficiencies (empty marker) from the MC calibration sample with MC truth values (solid marker). Plots are for an average of positive and negative kaons at $\sqrt{\mathbf{s}} = 0.9\,\text{TeV}$. 123

4.20 Comparison of unweighted (black) and weighted efficiencies (empty marker) from the MC calibration sample with MC truth values (solid marker). Plots are for an average of positive and negative pions at $\sqrt{\mathbf{s}} = 0.9\,\text{TeV}$. 124

4.21 Comparison of unweighted (black) and weighted efficiencies (empty marker) from the MC calibration sample with MC Truth values (solid marker). Plots are for an average of protons and antiprotons at $\sqrt{\mathbf{s}} = 7\,\text{TeV}$ . . . 125

4.22 Comparison of unweighted (black) and weighted efficiencies (empty marker) from the MC calibration sample with MC truth values (solid marker). Plots are for an average of positive and negative kaons at $\sqrt{\mathbf{s}} = 7\,\text{TeV}$. 126

4.23 Comparison of unweighted (black) and weighted efficiencies (empty marker) from the MC calibration sample with MC truth values (solid marker). Plots are for an average of positive and negative pions at $\sqrt{\mathbf{s}} = 7\,\text{TeV}$. 127

4.24 Purity of selected samples at $\sqrt{\mathbf{s}} = 0.9\,\text{TeV}$ (magnet polarity up). . . . 129

4.25 Purity of selected samples at $\sqrt{\mathbf{s}} = 7\,\text{TeV}$ (magnet polarity up). 130

4.26 Correlation between p_T and p for protons with $3 < |\eta| < 3.5$. The relationship between p, p_T and η is demonstrated by the limits within which the data lie. 131

4.27 Measurement of the inelastic and total cross sections in aluminium for proton and antiprotons as a function of momentum [2]. 132

4.28 Reconstruction efficiencies for reconstructed long tracks as a function of momentum at $\sqrt{\mathbf{s}} = 7\,\text{TeV}$, as determined from MC. 133

4.29 Reconstruction efficiencies for reconstructed long tracks as a function of η at $\sqrt{\mathbf{s}} = 0.9\,\text{TeV}$, integrated over the full p_T range as determined from MC. 134

4.30 Reconstruction efficiency for reconstructed long tracks as a function of η at $\sqrt{\mathbf{s}} = 7\,\text{TeV}$, integrated over the full p_T range as determined from MC. 135
4.31 Comparison of the fully corrected $\bar{p}/p$ ratio in MC and the generator level prediction at $\sqrt{\mathbf{s}} = 0.9\,\text{TeV}$. 138
4.32 Comparison of the fully corrected K^-/K^+ ratio in MC and the generator level prediction at $\sqrt{\mathbf{s}} = 0.9\,\text{TeV}$. 138
4.33 Comparison of the fully corrected π^-/π^+ ratio in MC and the generator level prediction at $\sqrt{\mathbf{s}} = 0.9\,\text{TeV}$. 139
4.34 Comparison of the fully corrected $\bar{p}/p$ ratio in MC and the generator level prediction at $\sqrt{\mathbf{s}} = 7\,\text{TeV}$. 140
4.35 Comparison of the fully corrected K^-/K^+ ratio in MC and the generator level prediction at $\sqrt{\mathbf{s}} = 7\,\text{TeV}$. 140
4.36 Comparison of the fully corrected π^-/π^+ ratio in MC and the generator level prediction at $\sqrt{\mathbf{s}} = 7\,\text{TeV}$. 141
4.37 Comparison of the fully corrected $(p+\bar{p})/(K^+ + K^-)$ ratio in MC and the generator level prediction at $\sqrt{\mathbf{s}} = 0.9\,\text{TeV}$. 141
4.38 Comparison of the fully corrected $(p+\bar{p})/(\pi^+ + \pi^-)$ ratio in MC and the generator level prediction at $\sqrt{\mathbf{s}} = 0.9\,\text{TeV}$. 141
4.39 Comparison of the fully corrected $(K^+ + K^-)/(\pi^+ + \pi^-)$ ratio in MC and the generator level prediction at $\sqrt{\mathbf{s}} = 0.9\,\text{TeV}$. 142
4.40 Comparison of the fully corrected $(p+\bar{p})/(K^+ + K^-)$ ratio in MC and the generator level prediction at $\sqrt{\mathbf{s}} = 7\,\text{TeV}$. 142
4.41 Comparison of the fully corrected $(p+\bar{p})/(\pi^+ + \pi^-)$ ratio in MC and the generator level prediction at $\sqrt{\mathbf{s}} = 7\,\text{TeV}$. 142
4.42 Comparison of the fully corrected $(K^+ + K^-)/(\pi^+ + \pi^-)$ ratio in MC and the generator level prediction at $\sqrt{\mathbf{s}} = 7\,\text{TeV}$. 143

5.1 LHEP and CHIPS predictions for the inelastic and elastic cross sections of protons (antiprotons) on aluminium and beryllium as a function of momentum. Predictions for protons with a momentum above 5 GeV/c differ at the $\sim 20\%$ level. 147

5.2 Distributions of (a) N_{TT}, (b) N_{exp} and (c) $N_{diff} = N_{TT} - N_{exp}$ for tracks in the pion analysis with a measured momentum below the Cherenkov threshold for pions with $3.5 < \eta < 4.0$ and $0.8 < p_T < 1.2$ GeV. 149

5.3 Pull distribution at $\sqrt{\mathbf{s}} = 0.9$ TeV for magnet up and down. 155

5.4 Pull distribution at $\sqrt{\mathbf{s}} = 7$ TeV for magnet up and down. 156

5.5 $\bar{p}/p$ ratio and total uncertainty as a function of pseudo-rapidity. 162

5.6 K^-/K^+ ratio and total uncertainty as a function of pseudo-rapidity. . . 163

5.7 π^-/π^+ ratio and total uncertainty as a function of pseudo-rapidity. . . 164

5.8 $(p+\bar{p})/(K^+ + K^-)$ ratio and total uncertainty as a function of pseudo-rapidity. 165

5.9 $(p+\bar{p})/(\pi^+ + \pi^-)$ ratio and total uncertainty as a function of pseudo-rapidity. 166

5.10 $(K^+ + K^-)/(\pi^+ + \pi^-)$ ratio and total uncertainty as a function of pseudo-rapidity. 167

5.11 $\bar{p}/p$ ratio as a function of Δy. 168

5.12 $\bar{p}/p$ ratio as a function of Δy averaged in p_T (a) for LHCb data alone and (b) compared with other experiments. 169

5.13 Fit to the $\bar{p}/p$ ratio as measured from the LHCb and ALICE experiments (others superimposed). 169

List of Tables

2.1 Characteristics of the three radiators used in the LHCb RICH detectors. 44

3.1 The functions used to fit the peak variable distributions. 73

3.2 Total transformation parameters as a function of the magnification and distortion coefficients for each order of R_A. 79

4.1 Data and Monte Carlo samples. 97

4.2 DLL cuts for proton selection. 102

4.3 DLL cuts for kaon selection. 102

4.4 Number of selected tracks for each sample at $\sqrt{\mathbf{s}} = 0.9\,\text{TeV}$. 102

4.5 Number of selected tracks for each sample at $\sqrt{\mathbf{s}} = 7\,\text{TeV}$. 102

4.6 Total numbers of candidates reconstructed in each of the calibration modes. 106

4.7 PDFs used to describe the signal and background contributions to the K^0_S, Λ and ϕ invariant-mass distributions. 110

4.8 Fitted gradient values at $\sqrt{\mathbf{s}} = 0.9\,\text{TeV}$. Errors of 0.00 are less than 0.005. 120

4.9 Fitted gradient values at $\sqrt{\mathbf{s}} = 7\,\text{TeV}$. Errors of 0.00 are less than 0.005. 121

5.1 The range of systematic uncertainties for the $\bar{p}/p$, K^-/K^+ and π^-/π^+ ratios at $\sqrt{\mathbf{s}} = 0.90\,\text{TeV}$. All values given in %. 152

5.2 The range of systematic uncertainties for the $(p+\bar{p})/(K^+ + K^-)$, $(p+\bar{p})/(\pi^+ + \pi^-)$ and $(K^+ + K^-)/(\pi^+ + \pi^-)$ ratios at $\sqrt{\mathbf{s}} = 0.9\,\text{TeV}$. Values are given in %. 152

5.3 The range of systematic uncertainties for the $\bar{p}/p$, K^-/K^+ and π^-/π^+ ratios at $\sqrt{\mathbf{s}} = 7.00\,\text{TeV}$. All values given in %. 153

5.4 The range of systematic uncertainties for the $(p+\bar{p})/(K^+ + K^-)$, $(p+\bar{p})/(\pi^+ + \pi^-)$ and $(K^+ + K^-)/(\pi^+ + \pi^-)$ ratios at $\sqrt{\mathbf{s}} = 7.0\,\text{TeV}$. Values are given in %. 153

5.5 The $\bar{p}/p$ ratio and uncertainty (statistical + systematic) for data taken at $\sqrt{\mathbf{s}} = 0.9\,\text{TeV}$ as a function of η. 158

5.6 The K^-/K^+ ratio and uncertainty (statistical + systematic) for data taken at $\sqrt{\mathbf{s}} = 0.9\,\text{TeV}$ as a function of η. 158

5.7 The π^-/π^+ ratio and uncertainty (statistical + systematic) for data taken at $\sqrt{\mathbf{s}} = 0.9\,\text{TeV}$ as a function of η. 158

5.8 The $\bar{p}/p$ ratio and uncertainty (statistical + systematic) for data taken at $\sqrt{\mathbf{s}} = 7.0\,\text{TeV}$ as a function of η. 159

5.9 The K^-/K^+ ratio and uncertainty (statistical + systematic) for data taken at $\sqrt{\mathbf{s}} = 7.0\,\text{TeV}$ as a function of η. 159

5.10 The π^-/π^+ ratio and uncertainty (statistical + systematic) for data taken at $\sqrt{\mathbf{s}} = 7.0\,\text{TeV}$ as a function of η. 159

5.11 The $(p+\bar{p})/(K^+ + K^-)$ ratio and uncertainty (statistical + systematic) for data taken at $\sqrt{\mathbf{s}} = 0.9\,\text{TeV}$ as a function of η. 159

5.12 The $(p+\bar{p})/(\pi^+ + \pi^-)$ ratio and uncertainty (statistical + systematic) for data taken at $\sqrt{\mathbf{s}} = 0.9\,\text{TeV}$ as a function of η. 160

5.13 The $(K^+ + K^-)/(\pi^+ + \pi^-)$ ratio and uncertainty (statistical + systematic) for data taken at $\sqrt{\mathbf{s}} = 0.9\,\text{TeV}$ as a function of η. 160

5.14 The $(p+\bar{p})/(K^+ + K^-)$ ratio and uncertainty (statistical + systematic) for data taken at $\sqrt{\mathbf{s}} = 7.0\,\text{TeV}$ as a function of η. 160

5.15 The $(p+\bar{p})/(\pi^+ + \pi^-)$ ratio and uncertainty (statistical + systematic) for data taken at $\sqrt{\mathbf{s}} = 7.0\,\text{TeV}$ as a function of η. 160

5.16 The $(K^+ + K^-)/(\pi^+ + \pi^-)$ ratio and uncertainty (statistical + systematic) for data taken at $\sqrt{\mathbf{s}} = 7.0\,\text{TeV}$ as a function of η. 161

5.17 The $\bar{p}/p$ ratio and uncertainty averaged in p_T as a function of the rapidity loss, Δy. 163

A.1 PID efficiencies for positive tracks with $p_T < 0.8\,\mathrm{GeV}/c$ and magnet polarity down. 172

A.2 PID efficiencies for positive tracks with $0.8\,\mathrm{GeV}/c \leq p_T < 1.2\,\mathrm{GeV}/c$ and magnet polarity down. 173

A.3 PID efficiencies for positive tracks with $p_T \geq 1.2\,\mathrm{GeV}/c$ and magnet polarity down. 174

A.4 PID efficiencies for negative tracks with $p_T < 0.8\,\mathrm{GeV}/c$ and magnet polarity down. 174

A.5 PID efficiencies for negative tracks with $0.8\,\mathrm{GeV}/c \leq p_T < 1.2\,\mathrm{GeV}/c$ and magnet polarity down. 175

A.6 PID efficiencies for negative tracks with $p_T \geq 1.2\,\mathrm{GeV}/c$ and magnet polarity down. 175

A.7 PID efficiencies for positive tracks with $p_T < 0.8\,\mathrm{GeV}/c$ and magnet polarity up. 176

A.8 PID efficiencies for positive tracks with $0.8\,\mathrm{GeV}/c \leq p_T < 1.2\,\mathrm{GeV}/c$ and magnet polarity up. 176

A.9 PID efficiencies for positive tracks with $p_T \geq 1.2\,\mathrm{GeV}/c$ and magnet polarity up. 177

A.10 PID efficiencies for negative tracks with $p_T < 0.8\,\mathrm{GeV}/c$ and magnet polarity up. 177

A.11 PID efficiencies for negative tracks with $0.8\,\mathrm{GeV}/c \leq p_T < 1.2\,\mathrm{GeV}/c$ and magnet polarity up. 178

A.12 PID efficiencies for negative tracks with $p_T \geq 1.2\,\mathrm{GeV}/c$ and magnet polarity up. 178

A.13 PID efficiencies weighted at $\sqrt{s} = 0.9\,\mathrm{TeV}$ for positive tracks with $p_T < 0.8\,\mathrm{GeV}/c$ and magnet polarity down. 179

A.14 PID efficiencies weighted at $\sqrt{s} = 0.9\,\text{TeV}$ for positive tracks with $0.8\,\text{GeV}/c \leq p_T < 1.2\,\text{GeV}/c$ and magnet polarity down. 180

A.15 PID efficiencies weighted at $\sqrt{s} = 0.9\,\text{TeV}$ for positive tracks with $p_T \geq 1.2\,\text{GeV}/c$ and magnet polarity down. 180

A.16 PID efficiencies weighted at $\sqrt{s} = 0.9\,\text{TeV}$ for negative tracks with $p_T < 0.8\,\text{GeV}/c$ and magnet polarity down. 181

A.17 PID efficiencies weighted at $\sqrt{s} = 0.9\,\text{TeV}$ for negative tracks with $0.8\,\text{GeV}/c \leq p_T < 1.2\,\text{GeV}/c$ and magnet polarity down. 181

A.18 PID efficiencies weighted at $\sqrt{s} = 0.9\,\text{TeV}$ for negative tracks with $p_T \geq 1.2\,\text{GeV}/c$ and magnet polarity down. 182

A.19 PID efficiencies weighted at $\sqrt{s} = 0.9\,\text{TeV}$ for positive tracks with $p_T < 0.8\,\text{GeV}/c$ and magnet polarity up. 182

A.20 PID efficiencies weighted at $\sqrt{s} = 0.9\,\text{TeV}$ for positive tracks with $0.8\,\text{GeV}/c \leq p_T < 1.2\,\text{GeV}/c$ and magnet polarity up. 183

A.21 PID efficiencies weighted at $\sqrt{s} = 0.9\,\text{TeV}$ for positive tracks with $p_T \geq 1.2\,\text{GeV}/c$ and magnet polarity up. 183

A.22 PID efficiencies weighted at $\sqrt{s} = 0.9\,\text{TeV}$ for negative tracks with $p_T < 0.8\,\text{GeV}/c$ and magnet polarity up. 184

A.23 PID efficiencies weighted at $\sqrt{s} = 0.9\,\text{TeV}$ for negative tracks with $0.8\,\text{GeV}/c \leq p_T < 1.2\,\text{GeV}/c$ and magnet polarity up. 184

A.24 PID efficiencies weighted at $\sqrt{s} = 0.9\,\text{TeV}$ for negative tracks with $p_T \geq 1.2\,\text{GeV}/c$ and magnet polarity up. 185

A.25 PID efficiencies weighted at $\sqrt{s} = 7\,\text{TeV}$ for positive tracks with $p_T < 0.8\,\text{GeV}/c$ and magnet polarity down. 186

A.26 PID efficiencies weighted at $\sqrt{s} = 7\,\text{TeV}$ for positive tracks with $0.8\,\text{GeV}/c \leq p_T < 1.2\,\text{GeV}/c$ and magnet polarity down. 187

A.27 PID efficiencies weighted at $\sqrt{s} = 7\,\text{TeV}$ for positive tracks with $p_T \geq 1.2\,\text{GeV}/c$ and magnet polarity down. 187

A.28 PID efficiencies weighted at $\sqrt{s} = 7\,\text{TeV}$ for negative tracks with $p_T < 0.8\,\text{GeV}/c$ and magnet polarity down. 188

A.29 PID efficiencies weighted at $\sqrt{s} = 7\,\text{TeV}$ for negative tracks with $0.8\,\text{GeV}/c \leq p_T < 1.2\,\text{GeV}/c$ and magnet polarity down. 188

A.30 PID efficiencies weighted at $\sqrt{s} = 7\,\text{TeV}$ for negative tracks with $p_T \geq 1.2\,\text{GeV}/c$ and magnet polarity down. 189

A.31 PID efficiencies weighted at $\sqrt{s} = 7\,\text{TeV}$ for positive tracks with $p_T < 0.8\,\text{GeV}/c$ and magnet polarity up. 189

A.32 PID efficiencies weighted at $\sqrt{s} = 7\,\text{TeV}$ for positive tracks with $0.8\,\text{GeV}/c \leq p_T < 1.2\,\text{GeV}/c$ and magnet polarity up. 190

A.33 PID efficiencies weighted at $\sqrt{s} = 7\,\text{TeV}$ for positive tracks with $p_T \geq 1.2\,\text{GeV}/c$ and magnet polarity up. 190

A.34 PID efficiencies weighted at $\sqrt{s} = 7\,\text{TeV}$ for negative tracks with $p_T < 0.8\,\text{GeV}/c$ and magnet polarity up. 191

A.35 PID efficiencies weighted at $\sqrt{s} = 7\,\text{TeV}$ for negative tracks with $0.8\,\text{GeV}/c \leq p_T < 1.2\,\text{GeV}/c$ and magnet polarity up. 191

A.36 PID efficiencies weighted at $\sqrt{s} = 7\,\text{TeV}$ for negative tracks with $p_T \geq 1.2\,\text{GeV}/c$ and magnet polarity up. 192

B.1 Ghost track information for protons, magnet down, $p_T < 0.8$ and $\sqrt{\mathbf{s}} = 0.9\,\text{TeV}$. 193

B.2 Ghost track information for protons, magnet down, $0.8 < p_T < 1.2$ and $\sqrt{\mathbf{s}} = 0.9\,\text{TeV}$. 193

B.3 Ghost track information for protons, magnet down, $p_T > 1.2$ and $\sqrt{\mathbf{s}} = 0.9\,\text{TeV}$. 194

B.4 Ghost track information for kaons, magnet down, $p_T < 0.8$ and $\sqrt{\mathbf{s}} = 0.9\,\text{TeV}$. 194

B.5 Ghost track information for kaons, magnet down, $0.8 < p_T < 1.2$ and $\sqrt{\mathbf{s}} = 0.9\,\text{TeV}$. 194

B.6 Ghost track information for kaons, magnet down, $p_T > 1.2$ and $\sqrt{\mathbf{s}} =$ 0.9 TeV. 195

B.7 Ghost track information for pions, magnet down, $p_T < 0.8$ and $\sqrt{\mathbf{s}} =$ 0.9 TeV. 195

B.8 Ghost track information for pions, magnet down, $0.8 < p_T < 1.2$ and $\sqrt{\mathbf{s}} = 0.9$ TeV. 195

B.9 Ghost track information for pions, magnet down, $p_T > 1.2$ and $\sqrt{\mathbf{s}} =$ 0.9 TeV. 196

B.10 Ghost track information for protons, magnet down, $p_T < 0.8$ and $\sqrt{\mathbf{s}} =$ 7.0 TeV. 196

B.11 Ghost track information for protons, magnet down, $0.8 < p_T < 1.2$ and $\sqrt{\mathbf{s}} = 7.0$ TeV. 196

B.12 Ghost track information for protons, magnet down, $p_T > 1.2$ and $\sqrt{\mathbf{s}} =$ 7.0 TeV. 197

B.13 Ghost track information for kaons, magnet down, $p_T < 0.8$ and $\sqrt{\mathbf{s}} =$ 7.0 TeV. 197

B.14 Ghost track information for kaons, magnet down, $0.8 < p_T < 1.2$ and $\sqrt{\mathbf{s}} = 7.0$ TeV. 197

B.15 Ghost track information for kaons, magnet down, $p_T > 1.2$ and $\sqrt{\mathbf{s}} =$ 7.0 TeV. 198

B.16 Ghost track information for pions, magnet down, $p_T < 0.8$ and $\sqrt{\mathbf{s}} =$ 7.0 TeV. 198

B.17 Ghost track information for pions, magnet down, $0.8 < p_T < 1.2$ and $\sqrt{\mathbf{s}} = 7.0$ TeV. 198

B.18 Ghost track information for pions, magnet down, $p_T > 1.2$ and $\sqrt{\mathbf{s}} =$ 7.0 TeV. 199

C.1 Non-prompt contamination information from MC for protons, magnet down, $p_T < 0.8$ and $\sqrt{\mathbf{s}} = 0.9$ TeV. 200

C.2 Non-prompt contamination information from MC for protons, magnet down, $0.8 < p_T < 1.2$ and $\sqrt{\mathbf{s}} = 0.9\,\text{TeV}$. 200
C.3 Non-prompt contamination information from MC for protons, magnet down, $p_T > 1.2$ and $\sqrt{\mathbf{s}} = 0.9\,\text{TeV}$. 200
C.4 Non-prompt contamination information from MC for kaons, magnet down, $p_T < 0.8$ and $\sqrt{\mathbf{s}} = 0.9\,\text{TeV}$. 201
C.5 Non-prompt contamination information from MC for kaons, magnet down, $0.8 < p_T < 1.2$ and $\sqrt{\mathbf{s}} = 0.9\,\text{TeV}$. 201
C.6 Non-prompt contamination information from MC for kaons, magnet down, $p_T > 1.2$ and $\sqrt{\mathbf{s}} = 0.9\,\text{TeV}$. 201
C.7 Non-prompt contamination information from MC for pions, magnet down, $p_T < 0.8$ and $\sqrt{\mathbf{s}} = 0.9\,\text{TeV}$. 201
C.8 Non-prompt contamination information from MC for pions, magnet down, $0.8 < p_T < 1.2$ and $\sqrt{\mathbf{s}} = 0.9\,\text{TeV}$. 201
C.9 Non-prompt contamination information from MC for pions, magnet down, $p_T > 1.2$ and $\sqrt{\mathbf{s}} = 0.9\,\text{TeV}$. 201
C.10 Non-prompt contamination information from MC for protons, magnet down, $p_T < 0.8$ and $\sqrt{\mathbf{s}} = 7.0\,\text{TeV}$. 201
C.11 Non-prompt contamination information from MC for protons, magnet down, $0.8 < p_T < 1.2$ and $\sqrt{\mathbf{s}} = 7.0\,\text{TeV}$. 202
C.12 Non-prompt contamination information from MC for protons, magnet down, $p_T > 1.2$ and $\sqrt{\mathbf{s}} = 7.0\,\text{TeV}$. 202
C.13 Non-prompt contamination information from MC for kaons, magnet down, $p_T < 0.8$ and $\sqrt{\mathbf{s}} = 7.0\,\text{TeV}$. 202
C.14 Non-prompt contamination information from MC for kaons, magnet down, $0.8 < p_T < 1.2$ and $\sqrt{\mathbf{s}} = 7.0\,\text{TeV}$. 202
C.15 Non-prompt contamination information from MC for kaons, magnet down, $p_T > 1.2$ and $\sqrt{\mathbf{s}} = 7.0\,\text{TeV}$. 202

C.16 Non-prompt contamination information from MC for pions, magnet down, $p_T < 0.8$ and $\sqrt{\mathbf{s}} = 7.0\,\text{TeV}$. 202

C.17 Non-prompt contamination information from MC for pions, magnet down, $0.8 < p_T < 1.2$ and $\sqrt{\mathbf{s}} = 7.0\,\text{TeV}$. 202

C.18 Non-prompt contamination information from MC for pions, magnet down, $p_T > 1.2$ and $\sqrt{\mathbf{s}} = 7.0\,\text{TeV}$. 203

D.1 Mean rapidity values for protons in MC and Data for $p_T < 0.8$ GeV and $\sqrt{\mathbf{s}} = 0.9\,\text{TeV}$. 204

D.2 Mean rapidity values for protons in MC and Data for $0.8 < p_T < 1.2$ GeV and $\sqrt{\mathbf{s}} = 0.9\,\text{TeV}$. 204

D.3 Mean rapidity values for protons in MC and Data for $p_T > 1.2$ GeV and $\sqrt{\mathbf{s}} = 0.9\,\text{TeV}$. 205

D.4 Mean rapidity values for kaons in MC and Data for $p_T < 0.8$ GeV and $\sqrt{\mathbf{s}} = 0.9\,\text{TeV}$. 205

D.5 Mean rapidity values for kaons in MC and Data for $0.8 < p_T < 1.2$ GeV and $\sqrt{\mathbf{s}} = 0.9\,\text{TeV}$. 205

D.6 Mean rapidity values for kaons in MC and Data for $p_T > 1.2$ GeV and $\sqrt{\mathbf{s}} = 0.9\,\text{TeV}$. 205

D.7 Mean rapidity values for pions in MC and Data for $p_T < 0.8$ GeV and $\sqrt{\mathbf{s}} = 0.9\,\text{TeV}$. 205

D.8 Mean rapidity values for pions in MC and Data for $0.8 < p_T < 1.2$ GeV and $\sqrt{\mathbf{s}} = 0.9\,\text{TeV}$. 206

D.9 Mean rapidity values for pions in MC and Data for $p_T > 1.2$ GeV and $\sqrt{\mathbf{s}} = 0.9\,\text{TeV}$. 206

D.10 Mean rapidity values for protons in MC and Data for $p_T < 0.8$ GeV and $\sqrt{\mathbf{s}} = 7.0\,\text{TeV}$. 206

D.11 Mean rapidity values for protons in MC and Data for $0.8 < p_T < 1.2$ GeV and $\sqrt{\mathbf{s}} = 7.0\,\text{TeV}$. 206

D.12 Mean rapidity values for protons in MC and Data for $p_T > 1.2$ GeV and $\sqrt{\mathbf{s}} = 7.0\,\text{TeV}$. 206

D.13 Mean rapidity values for kaons in MC and Data for $p_T < 0.8$ GeV and $\sqrt{\mathbf{s}} = 7.0\,\text{TeV}$. 207

D.14 Mean rapidity values for kaons in MC and Data for $0.8 < p_T < 1.2$ GeV and $\sqrt{\mathbf{s}} = 7.0\,\text{TeV}$. 207

D.15 Mean rapidity values for kaons in MC and Data for $p_T > 1.2$ GeV and $\sqrt{\mathbf{s}} = 7.0\,\text{TeV}$. 207

D.16 Mean rapidity values for pions in MC and Data for $p_T < 0.8$ GeV and $\sqrt{\mathbf{s}} = 7.0\,\text{TeV}$. 207

D.17 Mean rapidity values for pions in MC and Data for $0.8 < p_T < 1.2$ GeV and $\sqrt{\mathbf{s}} = 7.0\,\text{TeV}$. 207

D.18 Mean rapidity values for pions in MC and Data for $p_T > 1.2$ GeV and $\sqrt{\mathbf{s}} = 7.0\,\text{TeV}$. 208

E.1 Relative statistical and systematic uncertainties in for the ratio $\bar{p}/p$ in the range $p_T < 0.8$ for each bin of η at $\sqrt{\mathbf{s}} = 0.9\,\text{TeV}$. 209

E.2 Relative statistical and systematic uncertainties in for the ratio $\bar{p}/p$ in the range $0.8 < p_T < 1.2$ for each bin of η at $\sqrt{\mathbf{s}} = 0.9\,\text{TeV}$. 209

E.3 Relative statistical and systematic uncertainties in for the ratio $\bar{p}/p$ in the range $p_T > 1.2$ for each bin of η at $\sqrt{\mathbf{s}} = 0.9\,\text{TeV}$. 210

E.4 Relative statistical and systematic uncertainties in for the ratio K^-/K^+ in the range $p_T < 0.8$ for each bin of η at $\sqrt{\mathbf{s}} = 0.9\,\text{TeV}$. 210

E.5 Relative statistical and systematic uncertainties in for the ratio K^-/K^+ in the range $0.8 < p_T < 1.2$ for each bin of η at $\sqrt{\mathbf{s}} = 0.9\,\text{TeV}$. 210

E.6 Relative statistical and systematic uncertainties in for the ratio K^-/K^+ in the range $p_T > 1.2$ for each bin of η at $\sqrt{\mathbf{s}} = 0.9\,\text{TeV}$. 211

E.7 Relative statistical and systematic uncertainties in for the ratio π^-/π^+ in the range $p_T < 0.8$ for each bin of η at $\sqrt{\mathbf{s}} = 0.9\,\text{TeV}$. 211

E.8 Relative statistical and systematic uncertainties in for the ratio π^-/π^+ in the range $0.8 < p_T < 1.2$ for each bin of η at $\sqrt{\mathbf{s}} = 0.9\,\text{TeV}$. 211

E.9 Relative statistical and systematic uncertainties in for the ratio π^-/π^+ in the range $p_T > 1.2$ for each bin of η at $\sqrt{\mathbf{s}} = 0.9\,\text{TeV}$. 212

E.10 Relative statistical and systematic uncertainties in for the ratio $(p + \bar{p})/(K^+ + K^-)$ in the range $p_T < 0.8$ for each bin of η at $\sqrt{\mathbf{s}} = 0.9\,\text{TeV}$. 212

E.11 Relative statistical and systematic uncertainties in for the ratio $(p + \bar{p})/(K^+ + K^-)$ in the range $0.8 < p_T < 1.2$ for each bin of η at $\sqrt{\mathbf{s}} = 0.9\,\text{TeV}$. 212

E.12 Relative statistical and systematic uncertainties in for the ratio $(p + \bar{p})/(K^+ + K^-)$ in the range $p_T > 1.2$ for each bin of η at $\sqrt{\mathbf{s}} = 0.9\,\text{TeV}$. 213

E.13 Relative statistical and systematic uncertainties in for the ratio $(p + \bar{p})/(\pi^+ + \pi^-)$ in the range $p_T < 0.8$ for each bin of η at $\sqrt{\mathbf{s}} = 0.9\,\text{TeV}$. . 213

E.14 Relative statistical and systematic uncertainties in for the ratio $(p + \bar{p})/(\pi^+ + \pi^-)$ in the range $0.8 < p_T < 1.2$ for each bin of η at $\sqrt{\mathbf{s}} = 0.9\,\text{TeV}$.213

E.15 Relative statistical and systematic uncertainties in for the ratio $(p + \bar{p})/(\pi^+ + \pi^-)$ in the range $p_T > 1.2$ for each bin of η at $\sqrt{\mathbf{s}} = 0.9\,\text{TeV}$. . 214

E.16 Relative statistical and systematic uncertainties in for the ratio $(K^+ + K^-)/(\pi^+ + \pi^-)$ in the range $p_T < 0.8$ for each bin of η at $\sqrt{\mathbf{s}} = 0.9\,\text{TeV}$. 214

E.17 Relative statistical and systematic uncertainties in for the ratio $(K^+ + K^-)/(\pi^+ + \pi^-)$ in the range $0.8 < p_T < 1.2$ for each bin of η at $\sqrt{\mathbf{s}} = 0.9\,\text{TeV}$. 214

E.18 Relative statistical and systematic uncertainties in for the ratio $(K^+ + K^-)/(\pi^+ + \pi^-)$ in the range $p_T > 1.2$ for each bin of η at $\sqrt{\mathbf{s}} = 0.9\,\text{TeV}$. 215

E.19 Relative statistical and systematic uncertainties in for the ratio $\bar{p}/p$ in the range $p_T < 0.8$ for each bin of η at $\sqrt{\mathbf{s}} = 7.0\,\text{TeV}$. 216

E.20 Relative statistical and systematic uncertainties in for the ratio $\bar{p}/p$ in the range $0.8 < p_T < 1.2$ for each bin of η at $\sqrt{\mathbf{s}} = 7.0\,\text{TeV}$. 216

E.21 Relative statistical and systematic uncertainties in for the ratio $\bar{p}/p$ in the range $p_T > 1.2$ for each bin of η at $\sqrt{\mathbf{s}} = 7.0\,\text{TeV}$. 216

E.22 Relative statistical and systematic uncertainties in for the ratio K^-/K^+ in the range $p_T < 0.8$ for each bin of η at $\sqrt{\mathbf{s}} = 7.0\,\text{TeV}$. 217

E.23 Relative statistical and systematic uncertainties in for the ratio K^-/K^+ in the range $0.8 < p_T < 1.2$ for each bin of η at $\sqrt{\mathbf{s}} = 7.0\,\text{TeV}$. 217

E.24 Relative statistical and systematic uncertainties in for the ratio K^-/K^+ in the range $p_T > 1.2$ for each bin of η at $\sqrt{\mathbf{s}} = 7.0\,\text{TeV}$. 217

E.25 Relative statistical and systematic uncertainties in for the ratio π^-/π^+ in the range $p_T < 0.8$ for each bin of η at $\sqrt{\mathbf{s}} = 7.0\,\text{TeV}$. 218

E.26 Relative statistical and systematic uncertainties in for the ratio π^-/π^+ in the range $0.8 < p_T < 1.2$ for each bin of η at $\sqrt{\mathbf{s}} = 7.0\,\text{TeV}$. 218

E.27 Relative statistical and systematic uncertainties in for the ratio π^-/π^+ in the range $p_T > 1.2$ for each bin of η at $\sqrt{\mathbf{s}} = 7.0\,\text{TeV}$. 218

E.28 Relative statistical and systematic uncertainties in for the ratio $(p + \bar{p})/(K^+ + K^-)$ in the range $p_T < 0.8$ for each bin of η at $\sqrt{\mathbf{s}} = 7.0\,\text{TeV}$. 219

E.29 Relative statistical and systematic uncertainties in for the ratio $(p + \bar{p})/(K^+ + K^-)$ in the range $0.8 < p_T < 1.2$ for each bin of η at $\sqrt{\mathbf{s}} = 7.0\,\text{TeV}$. 219

E.30 Relative statistical and systematic uncertainties in for the ratio $(p + \bar{p})/(K^+ + K^-)$ in the range $p_T > 1.2$ for each bin of η at $\sqrt{\mathbf{s}} = 7.0\,\text{TeV}$. 219

E.31 Relative statistical and systematic uncertainties in for the ratio $(p + \bar{p})/(\pi^+ + \pi^-)$ in the range $p_T < 0.8$ for each bin of η at $\sqrt{\mathbf{s}} = 7.0\,\text{TeV}$. . 220

E.32 Relative statistical and systematic uncertainties in for the ratio $(p + \bar{p})/(\pi^+ + \pi^-)$ in the range $0.8 < p_T < 1.2$ for each bin of η at $\sqrt{\mathbf{s}} = 7.0\,\text{TeV}$. 220

E.33 Relative statistical and systematic uncertainties in for the ratio $(p + \bar{p})/(\pi^+ + \pi^-)$ in the range $p_T > 1.2$ for each bin of η at $\sqrt{\mathbf{s}} = 7.0\,\text{TeV}$. . 220

E.34 Relative statistical and systematic uncertainties in for the ratio $(K^+ + K^-)/(\pi^+ + \pi^-)$ in the range $p_T < 0.8$ for each bin of η at $\sqrt{\mathbf{s}} = 7.0\,\text{TeV}$. 221

E.35 Relative statistical and systematic uncertainties in for the ratio $(K^+ + K^-)/(\pi^+ + \pi^-)$ in the range $0.8 < p_T < 1.2$ for each bin of η at $\sqrt{\mathbf{s}} = 7.0\,\text{TeV}$. 221

E.36 Relative statistical and systematic uncertainties in for the ratio $(K^+ + K^-)/(\pi^+ + \pi^-)$ in the range $p_T > 1.2$ for each bin of η at $\sqrt{\mathbf{s}} = 7.0\,\text{TeV}$. 221

Chapter 1

High energy pp collisions in the forward region

The experiments at the LHC are specifically designed to investigate the Standard Model (SM) and search for New Physics (NP) in a hadronic environment. Therefore, a proper understanding of strong interaction is required to interpret data and produce precise physics results.

Within the SM, Quantum Chromodynamics (QCD) is the theory of strong interactions describing the interaction between the hadron constituents, quarks and gluons. While QCD is well established on a purely theoretical level and in principle allows arbitrarily precise calculations for hadronic processes, other important effects are currently better described by phenomenological models. In fact, relevant quantities in QCD, such as interaction cross-sections, can be expressed as a power series, or *perturbative* series, of the strong coupling constant, α_s, which is a function of the energy scale. Usually only the first orders can be calculated in practice, meaning that α_s is required to be $\ll 1$ for the series to converge quickly. However, as described in Section 1.1, α_s approaches unity towards low energy scales. Therefore, at energy scales below $\sim 1\,\text{GeV}$, commonly referred to as the *soft-QCD* regime, perturbative calculations become practically impossible and hence phenomenological approaches are preferred.

Several Monte Carlo (MC) event generators, in the form of software packages, try to combine the theoretical description of the *hard* (perturbative) part and the *soft*

(non-perturbative) part of the hadronic interactions into a realistic simulation of the proton-proton (pp) collision event. They differ in the modelling of some aspect of the interaction and need some degree of *tuning* to optimise model parameters, particularly for the non-perturbative part. The *tuning* of a generator is that process in which existing data are used to constrain free parameters of theoretical models. The LHC produces a copious number of soft events, that can be exploited to understand the phenomenology and tune the MC generators.

Soft-QCD measurements from LHCb can provide a valuable input to MC models in the forward region, in the pseudorapidity[1] range of $2 < \eta < 5$, and at transverse momenta as low as $\sim 100\,\mathrm{MeV}/c$. These measurements are usually performed through the analysis of "minimum bias" events. The term "minimum bias" is an experimental term that defines a certain class of events selected using loose trigger requirements to ensure they are as inclusive as possible [3].

This chapter is organised as follows: first a brief introduction on the general landscape of soft pp interactions will be given, to concentrate afterwards on the baryon number transport (BNT) and the hadronisation process; these concepts will then be connected to the measurement of prompt hadron production ratios for which recent results at the LHC will be provided.

Given the complexity and vastness of the subject, only the aspects relevant for the analysis presented in Chapter 4 and 5 will be addressed.

1.1 Quantum Chromodynamics

In QCD, quarks and gluons carry a *colour charge* which is the analogy of the electric charge in electrodynamics. While electrically charged particles carry two different charges, conventionally labelled as "positive" and "negative", quarks (antiquarks) carry colour charges conventionally labelled *green* (*antigreen*), *red* (*antired*) and *blue* (*antiblue*). QCD is a gauge theory based on the gauge group SU(3) which can be explicitly

[1] The pseudorapidity of a particle is defined in terms of its momentum, p, and the momentum component along the beam axis, p_z, as $\eta = (p - p_z)/(p + p_z)$.

identified by a set of unitary 3×3 matrices with a determinant of unity representing gluons in colour space. The SU(3) group has height generators often represented by the Gell-Mann matrices (the analogue of the Pauli matrices in SU(2)), λ^a. These matrices can act both on each other (gluon self-interactions) and on a set of complex 3-vectors which represent quarks in colour space.

The Lagrangian of QCD is

$$\mathcal{L} = \bar{\psi}_q^i (i\gamma^\mu)(D_\mu)_{ij}\psi_q^j - m_q \bar{\psi}_q^i \psi_{qi} - \frac{1}{4} F_{\mu\nu}^a F^{a\mu\nu}, \tag{1.1}$$

where ψ_q^i denotes a quark field with colour index i, γ^μ is a Dirac matrix to express the vector nature of strong interaction, m_q is the quark mass, $F_{\mu\nu}^a$ is the field strength tensor for a gluon with colour index a, μ and ν are Lorentz indices and D_μ is the covariant derivative in QCD:

$$(D_\mu)_{ij} = \delta_{ij}\partial_\mu - i g_s \frac{1}{2} \lambda_{ij}^a A_\mu^a, \tag{1.2}$$

where g_s is related to the strong coupling α_s ($g_s = 4\pi\alpha_s$) and A_μ^a is the gluon field. Expanding the $F_{\mu\nu}^a F^{a\mu\nu}$ term in Eq. 1.1, it can be seen that, since the λ matrices do not commute (i.e. SU(3) is non-abelian) there are three-gluon and four-gluon vertices. The presence of gluon self-interaction terms means that gluons carry a colour charge. This is the major difference between QCD and other quantum field theories, such as Quantum Electrodynamic (QED) where the photon does not carry an electric charge. These extra-terms are partially responsible for the so-called *colour confinement*. The colour confinement forces the quarks to be always bound into hadrons and not being observed as isolated particles. In fact, if two quarks are pulled apart, the energy stored in the field lines grows with the distance between the quarks; hence they cannot exist as free particles. The field lines can only be broken by the creation of a new quark-antiquark ($q\bar{q}$) pair which screens the colour field and leads to the production of two separate hadrons, as described in Section 1.4.

To a first approximation, QCD is also *scale invariant*. This feature, also known

as Bjorken scaling, implies that, in the final state of a generic hadronic interaction, at any scale one finds a repeated pattern of jets within jets, similar to a fractal. In practice, this would allow the properties of high energy interactions to be determined only by dimensionless kinematic quantities such as scattering angles or ratios of energy. However, the scale invariance is broken by the running of the strong coupling constant with energy. The dependence can be parametrized as a function of the energy scale of the process, Q:

$$\alpha_s(Q^2) = \alpha_s(M_Z^2)\frac{1}{1 + b_0\alpha_s(M_Z^2)\log\frac{Q^2}{M_Z^2} + \mathcal{O}(\alpha_s^2)}, \tag{1.3}$$

where the $\alpha_s(M_Z^2)$ is the coupling constant at an energy scale equal to the Z boson mass and b_0 is a parameter which depends on the structure of QCD and the number of contributing quark flavours but is in general positive. Therefore, as the energy scale increases the coupling constant decreases, this is the famous *asymptotic freedom*. If the energy scale is sufficiently high, quarks inside hadrons act almost as free particles when probed and perturbative QCD calculations can be performed. On the other hand, as the energy scale decreases, the coupling constant increases to a point at which perturbative calculations are not practically feasible as higher and higher order terms in α_s are no longer negligible. The latter regime is typical of *soft-QCD* physics and of particular relevance for the topics exposed in this thesis.

1.2 Regge Theory for Strong Interacting Particles

Regge theory was initially developed by Tullio Regge [4] to study non-relativistic scattering by a Yukawa potential. Subsequently, it has been extended to models for the relativistic collision of strongly interacting particles [5, 1] and it is commonly used to describe minimum soft hadronic scattering. The theory is concerned with the study of the analytic properties of the scattering amplitude as a function of angular momentum, l, which in general is allowed to take any complex value.

Considering the scattering process between two spinless particles with four-momenta

p_1 and p_2, within Regge theory the partial wave amplitude, f_l, is analytically extended to $f(l, s)$, where $l \in \mathbb{C}$. It holds that, for integer values of l we can write

$$f(l, s) = f_l(s), \tag{1.4}$$

where $s = (p_1 + p_2)^2$ is one of the well-known Mandelstam variables [6].

Interaction cross sections are enhanced when s corresponds to a resonance. If the resonance corresponds to a state of (integer) angular momentum l, the partial wave amplitude has a pole (a *Regge pole*) of the form [7]

$$f(l, s) \propto \frac{1}{l - \alpha_0(s)}, \tag{1.5}$$

where $\alpha(s)$ is the so called *Regge trajectory*.

In general, the Regge pole model states that there exist (complex) Regge trajectories $\alpha_n(s)$ that correlate certain resonance sequences such that, whenever $s = m_r^2$ (where m_r is the mass of a resonance), then $\alpha(m_r^2) = J_r$ (where J_r is the spin of the particle)[7]. Similarly, Regge trajectories can also be a function of the Mandelstam variable t [6].

In the case of sequences of nuclear resonances, experimental results suggest that Regge trajectories are approximately linear in s. As an example, Figure 1.1 shows two resonance sequences seen in proton-pion scattering. The trajectory for the N sequence

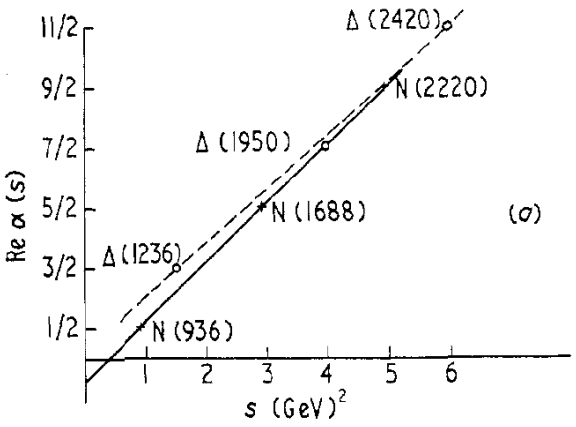


Figure 1.1: Chew-Frautschi diagrams [1] showing N and Δ Regge trajectories.

can be approximated to a straight line:

$$\mathrm{Re}\,\{\alpha_N(s)\} \simeq \alpha_N^0 + \alpha_N' s, \tag{1.6}$$

where $\alpha_N^0 \simeq -0.37$ is the so-called *Regge intercept* and $\alpha_N' \simeq 1.0\,\mathrm{GeV}^{-2}$ [7].

The particles associated to a given $\alpha_n(s)$ ($\alpha_n(t)$) have the same quantum numbers (strangeness, baryon number, isospin, etc.). Figure 1.2 show several diagrams in which resonances with different quantum numbers are produced or *exchanged* between the two colliding particles. These exchanged objects are also called *Reggeons*. Of particular

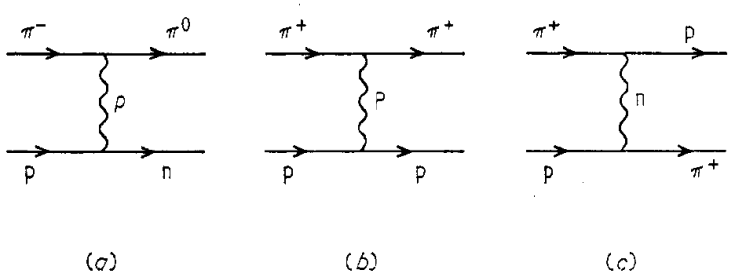


Figure 1.2: Regge exchange diagrams illustrating: (a) exchange of a ρ meson trajectory in pion-nucleon charge exchange, (b) Pomeron exchange in elastic $\pi - p$ scattering and (c) neutron exchange in backward $\pi^+ p$ scattering.

relevance in soft pp collisions is the diagram in Figure 1.2(b), in which a Reggeon carrying no internal quantum numbers is exchanged. This Reggeon is commonly referred to as the *Pomeron*. The Pomeron trajectory has the form

$$\alpha_P(t) = 1.0 + \alpha_P' t \tag{1.7}$$

so its Regge intercept is identical to unity [7]. The existence of a counterpart of the Pomeron with negative C-parity, the *Odderon*, has been theoretically introduced in [8] and it will be investigated in this thesis.

1.3 High Energy pp Interactions

This section is focused on a description of how high energy pp collisions are believed to occur, dividing the process into different stages which are often described by various

theoretical and phenomenological approaches depending on the energy scale. The description is built in a roughly temporal order, however, since the interactions are intrinsically of a quantum-mechanical origin, this is just a convenient way to explain them and to guide the structure of MC event generators. The interaction process can be summarised as follows:

1. The initial state composed of two protons. Protons are complex objects and their interaction is better described in terms of "partons", namely quarks and gluons. The complexity of the proton structure is modelled in terms of "parton densities" which quantify the probability of finding a given parton with a certain fraction of the proton momentum. Parton densities can be extracted, for instance, from deep inelastic scattering data.

2. The collision between two partons, one from each proton, gives the "hard process" of interest that may involve physics within or beyond the SM: $ug \to ug$, $u\bar{d} \to W^+$ $gg \to h^0$, etc. However, the total pp cross section is given for the most part by elastic or diffractive final states with soft jets.

3. Decay chains of short-lived particles produced in the hard process, such as top or $W^{\pm}$, must be considered part of the process itself to allow for spin correlations to be transferred.

4. Accelerated colour and electromagnetic charges emit bremsstrahlung radiation. Depending on the emission being associated to the incoming or outgoing partons, bremsstrahlung is called Initial-State Radiation (ISR) or Final State Radiation (FSR) respectively.

5. Since hadrons are bounded states of a number of partons, a so-called multi-parton interaction (MPI) may occur, in which more then one parton pair interacts within a single pp collision. This process should not be confused with "pile-up" events in which several pp pairs collide in the same bunch crossing. Both MPI and pile-up may have ISR and/or FSR associated.

6. The colliding partons take only a fraction of the initial proton's energy, the remainder of the energy is taken by the beam remnants that continue to travel essentially in the original proton direction.

7. During the hard interaction, at short timescales and small distances between partons, the strong coupling constant allow for a perturbative description of the physical process. However, as time evolves (either forward or backward), the energy scale decreases and partons become confined within hadrons. Currently, the time evolution of the colour force-fields between the initial state and the final state cannot be described from first principles so that phenomenological models must be introduced. The most common approach is to assume that separate confinement fields are stretched between each colour and its matching anticolour, and all colours are distinguishable (the $N_C \to \infty$ limit).

8. Naively, the field lines can be imagined as a string connecting the two partons. The potential energy stored in the string increases with distance. Eventually, once a sufficient energy is stored, strings can break up into new $q\bar{q}$ pairs that screen the endpoint colours. As long as there is sufficient energy in the system, this process may happen iteratively, until all $q\bar{q}$ pairs from adjacent breaks combine into a hadron. This effect is also called hadronisation and will be discussed in Section 1.4.

9. The majority of these primary hadrons are unstable and decay further. Some of them, like protons, kaons and pions are (almost) stable and can be directly detected by tracking and calorimeter systems. At this energy scale, the event-generator description has to match the detector simulation framework. Then the experimental information can be used to reconstruct what may have happened during the collision.

In MC event generators, these steps, each with their own set of rules, can be considered sequentially to build complicated final states.

For obvious reasons it is beyond the purpose of this thesis to cover all the details of this subject. Only the aspects relevant to the analysis outlined in Chapters 4-5, such as hadronisation and BNT, will be addressed below.

1.4 Hadronisation

The hadronisation mechanism is the process responsible for combining almost free partons, present in the first instant of the hard interaction, into the final-state hadrons. The energy scales involved are of the order of $\sim 1\,\mathrm{GeV}$, therefore the hadronisation is a non-perturbative QCD phenomenon. Currently, there are two main phenomenological approaches that give a reliable description of the process, at least in terms of agreement with the experimental data: string fragmentation [9] and cluster fragmentation [10].

1.4.1 String Fragmentation

When a quark q and an antiquark $\bar{q}$ recede back-to-back from each other, the field lines cannot spread out over all space due to the self-coupling of the gluon. On the contrary, the field lines are compressed into a thin tube-like region of constant cross section ($\approx 1\,\mathrm{fm}$ in diameter) and the potential energy stored increases linearly with the distance between the partons. The energy stored per unit length is roughly

$$\begin{aligned} \kappa &\approx 1 \quad \mathrm{GeV/fm} \\ &\approx 0.2\,\mathrm{GeV}^2 \ \ (\text{in natural units}) \end{aligned} \tag{1.8}$$

Corrections from the short-distance Coulomb potential near the flux tube ends are expected to be small. Support for this linear confinement picture is also provided by Regge phenomenology, *charmonium* and *bottomonium* spectroscopy and lattice QCD.

According to the string fragmentation model, within the tube, new $q\bar{q}$ pairs in a colour singlet state can be created from the available field energy through a "tunnelling process" and the original system breaks into less and less energetic sub-systems, until ordinary hadrons remain. The momentum of these particles is approximately aligned

along the original $q\bar{q}$-axis. In this picture, the transverse momentum is generated from quantum fluctuations in the tunnelling mechanism and is a consequence of the finite radius of the flux tube $\langle r^2 \rangle \simeq \pi/2\kappa$.

The assumption of uniformity in the force field implies the property that there are no concentrations of energy, transverse momentum or angular momentum along the field. These field properties forbid massive $q\bar{q}$ pairs (of mass μ) production at a single space-time point. Classically, the $q\bar{q}$ pairs must be produced at a distance $2l$ apart so that the field energy in between can be used for the production of mass:

$$2\kappa l = 2\mu. \tag{1.9}$$

In this way, the production process is intrinsically of a quantum mechanical nature. The quark-pair production can be viewed as a tunnelling process in a linear potential (the *Lund* model [9, 11]). It can be demonstrated [9] that the dependence of tunnelling probability of the pair mass is

$$|\mathcal{M}|^2 \propto \exp - \left(\frac{\pi \mu^2}{\kappa} \right). \tag{1.10}$$

This fact leads directly to suppression of heavy quark production such as that of strange (s) and charm (c) quarks. Using the κ value in Eq. 1.8, the production rates are estimated to be in the following proportions:

$$u : d : s : c \simeq 1 : 1 : \frac{1}{3} : 10^{-11}. \tag{1.11}$$

Charm and heavier quarks are therefore not expected to be produced in significant amounts during the soft hadronisation processes but will mainly arise during the hard interaction.

Once the breaking of the first string stretched between the quark pair, $q_0\bar{q}_0$, occurs, a second quark pair, $q_1\bar{q}_1$, is created. The system is now re-ordered into the pairs $q_0\bar{q}_1$ and $q_1\bar{q}_0$. These pairs may break further, generating other $q\bar{q}$ pairs. This process

continues until all the partons are confined into hadrons as shown in Figure 1.3.

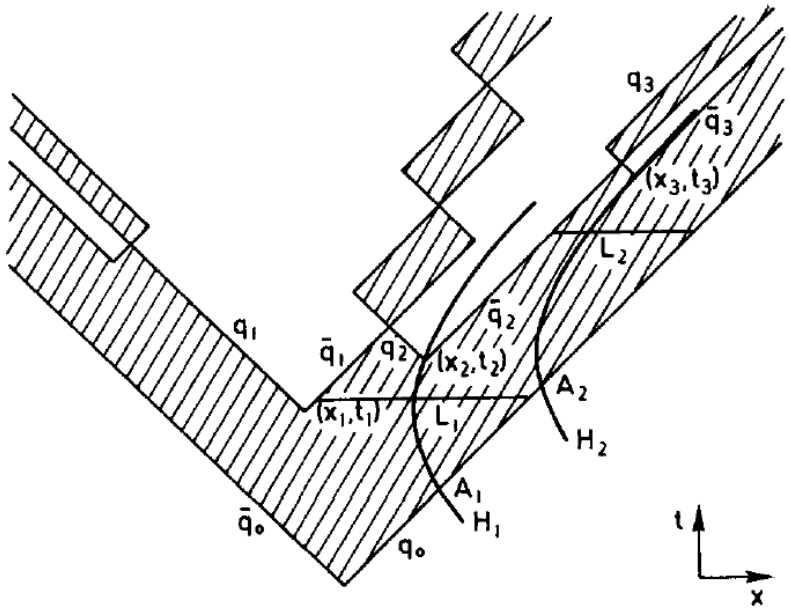


Figure 1.3: Sketch of the string fragmentation process in the centre of mass frame of two receding quarks, $q_0\bar{q}_0$. The hatched area shows where the field is non-vanishing. $q_i\bar{q}_i$ pairs are produced in the same space-time point (x_i, t_i). Nearby vertices are related by mass constraints.

It is obvious that, in this way, only mesons are produced; the production of baryons and antibaryons, within the string fragmentation model, is explained by replacing quark pairs by diquark pairs in a colour triplet state [12]. In this model, the suppression of baryon production, as compared to mesons, is determined simply by the larger diquark mass. This does not mean that the diquark is treated as a point-like object. In fact, given the small momentum transfers involved in soft hadronisation, even an extended object may have an effective strong coupling. Furthermore, it is expected that the density of virtual quarks along the string is high enough so that the probability to find a partner quark in a colour antitriplet diquark state is effectively one. Therefore, the production probability for diquark-antidiquark pairs can be treated with the same tunnelling mechanism as in Eq 1.10.

A more recent approach to baryon production, through the so-called "pop-corn" mechanism, is described in [13]. The crucial assumption of this model is that the space-time history of a confined force field contains regions of quantum colour fluctuation.

The example in Figure 1.4 shows a string field between two receding red, r, and antired, $\bar{r}$, quarks in one space and one time dimension. Green-antigreen ($g\bar{g}$) and blue-antiblue $b\bar{b}$ fluctuations are indicated with A and B respectively. Assuming that the pair $q'\bar{q}'$

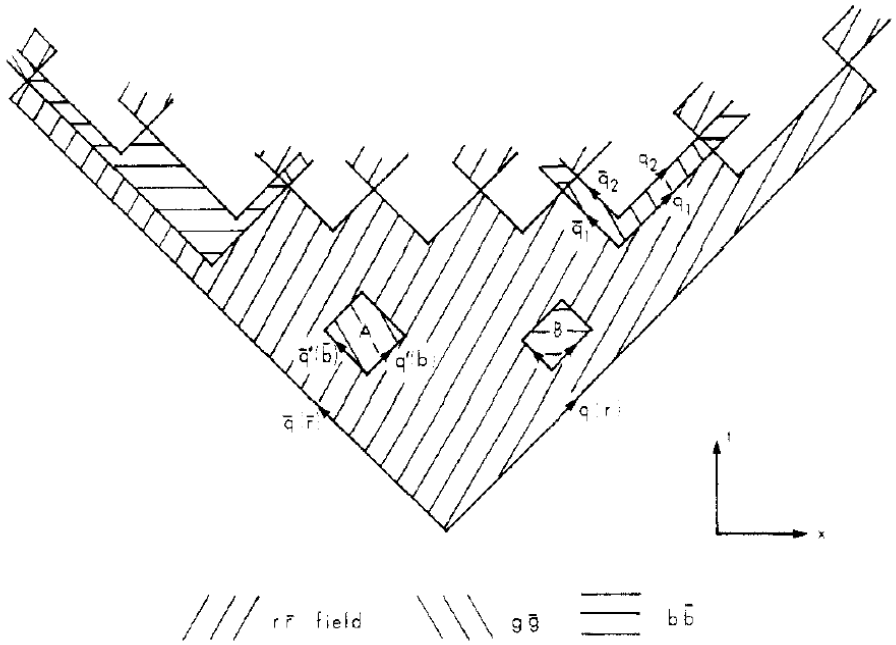


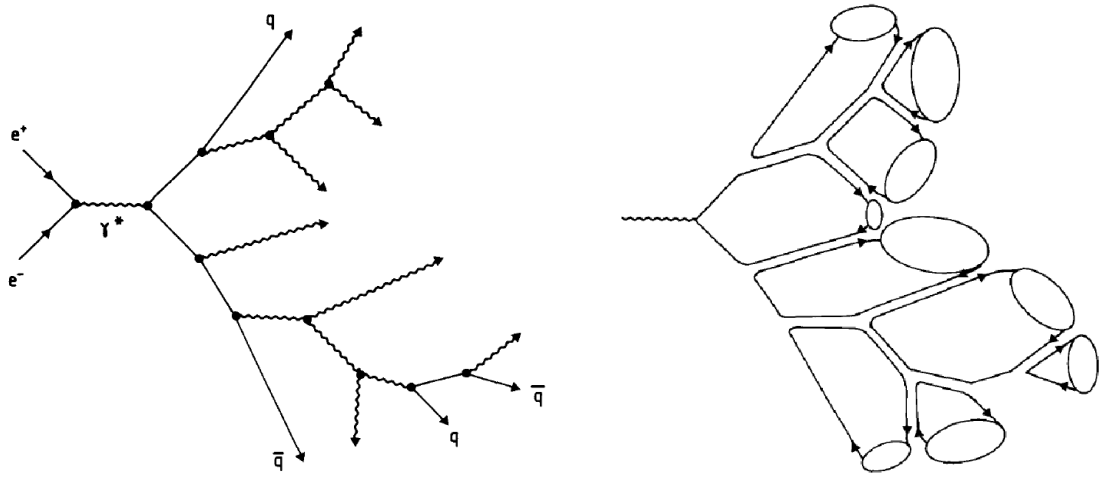
Figure 1.4: A colour field is stretched between a quark q and an antiquark $\bar{q}$. If virtual $q\bar{q}$ pairs are produced, the colour field can be changed from $r\bar{r}$ to $g\bar{g}$ or $b\bar{b}$. If a second pair is produced inside such a region the colour field can break and a baryon-antibaryon pair can be produced.

in region A is $b\bar{b}$ and that the red and blue form a colour antitriplet (antigreen), the region inside A has a colour triplet field with opposite direction. The field strength and the energy per unit length are the same outside and inside the region. Therefore the $q'\bar{q}'$ pairs feel no net force and can "float around" in the force field. As in the string model, the $r\bar{r}$ string field can break with the production of a $r\bar{r}$ pair. Moreover, a string breaking can also occur within one of the fluctuation regions, as shown in Figure 1.4. In this case a $g\bar{g}$ pair, $q_2\bar{q}_2$, is produced inside the *blue-antiblue* ($b\bar{b}$) pair, $q_1\bar{q}_1$. Hence q_2 is dragged towards q_1 and $\bar{q}_2$ towards $\bar{q}_1$ to form rb and $\bar{r}\bar{b}$ diquarks respectively that may lead to the production of a baryon-antibaryon pair. The density of the fluctuations determines the baryon production rates while their size is related to the possibility of meson production between the baryon-antibaryon pair. The main difference between the simple diquark model and the pop-corn mechanism is essentially

in a slightly different correlation of the outgoing baryon-antibaryon pairs. However, the two mechanisms do not exclude one another and are often used in combination in MC generators.

1.4.2 Cluster Fragmentation

An alternative representation of the hadronization process is the so-called "cluster fragmentation" [10]. This model is based on a QCD parton branching mechanism with a correct treatment of leading collinear and infra-red singularities. Within this scheme, the hadronisation occurs via the formation of colour singlet clusters after the perturbative phase of the jet development (see Figure 1.5(a)). These clusters then decay according to a phase-space scheme. A non-perturbative enhancement of the $g \to q\bar{q}$ splitting at low Q^2, which is relatively uncommon in the perturbative regime, is assumed. This causes all the gluons to split in $q\bar{q}$ pairs. Adjacent index



(a) Perturbative QCD branching process following $e^+e^- \to q\bar{q}$

(b) Dominant colour index structure of a). The blobs represent colour singlet clusters to be used as the basis for hadronisation.

Figure 1.5: Scheme of hadronisation according to the cluster fragmentation scheme.

pairs form colour singlet clusters, as shown in Figure 1.5(b), with the assumption that the two indices associated to each gluon are dynamically separated. Being formed typically from partons coming from adjacent shower branches, colour-singlet clusters have in general small masses and a cut-off at masses $\sim 2m_{u,d}$ has to be introduced.

The clusters, completely characterised by their mass and flavour content, finally go through a resonance-like two body decay, according to a simple phase space scheme (i.e. ignoring spin correlation). Although tightly constrained, this model is in good agreement with e^+e^- annihilation data.

1.5 Baryon Number Transport

The Baryon Number Transport (BNT) has been theoretically debated in several papers [14, 15, 16, 17, 18, 19, 20, 21, 22, 23]. The BNT can be included among the initial state properties that propagate to the final state after the initial hard collision has occurred, similarly to the total electric charge and the quark flavour content. The concept of BNT is actually most commonly discussed in the context of high energy ion collisions, since it can be probed in the formation of a *quark-gluon plasma* [24].

An interesting measurement to probe the BNT is the inclusive production ratio of antiprotons and protons, hereafter indicated by $\bar{p}/p$. In a simplistic view of this phenomenon, known as the *Leading Particle Effect*, the production of antiprotons in pp collisions must be energetically disfavoured with respect to protons, because the valence quarks in the $\bar{p}$ ($\bar{u}\bar{u}\bar{d}$) are not available in the initial state and have to be produced from the available energy in the collision. In order to investigate the BNT, the $\bar{p}/p$ is often expressed in terms of rapidity[2] loss:

$$\Delta y = y_{beam} - y_{hadron}, \tag{1.12}$$

where y_{beam} is the rapidity of the particles in the beam and y_{hadron} is the rapidity of the outgoing hadron.

From the theoretical point of view, two primary models have been developed to explain the BNT, both of which emerge from non-perturbative approaches to quark confinement. According to the Dual Parton Model (DPM) [15], the BNT can be explained in terms of the breaking of one of the incoming protons into a quark and a

[2]The rapidity of a particle is defined in terms of its energy, E, and its momentum component along the beam axis, p_z, as $y = (E - p_z)/(E + p_z)$.

diquark. The baryon number information is carried by the diquark that hadronises, as outlined in Section 1.4, into a proton. However, this model cannot account for transport over more than one or two Δy units since the diquark carries a large fraction of the initial proton momentum. Moreover, this picture is based on a naive quark model classification which assigns the baryon number $B = 1/3$ exclusively to quarks. Although this may seem natural since quarks also carry charge and flavour, it is not dictated by any intrinsic structure of QCD. Therefore, an alternative mechanism to trace the baryon number has been investigated in [14, 20]. This more rigorous approach is based on the gauge invariance that must be satisfied of any hadron state constructed from quarks and gluons in QCD. This severe constraint forces the colour part of the baryon state into the following form [20]:

$$\begin{aligned} B &= \epsilon^{ijk} \left[P \exp\left(ig \int_{x_1}^{x} A_\mu dx^\mu \right) q(x_1) \right]_i \\ &\quad \times \left[P \exp\left(ig \int_{x_2}^{x} A_\mu dx^\mu \right) q(x_2) \right]_j \\ &\quad \times \left[P \exp\left(ig \int_{x_3}^{x} A_\mu dx^\mu \right) q(x_3) \right]_k \end{aligned} \tag{1.13}$$

where A_μ and $q(x)$ represent the gluon and quark fields respectively. The wavefunction can also be depicted in a "Y" configuration, shown in Figure 1.6, which is supported by lattice QCD calculations. The structure of Eq. 1.13 suggests that the trace of the baryon number should be associated to a non-perturbative configuration of the gluon field called "string-junction", located at the point x, rather than the valence quarks. Naively the mechanism can be understood within the string model (see Section 1.4.1): if the quarks are pulled away from the junction, $q\bar{q}$ production is initiated, however the baryon will always restore around the junction. In general the quark composition of the resulting baryon may differ from the initial one.

In order to probe the above mechanism, one must be able to separate the baryon number flow from the valence quark flow. This cannot be achieved by the study of the hard interactions used to probe the internal baryon structure. In fact, hard interactions usually act on single quarks, so that the baryon number can be associated to the remaining diquark, without specifying its internal structure. Therefore, the

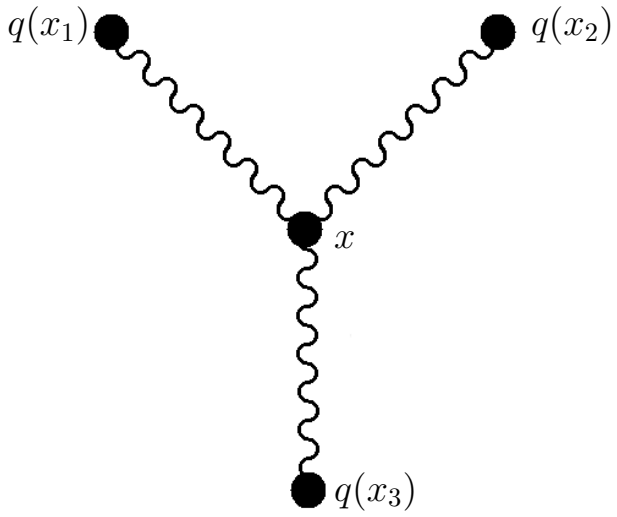


Figure 1.6: Three valence quarks located at x_1, x_2 and x_3 joined to the string junction in x.

transport can only be truly understood by the study of baryon production at high Δy in pp and heavy ion collisions, where the contribution from valence quarks should be negligible.

Quantitative predictions based on the Regge phenomenology [25] predict an exponential suppression of the BNT in pp collisions as a function of Δy. The introduction of processes involving a string junction introduces a contribution from the string-junction Regge intercept, α_J, so that the suppression is slightly modified in the following form:

$$p/\bar{p} \propto \exp\{-(\alpha_J - 1)\Delta y\}[26]. \tag{1.14}$$

Therefore, for a non-zero α_J, there should be a residual asymmetry at high Δy which corresponds to the central rapidity region for collider experiments.

The $\bar{p}/p$ ratio has been measured at the LHC in the central rapidity region by the ALICE collaboration [27]. Results are shown, together with measurements from other experiments, in Figure 1.7. The superimposed curve is fitted to the data to estimate the string-junction contribution, as will be described in Chapter 5.

The central region is not accessible by LHCb on account of the experiment's forward acceptance, however the shape of the $\bar{p}/p$ ratio as a function of Δy can still be studied over a wide rapidity interval, as will also be shown in Chapter 5.

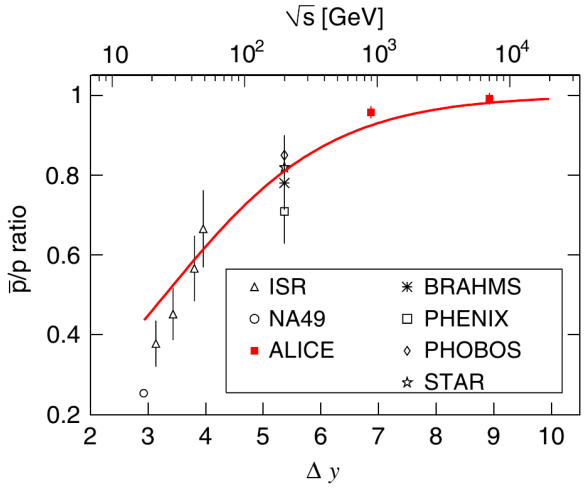


Figure 1.7: $\bar{p}/p$ ratio in the central rapidity as a function of Δy as measured by several experiments.

1.6 Prompt Hadron Production Ratios

Monte Carlo generators [28], such as PYTHIA [29], simulate pp interactions as described in Section 1.3. These generators usually describe the hard part of the interaction in terms of matrix elements obtained through perturbative expansion while the soft part is implemented using phenomenological parametrisations. Within LHCb, a particular tuning of the PYTHIA generator, the LHCb MC[3], is used to simulate pp collisions.

The current predictions for the $\bar{p}/p$ ratio, obtained with several tunings of the PYTHIA generator, are shown as a function of pseudorapidity in Figure 1.8. It can be seen that, while different PYTHIA tunings give a similar prediction in the central pseudorapidity region, the tunings differ significantly in the LHCb acceptance region ($1.9 < \eta < 4.9$). Here the evolution of the ratio is more pronounced, particularly at low energy. The same plots for high energy show a flatter ratio due to a stronger BNT suppression and a general agreement between all the tunings. A full comparison of MC simulation and theoretical models with respect to LHCb experimental results for

[3]The LHCb MC is a tuning of PYTHIA 6.421, and include process types 11, 13, 28, 53, 68, 91, 95, 421, 439, 461, 479 with non-default parameter values ckin(41)=3.0, mstp(2)=2, mstp(33)=3, mstp(128)=2, mstp(81)=21, mstp(82)=3, mstp(52)=2, mstp(51)=10042, parp(67)=1.0, parp(82)=4.28, parp(89)=14000, parp(90) =0.238, parp(85)=0.33, parp(86)=0.66, parp(91)=1.0, parp(149)=0.02, parp(150)=0.085, parj(11)=0.5, parj(12)=0.4, parj(13)=0.79, parj(14)=0.0, parj(15)=0.018, parj(16)=0.054, parj(17)=0.131, mstj(26)=0, parj(33)=0.4. The particles are decayed by EVTGEN, with radiative corrections generated by PHOTOS.

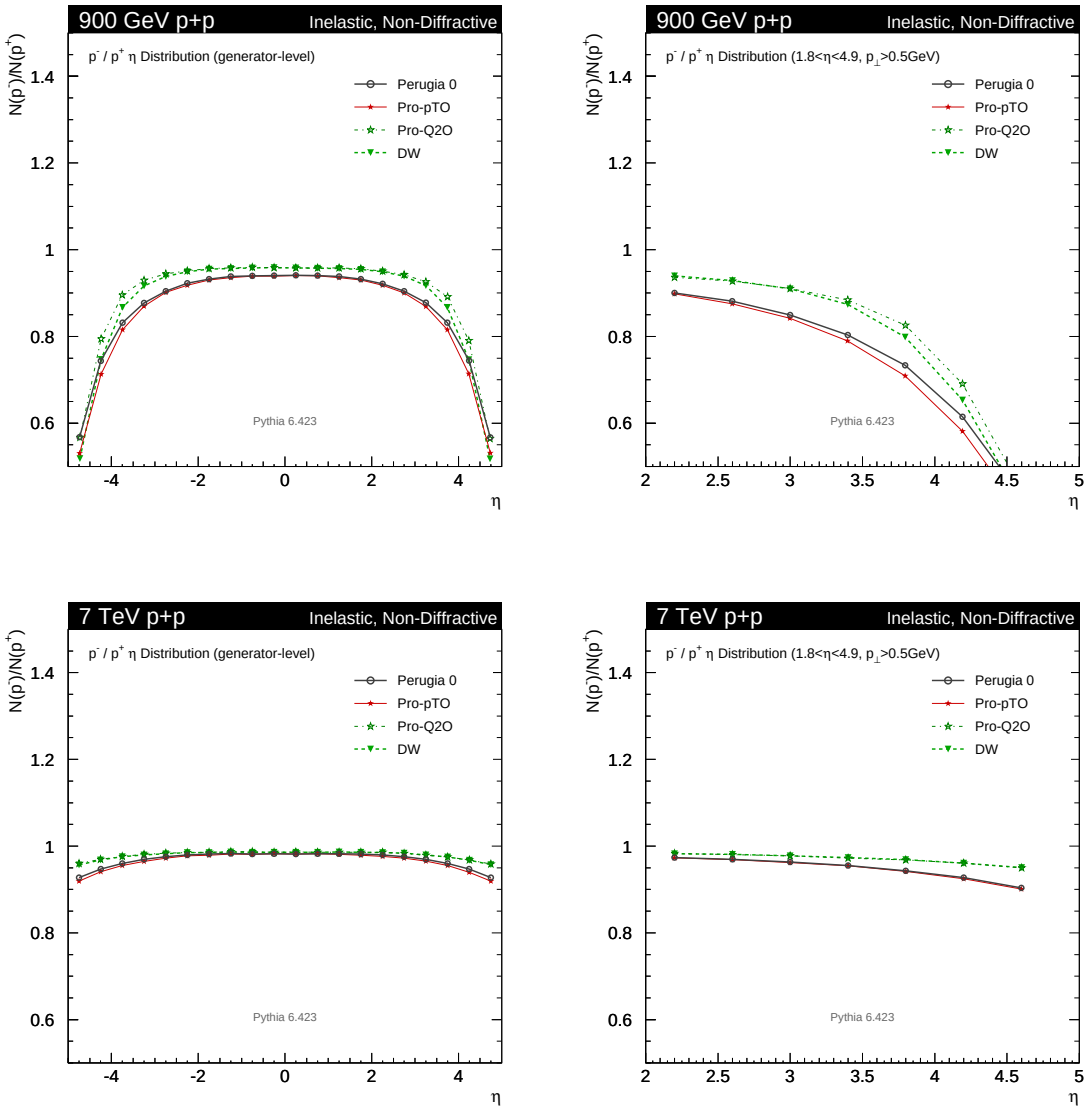


Figure 1.8: Theoretical predictions for the $\bar{p}/p$ production ratio from MC simulations using different PYTHIA tunings. The plots on the right focus on the LHCb pseudorapidity region.

$\bar{p}/p$ and other charged hadron ratios is given in Chapter 5. Existing measurements of the production of protons, kaons and pions at the LHC have also been performed by the ALICE collaboration [30, 31].

Chapter 2

The LHCb experiment

2.1 Introduction

In the following chapter, the LHCb detector will be described in detail as well as its commissioning and performances. After an overview of the detector (Section 2.2), the next section is dedicated to the RICH system (Section 2.4). This will provide the reader with sufficient detail to subsequently follow the studies described in Chapters 3-5.

2.2 The LHC

The Large Hadron Collider (LHC) at CERN is the most powerful particle accelerator ever built. The LHC exploits the same 27 km circumference tunnel previously occupied by the Large Electron-Positron (LEP) collider and is capable of accelerating proton beams, injected from the Super Proton Synchrotron (SPS) at 450 GeV, up to 7 TeV. Two proton beams, structured in 25 ns bunches, circulate in opposite directions inside separate vacuum pipes. In order to confine the beams in a circular trajectory, superconducting dipole magnets operating at a temperature of 1.9 K provide a bending magnetic field up to 8.3 T. The beams cross at four locations that correspond to the main LHC experiments: ALICE [32], ATLAS [33], CMS [34] and LHCb [35]. By design, the maximum centre of mass energy and luminosity are 14 TeV and $10^{34}\,\mathrm{cm}^{-2}\mathrm{s}^{-1}$ respectively. A schematic view of the CERN accelerator complex is shown in Figure 2.1.

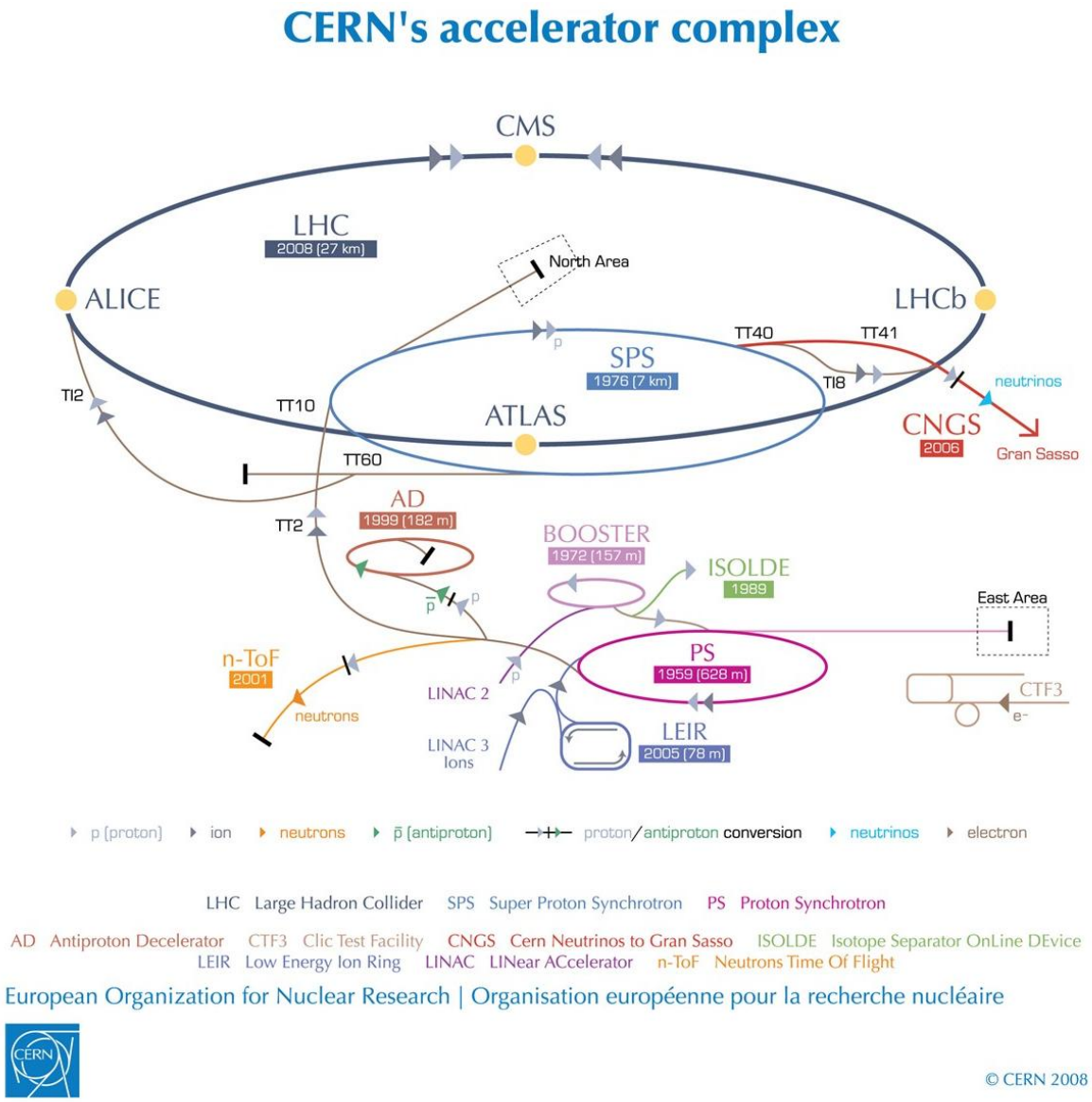


Figure 2.1: Layout of the CERN accelerator complex. Before reaching the LHC protons are injected from the linear accelerator (LINAC2) into the PS Booster, then the Proton Synchrotron (PS), followed by the Super Proton Synchrotron (SPS).

Since the pilot run in 2009, the LHC has been delivering proton-proton collision data at centre of mass energies of 0.9 TeV (twice the injection energy) and 7 TeV, the latter with increasing luminosity.

The next section will provide an overview of the LHCb detector. Particular emphasis will be placed on describing aspects of the experiment most relevant to the studies performed in Chapters 3, 4 and 5 of this thesis. A full description of the relevant

detector elements can be found in either the detector overview paper [35] or from the series of technical design reports [36, 37, 38, 39, 40, 41, 42, 43, 44, 45, 46, 47].

2.3 The LHCb Detector Overview

The LHCb experiment is dedicated to precision measurements of CP violation and rare decays in beauty(b) and charmed(c) hadrons as an indirect search of new physics beyond the Standard Model.

The detector layout, shown in Figure 2.2, has been designed to cover the region from 10 mrad to 300 (250) mrad in the magnet bending (non-bending) plane. This structure, typical of a single arm spectrometer, is necessary to detect the decay products of b-hadrons and c-hadrons which are copiously produced in the forward region at centre of mass energies above ~ 1 TeV.

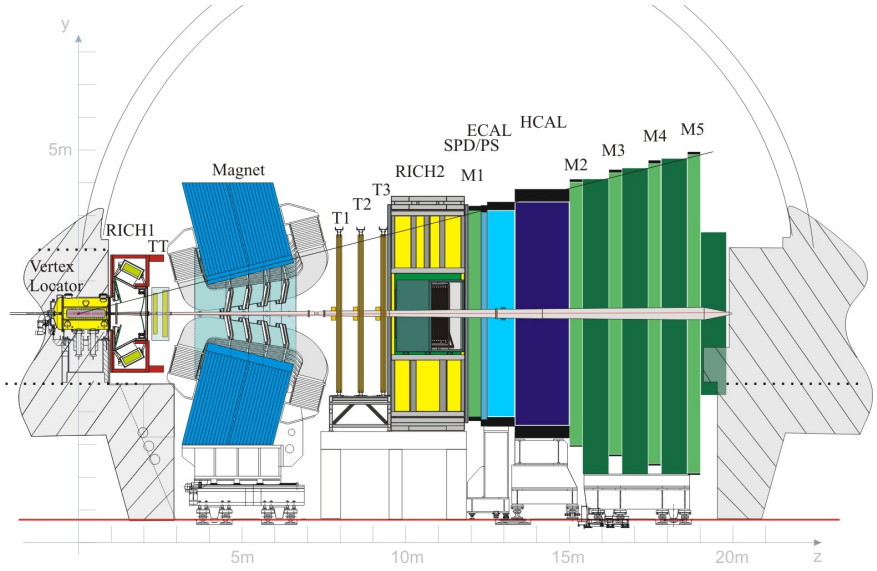


Figure 2.2: Schematic of the LHCb detector shown in the magnet non-bending plane. The right-handed coordinate system used has the z axis along the beam direction, the y axis vertically upwards and the x axis pointing towards the centre of the LHC ring.

LHCb allows the full reconstruction of exclusive decays of the b- and c-hadrons in a variety of leptonic, semi-leptonic and purely hadronic final states. In order to achieve this goal and extract the physics of interest, the LHCb detector incorporates specialised sub-detectors to perform the following important tasks:

- Precision vertexing: a sufficient separation between primary and secondary ver-

tices is required to efficiently select b-hadron candidates and allow time dependent analyses to be performed. Such measurements are performed by the VErtex LOcator (VELO).

- Invariant mass determination: an excellent invariant mass resolution is required in order to maximise the significance of signal with respect to background. Therefore, precision energy and momentum estimates of reconstructed tracks must be performed. This is achieved by LHCb's tracking (charged particles) and calorimetry (mainly neutral particles) systems.

- Particle identification: hadronic decays of b- and c-hadrons, having identical topology but different flavour content in the final state, may peak at a common invariant mass; additional information is required to distinguish them from one another. Discrimination between charged hadrons (particularly pions and kaons) is achieved with a high performance Ring Imaging CHerenkov (RICH) system, whilst electrons, photons and muons are identified via the Calorimeter and Muon systems, respectively.

- Flexible and robust trigger and data acquisition: this is required in order to cope with rapid changes in running conditions and physics interests. A dedicated multi-stage trigger, capable of selecting many different final states in an hadronic environment, reduces the data rate from the initial $\sim 10\,\text{MHz}$ of "visible interactions" to $\sim 3\,\text{kHz}$ which is suitable for offline storage and analysis.

The arrangement of the detector sub-systems within the LHCb detector are shown in Figure 2.2. An overview of each sub-detector will now be given.

2.3.1 Tracking System

The LHCb tracking system is composed of the VELO and four tracking systems: the TT upstream of the dipole magnet and three tracking stations T1, T2 and T3 downstream of the magnet (shown in Figure 2.2). The latter three stations cover the entire

geometrical acceptance of the spectrometer. To achieve the excellent tracking performance and also due to track multiplicity considerations, these three stations are composed of two distinct parts called the Inner and Outer Trackers.

The VELO, TT and Inner Trackers use silicon strip technology while straw tubes are employed in the Outer Tracker. In fact, the TT and Inner Trackers share a common technology, called collectively the Silicon Tracker (ST). They have a very similar layout sharing the same silicon microstrip technology with a strip pitch of $\sim 200\,\mu$m. Each of the four ST stations is composed of four detector layers with the strip directions arranged in a so called $x-u-v-x$ layout: the first and fourth layers have vertical readout strips, while second (u) and third (v) layers have the strips rotated by a stereo angle of $+5^\circ$ and -5° respectively. This layout is designed to have the best hit resolution in the x direction (in the bending plane), without losing the stereo measurement of the tracks.

2.3.1.1 VELO

The VELO [38] is used to measure precisely the trajectories of particles very close to the interaction region. This information ensures an accurate reconstruction of the vertex positions, enabling a separation of the secondary vertices due to b- and c-hadron decays from the primary vertex (proton-proton interaction).

The VELO, shown in Figure 2.3, surrounds the interaction region. The detector consists of two sets of 21 planar silicon detector modules, placed perpendicularly to the beam line i.e. lying within the xy plane. The hits originating from charged particles are detected as a function of radial (r) and azimuthal (ϕ) coordinates. Two additional sensor planes, called the pile-up veto system, are located upstream of the VELO. These modules provide information for the Level-0 trigger pile-up veto (see Section 2.3.5), which allows rejection of events with multiple proton-proton interactions.

The VELO modules are arranged along the beam direction and placed at a radial distance of only 8 mm from the beam when the detector is operated in its *closed* position, as schematised in Figure 2.4. The two halves of the VELO are mounted on

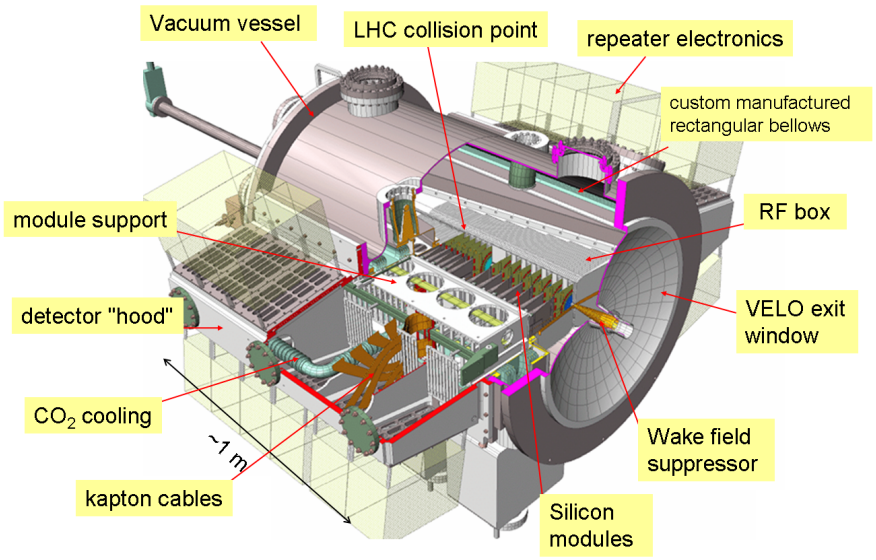


Figure 2.3: Layout of the Vertex Locator. The sensor modules are positioned in the very inner region, very close (8 mm) to the beams.

a controllable positioning system and can be retracted by 3 cm to allow a safe beam injection and ramping (*open* position), besides giving access for maintenance purposes. The positioning system can move the two halves with an accuracy of 10 μm in order for the sensor positions to be optimised, on a fill basis, around the beam. The detector is contained in a vessel maintained under the same ultra-high vacuum as the LHC beam-pipe (beam vacuum or primary vacuum, 10^{-8} mbar); however, the sensors themselves are held inside two vessels under a secondary lower vacuum (10^{-4} mbar). The walls of the vessels facing the beam side, the so called RF foils, are specially designed to prevent Radio-Frequency pick-up of the VELO sensors from the LHC beams and minimise the material budget traversed by particles from the interaction region.

Each VELO module consists of a pair of r- and ϕ-sensors to measure the radial and azimuthal variables respectively. The coordinate along the beam axis, z, is determined by the knowledge of each module position. The cylindrical geometry allows for a faster reconstruction of tracks and vertices in the LHCb trigger when compared to a cartesian one. Both r- and ϕ-sensors are constructed using the same technology, namely of silicon microstrip diodes 300 μm thick. Readout for both sensor types is placed at the outer

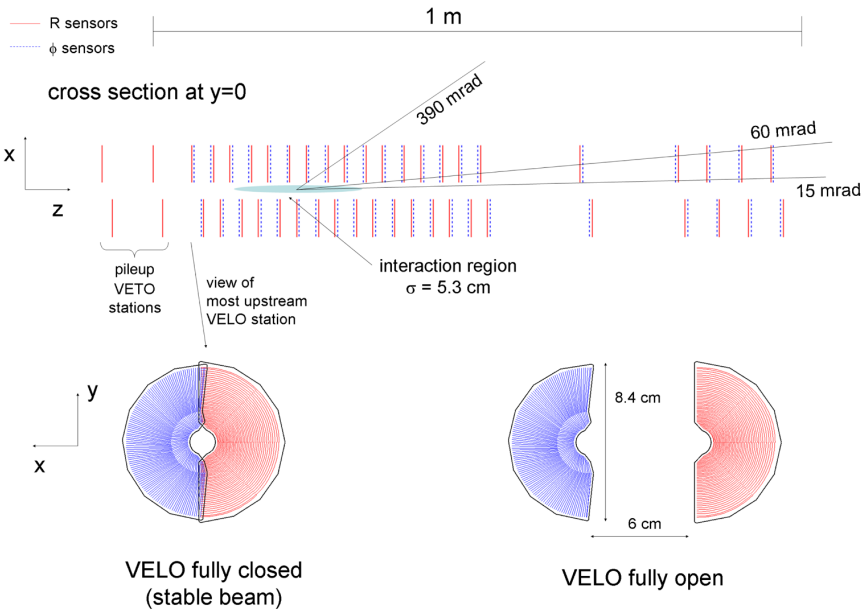
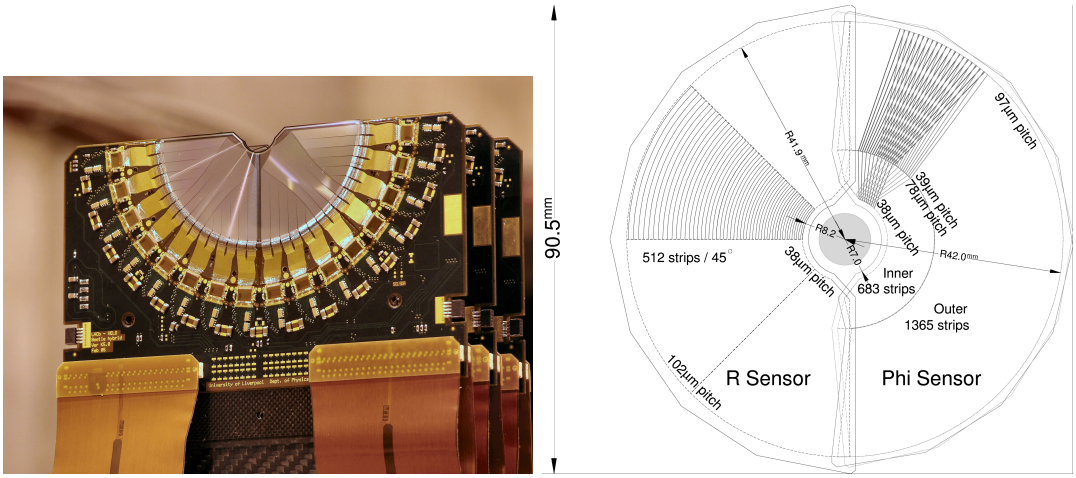


Figure 2.4: Design of the VELO sensor positions in the xz plane (top) for the fully closed position and in the xy plane for the fully closed (left bottom) and open (right bottom) positions.

radius.



(a) Photograph of a production VELO ϕ-sensor,

(b) Schematic of the r (left half) and ϕ (right half) VELO sensor types. The strips of two adjacent modules, with different bendings, are shown.

Figure 2.5: The VELO r- ϕ-sensors.

The layout of the two VELO sensor types is shown in Figure 2.5. The microstrips of the r-sensor are concentric semi-circles, with their centres coinciding with the LHC beam position. Each strip is divided in four segments 45° wide, this ensures a lower

occupancy per readout channel and lower strip capacitance. The strip pitch increases linearly from a minimum of 40 μm to a maximum of 101.6 μm, at the outer radius of 41.9 mm. This variable pitch design makes the various hits of a track contribute with equal weight to the impact parameter precision.

The ϕ-sensors are not simply made by radially disposed strips because this design would lead to unacceptably high occupancies of the strips due to a large area in the outer part. Therefore, they are instead divided in two regions at a radius of 17.25 mm as seen in Figure 2.5. In the inner part of the sensors, the pitch increases radially from 39.3 μm to 78.3 μm, while in the outer part it starts from 39.3 μm and ends at 97 μm. Moreover, strips are skewed with respect to the radial direction of 20° (10°) for the inner (outer) region; adjacent ϕ-sensors have opposite skew which improves the rejection of ghost hits. The individual strip resolution has been determined from test-beam measurements and found to be a strong function of the strip pitch. The best resolution achieved is 7 μm.

The proximity to the beam exposes the VELO to an extreme radiation environment. The damage caused to the most irradiated areas of the VELO after one nominal year of running, is equivalent to a flux of $1.3 \times 10^{14} n_{eq}\,\mathrm{cm}^{-2}$ of 1 MeV neutrons. However, the irradiation in the outer regions of the VELO does not exceed a flux of $5 \times 10^{12} n_{eq}\,\mathrm{cm}^{-2}$.

The dominant damage mechanism induced through high intensity radiation is Primary Knock on Atom (PKA), where a Si atom is displaced from its lattice site.

In order to limit radiation damage, during operation the silicon sensors are cooled to a temperature below −5 °C. The cooling system uses two-phase CO_2.

The VELO detector design has been optimised to minimise the amount of material traversed by particles, while still providing the designed geometrical acceptance. Each of the tracks originating from the interaction point and passing within the global LHCb acceptance pass through at least three VELO modules. Simulations have been performed to estimate the material budget traversed by outgoing tracks. The average value has been found to be 17.5% of a radiation length, with the largest contribution from the RF foil.

2.3.1.2 Dipole Magnet

In order to measure the momentum of charged particles, a dipole magnet is placed downstream of the VELO and the first RICH detector. The field orientation is such that the Lorentz force experienced by charged tracks is predominately in the horizontal plane. Consequently, tracks bend in the xz plane.

The magnet is in a dipole arrangement and is composed of two identical coils which are disposed symmetrically with respect to the horizontal plane, and with an angular opening which follows LHCb acceptance, as shown in Figure 2.6.

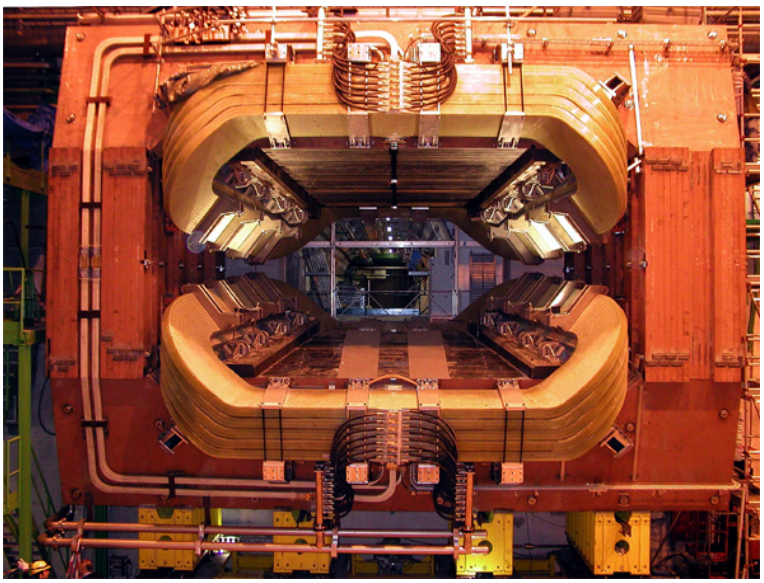


Figure 2.6: Photograph of the LHCb dipole magnet. As shown, the proton-proton interaction region lies behind the magnet.

The integrated dipole field strength is 3.6 Tm and has to be known to few per mil. Therefore, extensive field mapping campaigns have been performed, after the magnet installation, for both field polarities. Hall probes, which measure the three coordinates of the magnetic field, were used as field sensors. Measurements were compared to magnetic field calculations obtained with TOSCA (Vector Field TM). The final precision achieved for the field measurement is 4×10^{-4}.

During data taking periods, the magnet polarity is reversed periodically in order to perform physics systematics checks. Due to the dipole structure, opposite charged particles are bent towards different halves of the detector. Using data from both field

polarities helps understanding the detector response and reducing residual acceptance asymmetries.

2.3.1.3 TT

The TT or *Tracker Turicensis* is located upstream of the dipole magnet. Each of the four detector layers is housed in a module electrically and thermally insulated. The volume is maintained at a working temperature of 5°C. The four sensors are divided in two pairs separated by 27 cm along the beam axis to allow improved pattern recognition. The layout of one of the layers, consisting of differet modules placed side by side,

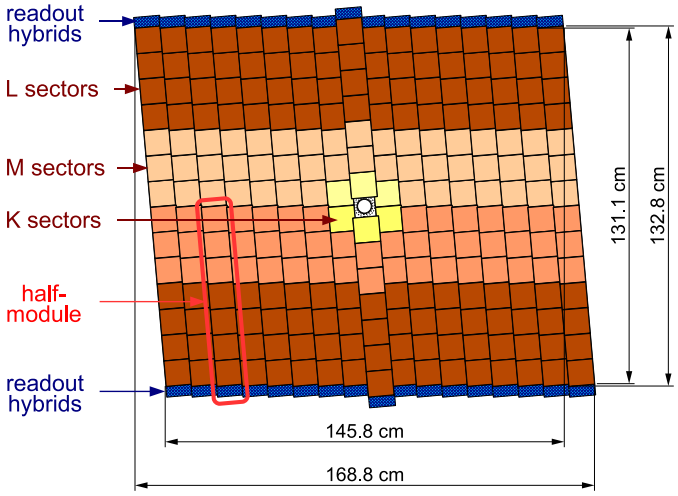


Figure 2.7: Layout of one of the TT layers. The different readout sectors are shown with different shadings.

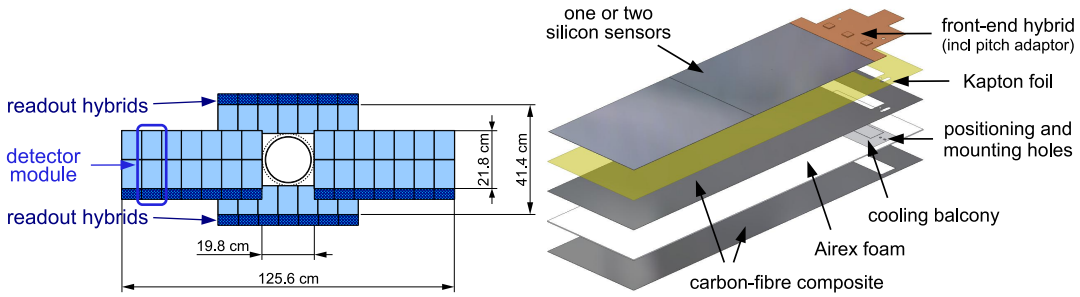
is shown in Figure 2.7. Each single module covers half of LHCb acceptance in height. Hits in this detector are used to reconstruct trajectories of long-lived neutral particles, such as the K_S^0 , that decay outside the fiducial volume of the VELO. Furthermore, the TT allows for the reconstruction of low momentum tracks that are steered out of the detector acceptance by the magnet before reaching the downstream tracking stations.

2.3.1.4 Inner Tracker

The Inner Tracker (IT) forms the inner-most region of tracking stations T1-T3, where particle fluxes are at their highest ($\sim 5 \times 10^5\,\mathrm{cm}^{-2}\mathrm{s}^{-1}$). Each IT station is composed of four detector boxes arranged into a cross-shaped area around the beam-pipe, as shown

in Figure 2.8(a). Although this formation only covers 1.3% of the total active area of each tracking station, $\sim$ 20% of all charged tracks produced close to the interaction point pass through this region.

The IT detector boxes, like the TT, are maintained at a constant temperature of 5°C. Each box contains four layers of sensors, organised in the $x-u-v-x$ configuration. Each layer consists of seven sensor modules. Each detector module consists of one (above and below the beam pipe) or two silicon sensors, almost identical in design to the ones of the TT, and a front-end readout hybrid. An exploded view of a two-sensor module is shown in Figure 2.8(b).



(a) (b)

Figure 2.8: (a) Layout of one of the IT layers and (b) exploded view of a two-sensor module of the IT.

2.3.1.5 Outer Tracker

The Outer Tracker (OT), shown in Figure 2.9, covers the remaining part of the tracking stations T1-T3. Each of the three stations consists of four layers, arranged in the $x-u-v-x$ geometry, and are composed of several discrete drift-tube modules. The gas tight modules, and so the drift tubes, are oriented vertically in order to perform better measurements in the bending plane of the experiment. The drift tube diameter, 4.9 mm, and the gas mixture, 70% Argon and 30% CO_2, allow for a drift time across the tube of < 50 ns (two bunch crossings) which is the performance required by the tracking algorithms.

The detector services and supports for the OT are located outside the LHCb acceptance, hence the material budget (3.2% of X_0 per station) is dominated by the active

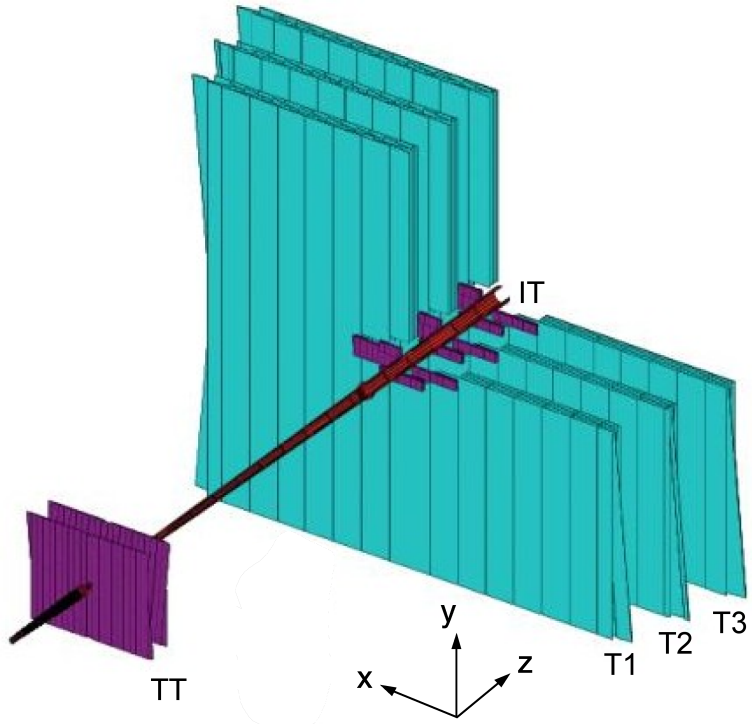


Figure 2.9: Layout of the Outer Tracker (light blue) together with the beam pipe (brown), the TT and the IT (purple).

part of the detector only.

2.3.2 Track Reconstruction

Hits produced by charged particles in the VELO, TT, IT and OT detectors are processed by pattern recognition algorithms to form track candidates. Tracks are classified into five categories, depending on the nature of the trajectory, as illustrated in Figure 2.10:

- **Long Tracks** traverse the entire tracking system from the VELO to the T stations. These tracks have the most precise momentum measurement. The track fitting is performed using hits from VELO and T stations only; TT hits would not introduce any significant improvement and are used as an independent cross check for fakes.

- **Upstream Tracks** traverse only the VELO and TT stations and, being in general lower momentum tracks, are bent out of the detector acceptance by the magnetic field. Passing through RICH1, these tracks can generate Cherenkov

photons (if the velocity is above threshold) that may be used for the RICH1 calibration.

- **Downstream Tracks** traverse only the TT and T stations. Usually these tracks are due to decay products of long-lived resonances which decay after the VELO, such as K_S^0 mesons.

- **VELO Tracks** exit the LHCb acceptance after traversing part of the VELO and are generally large angle or backward tracks used. These tracks are used for the primary vertex reconstruction. The magnetic field inside the VELO is negligible so that VELO tracks can be described by straight lines. A momentum estimation is not possible.

- **T Tracks** are tracks only measured in the T stations. They are typically produced in secondary interactions, but are useful to estimate the impact of downstream secondary particles for the RICH2 pattern recognition.

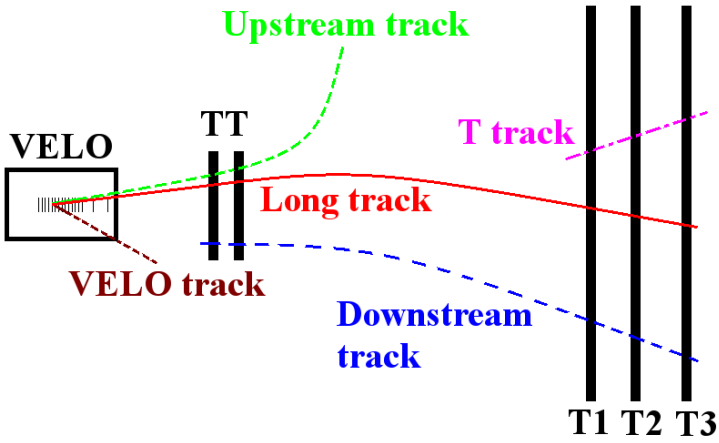


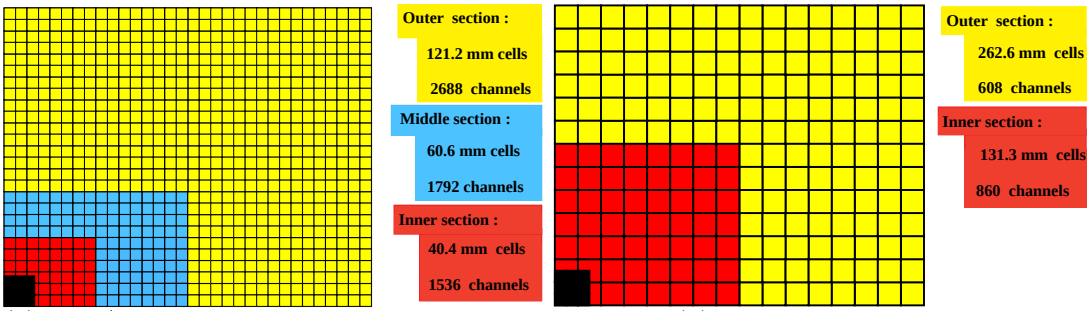
Figure 2.10: Classification of the different track types reconstructed by the LHCb tracking algorithms.

In order for each track type to be reconstructed, stub track segments within the VELO and T stations are required to act as a seed for the full track reconstruction. These segments are approximated to straight lines due to the minimal magnetic field at those locations. Once all track candidates have been found by matching seeds with other tracking detector hits, their properties are estimated with a Kalman filter fit that

takes into account the effects of multiple scattering and energy loss. The χ^2 of the fit is used to assess the track quality.

2.3.3 Calorimeters

The LHCb calorimeter system provides energy measurements and plays a fundamental role in particle identification and in the first level (L0) of the trigger by selecting high transverse energy (E_T) particles. Located downstream of RICH2, between the first two muon stations, the Calorimeter system is composed of: an Electromagnetic Calorimeter (ECAL) to detect electrons and photons, followed by an Hadronic Calorimeter (HCAL) for charged and neutral hadrons. A pre-shower (PS) and scintillator pad detector (SPD) are located before the ECAL to discriminate electrons from the overwhelming background of charged and neutral pions. The entire calorimeter system is segmented into tiles in the xy plane; the segmentation increases in dimension for different sections depending on the distance from the beam-pipe. In particular the SPD/PS and ECAL are segmented in three sections with scaling widths in a projective design. HCAL is segmented in only two sections with larger sizes. A schematic of this segmentation scheme is shown in Figure 2.11. A dedicated description of the four components of the Calorimeter system follows.



(a) SPD/PS and ECAL segmentation. Cell dimensions are given for the ECAL and reduce by a factor $\sim 1.5\%$ for SPD/PS.

(b) HCAL segmentation.

Figure 2.11: Segmentation of the calorimeter system. Only a quarter of the detector front face is shown.

2.3.3.1 Scintillator Pad and Pre-Shower detector

The SPD/PS detector consists of two planes of 15 mm thick scintillator tiles with a 2.5 X_0 lead converter in between. The SPD tile shape is a square of side either 39.2, 59.0 or 118.4 mm depending on its position in the detector. The PS tiles are slightly larger in order to accomplish the projectivity of the detector. The light generated in each tile is transmitted through a single wavelength-shifting (WLS) fibre to a multianode photomultiplier tube (MaPMT). When used in coincidence with data from the ECAL, SPD (PS) information assists in the rejection of $\pi^0 \to \gamma\gamma$ and γ ($\pi^\pm$) backgrounds from the e^- candidate selection. The performance for electron/pion separation was assessed in tests at the CERN SPS with electron and pion beams of momenta between 10 and 50 GeV/c. Pion rejection above 99.5% was achieved with electron retention between 91% and 97%, depending on the particle momentum. Photon/electron separation at the trigger level is achieved using the SPD information. Since other processes can contribute to photon background to the electron signal from photon conversion before the SPD, two other background have been investigated with photons of momentum between 20 and 50 GeV/c:

- photons interacting in the SPD may produce charged particles, measurements have shown a misidentification probability of about 0.8%;
- *back-splash* interactions due to backward-going particles from PS or ECAL electromagnetic showers. The measured probability is around 1%.

These effects are in agreement with expectations from LHCb Monte Carlo simulations.

2.3.3.2 Electromagnetic Calorimeter

The ECAL is a sampling calorimeter, designed with classical Shashlik technology, formed of 66 alternating layers of lead absorber and scintillator and read out by WLS fibres. The depth of each lead and scintillator layer is 2 and 4 mm respectively. Standard photomultiplier tubes are used to read out the scintillator light signals. The ECAL is segmented into cells, distributed in three regions, and follows the LHCb pro-

jectivity. Each cell corresponds to a total thickness of $25\,X_0$ so that showers from high energy photons can be fully contained.

2.3.3.3 Hadronic Calorimeter

The HCAL is a sampling calorimeter consisting of alternating layers of iron and scintillator. Due to space constraints, the detector thickness corresponds to only 5.6 interaction lengths. The signal readout is very similar to the ECAL. The HCAL is equipped with a special device, used for calibration, that can move a ^{137}Cs gamma source (with 10 mCi of activity) in front of each module. The driving system is computer-controlled. The HCAL is then calibrated by measuring the PMT anode current while scanning each module. An absolute energy calibration and a cross-check of the ECAL calibration can also be performed.

2.3.4 Muon System

Muon identification is vital in the detection of rare and CP-sensitive semi-leptonic b-decays. The LHCb muon system, shown in Figure 2.12, is composed of five stations, labelled M1 through M5, with an angular acceptance from 20 (16) mrad to 306 (258) mrad in the bending (non bending) plane. The first station (M1) is located upstream of the calorimeter system while the stations M2 to M5 are placed downstream and interleaved with 80 cm thick iron absorber plates. Including the calorimeters, the total thickness corresponds to $\sim$ 20 interaction lengths so that muons with a momentum above typically 6 GeV/c traverse all the five chambers. Multi-Wire Proportional Chamber (MWPC) technology was chosen throughout the muon system, except in the inner region of M1 where triple-GEM (Gas Electron Multiplier) detectors have been installed to cope with the intense particle flux. The GEM detectors are shown schematically in Figure 2.13(a). The MWPCs are arranged in groups of four anode wire layers. The wires, spaced by 2 mm, have a length between 20 and 30 cm and sit between a pair of cathode plates separated by 5 mm. In order to ensure a high efficiency M2-M5 (M1) are built with four(two) gaps connected in a logical OR configuration, as shown in

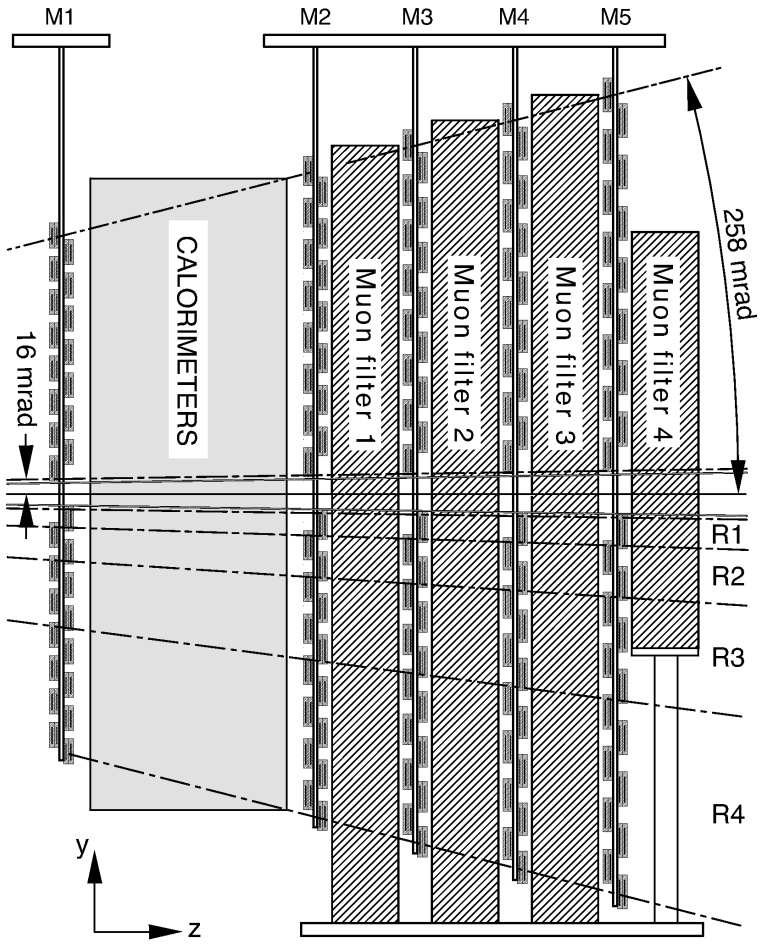
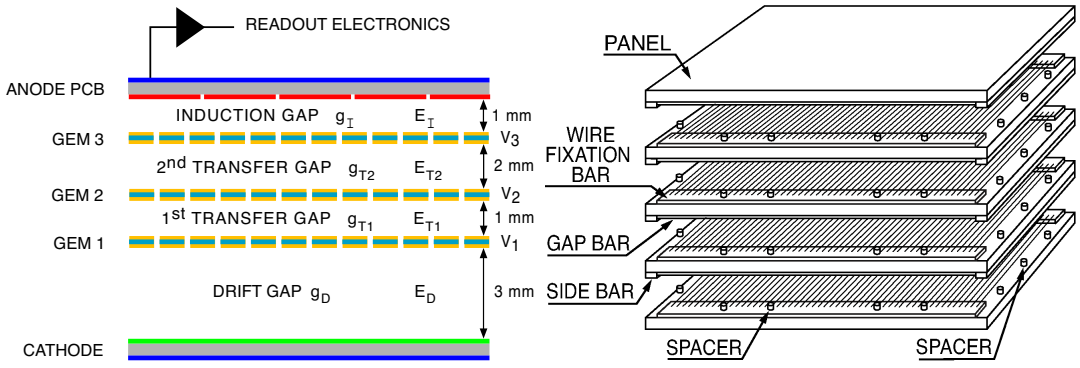


Figure 2.12: Schematic view of the muon system.

Figure 2.13(b). The gas mixture is composed of Ar_4, CO_2 and CF_4 for both MWPC and triple-GEM but in different proportions: 40 : 55 : 5 and 40 : 15 : 40, respectively. This design allows for a high detection efficiency ($> 95\%$) and a fast response (~ 5 ns).



(a) Schematic view of a triple-GEM detector. (b) Exploded view of a MWPC.

Figure 2.13: Muon system detection technologies.

2.3.5 Trigger

The LHCb detector is designed to operate at an average luminosity of $2 \times 10^{32}\,\mathrm{cm}^{-2}\mathrm{s}^{-1}$, reduced with respect to the LHC nominal luminosity (by a factor 50), in order to limit the average number of pp collisions per event. At the LHCb luminosity, the average rate of visible interactions is about 10 MHz. However, due to technical limitations in the amount of data that can be stored and the processing time required, the final output rate cannot exceed $\sim$ 3 kHz. The rate reduction is achieved via a two-level trigger scheme: the Level-0 (L0) hardware trigger, and the software-based High Level Trigger (HLT). This trigger layout, schematised in Figure 2.14, satisfies the event rate constraint whilst efficiently selecting the events of interest.

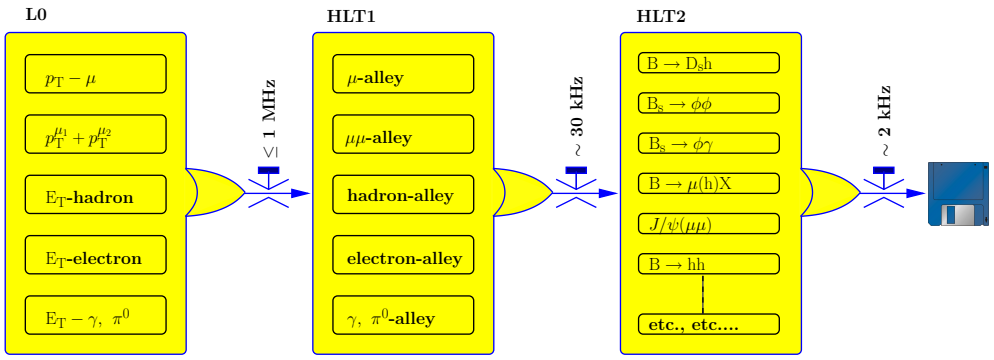


Figure 2.14: Overview of the data processing flow through the LHCb trigger system.

2.3.5.1 Level-0 Trigger

The L0 is designed to reduce the event rate from 10 to $\sim$ 1 MHz, allowing the HLT enough time to process the entire event information collected. Being the first trigger stage, it operates synchronously with the 40 MHz LHC clock; at this rate, only partial and prompt information from selected subdetectors can be processed. Three subsystems contribute to the L0 decision: the muon system, the pile-up system and the calorimeters. The collected information, for each event, is sent to the L0 decision unit (L0-DU) which is programmed to make the final decision (see Figure 2.15). The discriminating variables are coarse estimates of transverse energy, E_T, deposited in the calorimeters, the transverse momentum, p_T, of muons and the multiplicity of primary interaction.

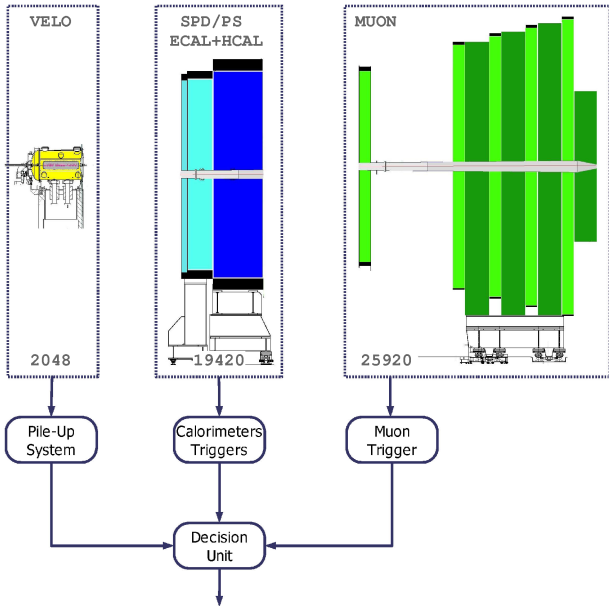


Figure 2.15: L0 schematic view.

The calorimeter trigger searches for high transverse energy particles within each event. Energy clusters are formed by adding the E_T of 2×2 calorimeter cells. The clusters are then associated to electron, photon and pion candidates, discriminated according to the information available in SPD, PS, ECAL and HCAL. In order to minimise the processing time only the cluster with highest E_T is considered for each event.

In order to allow a fast momentum estimation, the L0 muon trigger exploits tracks reconstructed from hits in the muon system only. Four processors, one for each sector, use hits in "logical pads" and the nominal position of the primary interaction to form tracks. The resolution on the transverse momentum achieved with this approximated method is $\sim 20\%$. The trigger then selects the two muon candidates with the highest p_T in each quadrant.

The pile-up system, placed upstream of the VELO, is dedicated to the rejection of events with multiple visible interactions. The system is equipped with two VELO r-sensor modules (see Section 2.3.1.1) in order to estimate the primary vertex positions by measuring the radii of traversing tracks. For each pair of hits in the two sensors

(herein labelled A and B) the quantity

$$PV_z = \frac{(r_B/r_A)z_A - z_B}{r_B/r_A - 1}$$

is an estimate of the primary vertex z position from which the particle originated. The distributions of the PV_z values from all hit combinations usually shows a peaking structure for each primary interaction. If, by masking the highest found peak, a second peak is found, the event can be vetoed and hence rejected by the L0.

The L0-DU processes the outputs of the three triggers described above and then forms the global, detector-wide L0 trigger decision for each bunch crossing. The time between the pp interaction and the arrival of the L0 trigger decision to the front-end electronics, the L0 latency, is fixed to a maximum of $4\,\mu$s.

The L0 trigger selectivity may be quickly adjusted depending on the running conditions. Typical requirements are at least one HCAL cluster with $E_T > 3.5\,\text{GeV}$ (hadrons), an ECAL cluster having $E_T > 2.5\,\text{GeV}$ ($e^{\pm}$, γ, π^0), a single muon with $p_T > 1.2\,\text{GeV}$ or two muons with $p_{T,1} + p_{T,2} > 1\,\text{GeV}$.

2.3.5.2 High Level Trigger

The High Level Trigger (HLT) is a software trigger implemented in C++. The trigger algorithms run on the Event Filter Farm (EFF) of $\sim$ 2000 CPUs and, in principle, have access to the full event information. However, given the high output rate of the L0, only part of this information can be processed. The input rate, the and amount of information per event that can be analysed, scale with the available CPU power. Being completely software-based, the HLT is significantly more flexible than the L0 and can be modified when needed to follow running conditions and physics requirements. The HLT is subdivided in two stages, HLT1 and HLT2. HLT1 further reduces the event rate to $\sim 30\,\text{MHz}$ so that the full pattern recognition can be performed in HLT2, allowing for the reconstruction of inclusive and exclusive final states.

The HLT1 design is aimed to confirm the L0 decision, hence the HLT1 is subdivided into "alleys", one for each L0 sub-trigger. L0 triggered *objects* (calorimeter clusters

and muon tracks) are further processed, exploiting additional information from the VELO and the T stations. As an example, in the muon alley, T and VELO hits are matched to L0 muon candidates, allowing for more precise tracking that can be used to impose a constraint on the minimum impact parameter of the muon with respect to the primary interaction vertex.

At the HLT1 output rate, the HLT2 is able to perform the full event reconstruction at the same precision as the offline analysis, with the exception of the track fitting which is not performed with a Kalman filter in the former case. Common resonances are formed with loose requirements (e.g. $\phi \to K^+K^-$ or $J/\psi \to \mu^+\mu^-$) which are subsequently used by different trigger inclusive (e.g. $B \to \phi X$) and exclusive (e.g. $B \to J/\psi\phi$) selections. The output of the HLT2 is the logical OR of all the inclusive and exclusive selections and it is sent to offline storage at a maximum rate of $\sim 3\,\text{kHz}$.

2.3.5.3 Trigger Strategies in First Data

In the early data-taking period, from December 2009 to July 2010, the instantaneous luminosity was sufficiently small such that very loose requirements could be imposed on the trigger. In order to assess detector performance and accrue data for minimum bias physics analyses, minimal trigger requirements were implemented at the HLT1 level. Hence these *minimum bias triggers* did not introduce any significant bias in the kinematical distributions of the reconstructed particles.

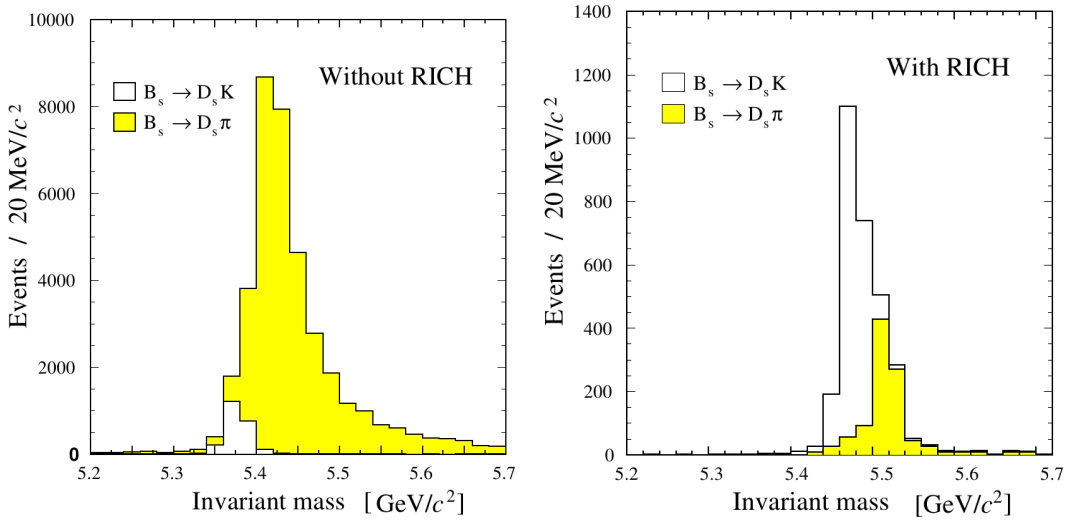
Particularly relevant for the analysis presented in Chapter 4-5 is the so called Micro Bias (μbias) trigger. The μbias trigger only requires the reconstruction of one VELO or one T track segment in order to accept the event, introducing a negligible bias even when compared to a plain random trigger.

Minimum bias triggers are still being used at LHCb, but due to the much higher luminosity, their output is severely *prescaled*[1] and analysed only for calibration and monitoring purposes.

[1]Special trigger algorithms, used to create unbiased event samples for monitoring and detector calibration, have usually a high output rate and only a fraction (the *prescaling factor*) of the sample can be stored.

2.4 The LHCb RICH System

Many decay modes of b- and c- hadrons involve hadronic multibody final states with very similar topology but different flavour content. Therefore, the invariant mass is not always sufficient to discriminate between different decays (see Figure 2.16).



(a) Mass spectrum of $B_s^0 \to D_s K$ candidates without RICH particle identification.

(b) Mass spectrum of $B_s^0 \to D_s K$ candidates with RICH particle identification applied.

Figure 2.16: Example of RICH performance for Monte-Carlo-simulated $B_s^0 \to D_s K$ events.

The LHCb experiment utilises two RICH detectors to provide particle identification of charged hadrons (protons, kaons and pions) over a momentum range of $2 - 100\,\mathrm{GeV/c}$. An overview of Cherenkov radiation and RICH detectors will now be presented.

2.4.1 Cherenkov Radiation

Cherenkov radiation is produced whenever a charged particle traverses a dielectric medium with a velocity in excess of the speed of light, c in that medium [48]. Cherenkov photons are emitted into a cone of half aperture θ_{CK} from the direction of the particle's propagation (see Figure 2.17). The value of the angle depends on the refractive index of the dielectric medium, n, and the velocity of the particle (in units of c), $\beta = v/c$:

$$\cos\theta_{CK} = \frac{1}{n\beta}. \tag{2.1}$$

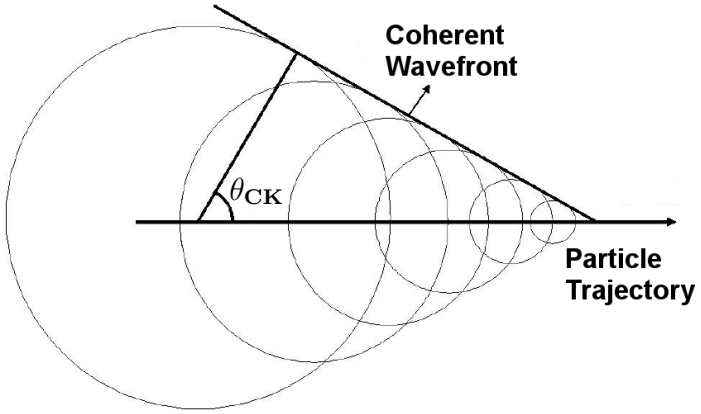


Figure 2.17: Huygens construction of the light emitted by a particle travelling faster than c in a medium. A coherent wave front is generated at a specific angle θ_{CK} to the particle's trajectory.

The distribution of Cherenkov photons around the azimuthal angle, ϕ_{CK}, is necessarily uniform. For a fixed n, the dependence on β predicts a maximum value of the Cherenkov angle:

$$\cos\theta_{CK}^{max} = \lim_{\beta\to 1}\frac{1}{n\beta} = \frac{1}{n}. \tag{2.2}$$

By expressing β in terms of the particle's momentum, p, and mass, m, Eq. 2.1 may also be written as

$$\cos\theta_{CK} = \frac{1}{n}\sqrt{1+\left(\frac{m}{p}\right)^2}, \tag{2.3}$$

where m is the particle's mass.

Therefore, knowledge of a charged particle momentum (tracking system) together with a measurement of the Cherenkov angle (RICH system), allows for a determination of its mass and, hence, species. In the regime that $\theta_{CK} \ll 1$ and $p \gg m$ Eq. 2.3 can be approximated to

$$1-\frac{\theta_{CK}^2}{2} = \frac{1}{n}\left(1+\frac{1}{2}\left(\frac{m}{p}\right)^2\right) \text{ [49]}. \tag{2.4}$$

Therefore, the difference in the squared Cherenkov angle for two charged particles, A and B, with the same momentum but different masses is given by

$$\theta_A^2 - \theta_B^2 = \frac{1}{n}\frac{\Delta(m^2)}{p^2}, \tag{2.5}$$

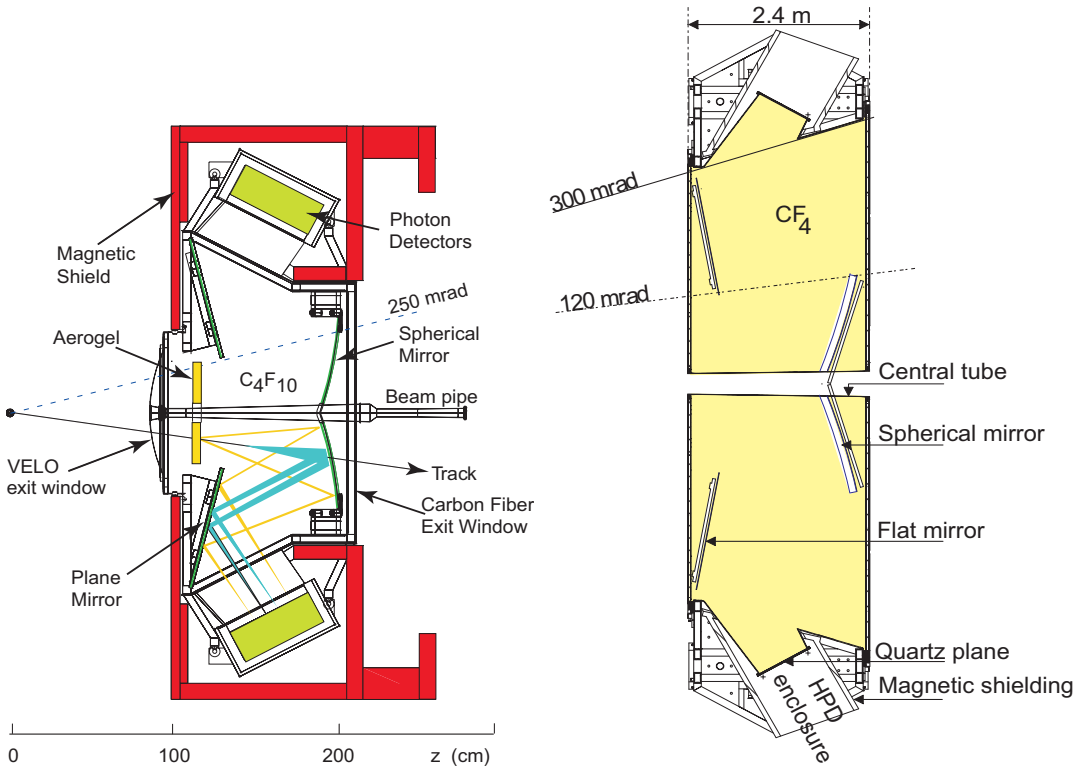
where $\Delta(m^2) = m_B^2 - m_A^2$. Typically for low density radiators, to a very good approximation, $(n-1) \sim\ll 1$, hence by defining $\delta\theta_{CK} = \theta_B - \theta_A$ as the difference in the Cherenkov angle between the two particle species, Eq. 2.4 can be rewritten as

$$\delta\theta_{CK} = -\frac{1}{2n\sqrt{2(n^2-1)}}\frac{\Delta(m^2)}{p^2}. \tag{2.6}$$

The RICH detectors exploit this difference to discriminate between two particle hypothesis. It can be seen that, for a given mass difference, the separation tends to zero as the momentum increases. Given the finite resolution of the detector, this fact ultimately limits the performance of the detector.

2.4.2 The LHCb RICH Layout

The LHCb RICH system provides measurements of Cherenkov angles, for photons emitted by charged particles in the LHCb detector [50]. The momentum measurement from the tracking system, combined with the RICH information, allow for the particle type to be determined. The two LHCb RICH detectors have a similar layout, shown in Figure 2.18. RICH1 is placed upstream of the magnet and provides particle identification in the low momentum range ($\sim 2 - 60\,\mathrm{GeV}/c$) with an angular acceptance of $\pm 250\,\mathrm{mrad}$. RICH2, located in front of the calorimeters, has an angular acceptance of $\pm 120\,\mathrm{mrad}$ and reconstructs Cherenkov photons from high momentum tracks ($\sim 20 - 100\,\mathrm{GeV}/c$). Cherenkov photons are focused onto the photon detector plane, by arrays of spherical and flat mirrors, to form a ring. The radius of the ring at the detector plane is directly related to θ_{CK}. The two-mirror design is motivated by the requirement to keep the photon detectors outside the LHCb acceptance. The photon detector plane is equipped with Hybrid Photon Detectors (HPDs), described in detail in Section 2.4.3.



(a) RICH1 (b) RICH2

Figure 2.18: RICH detectors layout.

2.4.2.1 Number of Detected Photons and Momentum Coverage

The number of photons, N_γ , emitted over a certain length, L, per unit photon energy, $E = \hbar\omega$, is governed by the well known Frank-Tamm relation:

$$\frac{dN_\gamma}{dE} = \frac{\alpha_e}{\hbar c} Z^2 \sin^2\theta_{CK}(E) L, \tag{2.7}$$

where Z is the charge of the traversing particle in units of e and α_e is the fine structure constant. However, due to unavoidable detector inefficiencies, the number of photons that can be detected is smaller and can be parametrised as follows:

$$N_{\text{pe}} = \frac{\alpha}{\hbar c} Z^2 \epsilon_A \epsilon_D \int Q(E) T(E) \sin^2\theta_{CK}(E) dE, \tag{2.8}$$

where ϵ_A is the geometric acceptance for Cherenkov photons, $T(E)$ is the probability that a photon reaches the detector plane (which includes the optical transmission losses

Property		RICH1		RICH2
		Aerogel	C_4F_{10}	CF_4
L	(mm)	50	950	1800
n		1.03	1.0014	1.0005
θ_C^{max}	(mrad)	242	53	32
$p_{tresh}(\pi)$	(GeV)	0.6	2.6	4.4
$p_{tresh}(K)$	(GeV)	2.0	9.3	15.6
$p_{tresh}(p)$	(GeV)	3.8	17.7	29.7
N_{pe}		6.8	30.3	23.2

Table 2.1: Characteristics of the three radiators used in the LHCb RICH detectors.

in the radiator medium and the mirror reflectivity), $Q(E)$ is the quantum efficiency of the photon detector (the probability that a incident photon is converted into a photoelectron as a function of photon energy), and ϵ_D is the efficiency with which the photoelectron is detected.

Cherenkov angle distributions reconstructed at LHCb are Gaussian in nature, with a resolution, $\Delta\theta_{CK}$, dependent on the type of radiator. To achieve a high efficiency, good separation (typically $3\times\Delta\theta_{CK}$) between Cherenkov angle distributions of differing particle types is required. This ability depends directly on the momentum scale as shown in Eq. 2.6. The significance of the separation, defined as $s_\Delta = |\delta\theta_{CK}|/\Delta\theta_{CK}$, can be used to write an expression for the maximum momentum at which the identification can be performed for a given degree of separation:

$$p_{max} = \frac{1}{2\Delta\theta_{CK} n\sqrt{2(n^2-1)}}\frac{\Delta(m^2)}{s_\Delta}. \tag{2.9}$$

The minimum momentum is simply given by the velocity threshold ($1/n\beta < 1$)

$$p_{min} \approx \frac{m}{\sqrt{n^2-1}}. \tag{2.10}$$

Therefore, in order to cover a momentum range up to $\sim 100\,\text{GeV}/c$, three radiators of specific refractive index have been chosen: silica aerogel (solid) and C_4F_{10} in RICH1 and CF_4 in RICH2. The characteristics of the RICH system can be seen for each of the three radiators in Figure 2.19 and Table 2.1.

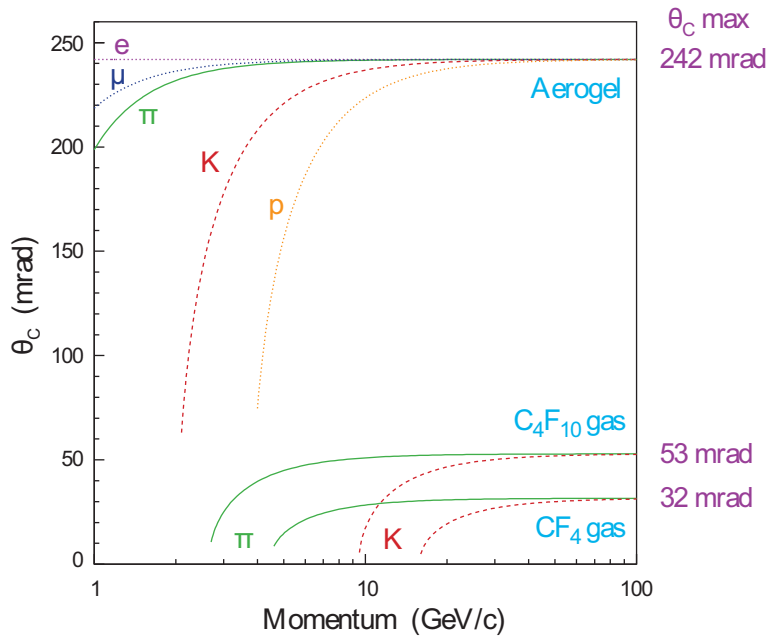


Figure 2.19: Cherenkov angle as a function of momentum for protons, kaons and pions in the three RICH radiators.

2.4.2.2 Resolution on the Cherenkov Angle Measurement

There are four main contributions to the uncertainty of the Cherenkov angle measured by the RICH detectors:

- **Emission Point Error**: Since it is not possible know the photon emission point along a particle track, the RICH reconstruction algorithms approximate that position to the mid-point of the track segment in the radiator. An additional uncertainty is introduced by the fact that photon trajectories do not necessarily pass through the centre of curvature of the mirror.

- **HPD Resolution**: The intrinsic spatial resolution of the HPD detectors is dominated by the finite pixel size of the silicon sensor.

- **Chromatic Dispersion**: Since the wavelength of the emitted photon is not known precisely, the dependence of the radiators' refractive index on the energy of the photon results in an irreducible uncertainty.

- **Tracking Resolution**: The tracking systems have a finite resolution, leading to an uncertainty in the trajectory of the particle within the RICH radiator volumes. This ultimately leads to an uncertainty on θ_{CK}.

2.4.3 The RICH Hybrid Photon Detectors

The four photon detector planes (two for each of RICH1 and RICH2) of the LHCb RICH system are equipped with HPDs [51] arranged in an hexagonal close-packed structure. The HPDs are mounted on retractable columns which insert into the magnetic shielding boxes, separated from the gas enclosure by quartz windows which allow clear passage for Cherenkov photons. HPD arrays consisting of seven columns of 14 HPDs in RICH1 and nine columns of 16 HPDs in RICH2 form the detection planes. These correspond to a total active area of $2 \times 0.72\,\mathrm{m}^2$ in RICH1 and $2 \times 1.05\,\mathrm{m}^2$ in RICH2.

The HPDs must satisfy stringent requirements:

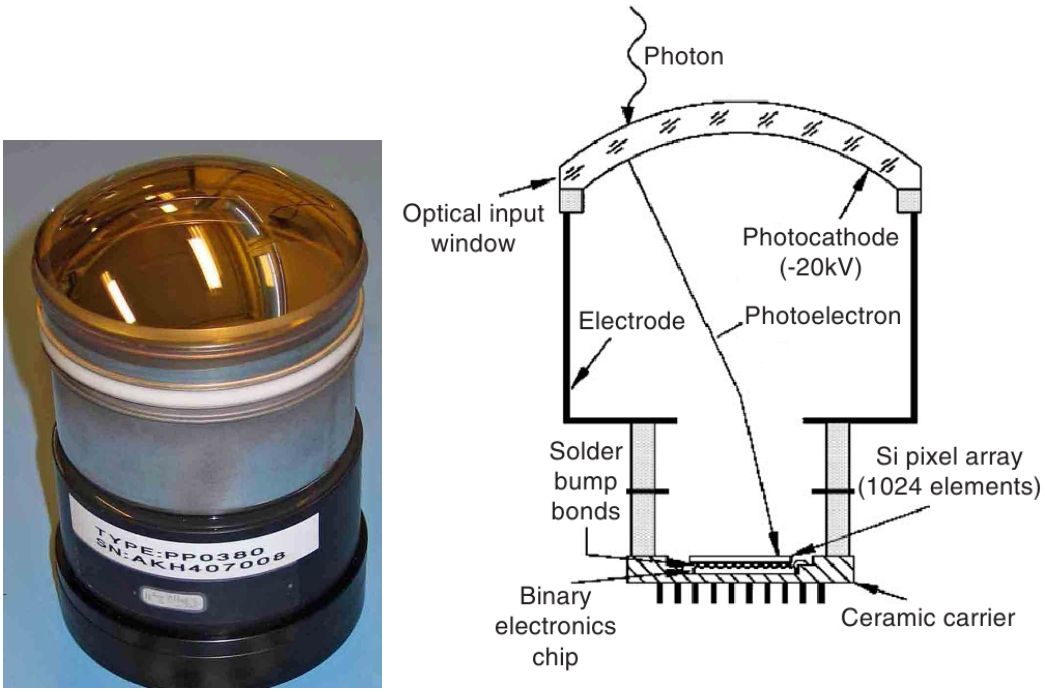
- Single photon sensitivity with high quantum efficiency ($\gtrsim 25\%$);
- Broad photon detection spectrum ($200 < \lambda < 600\,\mathrm{nm}$);
- High spatial sensitivity (effective pixel size $2.5 \times 2.5\,\mathrm{mm}^2$);
- Radiation tolerant to exposures up to 3 kRad/year;
- Tolerance to the magnetic fringe fields of the LHCb dipole magnet, up to $\sim$ 2.4 mT inside the RICH1 shielded volume.

In addition, the digitisation electronics that sample the analogue signals of this detector must satisfy the following requirements:

- Fast temporal response ($< 25\,\mathrm{ns}$);
- Maximum noise occupancy of 1%;
- Able to accept an average trigger rate of 1 MHz;
- Able to accommodate triggers within consecutive bunch crossings.

The HPD, shown in Figure 2.20, has been developed specifically for LHCb in collaboration with the company Photonis-DEP[2]. The HPD is composed of three main

[2]Photonis-Delft Electronische Producten, Roden, Netherlands.



(a) (b)

Figure 2.20: (a) photograph and (b) schematic of an HPD.

components: a photocathode, an electrostatic lensing focusing system and a silicon pixel sensor. The properties of the silicon sensor impose an additional requirement, the noise sensitivity must be less than $2000\,e^-$.

2.4.3.1 Photocathode

The HPD photon entrance window is a 7 mm thick quartz spherical segment with an S20-type multi-alkali photocathode deposited on the inner surface and a total sensitive diameter of 72 mm. The quantum efficiency (QE) of the photocathode varies between HPD. The QE of a highly efficient tube is shown in Figure 2.21 as a function of incident photon wavelength, which is $\sim$ 27% at maximum (4.6 eV/270nm), with sensitivity ranging from approximately $2 - 7\,\text{eV}(600 - 200\,\text{nm})$.

2.4.3.2 Photoelectron Focusing

Photoelectrons escaping the photocathode are subjected to an accelerating force as a result of the $-18\,\text{kV}$ potential difference applied between the photocathode and anode. In order to focus the photocathode image onto the anode, a pair of electrodes along

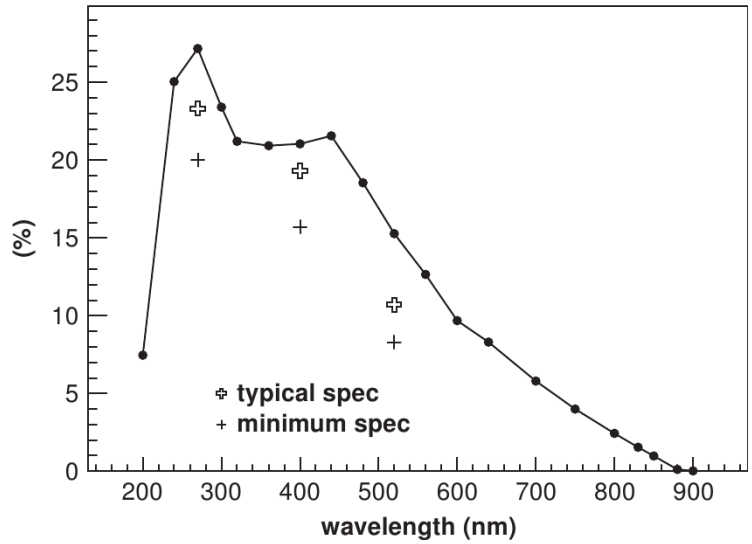


Figure 2.21: HPD photocathode quantum efficiency as a function of the photon wavelength.

the internal sides of the vacuum tube are used. These cross-focus the accelerating photoelectrons and demagnify the image by a factor of about 5.6. The photoelectron path can be modified by a fringe magnetic field inside the tube; this aspect will be discussed in detail in Chapter 3.

2.4.3.3 Silicon Pixel Sensor

The HPD anode is a 300 μm thick, square silicon sensor divided into 32×256 pixels, the "ALICE pixel", each of area $62.5 \times 500\,\mu\text{m}^2$. The silicon is doped, such that each pixel is a $p-n$ junction. A voltage of $\sim 80\,\text{V}$ is applied across the silicon sensor to force each $p-n$ junction into a reversed-biased diode. While silicon has an indirect band gap of 1.1 eV, it takes on average 3.6 eV to form an electron-hole pair, with the energy difference going into phonon excitations. The sensor is bump-bonded to the LHCBPIX1 pixel chip [52] which provides a preamplifier, a shaper and a discriminator circuit for each individual pixel, giving a binary output. The sensor and the readout chip are located inside the vacuum tube. The silicon chip readout is performed either in *ALICE* or *LHCb mode*. In ALICE mode, used for calibration purposes, the full resolution of the sensor is exploited. The LHCb mode, used for data taking during pp collision runs, makes use of a fast eight-fold logic OR to form a 32×32 array of square "super-pixels" of effective size $500 \times 500\,\mu$m (also called "LHCb pixel"), as shown in

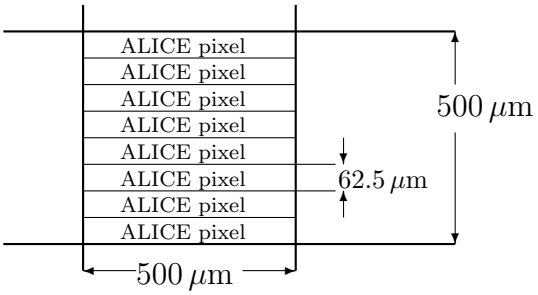


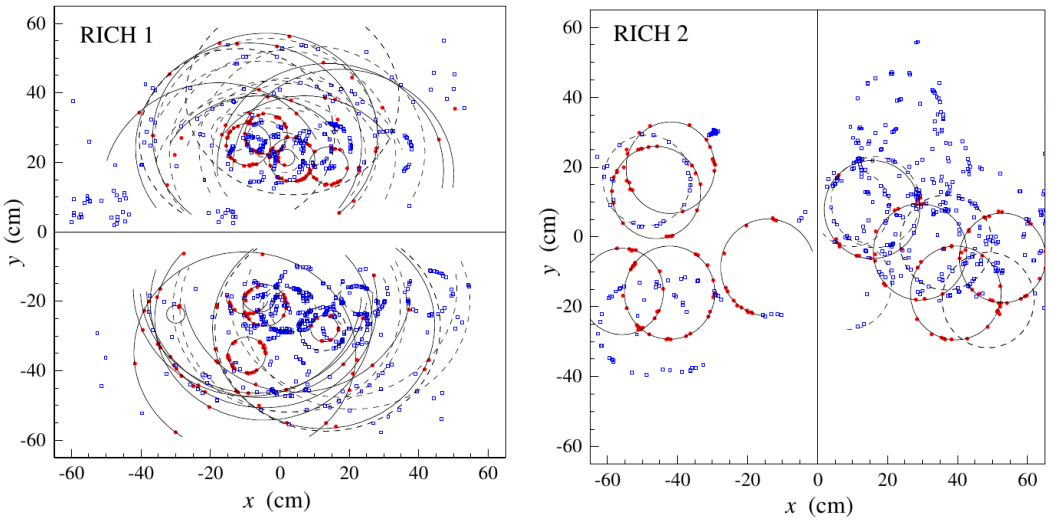
Figure 2.22: Sketch of an LHCb pixel. LHCb pixels are square super-pixels formed by the logic OR of eight ALICE pixels.

Figure 2.22.

2.4.3.4 RICH Pattern Recognition

The spherical focusing mirrors of the RICH detectors are tilted in order to project the Cherenkov photons outside the LHCb acceptance. Therefore, the images formed by Cherenkov photons on the photon detector planes are not perfect circles. Instead of trying to fit directly a distorted ring to determine the Cherenkov angle, the pattern recognition procedure is simplified to reconstruct both θ_{CK} and ϕ_{CK} for each detected photon under the assumption that it originated from a given track. It follows that, in the absence of chromatic dispersion, a photon emitted from a given track will have the same value of θ_{CK} whilst being uniformly distributed in ϕ_{CK}. Two independent pattern recognition techniques used to assign particle hypotheses to tracks have been investigated: the "local" and the "global" method [53].

In the local approach, each track is treated independently and a value of θ_{CK} is calculated for every hit in the photon detector plane. Assuming a Gaussian resolution for the Cherenkov angle, a likelihood function is calculated for each particle mass hypothesis. In case of overlapping rings, hits from other tracks form a background. Therefore, the local method performance is poor in regions of the detector where the track density is high. Since the dominant background is signal from other tracks, the global method implements a simultaneous fit to all tracks' hypotheses to take this into account. The global method considers all track information from both RICH1 and RICH2 simultaneously. A likelihood function is calculated for the entire event, by



(a) (b)

Figure 2.23: Simulated event display for a typical event in (a) RICH1 and (b) RICH2. Fitted rings are superimposed.

comparing the number of photoelectrons in each pixel with the number expected in that pixel from all possible sources, both genuine signal and background. The track mass hypotheses are then varied so as to maximise a log-likelihood of this form:

$$\ln \mathcal{L} = -\sum_{tracks\, j} \mu_j + \sum_{hits\, i} \left(n_i \ln \sum_{tracks\, j} a_{ij} \right) + \sum_{pixels\, i} \ln n_i! \qquad (2.11)$$

where n_i is the observed number of photoelectrons in pixel i, a_{ij} is the expected number of detected photoelectrons from track j in pixel i (under a given mass hypothesis), and $\mu_j = \sum_j a_{ij}$ is the total number of expected photoelectrons from track j. The last term is a constant and can be ignored. Eq. 2.11 can easily be generalised to include background sources, either pixel- or track-related. An example of fitted rings in simulated events is shown in Figure 2.23.

Although the RICH system is designed primarily to provide separation between hadrons (p, K and π), it can also provide information on leptons. Equally, information from the calorimeters and muon stations can provide some hadron identification. In order to maximise the PID performance, a global likelihood hypothesis for each particle type is formed by combining the particle likelihood hypotheses as determined

by each subdetector. However, the absolute likelihood value itself is not the useful quantity since the scale will be different for each event. Moreover, to limit the level of misidentified particles, it is more efficient to exploit the relative differences between particle hypothesis log-likelihoods. In case of $K - \pi$ separation, one would consider:

$$\Delta\mathcal{L}_{K\pi} = \ln \mathcal{L}(K) - \ln \mathcal{L}(\pi) \equiv DLL(K - \pi). \tag{2.12}$$

2.5 LHCb Detector Performance

In the following, a non-inclusive overview of the performance of the LHCb detector will be presented, as obtained either from recent collision or test-beam data.

2.5.1 Tracking Performance

When running at $\sqrt{\mathbf{s}} = 7\,\text{TeV}$ the beam size in the transverse direction is sufficiently small so that the two halves of the VELO can be safely positioned in their nominal fully closed position as described in Section 2.3.1.1. Therefore, the performance of the tracking system can be fully exploited. The primary vertex resolution in data has been assessed using the following procedure. For each collision event the tracks in the VELO were split into two samples (either randomly or in detector regions) and one primary vertex for each sample was fitted; the difference of the two positions is a measurement of the resolution. The results obtained with this method are shown in Figures 2.24-2.25. The resolution on the impact parameter (IP) with respect to the primary vertex can be measured. In Figure 2.26 the IP resolution as a function of the inverse of the transverse momentum is shown as obtained from 2011 data and compared to MC simulation. These resolutions are linear functions of the inverse transverse momentum and for 2011 data can be parametrised $\sigma_{IP_X} = 13.2 + 24.7/p_T\,\mu\text{m}$ and $\sigma_{IP_Y} = 12.2 + 24.4/p_T\,\mu\text{m}$ in the x and y directions, respectively. Although data still show a worse resolution when compared to MC simulations, the discrepancy is being constantly reduced with time, as the understanding of the detector improves.

The tracking efficiency in 2011 data for long tracks has been estimated using a

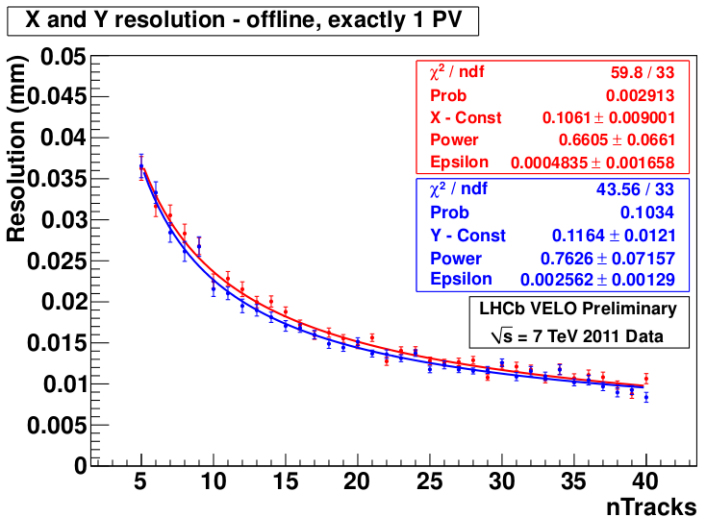


Figure 2.24: Primary vertex resolution in 2011 data in the (a) x and (b) y direction at $\sqrt{s} = 7\,\text{TeV}$ as a function of the number of tracks used to fit the vertex. Data results (in black) are compared with simulation (in red).

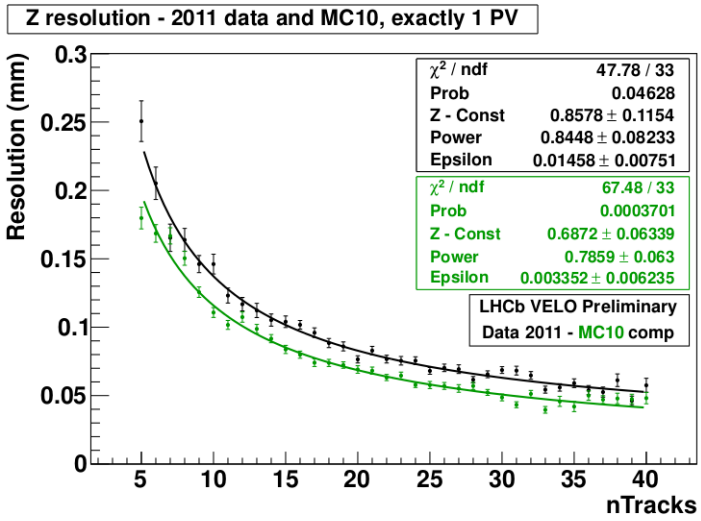
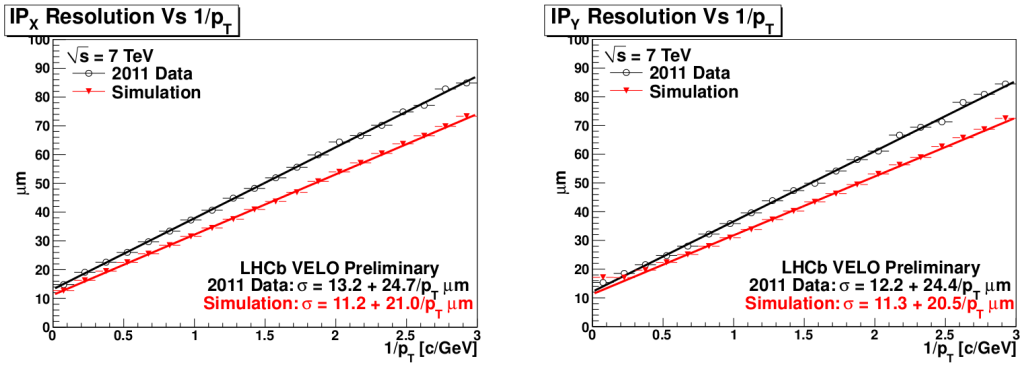


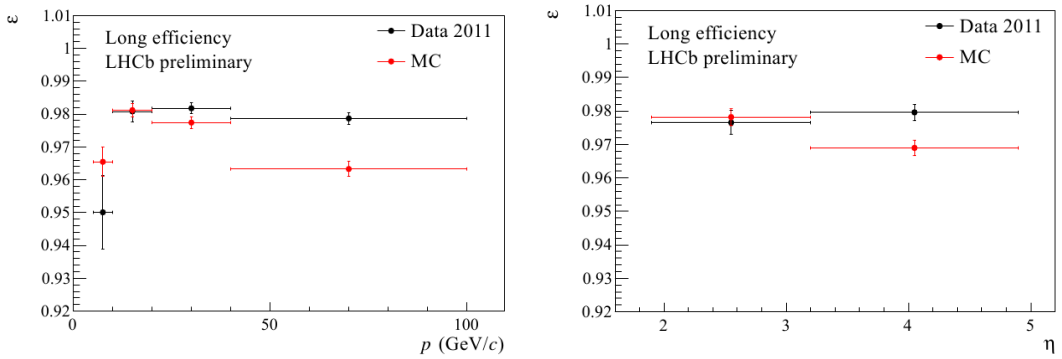
Figure 2.25: Primary vertex resolution in 2011 data in the z direction at $\sqrt{s} = 7\,\text{TeV}$ as a function of the number of tracks used to fit the vertex. Data results (in black) are compared with simulations (in red).

tag-and-probe approach for $J/\psi \to \mu^+\mu^-$ decays. In this approach, one of the muons, the "tag", has been fully reconstructed while the other muon, the "probe", is only partially reconstructed. The tracking efficiency is then obtained by trying to match the probe to a fully reconstructed track. The efficiency can be determined as a function of several parameters such as the momentum of the particle, the pseudorapidity and the multiplicity of the event, as shown in Figure 2.27.



(a) (b)

Figure 2.26: Impact parameter resolution in 2011 data in the (a) x and (b) y direction at $\sqrt{s} = 7\,\text{TeV}$. Data results (in black) are compared with simulation (in red).

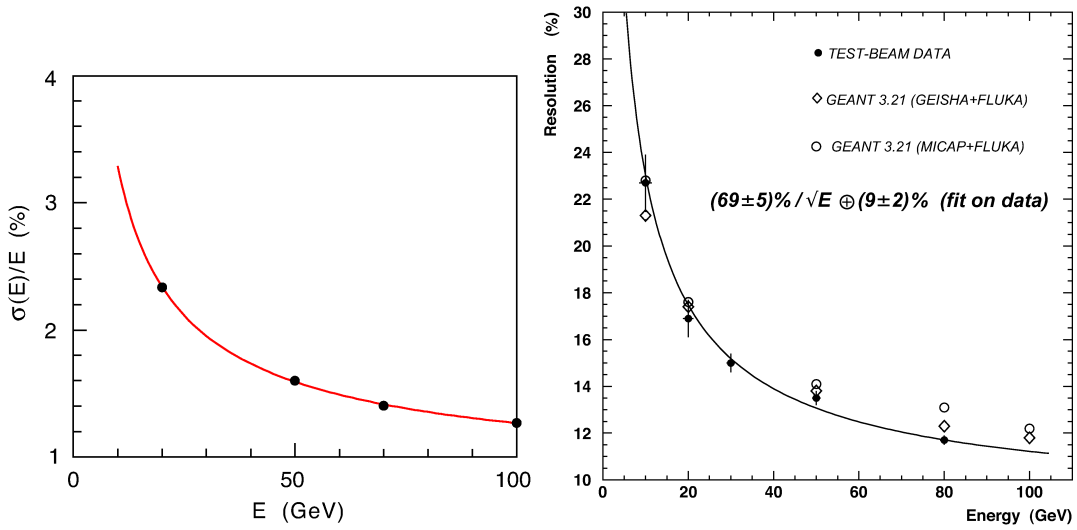


(a) (b)

Figure 2.27: Efficiency for long tracks in 2011 data as a function of (a) momentum and (b) pseudo-rapidity at $\sqrt{s} = 7\,\text{TeV}$. Data results (in black) are compared with simulation (in red).

2.5.2 Energy Resolution

The ECAL resolution is parametrised as a function of energy as $\sigma_E/E = a/\sqrt{E} \oplus b \oplus c/E$, where a represents the stochastic term, b is the constant term and c represents the noise in the system. Tests performed with electron beams measured a stochastic term of $8.5\% < a < 9.5\%$ and a constant term $b \sim 0.8\%$. The overall resolution, shown in Figure 2.28(a), exceeds the design performance of $\sigma_E/E = 10\%/\sqrt{E(GeV)} \oplus 1\%$. The energy response of the HCAL has been studied using pion beams from the SPS. Results, shown in Figure 2.28(b), give $\sigma_E/E = (69 \pm 5)\%/\sqrt{E(GeV)} \oplus (9 \pm 2)\%$.



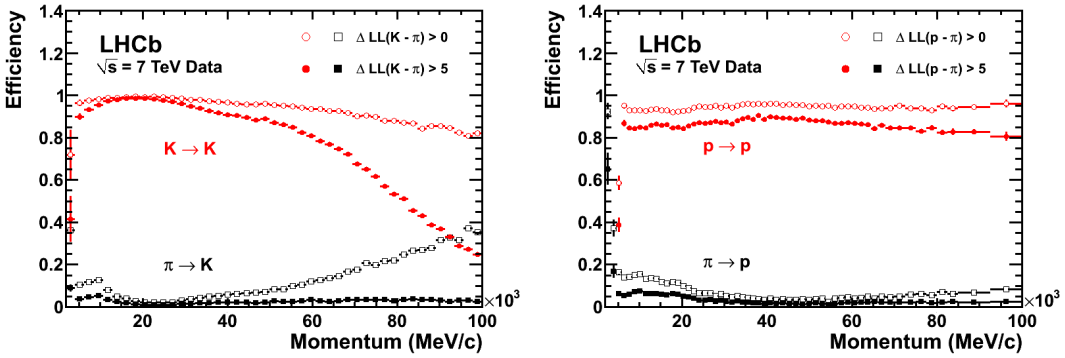
(a) ECAL (b) HCAL

Figure 2.28: Energy resolution of the LHCb calorimeter system.

2.5.3 Particle Identification Performance

The PID performance of the LHCb detector for hadrons can be determined directly from data using calibration samples of $\Lambda(\bar{\Lambda}) \to p\pi^-(\bar{p}\pi^+)$, $K^0_S \to \pi^+\pi^-$, $D^{*\pm} \to D^0(K^-\pi^+)\pi^\pm$ and $\phi \to K^+K^-$. These samples, selected with PID-unbiasing algorithms, provide background-free samples of protons, kaons and pions to calibrate efficiency and misidentification fractions for a given DLL value. The details of the procedure, based on the "tag" and "probe" approach, are described in Chapter 4. The performance for kaon identification is shown in Figure 2.29.

Muons are identified by extrapolating reconstructed tracks with $p > 3\,\mathrm{GeV}/c$ into the muon stations. A track is considered as a muon candidate when a minimum number of stations (2-4 depending on momentum) has associated hits. Similarly to hadrons, the muon identification is performed via a DLL cut and efficiencies are calibrated using $J/\psi \to \mu^+\mu$ decay data samples. The performance of the muon identification as a function of momentum is shown in Figure 2.30.



(a) Kaon-pion separation performance. (b) Proton-pion separation performance.

Figure 2.29: LHCb PID performance for long tracks in 2011 data. The efficiency to correctly identify (a) kaons and (b) protons are shown by the red data points and the corresponding pion misidentification probability by the black data points.

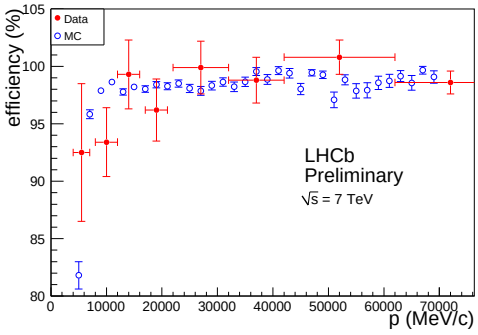


Figure 2.30: Muon identification efficiency as measured from 2010 data taken at $\sqrt{s} = 7\,\text{TeV}$. Data points (red) are compared to MC simulations (blue).

Chapter 3

The Magnetic Distortion Calibration System in RICH1

3.1 Introduction

Being located immediately upstream of the LHCb dipole magnet, RICH1 is exposed to significant magnetic fields. The magnitude of the field can be as high as 60 mT in the HPD plane without shielding. Extensive studies have been performed to estimate the distortions of the photoelectron path (Figures 3.1,3.3) by exposing a full-scale HPD to typical magnetic fields [54]. Considering a magnetic field parallel to the HPD tube axis, the HPD can operate at full geometric efficiency up to a field magnitude of 3 mT. Increasing the field to 5 mT introduces an effective loss of photocathode image on the readout sensor of about 4%, which become progressively worse for higher fields.

A factor $5-100$ reduction in field strength is achieved with magnetic shielding of the HPDs using two iron boxes, each of which contains each HPD array including readout electronics, and cylindrical shields surrounding individual HPDs. The overall screening reduces the magnetic field magnitude inside the HPD tube to less than 0.5 mT [54]. However, any residual field may still influence the HPD performance and ultimately degrade the resolution on the Cherenkov angle.

In order to calibrate our remaining magnetic distortion effects, a dedicated hardware device, the Magnetic Distortion Calibration System (MDCS), has been installed

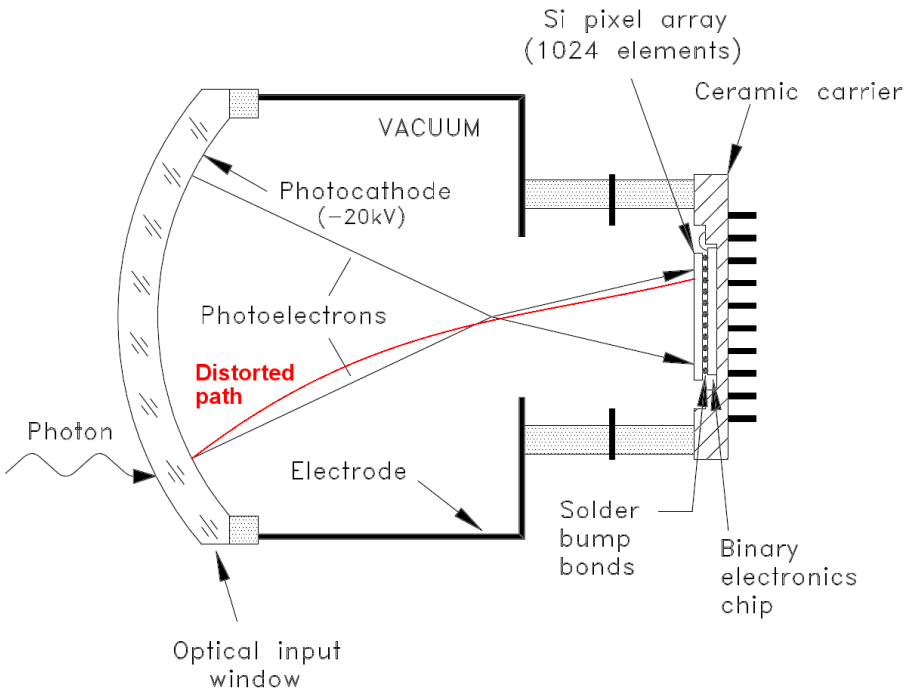


Figure 3.1: HPD layout showing the distortion introduced on the photoelectron trajectories due to a magnetic field.

in RICH1. The system is composed of two moveable carbon-fibre bars equipped with Light-Emitting Diode (LED) arrays. Each bar passes in front of the entire HPD plane, in the upper and lower HPD array respectively, illuminating the HPDs with a grid-like pattern. Special data-taking runs, "MDCS scans", are taken periodically when there is no beam in the LHC.

In this chapter the ensemble of hardware components, the analysis software and results are presented.

3.2 Magnetic Field Shielding in RICH1

The shielding design has been optimised with the TOSCA/OPERA1 finite element software package [55], which was also used to design the LHCb dipole magnet. The shielding boxes are made of "supra" iron, from 50 mm to 100 mm thick, with a saturation field of 1.8 T (see Figure 3.2). At full field, when magnetic forces are around 50 kN, the rigidity of the structure ensures that any displacement of the HPD assembly is less than 0.5 mm [56]. Measurements made with the shielding boxes in place and the LHCb

dipole at nominal field indicate that the HPD plane is exposed to a maximum field of 2.4 mT. Moreover, the resulting field orientation at the HPD planes is approximately parallel to the HPD tube axis, although small transverse fields are still present.

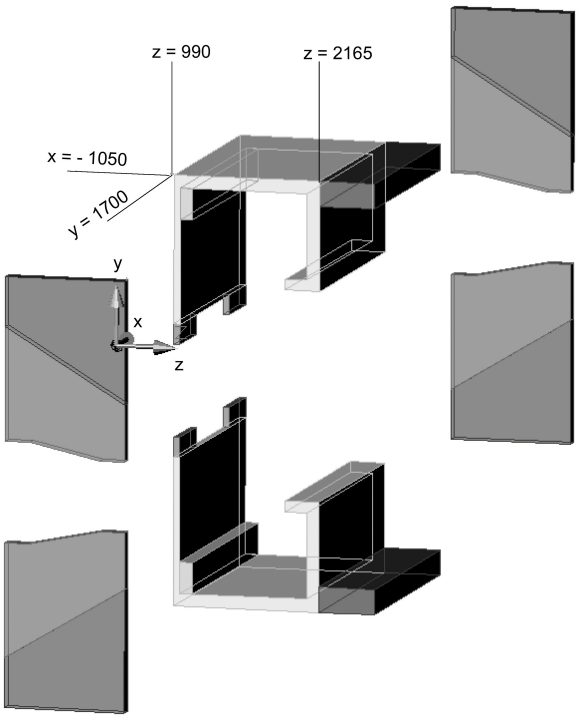
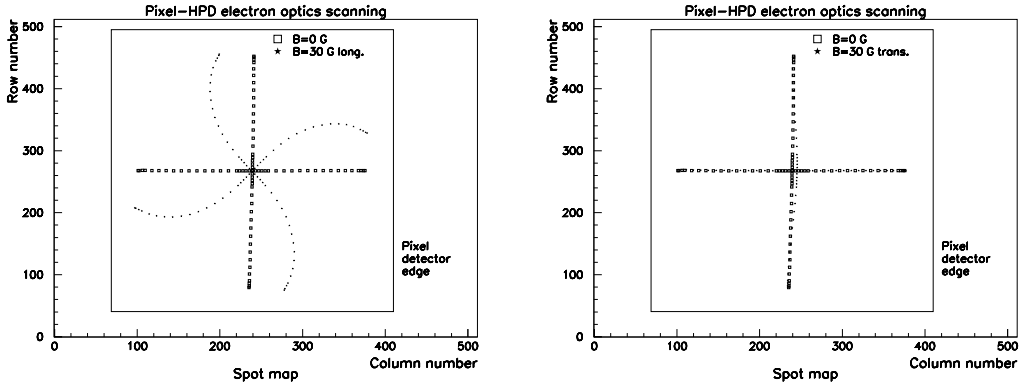


Figure 3.2: Magnetic shielding of the HPD boxes in RICH1.

The iron boxes reduce the magnetic field at the HPD plane to a level at which the entire photocathode image is contained on the silicon sensor. However, with no additional shielding, the image distortion is still significant, particularly for longitudinal fields (see Figure 3.3).

In order to further reduce the field within the photon detectors, individual HPDs are enveloped in Mu-metal (nickel-iron alloy) cylindrical shields, 200 mm long and 0.9 mm thick (Figure 3.4). Each shield is grounded and insulated from the HPD with a 250 μm Kapton foil. Mu-metal is chosen for its high permeability. These individual shields reduce the field strength within the HPD to less than 0.5 mT.

The residual magnetic field still produces a significant distortion of the HPD optics in the form of a rotation of the image due to the dominant longitudinal magnetic field component. Transverse components are more difficult to shield due to saturation of the Mu-metal and generally they produce a shift of the entire image. However, the



(a) Longitudinal field (b) Transverse field

Figure 3.3: Distortion introduced on an HPD image from a cross-shaped pattern without any shielding due to an external magnetic field of 3 mT (a) parallel and (b) perpendicular to the HPD tube axis.

shift is often negligible and masked by more important effects such as misalignments of the silicon assembly inside the HPD tube.



Figure 3.4: Mu-metal cylindrical shields surround the HPDs and extend 20 mm outwards towards the gas radiator.

3.3 MDCS System Design

The strategy for the MDCS implementation is as follows. A light spot is projected at a precisely-known position on the HPD plane. The spot is oriented front-on to minimise refractive effects at the HPD quartz window and shadowing by the Mu-metal shields. The light spot induces the production of photoelectrons at the photocathode that are cross-focused towards the HPD silicon sensor producing a narrow cluster of hits which is recorded by the LHCb data acquisition system. The spot position is moved to scan the HPD array in two dimensions, with small enough step size to map out the magnetic distortion of each HPD. The data taken from this scan form a direct mapping of the magnetic distortions at a given magnetic field.

A "mapping" is deduced by associating the cluster measured on the silicon sensor to the corresponding light-spot position at the HPD plane. The calibration is achieved for each HPD by a parametrised functional fit that provides an individual correction of the magnetic distortion for each HPD in the plane.

The basic system design is shown schematically in Figure 3.5. Instead of a single light spot moving in two dimensions, spatial constraints on the system size forced a solution having a bar spanning the HPD array with many individual LEDs, termed "light bar". Each LED in the light bar can be individually powered, and each is collimated to project a light spot onto the HPD plane. The light bar is mounted as a gantry between two linear motion control stages. The movement of a given light spot in the direction of the stages is very fine and nearly continuous, while the position of the light spot in the direction of the light bar is adjusted discretely by powering adjacent LEDs along the bar.

3.3.1 Hardware Description

RICH1 is equipped with two identical MDCS devices, one for each of the upper and lower HPD arrays. Each device is placed inside a "photon funnel", an aluminium structure between the HPD box and the RICH1 gas enclosure (see Figure 3.6). A 5 mm-thick quartz window at the entrance of the funnel isolates the C_4F_{10} Cherenkov gas

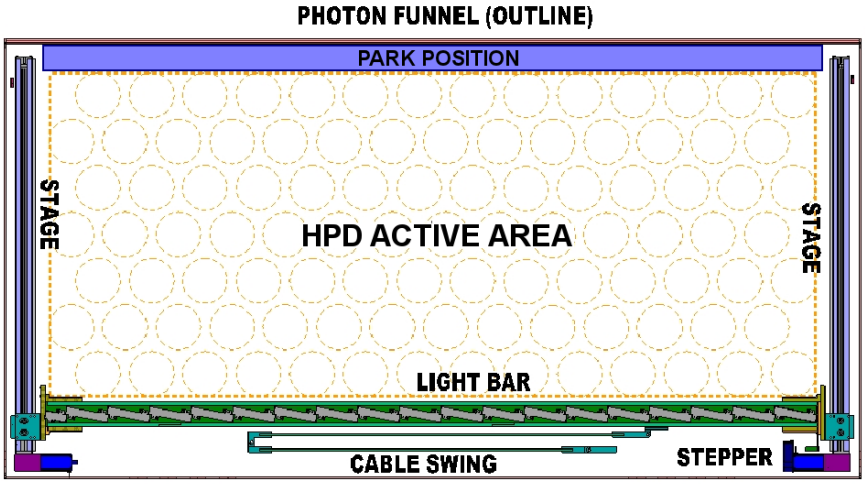


Figure 3.5: Scheme of the MDCS hardware for one of the HPD planes.

volume from the photodetectors whilst providing a transparent passage for Cherenkov photons over a wide range of wavelength. The design of the photon funnel imposed numerous constraints as it had to accommodate the MDCS device within a depth of 75 mm.

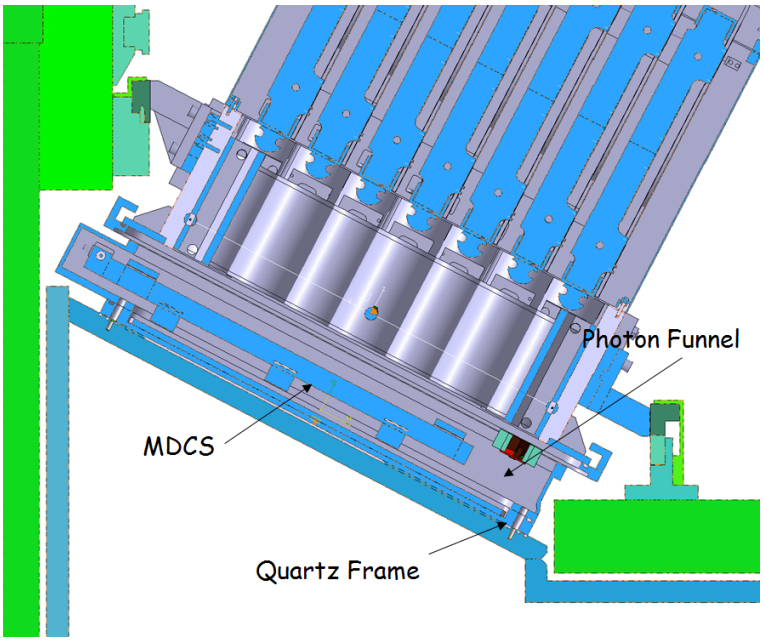


Figure 3.6: The MDCS system, shown here in projection, located inside the photon funnel.

3.3.1.1 Light Bar

The light bar consists of a series of 19 LED printed circuit board (PCB) modules mounted on two long carbon fibre bars. Four LED arrays consisting of a 5x7 matrix of green LEDs ($\langle\lambda\rangle = 563\,\text{nm}$) are mounted on each PCB to form a 5x28 LED matrix, as shown in Figure 3.7. The spacing between two consecutive LED centres is 2.54 mm.

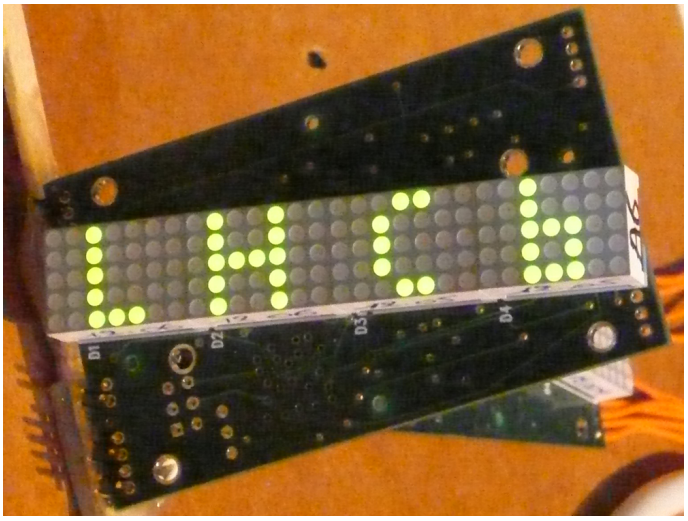


Figure 3.7: A MDCS PCB module with a 5x28 matrix of LEDs.

In order to focus the light and control the photon yield, a block with individual collimators is mounted on top of each module, as shown in Figure 3.8. The collimator geometry has two 6.35 mm lengths of 0.343 mm diameter holes separated by one 12.7 mm length of 1 mm diameter. This design minimises specular reflection from the collimator internal walls and provides an optimum spot size.

The modules are tilted in such a way that the long sides of bar and module form an angle of 11.31° (see Figure 3.9). This tilt gives a 0.5 mm granularity of LED centres, as projected in the long dimension of the light bar. All the modules are connected electronically in series with an input voltage of 5.1 V controlled by a regulator on the bar. Each bar is powered by an external 7.5 V supply, located approximately 20 m away from RICH1, connected via shielded 25 m cables.

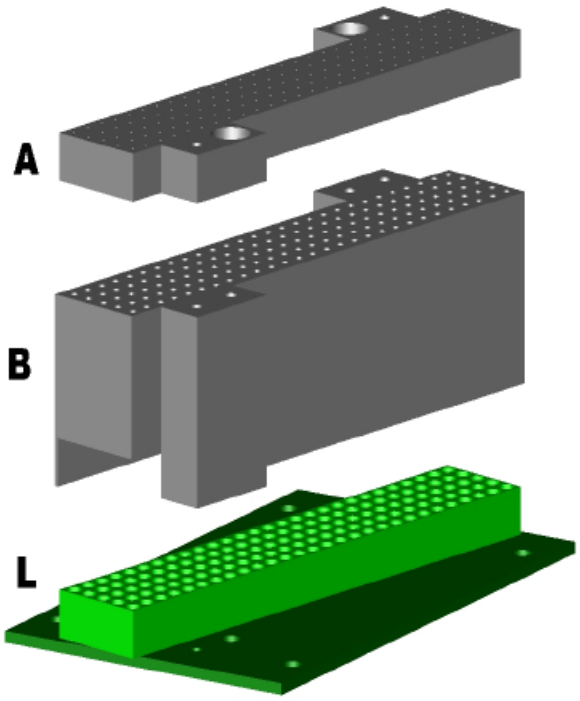


Figure 3.8: An exploded view of an LED PCB module. Light is emitted from LED array L into the collimator unit, encountering first part B having short small-diameter holes followed by longer larger-diameter holes, and then part A having the same short small-diameter holes. Light emerges upwards toward the HPD panel (not shown).

3.3.1.2 Motion Control

The light bar is mounted on a gantry connected to two 540 mm long aluminum linear stages, each mounted along the short sides of the photon funnel. The stages which drive the light bar are powered by a pair of Parker LD28 stepper-motors, synchronised by a single controller unit to avoid differential movement. A gear-box transmits the power from the motors to the gantry with a gear ratio such that 4,000 steps from the motor correspond to a bar movement of 3 mm. An LP28 positioner is used to monitor the position of the light bar. The motor movement is extremely precise; when the full 540 mm length of the stage is covered with $\sim$ 100 stop-and-go movements, the error on the final position reading is less than 40 μm. In comparison, the intrinsic resolution of an HPD, taken as the projection of a silicon pixel up to the outer side of the quartz window, is 2.8 mm.

The start position of the bar is defined by a "home" switch installed on the motor.

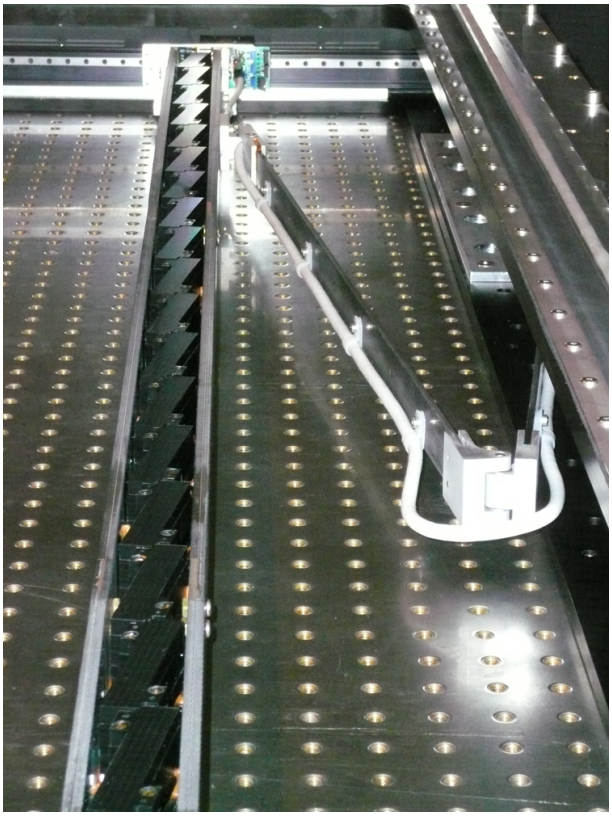


Figure 3.9: View of the photon funnel and LED modules mounted on the carbon-fibre bar during a test.

The switch is equipped with a Hall-effect sensor and is tripped by a magnet embedded in the carriage. The switch signals the motor to stop whenever the carriage is approaching the end of travel and provides a fixed reference point to which the carriage can be commanded to return repeatedly. The system has a position repeatability better than 100 μm when approaching from the same direction.

When the MDCS is inactive the light bar is kept at the "park" position, shown in Figure 3.5 on the left side in the funnel, where it does not block Cherenkov light entering the funnel. During an MDCS scan, the stages move the light bar to scan over the HPD plane.

3.3.2 Light Bar Operation

The light bars are controlled interactively via TCP/IP using a PVSS project[1], integrated into the RICH1 detector control system. A screenshot of the control panel is shown in Figure 3.10. MDCS scans can only occur when beams are not circulating in

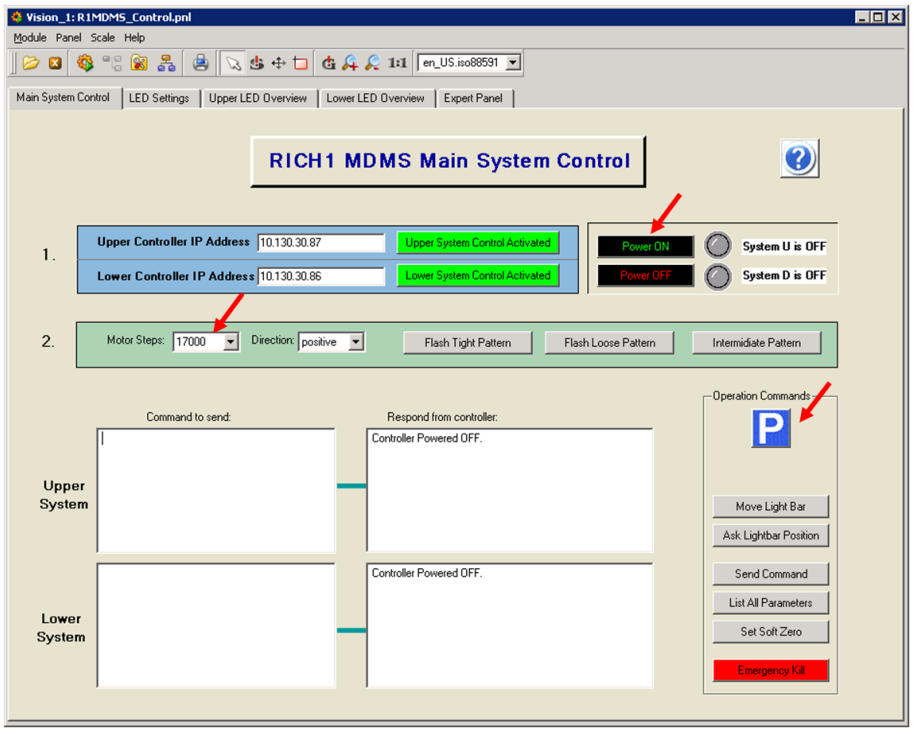


Figure 3.10: A screenshot of MDCS PVSS control panel.

the LHC and RICH1 can be taken under local control by a RICH expert. In order to exploit the full resolution of the position measurement, scans are taken in ALICE mode (Section 2.4.3) of the HPD chip.

The LEDs are synchronised with the light bar movement to generate a grid-like pattern of light spots over the entire HPD plane. A scan is divided into "steps", uniquely characterised by a fixed bar position and a given configuration of LED illumination. All PCB modules share the same configuration, with only one LED per module switched on for all configurations. The geometry of the system is such that at each step, an HPD can be illuminated by only one LED. In this way, hit clusters can be directly associated to the light spot which generated it.

During a step, the readout boards are triggered periodically at $\sim 2\,\mathrm{kHz}$ until 6000

[1]PVSS process control software, from ETM Professional Control GmbH, Eisenstadt, Austria.

pulses (events) have been recorded. Then the system moves to the next step configuration. In the transition between steps, the light bar may be moved if necessary to reproduce the grid. Once the new configuration is reached, the data acquisition starts again. Including dead-time (e.g. when the bar is moving and no data can be taken),

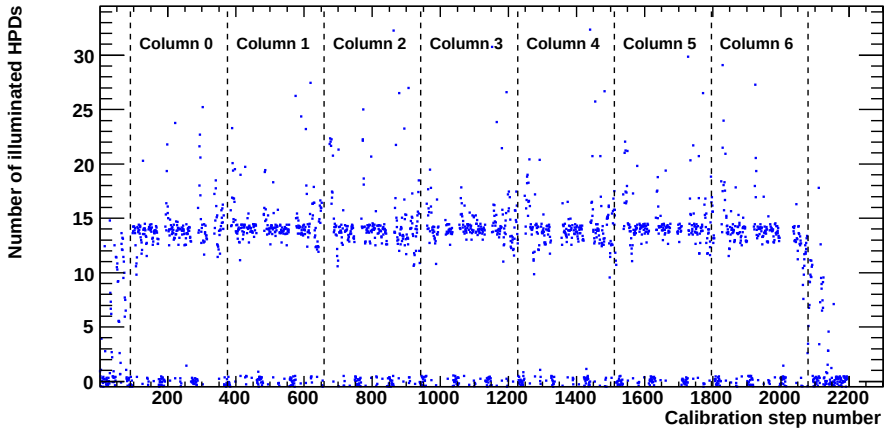


Figure 3.11: Number of illuminated HPDs in the upper box as a function on the calibration step (magnet polarity down).

1.8 hours and 2200 steps are needed to calibrate the entire HPD array and the light bar moves 42 times. The bar can illuminate directly only one column (14 HPDs) at a time, this is demonstrated in Figure 3.11 where the column structure is visible. The scan is performed for upper and lower HPD box simultaneously.

Even though the LED light is focused, typically several HPD pixels collect hits. Therefore, there is not a well-defined pixel to consider when performing the calibration analysis but rather a cluster of hits with a peaked structure (hereafter called "peaks"), as visible in Figure 3.12.

3.4 Data Processing

The first tasks in analysing the MDCS scan data are identifying the peaks and cleaning the images in order to distinguish peaks due to LED light spots from unwanted background processes.

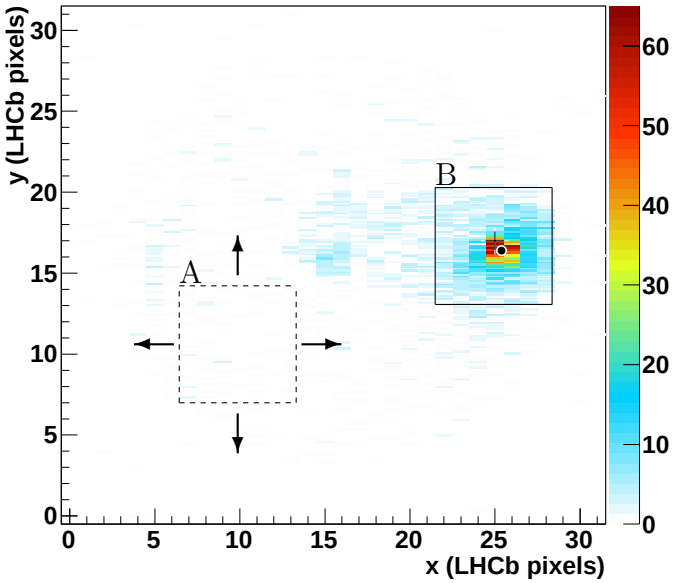


Figure 3.12: A typical HPD pixel hit map caused by a single position of LED light. The peak-finding algorithm uses a search window of 7x7 LHCb pixels that is moved (A), a peak candidate is formed when its position on the silicon sensor is centred around the hit cluster(B). The black dot marks the centre of a two-dimensional Gaussian fit, and the cross marks the position of the arithmetic mean, for comparison.

3.4.1 Peak Finder

The peak-finding algorithm forms peak candidates from the photoelectron hits recorded from the 6000 LED pulses at each step. ALICE pixels with more than 100 hits/step and with one or more of the eight neighbouring pixels having no hits, are flagged as noisy and removed from the analysis.

Since one LED typically illuminates an area covered by a matrix of 7×7 LHCb pixels in the silicon sensor, peak candidates are searched for in a square window of that size, shown in Figure 3.12. A peak candidate is formed if the position of the window is such that its central pixel contains at least 1% of the total hits in the HPD (for that particular step) and all surrounding pixels have less entries. Overlap of 7×7 windows for different peaks in the same step is not allowed.

The hit distribution within the square window is then fitted using a rotatable two-dimensional Gaussian probability density function (pdf):

$$\mathcal{G} = M \times \exp\left\{-\frac{1}{2}\left[\left(\frac{Z_1}{\sigma_1}\right)^2 + \left(\frac{Z_2}{\sigma_2}\right)^2\right]\right\}, \tag{3.1}$$

where

$$Z_1 = (X - x)\cos(\theta) + (Y - y)\sin(\theta),\ Z_2 = -(X - x)\sin(\theta) + (Y - y)\cos(\theta). \tag{3.2}$$

The fitted parameters are as follows: M is the peak height, X and Y identify the fitted peak position, the angle θ accounts for any rotation in the xy plane, and $\sigma_{1,2}$ are the widths of the peaks along the $Z_{1,2}$ directions. The peak properties extracted by the Gaussian fit are used in the next steps of the analysis.

An example of the output of the peak-finding algorithm is shown in Figure 3.13, where the underlying grid of signal peaks within each HPD from correctly reconstructed LED light is clearly visible. The presence of several background sources induces many fake peaks, e.g. the circular structure seen in every HPD.

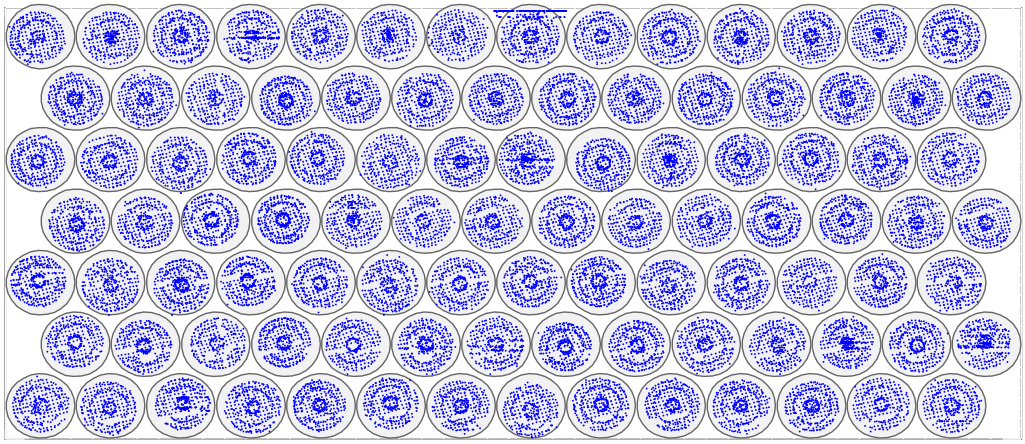


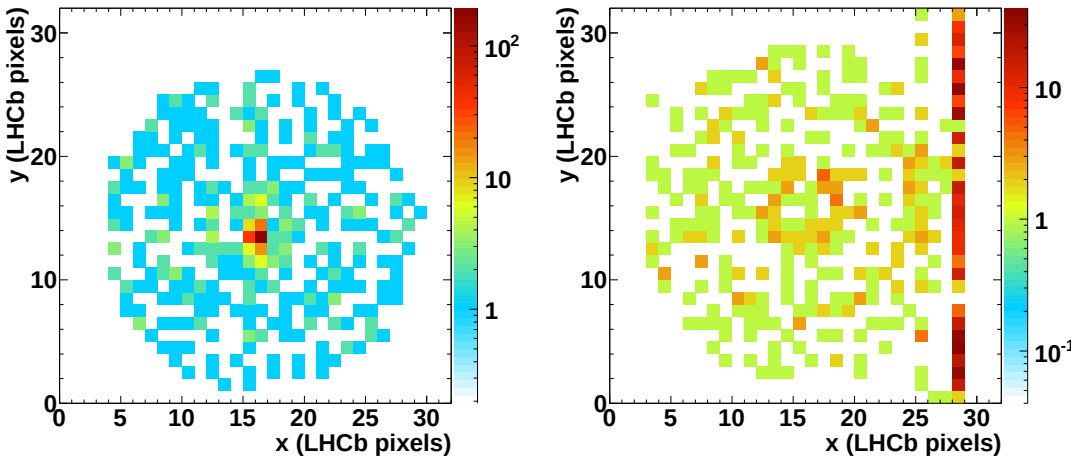
Figure 3.13: Fitted peak positions on the upper HPD plane (magnet polarity down) before cleaning.

3.4.2 Sources of Background

Fake peaks may arise from noisy pixels in the silicon chip, ion feedback (IFB)[57] and reflection of the LED light inside the HPD.

IFB occurs when a photoelectron ionises residual gas atoms inside the HPD tube.

The ion drifts slowly to the photocathode producing secondary electrons which are then focused onto the sensor with a typical delay of 200-300 ns. The reconstructed background peaks due to IFB are usually located in the vicinity of the sensor centre as shown in Figure 3.14(a).



(a) Ion Feedback (b) Noisy Pixels

Figure 3.14: Hit maps of an HPD affected by (a) IFB and (b) having noisy pixels.

The second major source of background is not related to a particular HPD as it depends on the position of the light spot relative to the tube. This is due to total internal reflection of LED light inside the HPD quartz window as shown in Figure 3.15. This effect occurs whenever the LED illuminates a narrow region, about 3 mm wide, close to the edge of an HPD and produces the characteristic hit structure shown in Figure 3.16. The structure is composed of three or more hit clusters at a well defined radius (measured from the HPD axis), defined by the radius of curvature and thickness of the window and quartz properties. During a scan the structure occurs several times, generating the circular features visible for each HPD in Figure 3.13.

HPDs with noisy pixels or affected by IFB can be easily flagged since they always have hits, even when the light bar is not above them. They usually have a mean number of reconstructed peaks, integrated over the entire scan, well above the average of all the HPDs. HPDs where the mean number is two standard deviations greater from the average are considered either noisy or IFB-affected. Figure 3.17 shows the

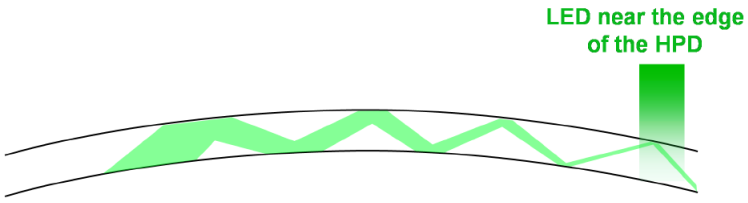


Figure 3.15: Total internal reflection in the HPD quartz window caused by LED light illuminating the edge of the window.

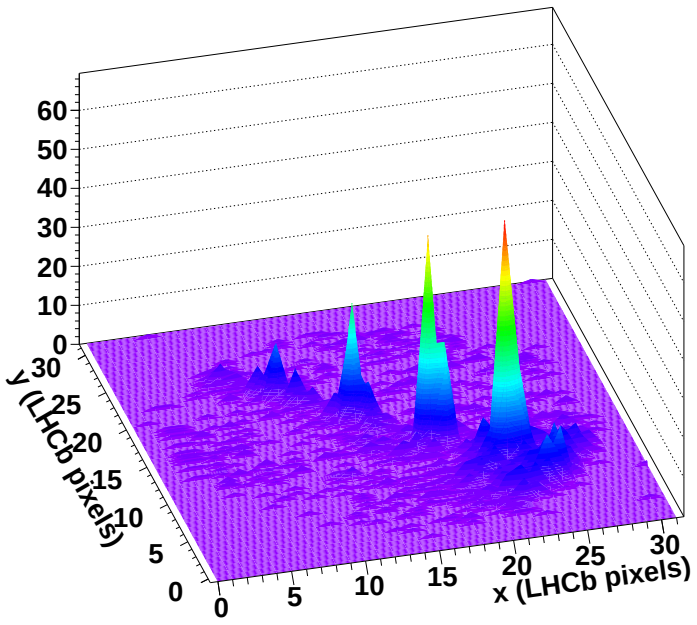


Figure 3.16: The hit structure caused by total refraction of LED light inside the quartz window.

distribution of number of peaks for a typical scan, where three outliers are clearly visible at high peak multiplicity.

The three background sources are independent and the reconstructed peaks from these sources depend on the particular HPD and scan step. In order to enhance the signal and remove the background, a cleaning procedure has been implemented.

3.5 Pattern Cleaning

The aim of the cleaning procedure is to distinguish signal peaks of correctly reconstructed LED light from the background sources described in 3.4.2. The likelihoods for signal and background are constructed using the peak properties, then a cut on

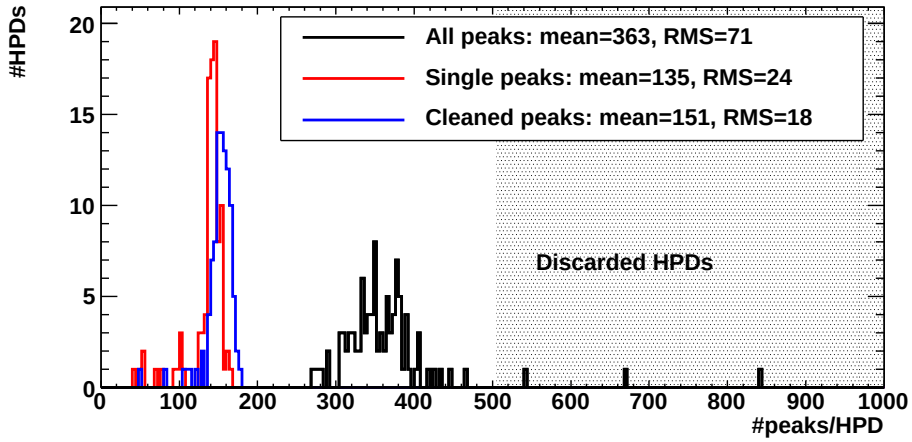


Figure 3.17: Integrated number of peaks per HPD in the upper box (magnet polarity down). The difference between "all peaks", "single peaks" and "cleaned peaks" are explained in Section 3.5.

the difference in the log likelihood (DLL), considering the two hypotheses, is applied to suppress the background.

3.5.1 Peak Properties

As there are 18 LED modules spanning 14 HPDs, each HPD is generally illuminated by only a single LED. Ideally this would produce just one peak per HPD per step, or "single" peaks. Considering only single peaks for the reconstructed pattern leaves a very clean sample of signal peaks. However, the efficiency of this method is generally poor since it is heavily dependent on the HPD and may not select peaks for particularly noisy ones (see Figure 3.18). Hence, due to background sources, a single peak requirement is not satisfactory. Therefore a likelihood-based method has been implemented to decide if a given peak is correctly reconstructed, regardless if it may not be unique on the HPD.

Since there is no Monte Carlo simulation of the system, a data-driven method is used to extract distributions and to build signal and background likelihoods. This method

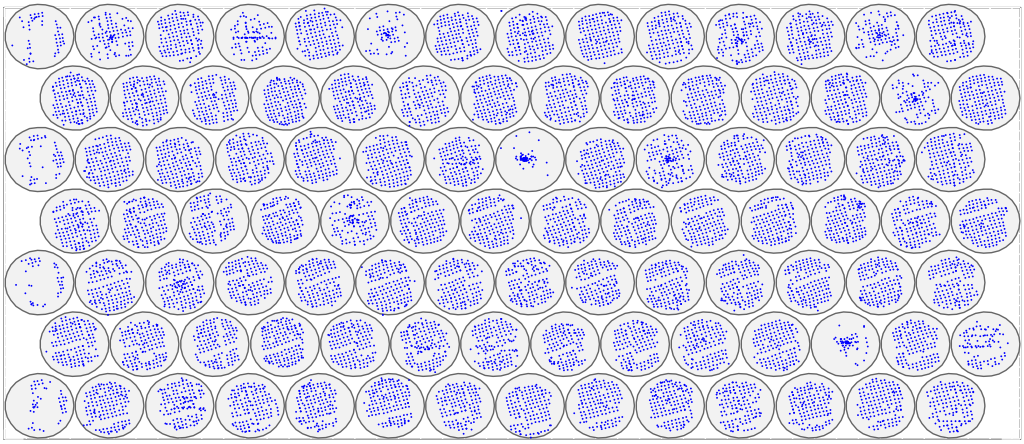


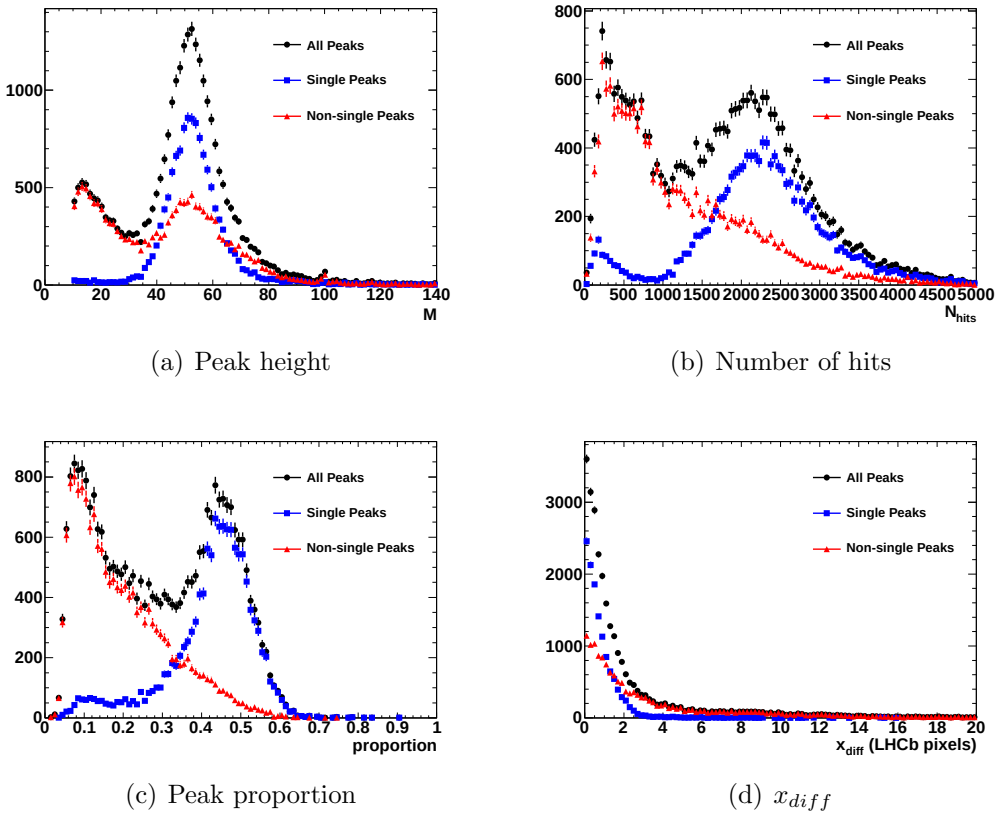
Figure 3.18: Single peak positions on the HPD upper box (magnet polarity down).

implicitly assumes that all HPDs have a similar response to the bar illumination. Four variables have been considered to characterise the peak properties and build the likelihood distributions:

- peak height M,
- total number of hits, N_{hits},
- peak proportion, p,
- a position dependent parameter, x_{diff}.

Here N_{hits} is the total number of hits forming the peak for a given scan step and p is the ratio between N_{hits} and the total number of hits for that particular HPD. This reflects the fact that the light in the peak should be a significant contribution to all hits in the HPD. The variable x_{diff} is defined as follows. Since the bar orientation is such that it covers an entire HPD column, by taking the direction of the bar movement (perpendicular to the columns) as a reference coordinate, x in the HPD reference frame, it must occur that, for a given step, signal peaks for HPDs in the same column must approximately lie around a mean position $\langle x \rangle$. The corresponding $\langle x \rangle$ for each peak is estimated using single peaks from HPDs in the same column. x_{diff} is simply defined as $|x_{meas} - \langle x \rangle|$.

Examples of single and non-single distributions are shown in Figure 3.19. It is clear that non-single peaks contain a substantial fraction of signal peaks.



(a) Peak height

(b) Number of hits

(c) Peak proportion

(d) x_{diff}

Figure 3.19: Distributions from the HPD upper box of the variables used to build the peak-finding likelihood (magnet polarity down). IFB-affected and noisy HPDs are not included.

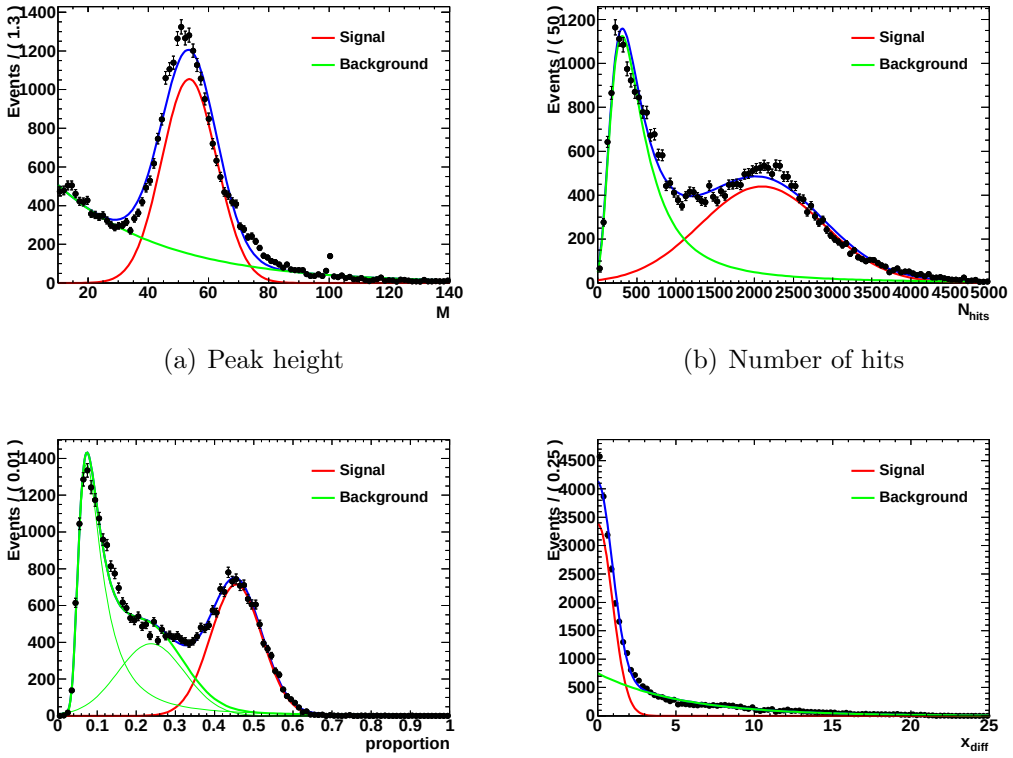
Variable	Signal pdf	Background pdf
Peak height (M)	Gaussian	Exponential
Number of hits (N_{hits})	Gaussian	Landau
Proportion (p)	Gaussian	Landau+Gaussian
x_{diff}	Gaussian	Exponential

Table 3.1: The functions used to fit the peak variable distributions.

3.5.2 Likelihood Determination

An important aspect of building the peak-finding likelihoods is the determination of signal and background shapes of the chosen variables. These are determined from signal-like distributions of single peaks and signal plus background distributions of all peaks. The choice of functional forms is summarised in Table 3.1.

An unbinned maximum likelihood fit is performed on the variable distributions, as shown in Figure 3.20. The signal and background shapes are subsequently com-



(a) Peak height

(b) Number of hits

(c) Peak proportion

(d) Difference between expected an measured position in x (HPD coordinates)

Figure 3.20: Fits to the distributions of the variables used to build the likelihood from the HPD upper box (magnet polarity down).

bined into likelihood distributions for the signal and the background hypotheses. The logarithmic difference between the two likelihoods (DLL) is taken as the discriminant variable for the peak selection. The DLL shape for single and non-single peaks is shown in Figure 3.21. Reconstructed peaks from HPDs flagged as noisy or IFB-affected are not included in the likelihood construction, however, they are considered in the final selection with the DLL. This is necessary to stabilise in time the cleaning response between different scans. In fact the number of HPDs with a significant IFB increases over time[2] and would change the shape of the likelihood distributions, making the cleaning unstable. Nevertheless, this has little impact on the performance; signal peaks have the same properties for all HPDs and not including those from a small number of problematic HPDs does not change the signal pdf. Peaks from IFB or noise are easily

[2]IFB degrades HPD performance, however affected HPDs are usually replaced during technical stops.

rejected as their properties are very different from signal. Although residual contamination from IFB peaks may resemble signal peaks in shape, IFB peaks always lie in the silicon sensor centre and are sensitive to criteria based on the position, such as x_{diff}.

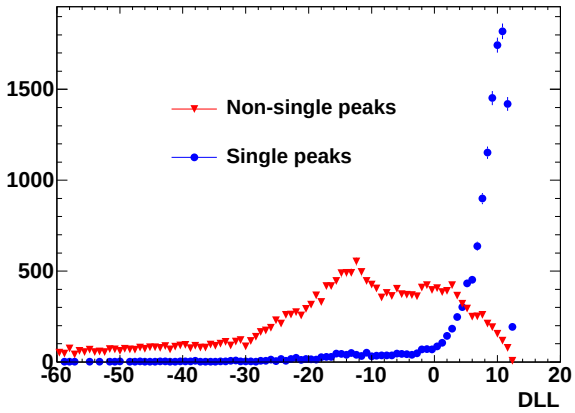


Figure 3.21: Delta Log Likelihood distribution from the HPD upper box (magnet polarity down).

3.5.3 Cleaning Performance

For a given scan, the cut in DLL can be varied depending on the purity needed. Usually a $DLL > 0$ is applied. If, in a given step and HPD, more than one peak passes the DLL cut, only the one with the highest DLL is retained. An example of the cleaned pattern is shown in Figure 3.22. Some HPDs close to the edge of the photon funnel (left in the figure) have a non-optimal cleaning. This is due to an atypical peak proportion p caused by reflections of the funnel. However, those HPDs are at the edge of the RICH1 acceptance and give relatively little contribution to its overall performance.

Compared to a single peak requirement, the likelihood method is more effective in suppressing backgrounds and enhancing signal content. Importantly, the grid pattern for several HPDs is recovered. Approximately 20% more signal peaks are available to the analysis by using this likelihood method. The cleaning procedure has performed in a stable way over time, regardless the magnet polarity or the HPD plane.

The cleaning is insensitive to the distortions in the pattern introduced by switching on the dipole magnet. This is expected since all the considered peak properties are not directly influenced by the presence of a magnetic field. The peak width distributions

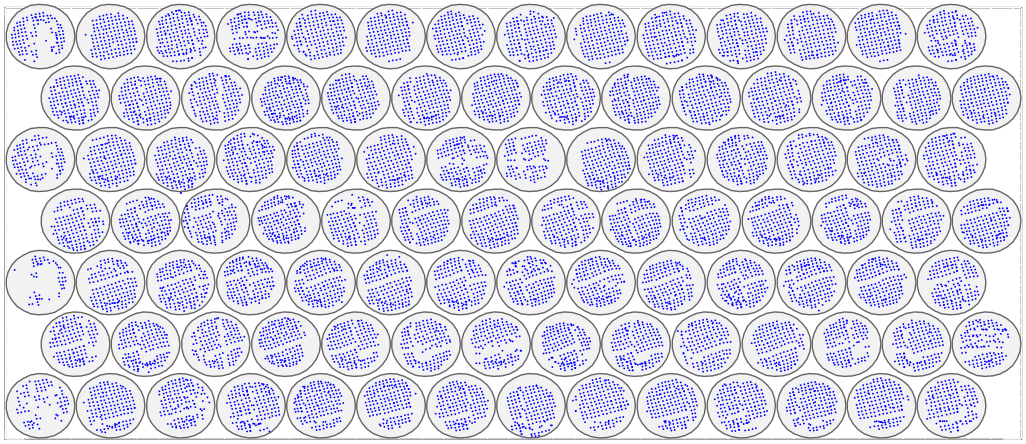


Figure 3.22: The cleaned final pattern, with $DLL > 0$, from the upper box (magnet polarity down).

for magnet off and on data are compared in Figure 3.23 and show good agreement. This fact, combined with the relatively small width of the peaks, ~ 0.84 pixels on average (0.42 mm at the anode), guarantees that the magnetic distortion does not introduce an additional spread in the photoelectron hits forming the peaks. Moreover, the vast majority of the peaks are approximately circular in shape as indicated by Figure 3.24 which shows the ratio σ_1/σ_2 peaking at one. Additionally an estimate can be made of the photon yield of the LEDs, shown in Figure 3.25. Assuming N_{hits} of signal, the peak amplitude is proportional to the number of photons emitted by one LED[3], and with a 13% photocathode quantum efficiency, the rate found is approximately 3 photons per 25 ns, consistent with expectations.

3.6 Calibration Parameter Extraction

The magnetic distortions of the HPD image are described by a parametrised function with radial and axial components. The parametrisation is extracted from the set of cleaned peaks and is the final part of the MDCS procedure. Calibration parameters are measured individually for each HPD and uploaded into the LHCb Conditions Database (CondDB) to be used to correct for the magnetic distortion in the event reconstruction.

[3]The time interval during which the HPD accepts hits after a trigger is received is 25 ns. During this time, the probability of having multiple hits on the same pixel is negligible.

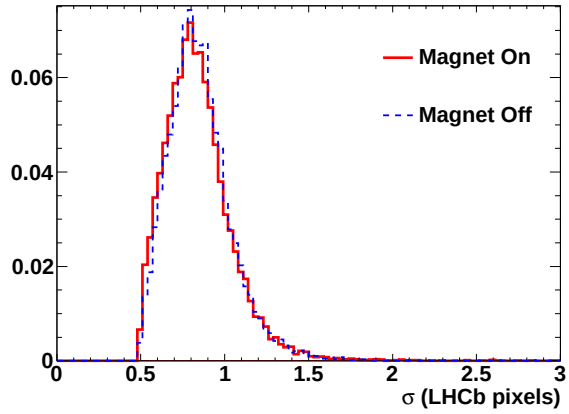


Figure 3.23: Distribution of fitted $\sigma = \sqrt{\sigma_1^2 + \sigma_2^2}$ of the cleaned peaks. Magnet on data are in red, magnet off in blue.

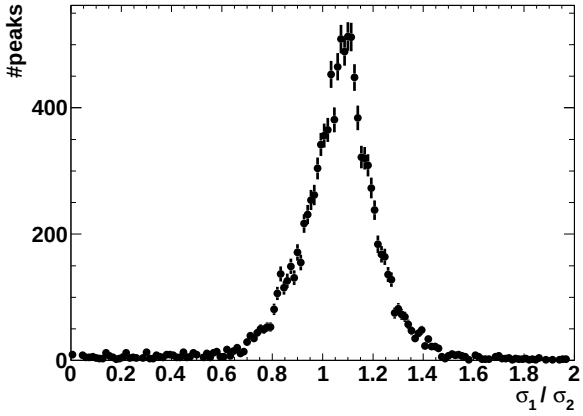


Figure 3.24: Distribution of the ratio between the orthogonal widths of the 2-dimensional Gaussian used to fit the peaks.

3.6.1 Distortion, Magnification and Refraction

Due to the RICH1 geometry and its shielding, the magnetic field inside the HPD tube is to a very good approximation parallel to the tube axis. The absence of a significant transverse field greatly simplifies the magnetic distortion correction as radial symmetry along the tube axis can be assumed.

The most convenient coordinate system is cylindrical with the z axis along the HPD tube axis. Each point on the silicon anode is defined by the coordinates R_A and ϕ_A which are the radius and azimuthal angle with the origin defined as the intersection

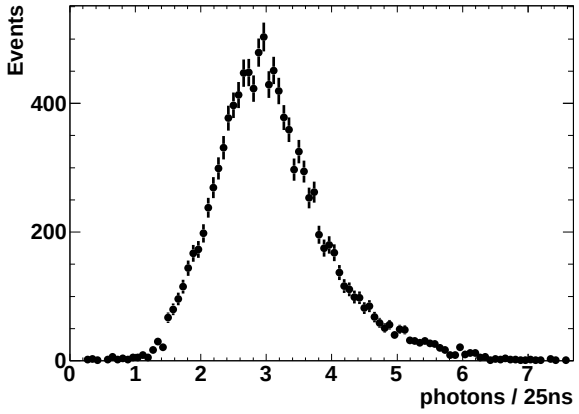


Figure 3.25: Single LED photon intensity per 25 ns.

between the silicon sensor and the tube axis[4]. Similarly, the corresponding points on the photocathode have coordinates R_C and ϕ_C.

The positions of reconstructed cleaned peaks (still at the chip level) are projected to the photocathode to provide the expected position of the incident photons. This procedure uses the "official" RICH reconstruction software which maps the electrostatic magnification of the HPD. If the magnetic field is absent, the transformation only has to describe the focusing from the electrostatic lensing inside the HPD. From laboratory measurements [58], confirmed later by MDCS results, the transformation is of the form

$$\begin{aligned} R'_C &= R_A\alpha + R_A^2\beta, \\ \phi'_C &= \phi_A. \end{aligned} \tag{3.3}$$

where the linear term in radius is dominant and the second order term becomes important only near the edge of the quartz window.

In the presence of a magnetic field inside the tube, photoelectrons follow a modified path and introduce a distortion in the pattern reconstruction, so that the transforma-

[4]The intersection, also called "chip centre", is determined from collision data by fitting a circle to the periphery of the image obtained on the silicon sensor by integrating photoelectron hits for a sufficient amount of time. The chip centre position is continuously monitored during data-taking periods.

Order	Radial	Axial
0	-	$\theta_0 = a_0$
1	$\rho_1 = (r_1 + 1)\alpha$	$\theta_1 = a_1\rho_1$
2	$\rho_2 = r_2\alpha^2 + (r_1 + 1)\beta$	$\theta_2 = a_1\rho_2 + a_2\rho_1^2$
3	-	$\theta_3 = a_1\rho_3 + 2a_2\rho_1\rho_2 + a_3\rho_1^3$

Table 3.2: Total transformation parameters as a function of the magnification and distortion coefficients for each order of R_A.

tion given by Eq 3.3 has to be modified:

$$\begin{aligned} R_C &= R'_C + \Delta R(R'_C), \\ \phi_C &= \phi'_C + \Delta\phi(R'_C). \end{aligned} \tag{3.4}$$

The axial symmetry guarantees that ΔR and $\Delta\phi$ only depend on the radial coordinate R'_C and these corrections are applied at the photocathode level, after the magnification. ΔR and $\Delta\phi$ are parametrised as second order polynomials

$$\begin{aligned} \Delta R &= R'_C r_1 + R'^2_C r_2, \\ \Delta\phi &= a_0 + R'_C a_1 + R'^2_C a_2, \end{aligned} \tag{3.5}$$

where the r_i and a_i are constant coefficients for a given HPD and unphysical constant term in the radial correction has been suppressed. The coefficients are combined with the magnification coefficients to give the total transformation from the silicon chip to the photocathode that can later be used by the reconstruction software:

$$\begin{aligned} R_C &= R_A\rho_1 + R_A^2\rho_2 + R_A^3\rho_3, \\ \phi_C &= \phi_A + \theta_0 + R_A\theta_1 + R_A^2\theta_2 + R_A^3\theta_3. \end{aligned} \tag{3.6}$$

The way in which the parameters in the total transformation are related to the parameters which account separately for the magnification and the magnetic distortion are given in Table 3.2. The final step is to map from the photocathode to the surface of the quartz window, which is also where the pattern originates and up to the mechanical

tolerance of the light bar, is exactly grid-like. A correction of the form

$$R_W - R_C = 0.03964R_C - 0.0002438R_C^2 + 0.00001386R_C^3 \tag{3.7}$$

is applied, where R_W is the radius of incidence of the photon on the outer side of the quartz window. No correction is applied to ϕ_C. This refraction contribution is actually very small ($< 4\%$) and has a negligible impact on the performance of the RICH1 reconstruction and is considered only for completeness.

Precise values of α and β for each HPD can be computed from MDCS scans with magnet off, however the values must be only reliable enough to make the parameter fit (outlined in Section 3.6.3) converge. In fact, the distortion parameters will self-correct to match the light bar pattern, regardless of the value of the magnification coefficients used. Therefore, common values of $\alpha = 5.56$ and $\beta = 0$, corresponding to the average magnification parameters, have been used for each HPD.

3.6.2 Effects of the Magnetic Field

In order to understand the effects of a magnetic field on the HPDs, it is useful to compare the peak pattern, extrapolated at the quartz window without any correction for magnetic distortion, for magnet off and magnet on scans. Corresponding patterns area shown in Figure 3.26. The transformation law used to project the peaks from the silicon chip to the HPD window is a simple radial magnification with a correction for refraction, described in Section 3.6.1. It can be seen that distortions are approximately symmetric around the tube axis (perpendicular to the origin) and involve a radial and an axial component.

In an initial approach to the magnetic distortion correction, the peak association was achieved by calculating at the difference in position of peaks at the quartz window projection (similar to Figure 3.26) from different runs having the same step number (in the same HPD) but different magnet conditions (on and off). Common image magnification and refraction laws were used for all HPDs. This method is very simple in concept as the electrostatic magnification and the magnetic distortion are treated

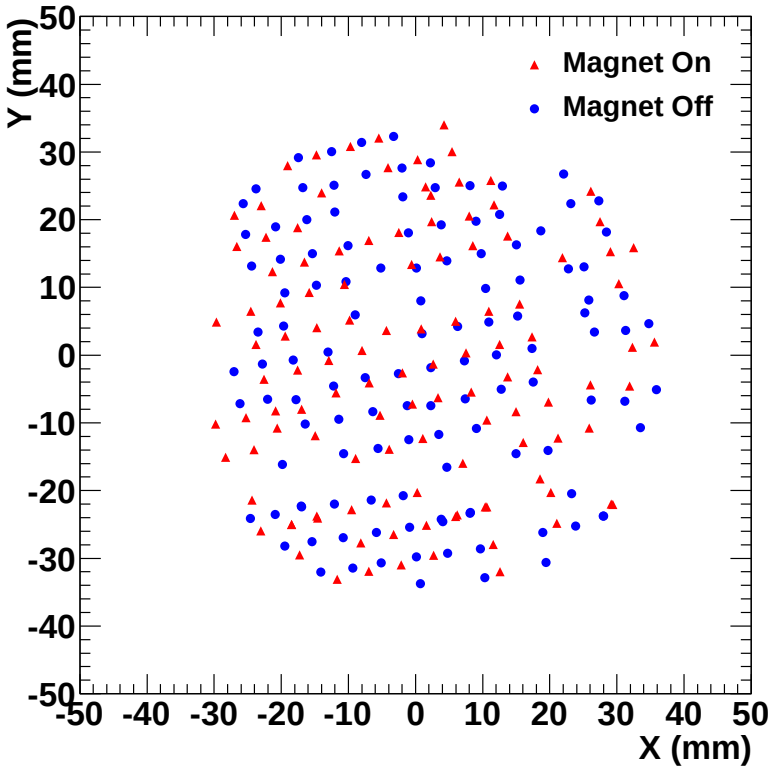


Figure 3.26: Distortion of the peak patterns extrapolated to the HPD quartz window with no magnetic correction applied.

as separate entities. In principle, this method does not even require the light pattern to be a perfect grid but rather peak pairs with the same step number. The main disadvantages are that the method is insensitive to differences in the magnification power between HPDs, and also that two scans close in time are required, one with magnet on and magnet off.

The approach actually adopted and described here exploits the bar geometry and movement logic as an external constraint. Hence both magnification and distortion parameters are extracted accounting for the full transformation from the sensor level up to the quartz window. This method is more effective and provides better correction factors. Moreover, it only requires one scan, hence the entire MDCS analysis can provide new calibration parameters in less than three hours.

3.6.3 Parameter Fitting

The fitting procedure extracts the calibration parameters by comparing cleaned peaks at the quartz window (using the default magnification and refraction described above) with the expected grid pattern from the light bar. Since the linear term in the refraction correction is largely dominant (see Eq. 3.7) and the effect is small in anyway, the approach of considering only a linear term hugely simplifies the problem without introducing any significant bias in the fit.

The expected peak pattern for each HPD is determined by the step number of reconstructed peaks (after the cleaning). Since the distance between two LEDs and the light bar positional movement are known very precisely, it is possible to assign to each peak a well defined expected position with respect to the other peaks reconstructed in that HPD. A small complication is introduced when one HPD contains peaks from more than one module. In this case peaks from different modules must be distinguished which is achieved by searching for discontinuities in the step number in the grid pattern (see Figure 3.27).

The relative shift between the two grid patterns is imposed using the bar specifications. The absolute position of the grids in the xy plane is not imposed but fitted together with the distortion parameters to allow for eventual misalignments of the HPD tubes in the HPD box. The initial position, before the fit, is calculated by minimising the sum of the mean distances between the peaks and the corresponding expectation from the geometry of the grid.

Each peak and the corresponding point on the grid form a "pair" of points. For each pair there is a corresponding value of ΔR and $\Delta\phi$ as a function of R_C. Outliers with a ΔR and/or $\Delta\phi \times R_C$ greater than twice the spacing between two consecutive LEDs on the bar are not considered in the fit, providing additional protection from residual backgrounds. Plots of ΔR and $\Delta\phi$ as a function of the radial position for a typical HPD are shown in Figure 3.28.

The fit provides seven parameters in total per HPD: five from Eq. 3.5 and two for the shifts of the grids (along x and y). Radial, axial and shift parameters are

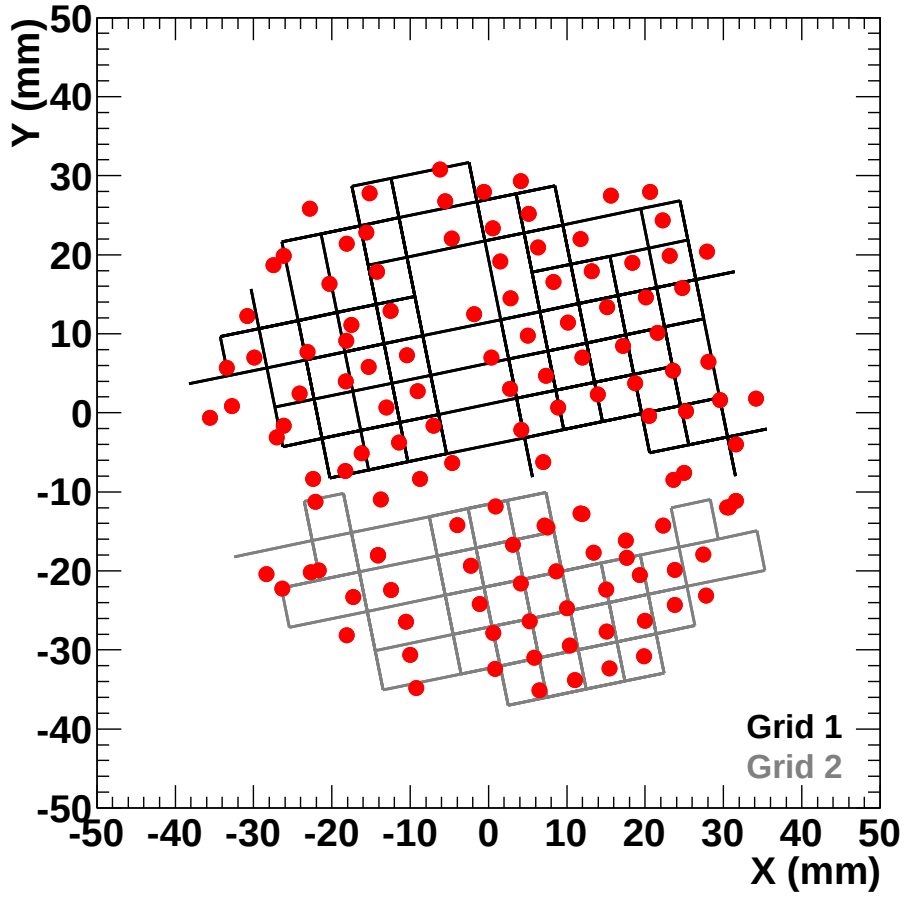


Figure 3.27: Reconstructed peak positions (red) at the exterior of the quartz window without distortion correction. The expected grid patterns from two LED modules are superimposed.

fitted iteratively until convergence is reached, usually after 4-5 iterations. Currently, the MDCS only provides axial and radial corrections though, in principle, could also provide corrections for the HPD tube misalignments.

The parameters are finally combined with the magnification coefficients to provide the full transformation from the photoelectron hit on the silicon chip to the photon incidence point on the quartz window. The peak positions after the full transformation (magnification $\otimes$ distortion $\otimes$ refraction) are shown for a typical HPD in Figure 3.29.

The distributions of the transformation parameters are shown in Figures 3.30-3.31. It is interesting to notice that the θ_0 coefficient, the leading term in the axial correction, has a bias towards negative angles, meaning that all HPDs in the same box are exposed to a similar sign magnetic field. With the opposite magnet polarity the rotation is in

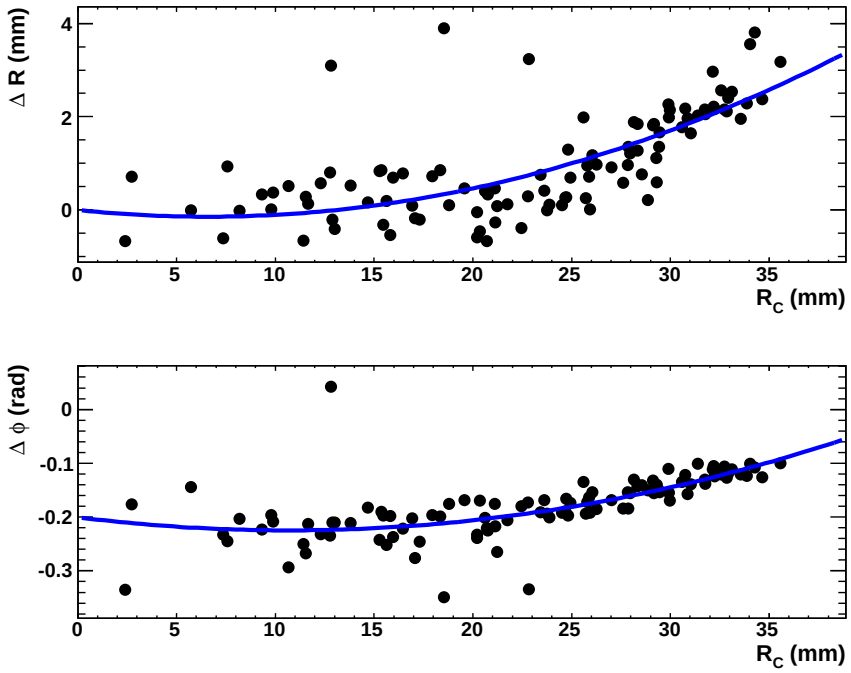


Figure 3.28: ΔR and $\Delta\phi$ data points as a function of radial position.

the opposite direction, as shown in Figure 3.32. As a cross-check, the same plot shows the distribution of θ_0, taken during a magnet off scan, to be centred around zero.

3.7 Performance on MDCS Data

3.7.1 Spatial Resolution

The first check of the MDCS performance is to test the peak position resolution that can be achieved. This is done by looking at the residuals between the corrected peak positions and the grid expectation, before and after correction, in a typical magnet on scan. The residuals in x and y are shown in Figure 3.33. A simple Gaussian fit provides a width of $\sim 0.5\,\text{mm}$ in both directions, with the y measurement along the ALICE pixel direction slightly improved with respect to x, as expected. All measurements lie roughly within $\pm 1\,\text{mm}$ around the mean value; this corresponds to a resolution $\lesssim 0.2\,\text{mm}$ at the silicon sensor. The value is significantly smaller than the LHCb pixel size of 0.5 mm and demonstrates that the corrections are robust to all approximations made. It can be inferred that further improvements to the calibration bring minimal

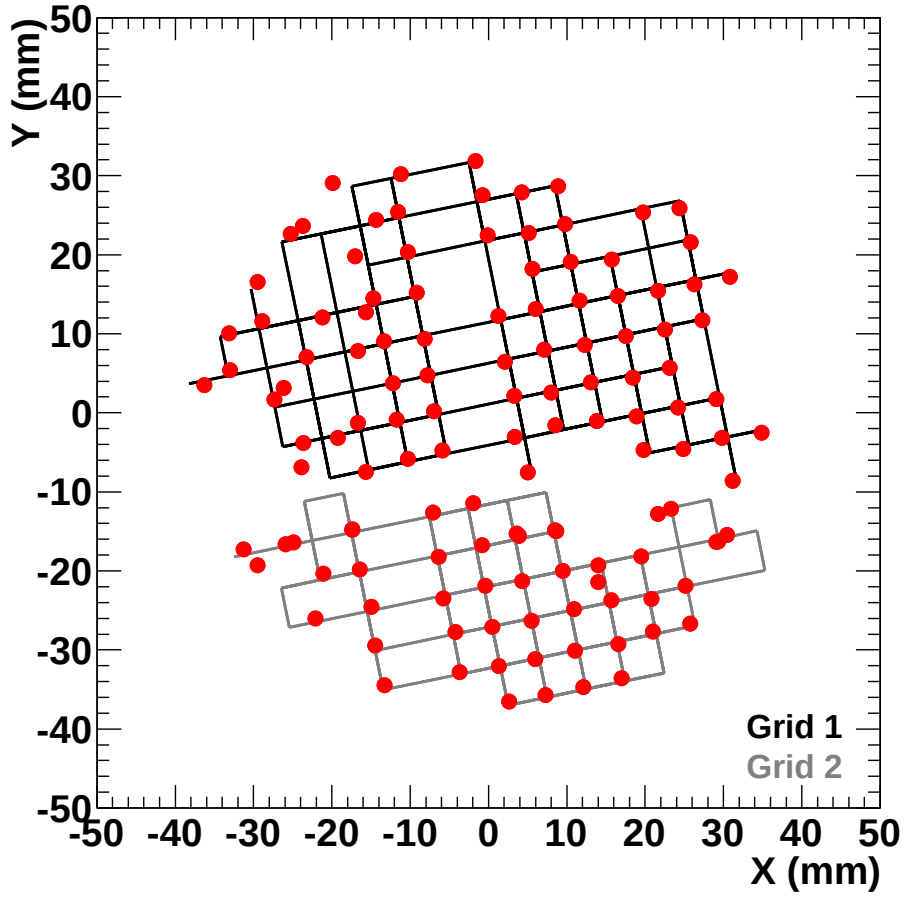


Figure 3.29: Reconstructed peak positions (red) at the quartz window after correction. Expected grid patterns from two LED modules are superimposed.

gain for collision data, which are taken in LHCb mode.

3.7.2 Magnification Estimation

The entire procedure has been applied to magnet off scans in order to measure the magnification power of individual HPDs. In the absence of magnetic distortions, the θ coefficients in Eq. 3.6 vanish, leaving a pure radial magnification to describe the $R_A \rightarrow R_C$ transformation. In these conditions, the axial correction is negligible and the radial distortion parameters have to be interpreted as a correction to α and β. Originally, the values for α and β were measured by testing a sample of HPDs in the laboratory. In fact very little fluctuation is expected amongst HPDs since the magnification only depends on the HPD geometry and the voltage applied to each

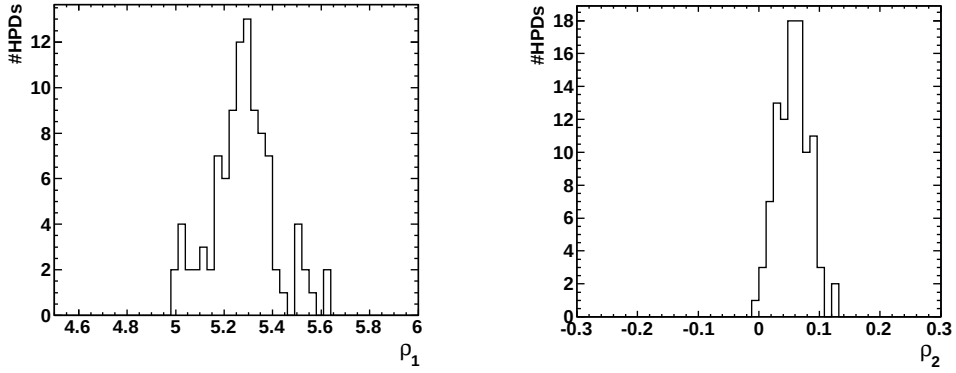


Figure 3.30: Distribution of the radial parameters (Eq. 3.6) for the HPDs in the upper box.

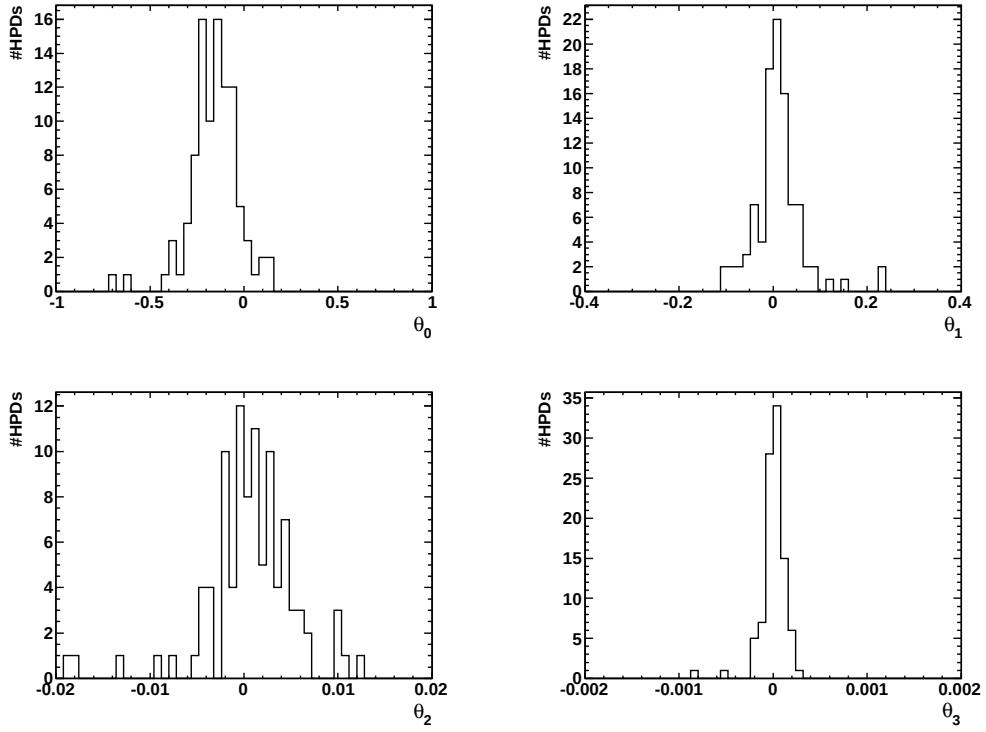
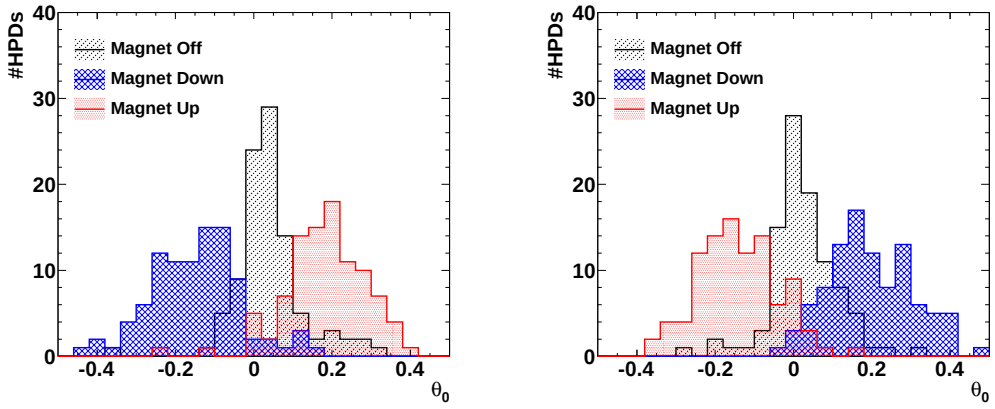


Figure 3.31: Distribution of the axial parameters (Eq. 3.6) for the HPDs in the upper box.

electrode. However, small perturbations may change this expectation when the HPDs are in place inside RICH1. The voltage applied is currently 18 kV (instead of the nominal 20 kV) and the chain of resistors that biases the electrostatic focusing are also different from the one used in the laboratory test.

A second order polynomial is sufficient to parametrise the magnification law, where the linear term dominates and the quadratic term becomes significant only at high



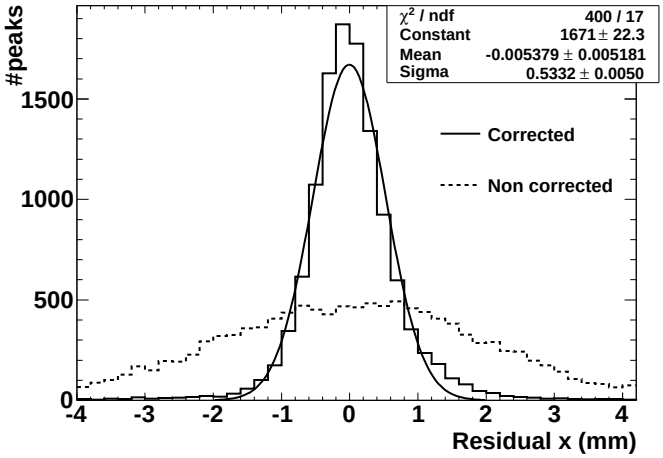
(a) Upper Box (b) Lower Box

Figure 3.32: Comparison of leading axial parameters for different magnet conditions. The axial correction has opposite sign for the two boxes.

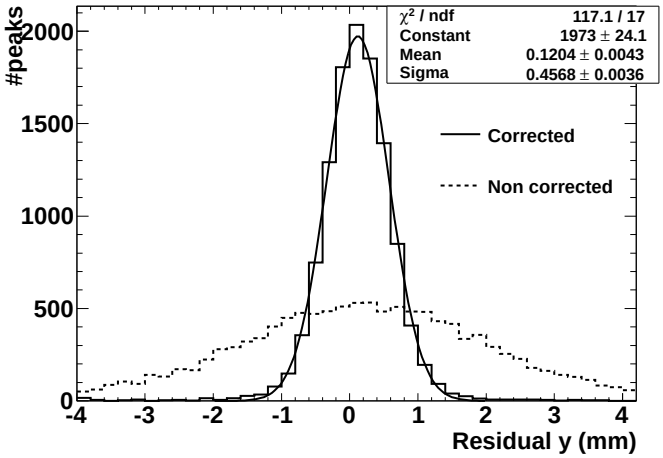
R_C, near the perimeter of the quartz window. The values of the terms are shown in Figure 3.34. The mean value of the dominant linear term for the upper HPD array is 5.3, while the average magnification factor over all HPDs is 5.6. The MDCS data shows that when in place inside RICH1, the magnification power is on average slightly higher than the expectation value, 5, extracted by considering only the electro-optics and neglecting refraction. Although separate magnification coefficients for each HPD are not used nor needed by this analysis, the estimation of the average magnification power has been useful in improving the Cherenkov angle resolution in RICH2, which is not equipped with an absolute position-sensitive MDCS system. In fact, since the HPD applied voltage and the chain of bias resistors are identical to RICH1, the magnification factor for HPDs in RICH2 is expected to be very similar.

3.7.3 Correction Stability

Another important aspect is the stability of the MDCS corrections over time. This is not strictly related to the calibration procedure but rather to the HPDs' behaviour and MDCS hardware performance. The light pattern has proved to be stable over time and the bar movement, tuned to reproduce the grid continuously, has not shown any anomalies. In fact, the bar layout was intentionally over-designed compared to the



(a) x (LHCb pixel direction)

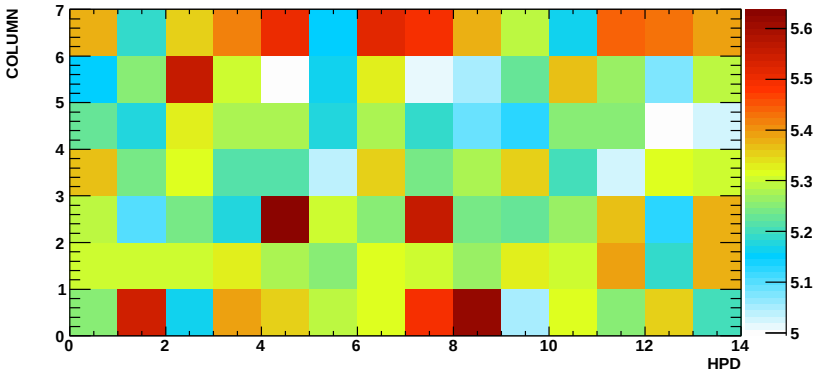


(b) y (ALICE pixel direction)

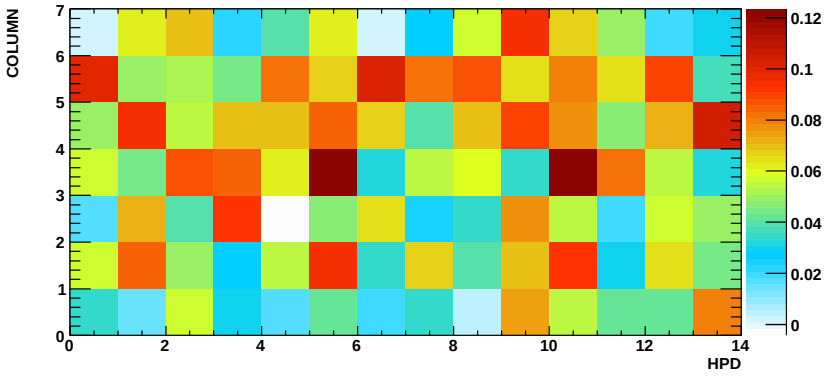
Figure 3.33: Resolution of MDCS data before and after correction in the x and y directions.

intrinsic resolution of the HPDs so that any trend on the fitted parameters over time is attributed to changes in the HPD behaviour. Figure 3.35 shows the fitted values of the leading correction coefficients for scans taken over a two year period.

The instability of individual parameters does not imply the instability of the full transformation. In fact a change in one parameter can be compensated by a change of the others in the final correction. Figure 3.36 shows the axial and radial corrections at the HPD window level for a typical HPD at different times and HV conditions. For the entire R_C range, the correction is very stable and well within the resolution of the method. Discrepancies become larger only above $R_C \simeq 38\,\text{mm}$, but in those regions



(a) First order term in the magnification for each HPD.



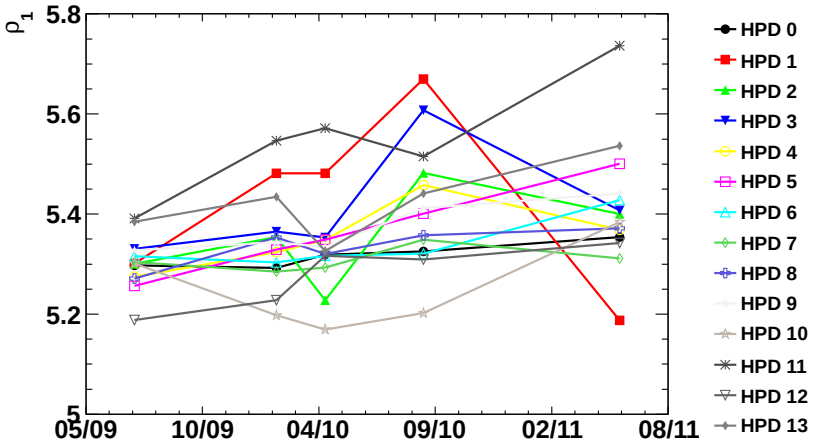
(b) Second order term in the magnification for each HPD.

Figure 3.34: Two dimensional maps of the magnification coefficients of each HPD in the upper panel with magnet off.

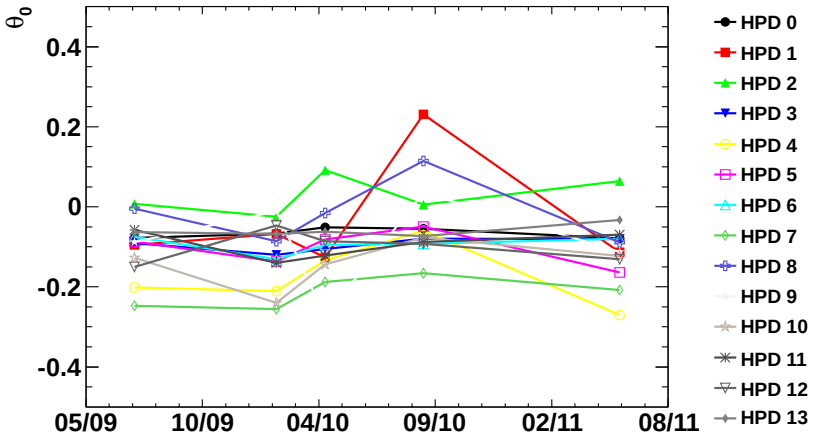
there are significantly fewer reconstructed peaks available in the calibration.

3.8 Performance on Collision Data

The ultimate test of the calibration procedure is its performance on collision data in terms of resolution on the Cherenkov angle in RICH1. The resolution is obtained by studying saturated Cherenkov rings in typical LHCb hadronic b decays. Figure 3.37 shows the resolution on the same data sample with and without the MDCS magnetic distortion corrections applied. The distribution with the corrections is fitted with a Gaussian (signal) plus a second order polynomial (background) returning a resolution of $\sim 1.597 \pm 0.002\,\text{mrad}$. If the distortion corrections are not applied, the Cherenkov



(a) ρ_1

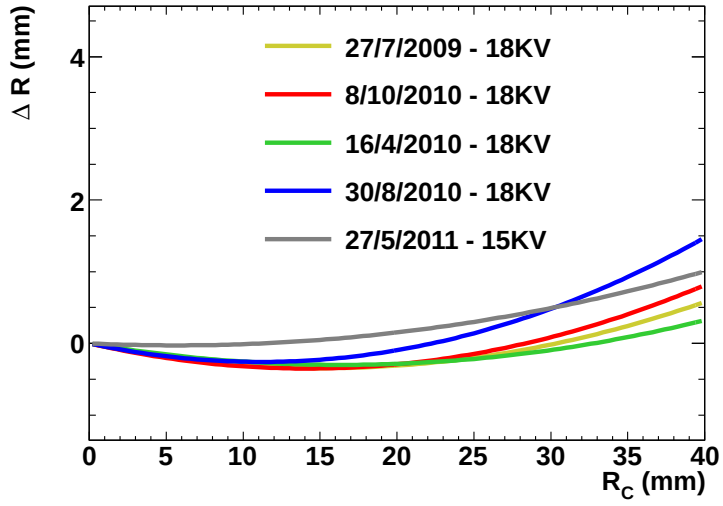


(b) θ_0

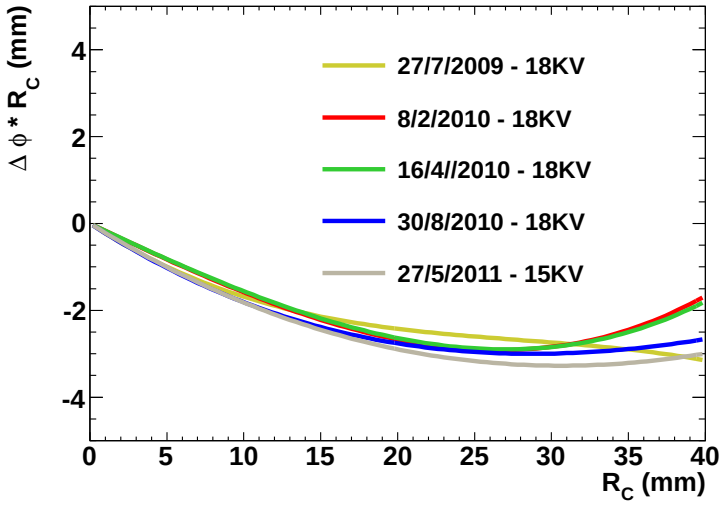
Figure 3.35: Leading correction terms for scans taken at different times for the upper box, column 1 and magnet polarity down. The data points taken in 5/11 corresponds to an HPD HV of 15 kV.

angle resolution is about a factor two worse, as determined by a comparison of the FWHM (calculated considering only the $\Delta\theta_{CK}$ range show in Figure 3.37).

Further checks can be performed on the uniformity of the performance in different regions of the HPD panels. The resolution for photons being reflected by spherical-flat mirror pairs (Figure 3.38) is broadly consistent. However, the scatter in the resolution achieved for different mirror pairs is larger than the typical statistical error of the fit.



(a) Radial corrections

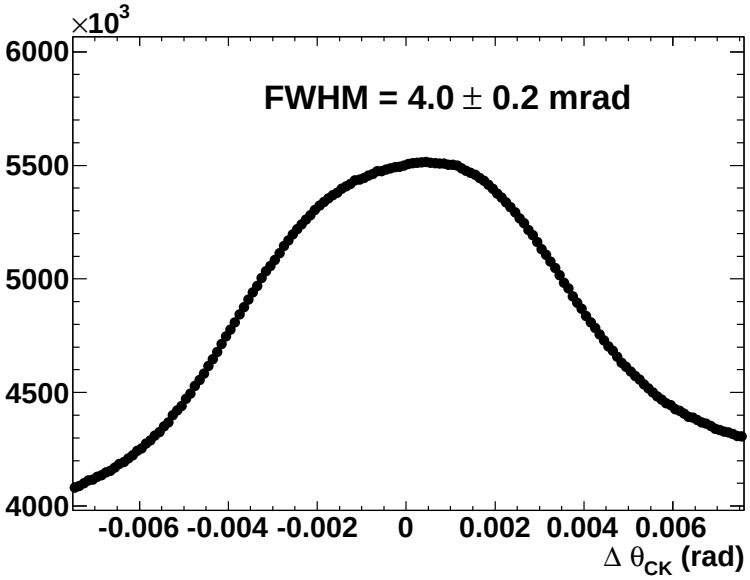


(b) Axial corrections

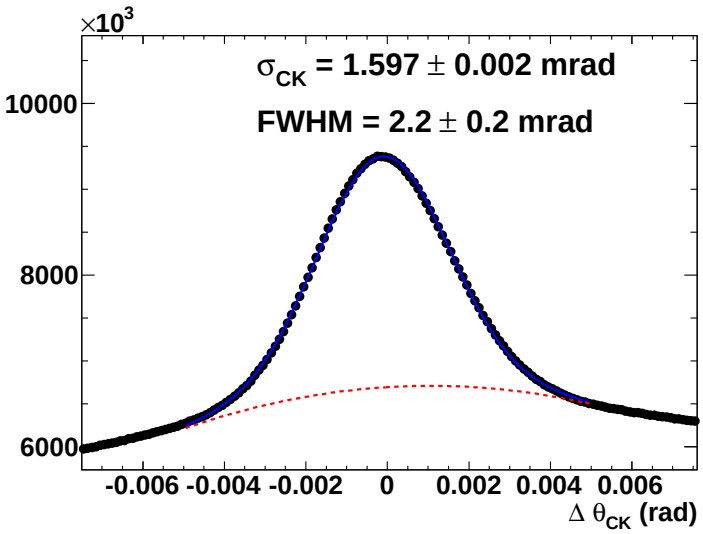
Figure 3.36: Correction to the magnification law for different scans. The data are taken for the upper box, column 1, HPD 5 and magnet polarity down.

These differences could be introduced by a non-optimal individual HPD alignment. However, taking the mirror pairs in Figure 3.38(c) and Figure 3.38(d) as an example, the resolution achieved for individual HPDs for photons reflected by the same pair, shown in Figure 3.39 and Figure 3.40 respectively, is very similar. Therefore, the differences are most likely due to the RICH optics varying across the system (see Section 2.4.2.2).

This analysis of MDCS data has provided a critical improvement to the overall



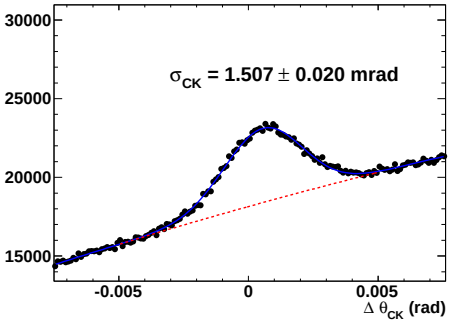
(a) MDCS corrections not included (HPD magnification only).



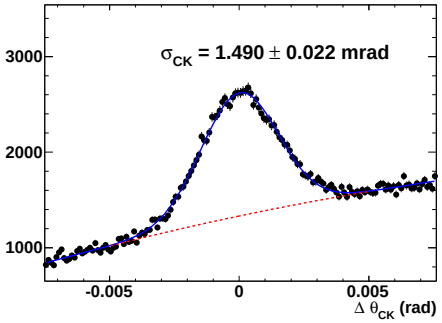
(b) MDCS corrections included.

Figure 3.37: Resolution of the Cherenkov angle in hadronic b decays (2011 data). The fit is only performed for (b), The full width half maximum, relative to the range shown in the plots, is shown for comparison.

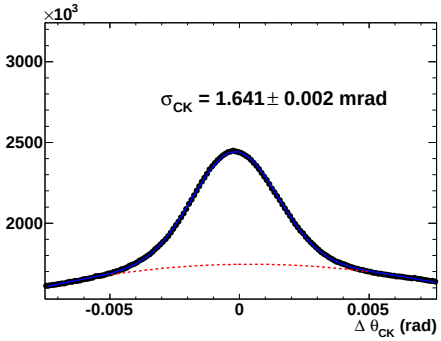
RICH system PID performance. The final Cherenkov angle resolution is close to the benchmark performance from Monte Carlo simulation of 1.55 mrad. The system has been constantly monitoring the magnetic distortion throughout the LHCb running period and the calibration procedure is observed to be robust and stable.



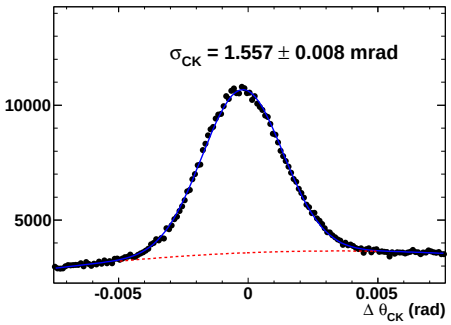
(a) Spherical mirror 2, flat mirror 9.



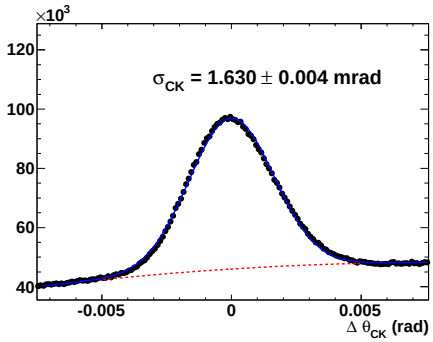
(b) Spherical mirror 2, flat mirror 11.



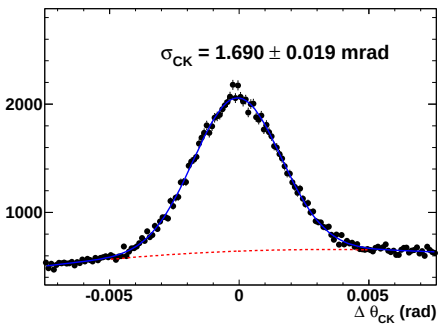
(c) Spherical mirror 2, flat mirror 12.



(d) Spherical mirror 2, flat mirror 13.



(e) Spherical mirror 2, flat mirror 14.



(f) Spherical mirror 2, flat mirror 15

Figure 3.38: Resolution on the Cherenkov angle for photons reflected by individual spherical-flat mirror pairs (2011 data).

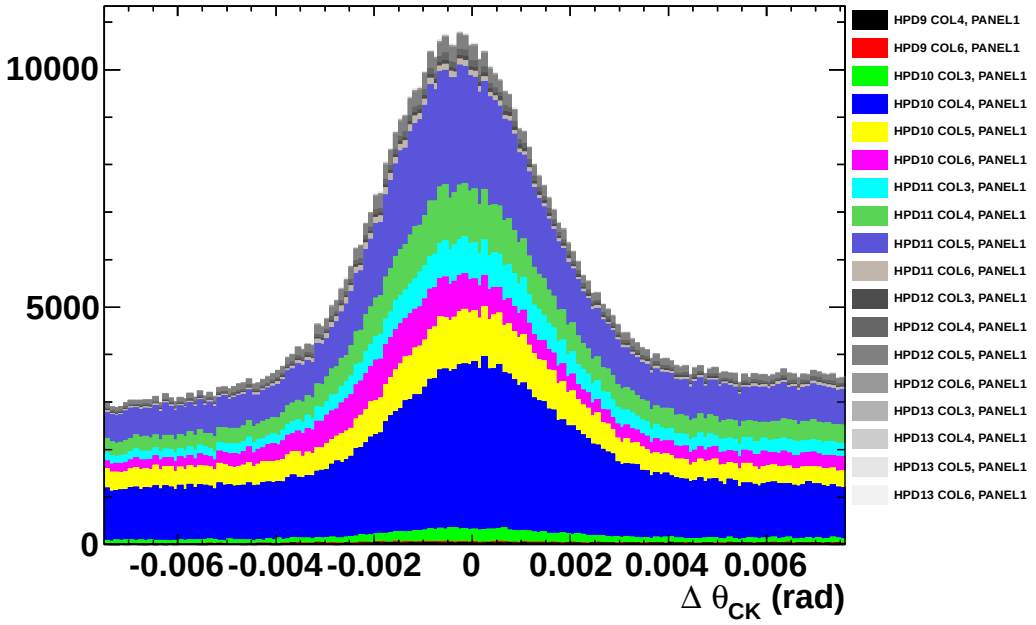


Figure 3.39: Resolution on the Cherenkov angle in 2011 data for individual HPDs in the lower panel for photons reflected by a particular spherical-flat mirror pair (spherical mirror 2, flat mirror 13).

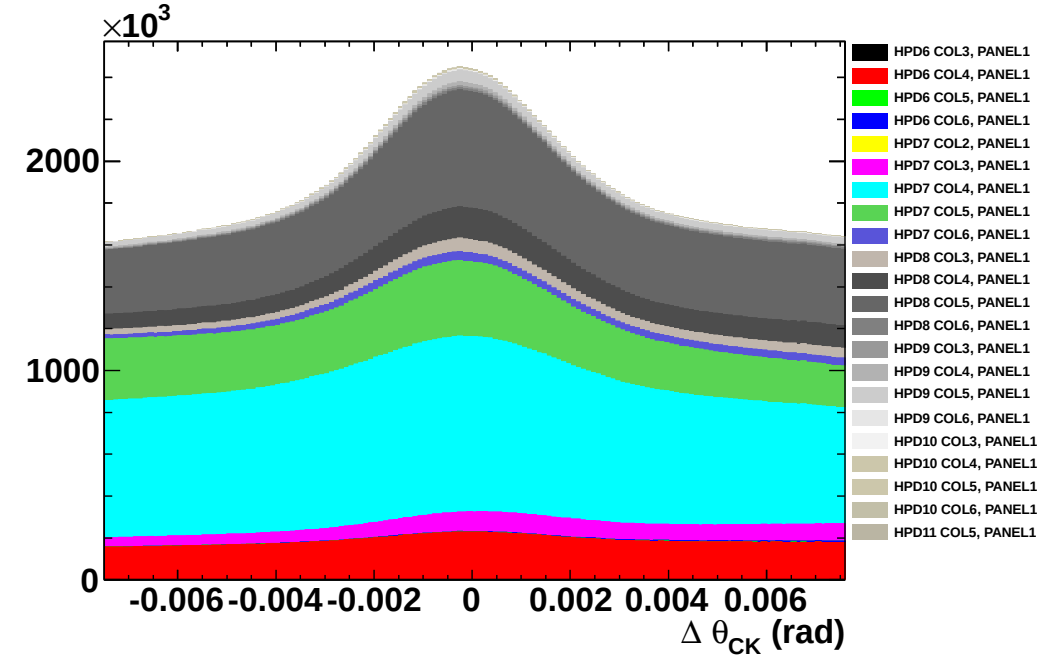


Figure 3.40: Resolution on the Cherenkov angle in 2011 data for individual HPDs in the lower panel for photons reflected by a particular spherical-flat mirror pair (spherical mirror 2, flat mirror 12).

Chapter 4

Hadron Ratios - Analysis Strategy

4.1 Introduction

As described in Chapter 1, the measurement of the prompt hadron production ratios provides a unique test of baryon number transport (BNT) and hadronisation mechanism in high energy pp collisions.

This chapter presents the analysis strategy for the measurement of the ratios of promptly produced protons, kaons and pions in minimum bias events as a function of pseudo-rapidity, η, and transverse momentum p_T, both at $\sqrt{\mathbf{s}} = 0.9\,\text{TeV}$ and $\sqrt{\mathbf{s}} = 7\,\text{TeV}$. The analysis benefits from the powerful particle identification capabilities of the LHCb RICH system. Making the measurement necessitates isolating track samples enriched in protons, kaons and pions. Moreover it is necessary to correct for the cross-contamination among them. Having these parallel samples means that the final analysis will then allow for various interesting observables to be extracted. These include the production ratios: $\bar{p}/p$, K^-/K^+, π^-/π^+, $(p+\bar{p})/(\pi^+ + \pi^-)$, $(p+\bar{p})/(K^+ + K^-)$ and $(K^+ + K^-)/(\pi^+ + \pi^-)$. The ratios above are generally defined as

$$\frac{A}{B} = \frac{\sigma(pp \to AX)}{\sigma(pp \to BX)}, \tag{4.1}$$

where A (B) represents a particle of a given type or charge and X denotes the inclusive nature of the cross section σ.

4.2 Promptness Definition

In order to study the underlying mechanism for hadron production, only *prompt* particles are considered. The prompt category includes all the particles produced directly at the primary vertex (PV) or in strong and electromagnetic decays of intermediate resonances (produced at the PV). The main reason behind this definition is that, because of the lifetimes involved, the two components are experimentally indistinguishable from direct production. The precise requirement for promptness used in this analysis, based on the sum of the lifetimes of all the intermediate resonances in the decay of the particle type, is the following:

$$\sum_i c\tau_i < 10^{-9}\,\mathrm{m}, \tag{4.2}$$

where τ_i is the lifetime of the i-th intermediate resonance in the decay chain. In order to limit the amount of non-prompt particles selected in data, a cut on the maximum impact parameter with respect to the primary vertex is applied. Residual contamination from non-prompt particles is taken from MC and accounted for in the acceptance and reconstruction efficiency determination. The treatment of the related systematic uncertainty is discussed in Section 5.2.6.

4.3 Data Samples and Binning

The analysis exploits data taken with the LHCb *minimum bias* triggers and a corresponding sample of simulated data generated within the LHCb Monte Carlo framework. Data and MC include both dipole magnet polarities and two centre of mass energies, as summarised in Table 4.1. At $\sqrt{\mathbf{s}} = 0.9\,\mathrm{TeV}$ the proton beams circulate the LHC at injection energy and are significantly broadened in size compared to higher energy accelerated beams. Under these conditions the two halves of the VELO were retracted from the beam by 10 mm to provide a wider aperture (where the nominal retraction is 8 mm).

Several samples are selected both from data and MC:

- Three track samples enriched in protons, kaons and pions respectively using

Table 4.1: Data and Monte Carlo samples.

Type	**Year**	$\sqrt{\mathbf{s}}$ **[TeV]**	**VELO**	**B field**	**Statistics**	L $[\mu\text{b}^{-1}]$
Data	2010	0.9	Closed 10 mm	Down	10M events	163
Data	2010	0.9	Closed 10 mm	Up	8.5M events	148
Data	2010	7	Fully Closed	Down	82M events	597
Data	2010	7	Fully Closed	Up	120M events	1193
MC	-	0.9	Closed 10 mm	Down	72M events	-
MC	-	0.9	Closed 10 mm	Up	72M events	-
MC	-	7	Fully Closed	Down	70M events	-
MC	-	7	Fully Closed	Up	60M events	-

RICH PID information, hereafter referred to as the *analysis* samples. These are the main samples from which the final measurement is extracted.

- High purity samples of $\Lambda(\bar{\Lambda}) \to p\pi^-(\bar{p}\pi^+)$, $K^0_S \to \pi^+\pi^-$ and $\phi \to K^+K^-$ are selected only from $\sqrt{\mathbf{s}} = 7\,\text{TeV}$ data, without using any RICH PID information. These samples, hereafter referred to as the RICH *calibration* samples, are used to determine the efficiency and misidentification rates of the PID selection for the different particle species, as described in Section 4.6. The same procedure is not performed on $\sqrt{\mathbf{s}} = 0.9\,\text{TeV}$ data due to the insufficient calibration statistics available. Therefore, the PID selection efficiency at $\sqrt{\mathbf{s}} = 0.9\,\text{TeV}$ is extracted through a procedure of *re-weighting* of the efficiency determined at $\sqrt{\mathbf{s}} = 7\,\text{TeV}$, as will be described in Section 4.6.4.

- A track sample without RICH PID requirements, hereafter called the *minimal track* sample, is selected both at $\sqrt{\mathbf{s}} = 0.9\,\text{TeV}$ and $\sqrt{\mathbf{s}} = 7\,\text{TeV}$ and used several times throughout the analysis. This sample contains a mixture of all particle species.

In addition to the above samples, minimal track samples of pure protons, kaons or pions can be selected from MC by associating reconstructed tracks to generated tracks. These samples will be simply referred to as "true" protons, kaons or pions. It is important to note that all the samples above, except the RICH calibration sample, are a subset of a minimal track sample.

All the results will be presented in bins of η and p_T. The motivation is that,

since η is a geometrical parameter, this is more sensible for understanding the cross-contaminations in the PID procedure in the different regions of the RICH detector. The binning is defined as follows:

- 8 bins of equal width 0.5 in η, from 1 to 5
- 3 bins in p_T:
  - $0 \leq p_T < 0.8\,\mathrm{GeV}/c$;
  - $0.8\,\mathrm{GeV/c} \leq p_T < 1.2\,\mathrm{GeV}/c$;
  - $p_T \geq 1.2\,\mathrm{GeV}/c$.

The binning in p_T has been tuned on $\sqrt{\mathbf{s}} = 0.9\,\mathrm{TeV}$ data to contain roughly the same amount of selected proton candidates in each bin.

4.4 Selection

A selection has been developed to obtain track samples enriched in prompt protons, kaons and pions. The purity of the selected samples is estimated directly from data using dedicated RICH Particle IDentification (PID) calibration samples. In the entire analysis only long tracks (see Section 2.3.2) have been considered.

4.4.1 Event Selection

A first selection on global event variables, based on trigger type and primary vertex reconstruction has been implemented. The following cuts have been applied to the events reconstructed by the LHCb detector:

- μbias triggered events (see Section 2.3.5.3);
- at least one Primary Vertex (PV) reconstructed;
- PV z-coordinate within $\pm 200\,\mathrm{mm}$ of the nominal interaction point.

The μbias trigger requires at least one reconstructed track in the detector and introduces a negligible bias in this analysis, almost equivalent to a random trigger. However, having a loose requirement, the selected event sample is contaminated by tracks produced from *beam-gas* interactions; namely interaction of beam protons with residual gas molecules in the beam-pipe. The constraint on the PV z position suppresses the number of tracks from beam-gas interactions at the $< 1‰$ level with respect to *beam-beam* collisions. Nevertheless, in order to estimate the residual contamination, the selection is applied to events corresponding to special bunches in which only the forward-going proton bunch is present at the interaction region; reconstructed tracks in these events can only be produced in a beam-gas interaction. The beam-gas contribution is then subtracted from the number of selected tracks, separately for each bin of the analysis.

4.4.2 Track Selection

When selecting all three particle species (p, K, π), it is necessary to have a good control of contamination effects. Track quality and geometrical cuts are a common requirement for all tracks, whereas different PID cuts are applied to select pure samples. The list of the common cuts is shown below:

- Track fit $\chi^2/\#DOF$[1] < 5;
- Impact parameter with respect to the PV $\chi^2/\#DOF < 49$. This is tuned to select a proton sample which is 95% "prompt" according to MC;
- Track momentum $> 5\,\mathrm{GeV}/c$, to limit material interaction effects in the detector;
- Application of the *clone* veto (described in Section 4.4.2.1).

All the samples listed in Section 4.3 share these common cuts.

The analysis samples are further selected using RICH PID information. As described in Chapter 2, the RICH reconstruction software associates to each track a

[1]Number of Degrees of Freedom

likelihood value for each particle hypothesis. The logarithmic difference between the likelihood values for two particle hypotheses (DLL) is used as a discriminating variable to select track samples enriched in protons, kaons and pions. The optimisation of the DLL cuts is performed in two separate steps. Initially, the selection cuts are tuned on $\sqrt{\mathbf{s}} = 0.9\,\text{TeV}$ MC to maximise the efficiency and require the purity of the sample to be greater than 95%, integrated over the entire LHCb acceptance. This initial procedure returns the set of cuts summarised below:

- proton selection: $\text{DLL}(\text{p} - \text{K}) > 10,\ \text{DLL}(\text{p} - \pi) > 18$ (95% purity on MC);
- kaon selection: $\text{DLL}(\text{p} - \text{K}) < -0.8,\ \text{DLL}(\text{K} - \pi) > 8.8$ (95% purity on MC);
- pion selection: $\text{DLL}(\text{K} - \pi) < 0$ (97% purity on MC).

However, the RICH performance assumed in the MC may differ from what is found from the calibration with data, and differences could also vary significantly across the (p_T, η) plane. In particular, lower efficiencies are measured in data with respect to MC for protons and kaons, especially at low transverse momentum, due to an overestimate of the aerogel radiator performance in MC. In order to mitigate this effect, a second data-driven bin-by-bin optimisation procedure has been implemented. This method uses PID efficiencies calculated from the RICH calibration samples for different DLL cut values and a sample of tracks without any DLL selection applied; the initial DLL values are taken as a starting point. At least a 10% efficiency (ϵ_{PID}) in each bin is required, and two cases are possible:

1. ϵ_{PID} is already $> 10\%$. Here the DLL-cut optimisation on purity is performed, while always keeping $\epsilon_{PID} > 10\%$;
2. ϵ_{PID} is below 10%. A search is performed for a new DLL working point to reach 10% or above. The optimisation on purity is then performed, while keeping $\epsilon_{PID} > 10\%$.

The determination of purity requires a full calculation of the cross-contamination between protons, kaons and pions and will be described in Section 4.6.5. However, the

sole maximisation of the purity, as required by 1), can be performed as follows. Considering the proton selection as an example, each set of DLL cuts, when applied to a minimal track sample, selects a certain fraction of kaons as well as pions. Each set is characterised by a *retention factor*, which is the fraction of tracks retained with respect to the total in a minimal track sample, and by the efficiency for selecting protons (which is determined from the calibration samples). For a fixed identification efficiency, the set of DLL cuts with the highest purity must also minimise the retention factor. Therefore, a scan over sets with the same efficiency is performed until the one with the lowest retention factor is found. The same procedure is then repeated for kaons and pions. The working point for the proton selection before and after the optimisation described above is shown in Figure 4.1 for an example (η, p_T) bin. The full list of optimised DLL cuts for the proton and kaon selection is summarised in Table 4.2 and Table 4.3 respectively.

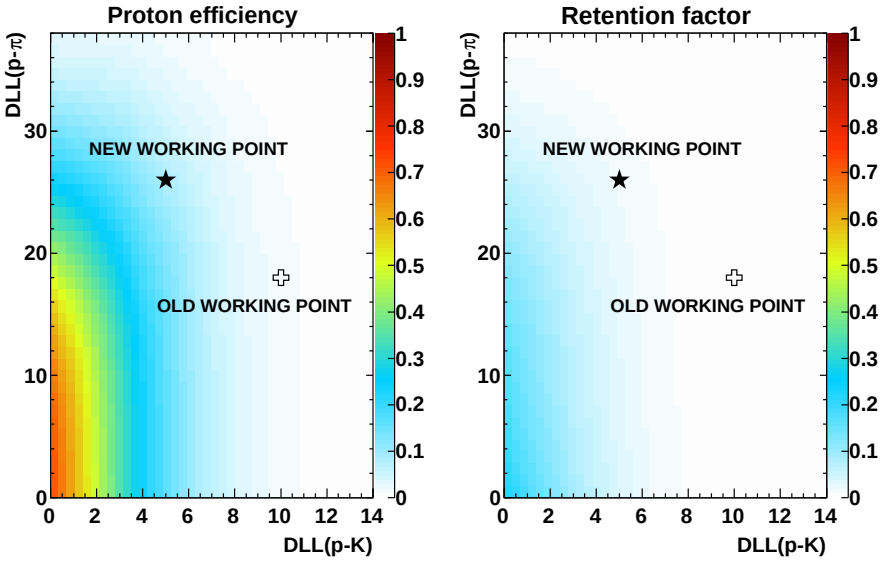


Figure 4.1: Identification efficiency on protons and corresponding retention factor on a minimal track sample, $p_T < 0.8\,\text{GeV}/c$ and $2.5 \leq \eta < 3.0$. The DLL working points before (cross) and after (star) the optimisation are shown.

The total numbers of selected candidates in the analysis sample, summing over magnet up and down data, are listed in Tables 4.4-4.5 at $\sqrt{\mathbf{s}} = 0.9\,\text{TeV}$ and $\sqrt{\mathbf{s}} = 7\,\text{TeV}$ respectively.

η	$P_T < 0.8$ GeV/c DLL(p − K), DLL(p − π)	$0.8 < P_T < 1.2$ GeV/c DLL(p − K), DLL(p − π)	$P_T > 1.2$ GeV/c DLL(p − K), DLL(p − π)
2.0-2.5	> 10, > 18	> 9, > 18	> 10, > 18
2.5-3.0	> 5, > 18	> 5, > 26	> 10, > 18
3.0-3.5	> 7, > 20	> 10, > 18	> 10, > 10
3.5-4.0	> 10, > 18	> 10, > 18	> 10, > 14
4.0-4.5	> 10, > 10	> 10, > 18	> 10, > 14
4.5-5.0	> 11, > 10	> 10, > 16	> 10, < 16

Table 4.2: DLL cuts for proton selection.

η	$P_T < 0.8$ GeV/c DLL(K − π), DLL(p − K)	$0.8 < P_T < 1.2$ GeV/c DLL(K − π), DLL(p − K)	$P_T > 1.2$ GeV/c DLL(K − π)DLL(p − K)
2.0-2.5	> 22, < 0	> 8, < -1	> 18, < 0
2.5-3.0	> 18, < 0	> 18, < 8	> -1, < 0
3.0-3.5	> 16, < 0	> 8, < 0	> 12, < 0
3.5-4.0	> 8, < -1	> 8, < -1	> 8, < -1
4.0-4.5	> 8, < -1	> 4, < -1	> 8, < -1
4.5-5.0	> 8, < -1	> 8, < -1	> 8, < -1

Table 4.3: DLL cuts for kaon selection.

η range		$p_T < 0.8\,\mathrm{GeV}/c$			$0.8 \le p_T < 1.2\,\mathrm{GeV}/c$			$p_T \ge 1.2\,\mathrm{GeV}/c$		
	charge	p	K	π	p	K	π	p	K	π
$2.5 - 3.0$	+	/	/	/	16k	39k	270k	19k	36k	130k
	−	/	/	/	13k	35k	270k	13k	31k	120k
$3.0 - 3.5$	+	21k	78k	1.1M	30k	63k	260k	34k	39k	120k
	−	17k	69k	1.1M	21k	55k	250k	20k	31k	100k
$3.5 - 4.0$	+	55k	120k	1.9M	55k	60k	240k	31k	33k	97k
	−	38k	100k	1.9M	33k	49k	230k	14k	23k	85k
$4.0 - 4.5$	+	26k	90k	1.2M	23k	30k	100k	14k	11k	39k
	−	21k	86k	1.2M	11k	22k	88k	4.2k	6.6k	30k

Table 4.4: Number of selected tracks for each sample at $\sqrt{\mathbf{s}} = 0.9\,\mathrm{TeV}$.

η range		$p_T < 0.8\,\mathrm{GeV}/c$			$0.8 \le p_T < 1.2\,\mathrm{GeV}/c$			$p_T \ge 1.2\,\mathrm{GeV}/c$		
	charge	p	K	π	p	K	π	p	K	π
$2.5 - 3.0$	+	/	/	/	59k	250k	2.0M	140k	360k	1.3M
	−	/	/	/	52k	240k	2.0M	130k	350k	1.3M
$3.0 - 3.5$	+	75k	450k	6.6M	120k	460k	1.9M	240k	400k	1.2M
	−	67k	420k	6.6M	110k	440k	1.9M	210k	390k	1.2M
$3.5 - 4.0$	+	230k	730k	11M	280k	450k	1.8M	250k	350k	1.0M
	−	200k	700k	11M	240k	420k	1.8M	200k	320k	1.0M
$4.0 - 4.5$	+	140k	950k	12M	140k	370k	1.3M	140k	170k	740k
	−	120k	900k	12M	120k	330k	1.2M	110k	170k	650k

Table 4.5: Number of selected tracks for each sample at $\sqrt{\mathbf{s}} = 7\,\mathrm{TeV}$.

4.4.2.1 Track Clones

Often in combinatoric problems such as pattern recognition in track-finding algorithms, *track clones* are created. Track clones can be produced when two or more reconstructed tracks share hits in the tracking detectors. These type of clones are automatically removed by the reconstruction algorithm by discarding the track with the lower quality, leading to inefficiency for distinct particles which contributed to the same hit. However, track clones may also be reconstructed in the absence of hits in common. In fact, in some cases the pattern-recognition algorithm splits a series of hits produced by a single particle into two groups that may be reconstructed as two distinct track segments. The splitting of the hits is particularly relevant for hits in the VELO [59]. The contribution from this latter type of clone is subtracted in the analysis sample by comparing the 3-momenta of pairs of tracks in events with multiple track candidates. If two tracks in a given sample have similar 3-momenta such that

$$d = \left| \frac{\vec{p}_i - \vec{p}_j}{\vec{p}_i + \vec{p}_j} \right| < 0.001 \,,$$

where $\vec{p}_{i,j}$ represent the 3-momenta, then one of the two tracks is discarded. Since it is found that track clones have very similar DLL values, the track to be retained is chosen randomly. A typical distribution of d in which the peak from track clones is clearly visible is shown in Figure 4.2. Clone rates, both before (minimal track sample) and after (analysis sample) DLL selection, are found to be in the range 1-6% for all η and p_T bins.

4.5 Raw Ratios Observed and Corrections Needed

Comparisons of the raw ratios (i.e. without any correction for detector effects) in the analysis sample are shown in Figures 4.3-4.6 for magnet polarity down, considering only the statistical uncertainties on the numbers of observed particles. It can be seen that the $\bar{p}/p$ ratio exhibits a behaviour inconsistent with unity. To some degree this is also seen for K^-/K^+. The π^-/π^+ ratio is much closer to unity, although η and p_T

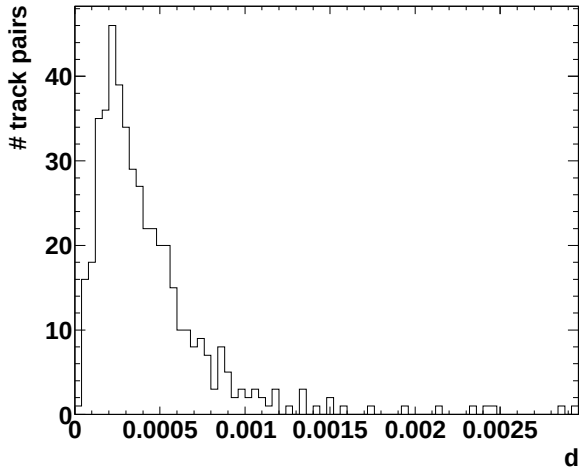


Figure 4.2: Distribution of d (see text) in the proton sample for $0.8 \leq p_T < 1.2\,\mathrm{GeV}/c$ at $\sqrt{\mathrm{s}} = 0.9\,\mathrm{TeV}$.

dependent.

The raw ratios now have to be corrected for the following effects, which are applied in the order specified:

1. Contamination from other hadron species;

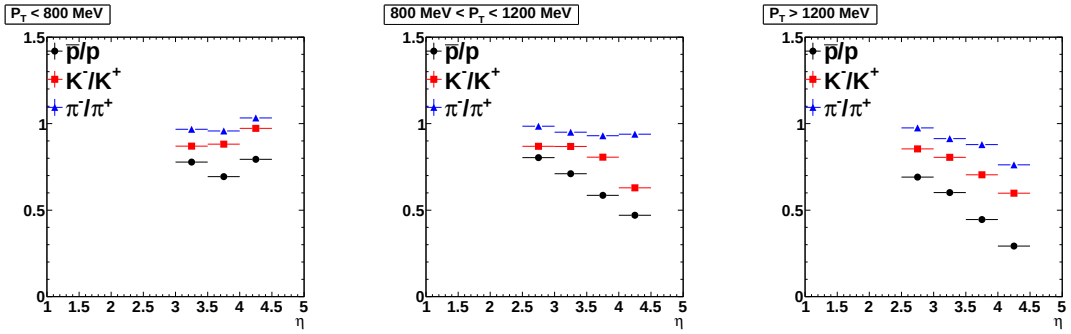
2. Acceptance and detector-material effects: corrections are taken from MC and include the geometrical acceptance of LHCb, the track reconstruction efficiency and the interaction of particles with the detector material;

3. Residual systematics such as biases in the PID performance estimation, and non-optimal MC predictions and detector simulation.

These corrections are discussed in the following sections.

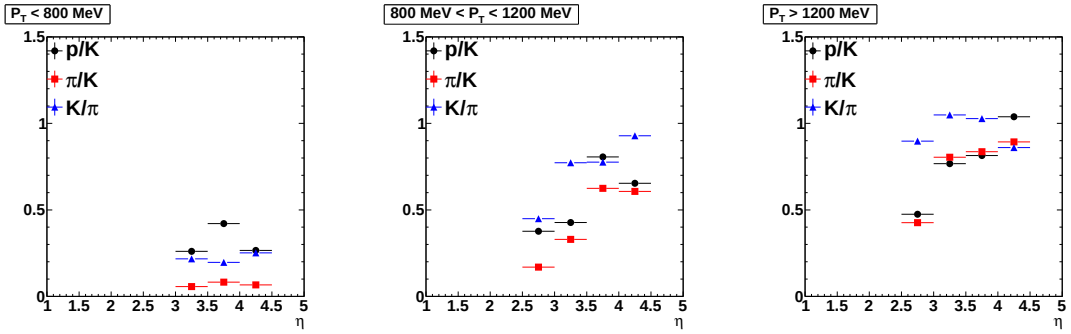
4.6 RICH Calibration Samples and Results

The correction for the cross-contamination between the three hadron species is estimated from data using the dedicated RICH calibration samples: $\Lambda(\bar{\Lambda}) \to p\pi^-(\bar{p}\pi^+)$, $K^0_S \to \pi^+\pi^-$ and $\phi \to K^+K^-$. Details describing the selections of these decays, and the background subtraction technique used, will now be given.



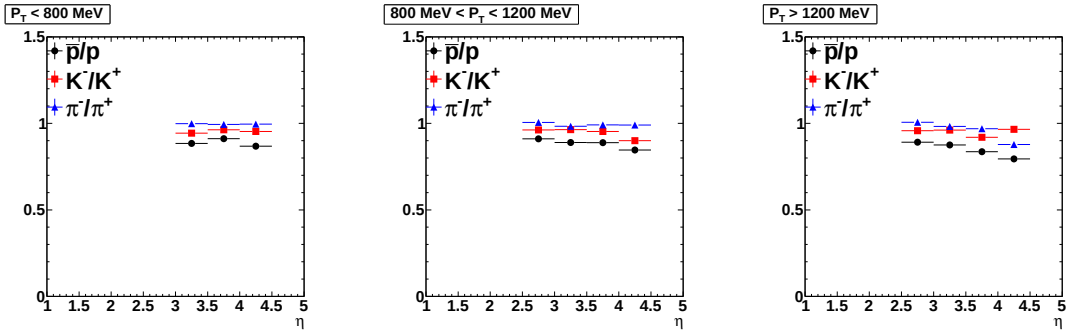
(a) $p_T < 0.8\,\mathrm{GeV}/c$ (b) $0.8\,\mathrm{GeV}/c \leq p_T < 1.2\,\mathrm{GeV}/c$ (c) $p_T \geq 1.2\,\mathrm{GeV}/c$

Figure 4.3: Raw antiparticle/particle ratios at $\sqrt{s} = 0.9\,\mathrm{TeV}$ and magnet polarity down.



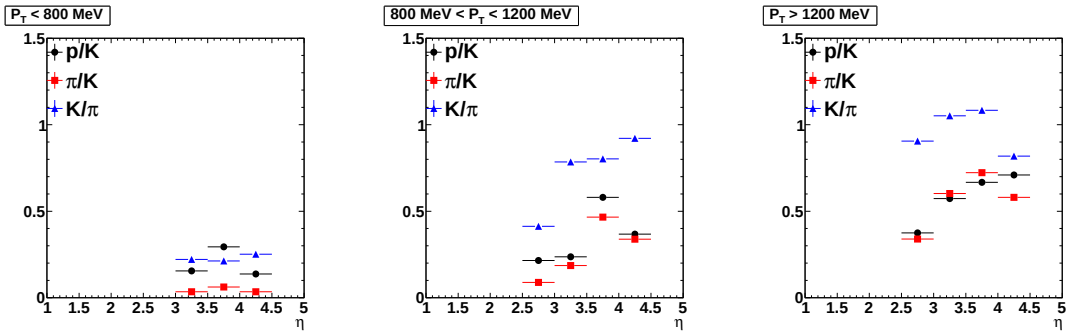
(a) $p_T < 0.8\,\mathrm{GeV}/c$ (b) $0.8\,\mathrm{GeV} \leq p_T < 1.2\,\mathrm{GeV}/c$ (c) $p_T \geq 1.2\,\mathrm{GeV}/c$

Figure 4.4: Raw ratios of different particle species at $\sqrt{s} = 0.9\,\mathrm{TeV}$ and magnet polarity down.



(a) $p_T < 0.8\,\mathrm{GeV}/c$ (b) $0.8\,\mathrm{GeV}/c \leq p_T < 1.2\,\mathrm{GeV}/c$ (c) $p_T \geq 1.2\,\mathrm{GeV}/c$

Figure 4.5: Raw antiparticle/particle ratios at $\sqrt{s} = 7\,\mathrm{TeV}$ and magnet polarity down.



(a) $p_T < 0.8\,\text{GeV}/c$ (b) $0.8\,\text{GeV}/c \leq p_T < 1.2\,\text{GeV}/c$ (c) $p_T \geq 1.2\,\text{GeV}/c$

Figure 4.6: Raw ratios of different particle species at $\sqrt{s} = 7\,\text{TeV}$ and magnet polarity down.

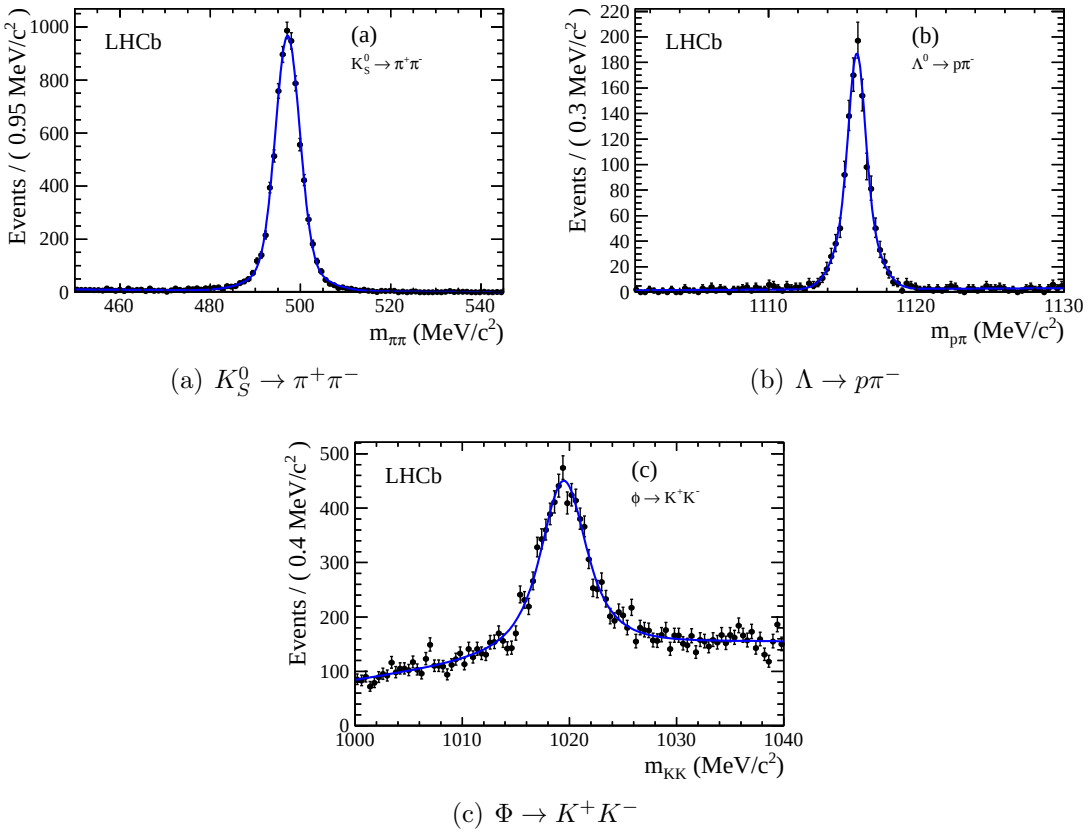
4.6.1 Selection of RICH Calibration Modes

The Λ, K^0_S and ϕ samples are obtained using PID-unbiased selections from the LHCb calibration triggers for $\sqrt{s} = 7$ TeV data. The yields obtained in each sample and in each magnetic field orientation are given in Table 4.6. Example fits to the invariant-mass distributions from a sub-sample of these data, without recourse to PID information, are shown in Figure 4.7. The purities of the samples vary across the (η, p_T) binning of the analysis; purities for the Λ and K^0_S samples lie in the range $85 - 99\%$ (94% on average), whilst for the ϕ sample, which are significantly less pure, purities are in the range $25 - 68\%$ (50% on average). All $\pi^\pm$, $\bar{p}$ and p tracks associated

Table 4.6: Total numbers of candidates reconstructed in each of the calibration modes.

Mode	Magnet down	Magnet up
K^0_S	3 M	1.7 M
$\Lambda + \bar{\Lambda}$	900 k	500 k
ϕ	3.5 M	2 M

with the decays $\Lambda(\bar{\Lambda}) \to p\pi^-(\bar{p}\pi^+)$ and $K^0_S \to \pi^+\pi^-$ may be used for assessing RICH performance, however not all $K^\pm$ tracks from the ϕ sample can. In order to resolve a signal ϕ peak, it must be imposed that at least one of the two daughter tracks satisfies the requirement $DLL(K - \pi) > 15$. The track satisfying this requirement is referred



(a) $K^0_S \to \pi^+\pi^-$ (b) $\Lambda \to p\pi^-$

(c) $\Phi \to K^+K^-$

Figure 4.7: Invariant mass distributions reconstructed from the magnet down $\sqrt{s} = 7\,\text{TeV}$ data in the analysis bin for which the positive final-state particle has $p_T \geq 1.2$ GeV and $3.5 \leq \eta < 4.0$ for (a) $K^0_S \to \pi^+\pi^-$, (b) $\Lambda^0 \to p\pi^-$ and (c) $\phi \to K^+K^-$. The results of unbinned maximum likelihood fits to the data are superimposed.

to as the *tag*, and is consequently PID-biased. However, the opposite-side *probe* track will be an unbiased kaon which is then used to assess the RICH PID performance.

4.6.2 Background Subtraction Technique

Whilst the backgrounds present within the Λ and K^0_S samples are generally small, the ϕ sample is dominated by combinatoric background. Therefore, a method is needed to separate or *unfold* the $\phi \to K^+K^-$ signal from the background. This would then allow a determination of the RICH PID performance for kaons.

Such a result can be achieved using the *sPlot* technique [60]. This method involves performing an extended likelihood fit to the ϕ invariant-mass distribution, using a

combined probability density function (PDF) to describe the signal and background distributions, respectively. From this fit result, *sWeights*, ${}_sW$, are calculated for each candidate to be associated with either the signal or background PDF:

$$ {}_sW_n(y_e) = \frac{\sum_{j=1}^{N_s} \mathbf{V}_{nj} f_j(y_e)}{\sum_{k=1}^{N_s} N_k f_k(y_e)} \quad , \tag{4.3} $$

where N_s is the number of event types (two in this specific case: signal and background), $\mathbf{V}$ is the resulting covariance matrix of the likelihood fit, f are the PDFs of the various species in variable y (here, invariant mass), subscript n refers to the particle type of interest and subscript e refers to the event under consideration. It then follows that these weights satisfy

$$ \sum_{e=1} {}_sW_n(y_e) = N_n. \tag{4.4} $$

That means that the sum of weights for a given n over all events is equal to the number of events, or yield, associated with type n. The particle types of interest, represented by the subscript n, may be identified as the *signal* and *background* components in the invariant mass distribution, e.g. the peak from $\phi \to K^+K^-$ and the combinatorial background respectively. Hence, background-subtracted distributions for any variable can be obtained by weighting each event by its corresponding sWeight for the signal, ${}_sW_{\phi \to K^+K^-}$.

The sPlot technique allows the signal distributions associated with the probe-kaon track from ϕ decays to be resolved, such as the distribution of $DLL(K - \pi)$. Consequently, the efficiency of a given cut on this distribution can be determined.

A simplified technique to that described above would be to perform an extended likelihood fit to the ϕ invariant mass distribution, with appropriate PDFs for signal and background, both before and after the application of the PID requirement. The ratio of the respective signal yields would then provide a measure of the kaon performance

efficiency. The shortcoming of this method is that a fit would have to be performed twice. Determining the weight for each candidate to be signal or background through the *sPlot* technique allows for the CPU-intensive likelihood fit to be performed only once.

For consistency, and to account for the residual backgrounds present within the V^0 selections, the *sPlot* technique is also applied to the K^0_S and Λ calibration samples in order to resolve the signal $\pi^{\pm}$, $\bar{p}$ and p distributions.

4.6.3 Binning and PID Efficiency Determination

As has been described earlier, the analysis is performed within bins of η and p_{T}. It is therefore necessary to determine the corresponding RICH performance, integrated within each bin, for each track type.

In general, the invariant-mass resolution varies as a function of position within the $\eta - p_T$ plane, hence it is necessary to perform the extended likelihood fits to the K^0_S, Λ and ϕ mass distributions within each bin of the RICH calibration samples. This ensures that the signal and background components within each bin are correctly modelled, and reliable sWeights are determined. To perform the binning and sWeight determination, the RooFit framework [61], embedded in the LHCb software, is used. An extended likelihood fit is then performed upon the invariant-mass distribution observed in each bin, for each calibration sample. The PDFs used to model the signal and background distributions in each calibration sample, respectively, are given in Table 4.7.

The ϕ is a strong decay, whilst $K^0_S \to \pi\pi$ and $\Lambda \to p\pi$ are both weak. Consequently, the ϕ lineshape is best described by a Voigt function (a Breit-Wigner convolved with a Gaussian to account for detector resolution) while the weak decays are best described by double Gaussians.

Once the likelihood fits have been performed on the invariant-mass distributions of Λ, ϕ and K^0_S candidates, the identification (ID) and misidentification (*mis*ID) rates for

Table 4.7: PDFs used to describe the signal and background contributions to the K^0_S, Λ and ϕ invariant-mass distributions.

Mode	Signal PDF	Background PDF
K^0_S	Double-Gaussian	Linear
	$e^{-(m-\mu)^2/2\sigma_1^2} + e^{-(m-\mu)^2/2\sigma_2^2}$	$1 + c_1 m$
Λ	Double-Gaussian	Linear
	$e^{-(m-\mu)^2/2\sigma_1^2} + e^{-(m-\mu)^2/2\sigma_2^2}$	$1 + c_1 m$
ϕ	Voigt Function	Cubic
	$\frac{1}{(m-\mu)^2+\frac{1}{4}\Gamma^2} \otimes e^{-(m-\mu)^2/2\sigma^2}$	$1 + c_1 m + c_2 m^2 + c_3 m^3$

a given PID selection are determined for protons, kaons and pions respectively. The identification efficiency in each (η, p_T) bin is simply given by the ratio

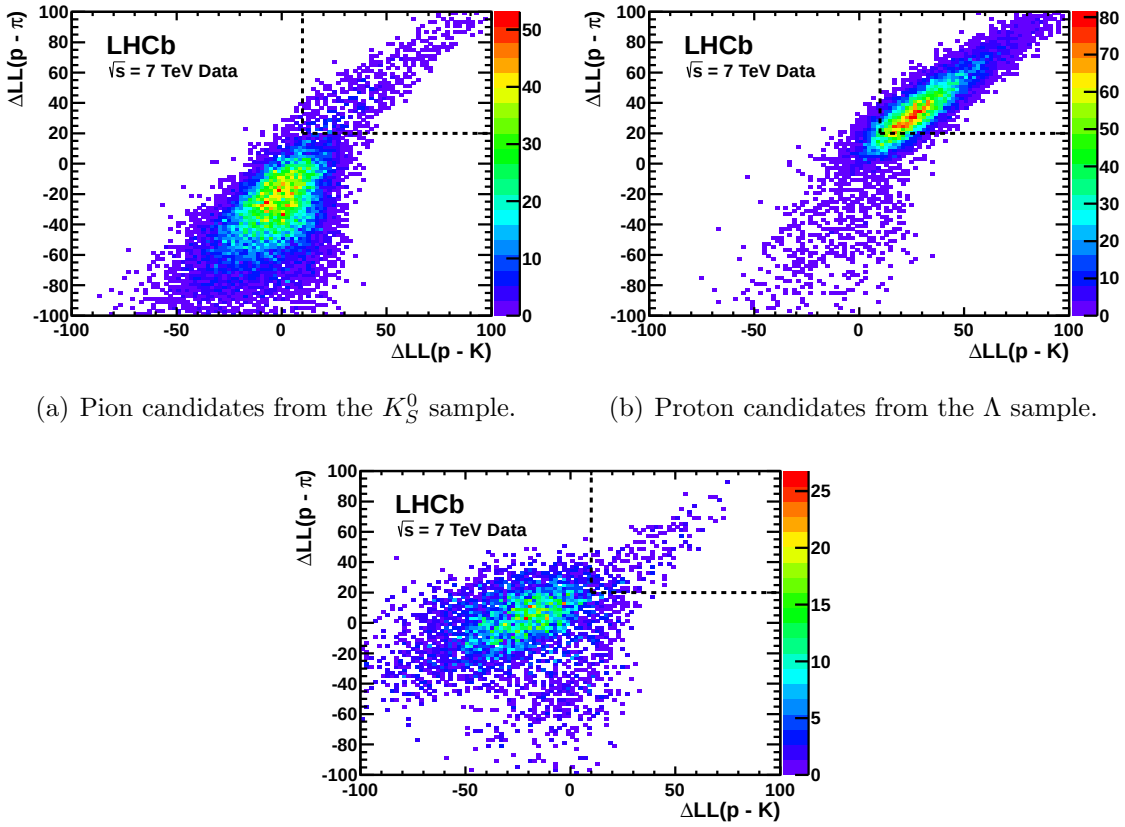
$$\epsilon^{\alpha,\beta}_{PID} = \frac{N^{\alpha,\beta}_{DLL}}{N^{\alpha,\beta}}, \tag{4.5}$$

where α and β identify the (η, p_T) bin, $N^{\alpha,\beta}$ is number of calibration tracks in that bin and $N^{\alpha,\beta}_{DLL} \leq N^{\alpha,\beta}$ is the number of tracks in the calibration sample that passed the DLL selection. Both numerator and denominator are background-subtracted using the *sPlots* technique.

Plots demonstrating the power of the RICH to isolate a pure proton sample are shown in Figure 4.8. The dotted boxes represent the regions in which protons are selected in the DLL space.

4.6.4 PID Efficiencies Re-Weighting

Once the calibration samples are background-subtracted via the *sPlot* technique, it is then possible to determine identification and misidentification rates for a given PID requirement on each particle species. However, since the RICH particle identification is dependent on track kinematic variables and also the detector occupancy, the determined ID and *mis*ID rates are specific to the calibration tracks themselves. In order to



(a) Pion candidates from the K^0_S sample.

(b) Proton candidates from the Λ sample.

(c) Kaon candidates from the ϕ sample.

Figure 4.8: Distribution of $DLL(p-K)$ vs. $DLL(p-\pi)$ for particles from the RICH calibration samples with $p_{\mathrm{T}} > 1.2$ GeV/c and $3.5 < \eta \leq 4.0$. The dotted boxes represent the regions in which protons are selected in the DLL space.

determine ID and *mis*ID rates corresponding to the minimum-bias samples studied in this analysis, it is necessary to "weight" the kinematic distributions of the calibration samples to model those of the minimum-bias tracks.

It is well known that the RICH performance varies with momentum (this is due to the nature of the Cherenkov process itself), the finite resolution of the detector, and the proximity of the track to the beam line (at low angles the track and hit densities are higher and pattern recognition becomes more difficult). The variables η and p_T, in which we choose to measure the dependence of the physics observables, are therefore very suitable for characterising the variation in performance of the RICH system.

It should be sufficient to measure the RICH PID performance of identified particles in the calibration sample over a given (p_T, η) bin, and apply the efficiency and background contributions to the analysis sample. However two effects mean that this

procedure needs refinement. The first is that the bins are not so small that within the bin the momentum distribution of the tracks can be assumed to be identical in the analysis and RICH calibration samples. Secondly, the overall multiplicity scale of the events can be very different in the two samples. An obvious example of how this arises is the fact that the calibration events are selected at $\sqrt{\mathbf{s}} = 7\,\mathrm{TeV}$, whereas one of the analysis samples is at $\sqrt{\mathbf{s}} = 0.9\,\mathrm{TeV}$ where the mean particle multiplicity is much lower. In order to account for these differences it is necessary to re-weight the calibration samples within each bin as a function of the momentum (p) and track multiplicity ($nTrack$) using a minimal track sample as a "reference" sample.

Within each (p_T, η) bin, the calibration and reference samples are further subdivided into cells of p and $nTracks$. Within a cell, i, a weight, W_i, is then determined and assigned to the calibration events in that bin:

$$W_i = N \times \frac{n_i^{ref}}{n_i^{cal}}, \tag{4.6}$$

where N is a normalisation constant and $n_i^{ref(cal)}$ is the number of reference (calibration) events. To preserve the overall number of calibration events, the normalisation constant is calculated as

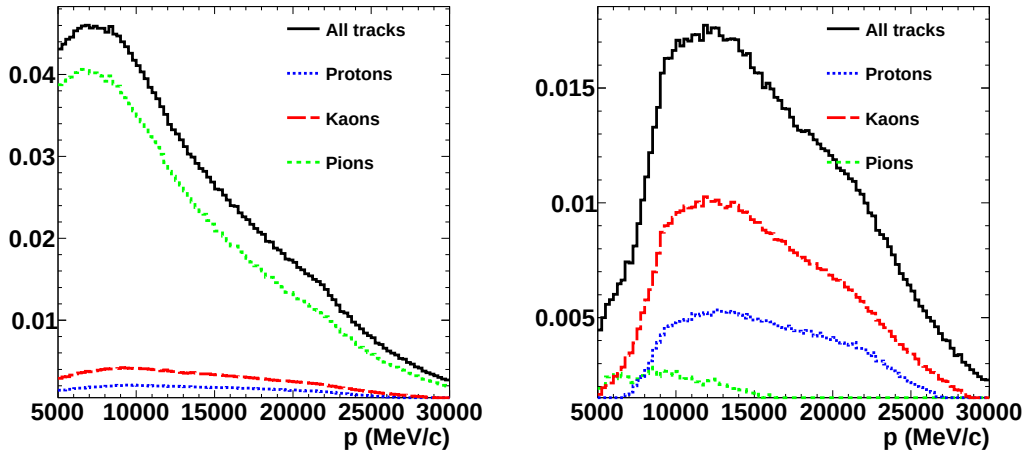
$$N = \frac{\sum_i n_i^{cal}}{\sum_i n_i^{ref}}. \tag{4.7}$$

The weights, W_i, are then applied to the calibration sample in order to resemble the kinematic and event occupancy distributions of the reference sample. Consequently, the re-weighted calibration DLL distributions will model those associated with minimum-bias events.

4.6.4.1 Approximations in the Re-Weighting Procedure

Ideally, separate minimal track samples containing pure protons, kaons and pions in minimum-bias events, without any PID cut applied, should be provided as a *reference sample* to re-weight the Λ, ϕ and K_S^0 samples respectively. However, obtaining pure samples from a minimal track sample, which contains in general a mixture of

all particle species, is inherently impossible in data without using RICH information. Moreover, since the minimal track sample is statistically dominated by pions, the re-weighting would be always performed using a pion-dominated reference sample (see Figure 4.9(a)). This would not be an issue if the distributions of $nTracks$ and p were identical for protons, kaons and pions. The track multiplicity, as a global event variable, has a very weak dependence on the particle species, however, according to MC, the momentum distributions of the three species in a minimal track sample may differ significantly, particularly in the lowest p_T bin.



(a) Reconstructed tracks (b) Reconstructed tracks with DLL(p-π)>8

Figure 4.9: Momentum distributions for different particle species in MC at $\sqrt{\mathbf{s}} = 0.9\,\text{TeV}$ and $p_T < 0.8\,\text{GeV/c}$, for a minimal track sample. If no DLL cut is applied, the momentum shape is dominated by pions.

The above problem is partially circumvented with a slight modification of the samples used for the re-weighting, as described below. An alternative reference sample is formed by applying a loose DLL cut to a minimal track sample in order to enhance as much as possible the content of the particle of interest, as shown in Figure 4.9(b). Then the re-weighting is performed using this new reference sample and the corresponding RICH calibration sample with the same DLL cut applied. Note that this loose cut is imposed solely for determining the weights in Eq. 4.6 and is not applied elsewhere in the analysis. The cut is set to $\text{DLL}(p-\pi) > 8$ and $\text{DLL}(K-\pi) > 8$ for the re-weighting of protons in the Λ sample and kaons in the ϕ sample respectively,

while DLL$(K-\pi)<0$ is used for pions in the K^0_S sample. In the case of protons, by applying this DLL cut to a minimal sample in MC, the purity rises from 6% to 35%.

The justification for the above procedure is related to how PID efficiency is calculated. Similar to Eq. 4.5, the PID efficiency for a given DLL cut in a $(p, nTracks)$ cell is a ratio in which the numerator is the number of calibration tracks passing the cut and the denominator is the total number of calibration tracks, both in that cell. Supposing a pure sample of protons could be selected from the minimal track sample by means other than a PID cut and used as the reference sample, then the re-weighting of the protons in the Λ sample could be performed with the correct reference sample and the weight in each cell could be calculated exactly. However, this weight must be the same for the numerator and the denominator of the efficiency for the weighting procedure to be consistent. Since the placement of the DLL cut can be arbitrary, it follows that the weights do not depend on its exact value, and that they can be calculated by applying the same DLL cut to the minimal track sample and RICH calibration sample.

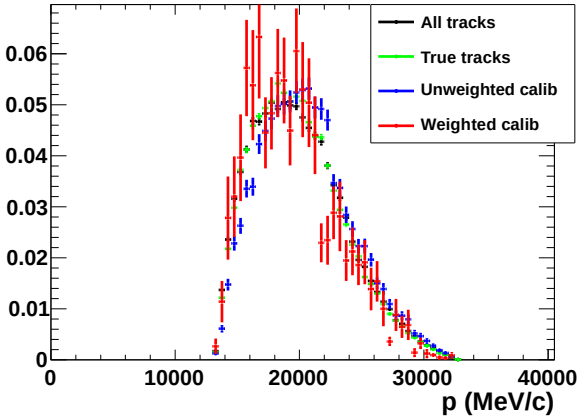
The method we use exploits the independence of the weight on the DLL cut and takes advantage of the reference sample becoming more pure using a PID cut. Since this cut has to be loose enough to guarantee reasonable statistics in each $(p, nTracks)$ cell for the weight estimation, the reference sample cannot be 100% pure. This approximation leads ultimately to biases in the estimation of the PID efficiency.

4.6.4.2 Choice of Cell Sub-Division in Momentum and Track Multiplicity

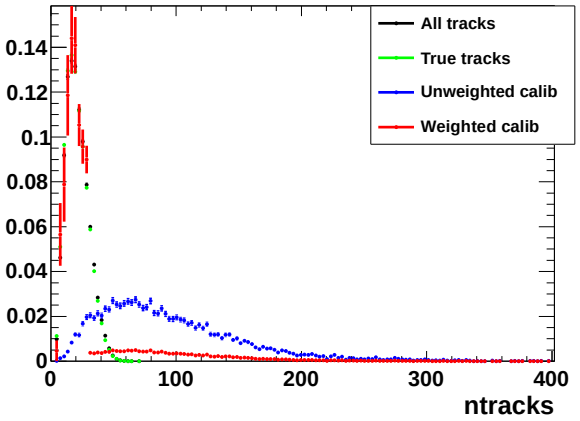
The sub-division into cells of p and $nTracks$ to perform the weighting must be fine enough to describe the distributions reasonably well and coarse enough to allow sufficient statistics in each cell. The number of $(p, nTracks)$ cells per bin is fixed to 24, having six and four divisions respectively in p and $nTracks$. The internal cell division is dynamically defined according to the reference sample distributions so that each cell has the same statistics, provided that at least 100 tracks from the calibration sample are in the same cell. If the statistical requirement is not satisfied, the bin size is widened and the overall binning rearranged. In order to check the performance of the

method, the procedure has been performed on MC, where complete control is possible. Unweighted and weighted distributions of momentum, track multiplicity and DLL for protons in the Λ MC calibration sample are shown in Figures 4.10 and 4.11, compared to a minimal track and a *true* proton sample in MC. The agreement between the DLL distribution of the weighted calibration sample and the corresponding true track sample is generally good in the vast majority of the bins. Residual differences are essentially due to the purity of the reference sample, as described in Section 4.6.4.1, and will be addressed in Section 4.8.

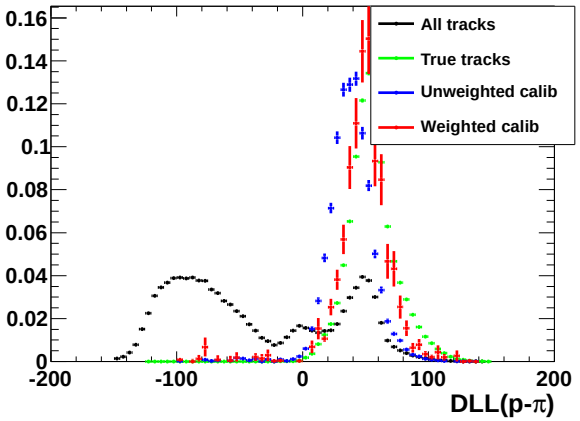
A significant difference between the multiplicity distribution for a minimal track sample at $\sqrt{\mathbf{s}} = 0.9\,\text{TeV}$ and the calibration samples at $\sqrt{\mathbf{s}} = 7\,\text{TeV}$ is clearly visible in Figure 4.10(b). Several elements contribute to the difference such as the evolution of the total pp interaction cross section with the centre of mass energy, the number of interactions per bunch crossing and the partially open VELO that reduces the LHCb acceptance for long tracks. The impact on the analysis of this difference after the reweighting procedure is negligible in terms of biases in the PID efficiencies estimation. However, it is noted a significant loss in statistical power (up to 80%) in the calibration sample since only events at $nTracks$ contribute to the PID efficiency calculation.



(a) Momentum

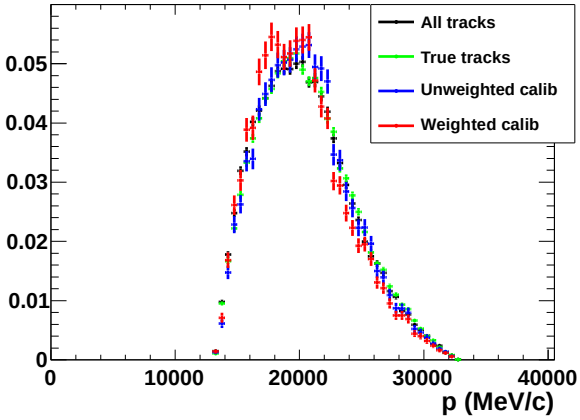


(b) Track multiplicity

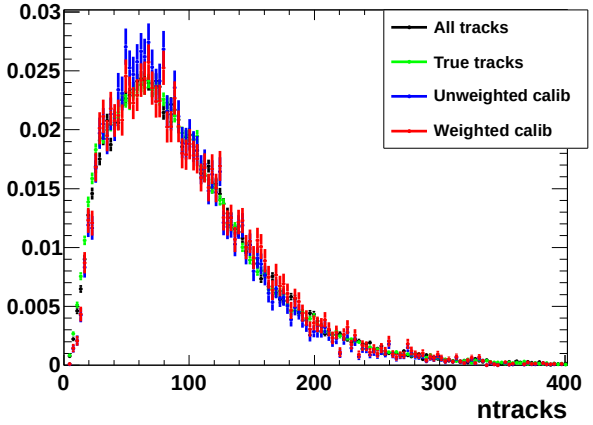


(c) DLL($p - \pi$)

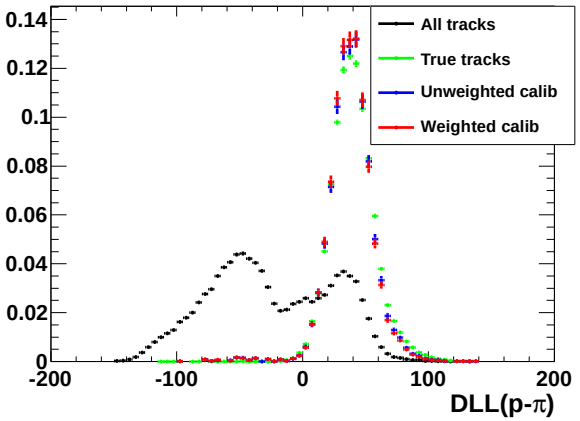
Figure 4.10: Weighted distributions for protons in MC for $\sqrt{s} = 0.9\,\text{TeV}$, $0.8 < p_T < 1.2\,\text{GeV/c}$ and $3.5 < \eta < 4$. Weighted protons from Λ decay in the calibration sample (red) are compared to true protons (green), unweighted calibration sample (blue) and all tracks (black).



(a) Momentum



(b) Track multiplicity



(c) DLL($p - \pi$)

Figure 4.11: Weighted distributions for protons in MC for $\sqrt{s} = 7\,\text{TeV}$, $0.8 < p_T < 1.2\,\text{GeV/c}$ and $3.5 < \eta < 4$. Weighted protons from Λ decay in the calibration sample (red) are compared to true protons (green), unweighted calibration sample (blue) and all tracks (black).

4.6.4.3 Comparison of Results with MC Truth after Re-Weighting

In principle the efficiencies obtained through the re-weighting procedure should be consistent with the MC truth of the track sample (within statistical errors). However, due to the approximations made (e.g. the reference sample not being pure) and to a lack of statistics in some bins, the shape of the DLL is not always perfectly reproduced and, ultimately, this has an impact on the efficiency estimation. For each (p_T, η) bin and perfectly-performing weighting, we can write

$$\epsilon_{calib} \simeq \epsilon_{truth}, \tag{4.8}$$

where ϵ_{calib} is the weighted efficiency from the calibration sample and ϵ_{truth} is its true value in the minimal track sample. However, from scrutiny of plots of ϵ_{calib} against ϵ_{truth} for MC (Figures 4.12-4.17), it is evident that the calibration procedure is not perfect. In particular for protons and kaons in the lowest p_T bin, biases remain. It is noted that for many of these plots there is an approximately linear relationship between ϵ_{calib} and ϵ_{truth} ($\epsilon_{truth} \approx \alpha\epsilon_{calib}$), and so the residual bias may be reduced by fitting the gradient α separately for each p_T bin and particle category such that

$$\epsilon_{corr} = \alpha\epsilon_{calib}, \tag{4.9}$$

where ϵ_{corr} is the corrected efficiency.

The values for the gradients fitted in MC are summarised in Tables 4.8-4.9 and represented by the dotted lines in Figures 4.12-4.17. In general these values are close to unity, but significant differences are seen in the low p_T bin, both for kaons and protons. Therefore corrections to the efficiency are applied only to those two particle species in the lowest p_T bin. However, rather than apply the values found in Tables 4.8 and 4.9, alternative gradients are determined from a full MC validity check of the entire analysis procedure, as detailed in Section 4.8. In this way the full analysis chain is tested and other potential biases, for example those associated with the calibration of the misidentification efficiencies, are also absorbed. These validity checks are also used to

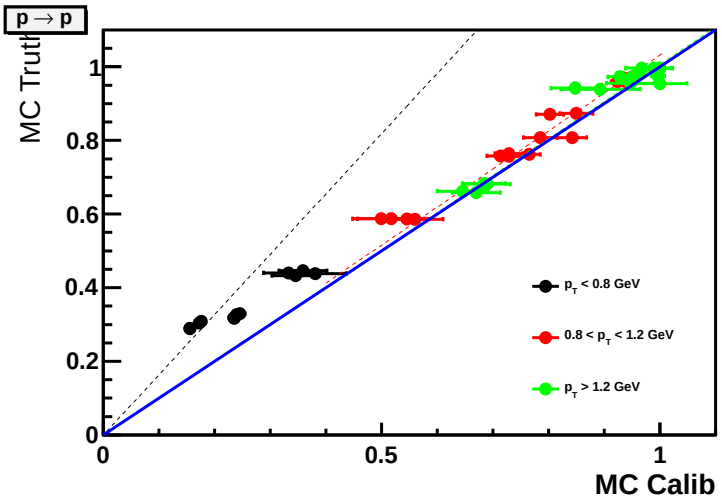


Figure 4.12: MC truth PID efficiency of protons in the minimal track sample as a function of the estimated efficiency from the RICH calibration samples, also in MC. Data points are from negative and positive protons and both magnet polarities at $\sqrt{s} = 0.9\,\text{TeV}$. The dotted lines represent the gradient fit performed for each p_T bin while the blue line for which MC Truth = MC Calib is shown as a reference.

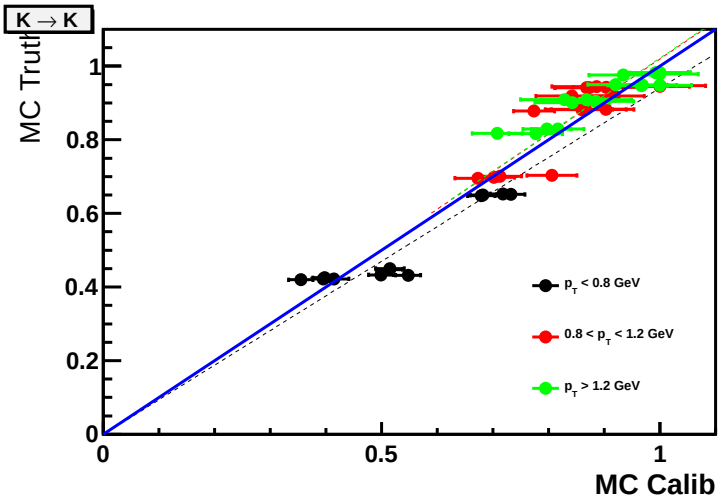


Figure 4.13: MC truth PID efficiency of kaons in the minimal track sample as a function of the estimated efficiency from the RICH calibration samples, also in MC. Data points are from negative and positive kaons and both magnet polarities at $\sqrt{s} = 0.9\,\text{TeV}$. The dotted lines represent the gradient fit performed for each p_T bin while the blue line for which MC Truth = MC Calib is shown as a reference.

assign uncertainties associated with residual biases that remain after these corrections, and also with the possible small biases that exist for the PID calibration of the other particle types and other p_T bins.

The unweighted and weighted efficiencies (statistical errors only) obtained in MC after the gradient correction are shown in Figures 4.18-4.23.

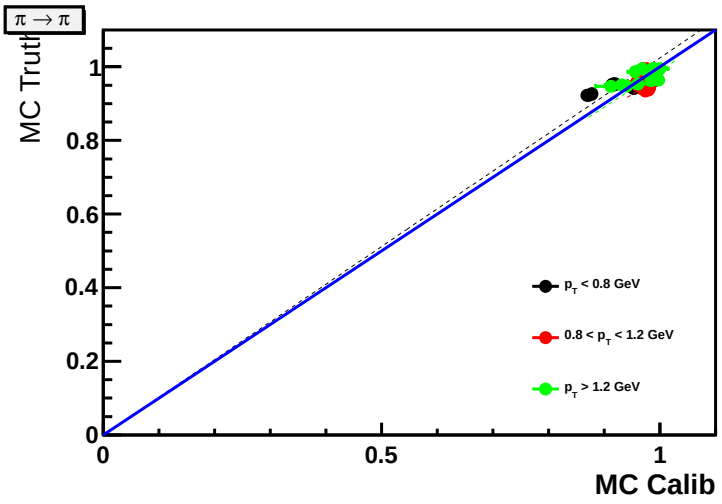


Figure 4.14: MC truth PID efficiency of pions in the minimal track sample as a function of the estimated efficiency from the RICH calibration samples, also in MC. Data points are from negative and positive pions and both magnet polarities at $\sqrt{s} = 0.9\,\text{TeV}$. The dotted lines represent the gradient fit performed for each p_T bin while the blue line for which MC Truth = MC Calib is shown as a reference.

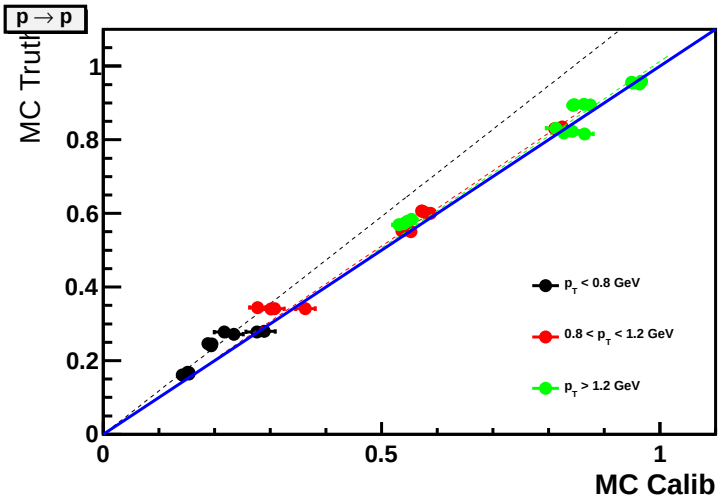


Figure 4.15: MC truth PID efficiency of protons in the minimal track sample as a function of the estimated efficiency from the RICH calibration samples, also in MC. Data points are from negative and positive protons and both magnet polarities at $\sqrt{s} = 7\,\text{TeV}$. The dotted lines represent the gradient fit performed for each p_T bin while the blue line for which MC Truth = MC Calib is shown as a reference.

Table 4.8: Fitted gradient values at $\sqrt{s} = 0.9\,\text{TeV}$. Errors of 0.00 are less than 0.005.

	α_{proton}	α_{kaon}	α_{pion}
$p_T < 0.8\,\text{GeV}/c$	1.64 ± 0.02	0.94 ± 0.01	1.02 ± 0.00
$0.8 < p_T < 1.2\,\text{GeV}/c$	1.03 ± 0.01	1.02 ± 0.02	0.97 ± 0.00
$p_T > 1.2\,\text{GeV}/c$	1.01 ± 0.01	1.02 ± 0.02	0.99 ± 0.00

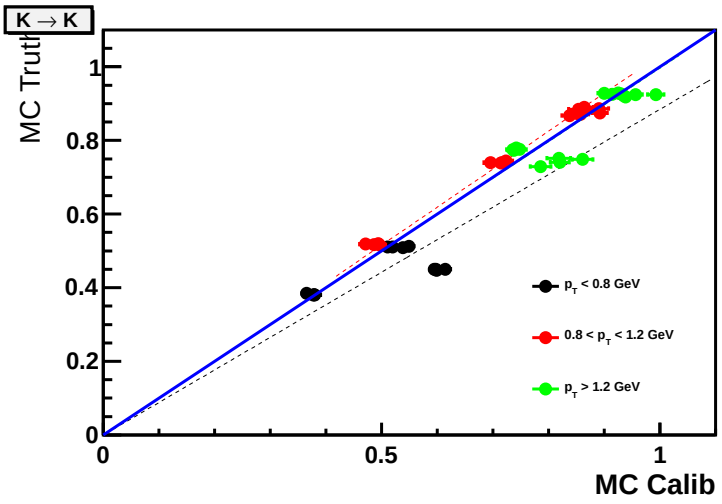


Figure 4.16: MC truth PID efficiency of kaons in the minimal track sample as a function of the estimated efficiency from the RICH calibration samples, also in MC. Data points are from negative and positive kaons and both magnet polarities at $\sqrt{s} = 7\,\text{TeV}$. The dotted lines represent the gradient fit performed for each p_T bin while the blue line for which MC Truth = MC Calib is shown as a reference.

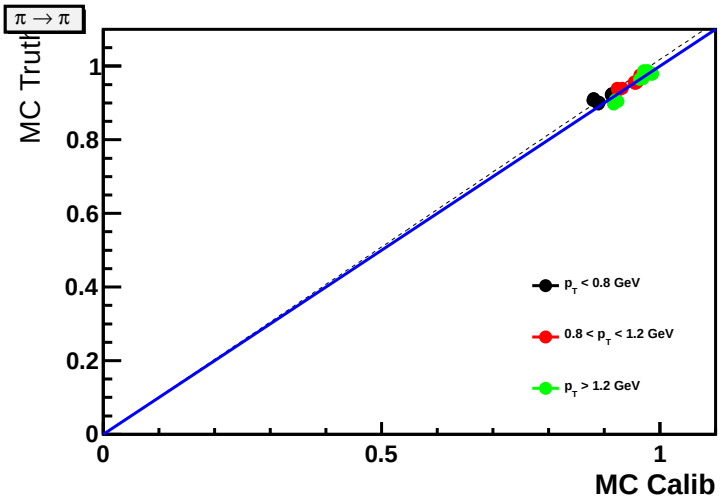
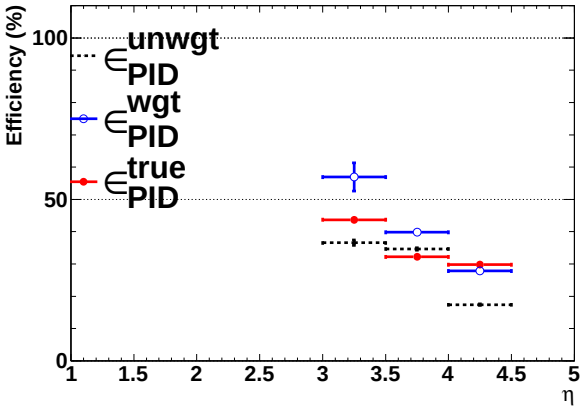


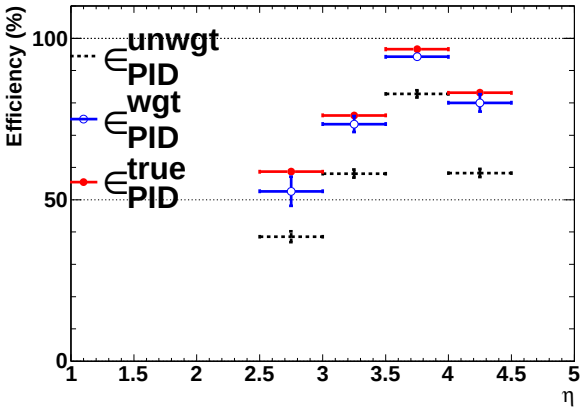
Figure 4.17: MC truth PID efficiency of pions in the minimal track sample as a function of the estimated efficiency from the RICH calibration samples, also in MC. Data points are from negative and positive pions and both magnet polarities at $\sqrt{s} = 7\,\text{TeV}$. The dotted lines represent the gradient fit performed for each p_T bin while the blue line for which MC Truth = MC Calib is shown as a reference.

Table 4.9: Fitted gradient values at $\sqrt{s} = 7\,\text{TeV}$. Errors of 0.00 are less than 0.005.

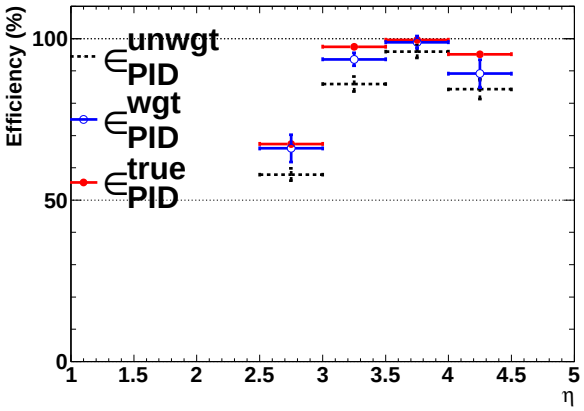
	α_{proton}	α_{kaon}	α_{pion}
$p_T < 0.8\,\text{GeV}/c$	1.18 ± 0.01	0.88 ± 0.00	1.02 ± 0.00
$0.8 < p_T < 1.2\,\text{GeV}/c$	1.02 ± 0.00	1.03 ± 0.00	1.00 ± 0.00
$p_T > 1.2\,\text{GeV}/c$	1.01 ± 0.00	1.00 ± 0.00	1.00 ± 0.00



(a) $p_T < 0.8\,\mathrm{GeV}/c$

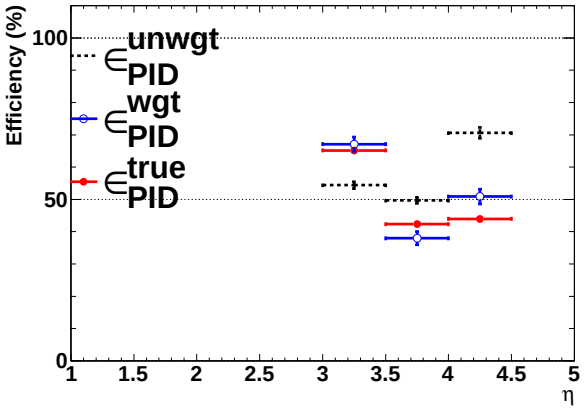


(b) $0.8\,\mathrm{GeV}/c \leq p_T < 1.2\,\mathrm{GeV}/c$

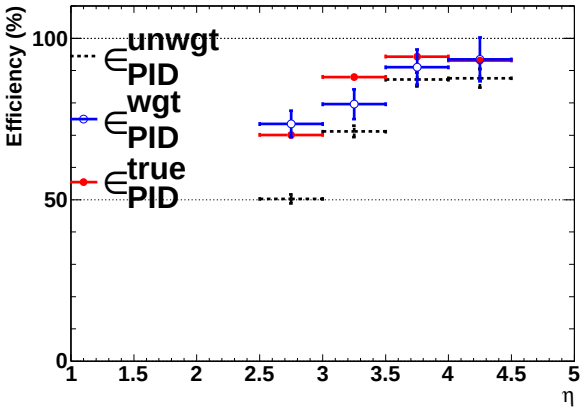


(c) $p_T > 1.2\,\mathrm{GeV}/c$

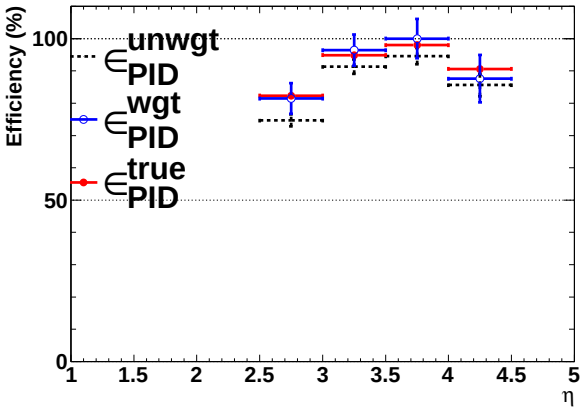
Figure 4.18: Comparison of unweighted (black) and weighted efficiencies (empty marker) from the MC calibration sample with MC truth values (solid marker). Plots are for an average of protons and antiprotons at $\sqrt{\mathrm{s}} = 0.9\,\mathrm{TeV}$.



(a) $p_T < 0.8\,\mathrm{GeV}/c$

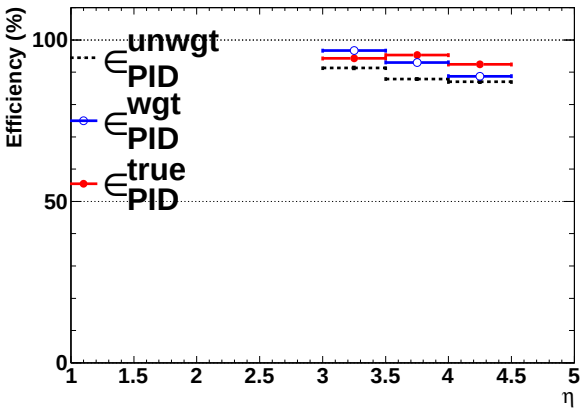


(b) $0.8\,\mathrm{GeV}/c \leq p_T < 1.2\,\mathrm{GeV}/c$

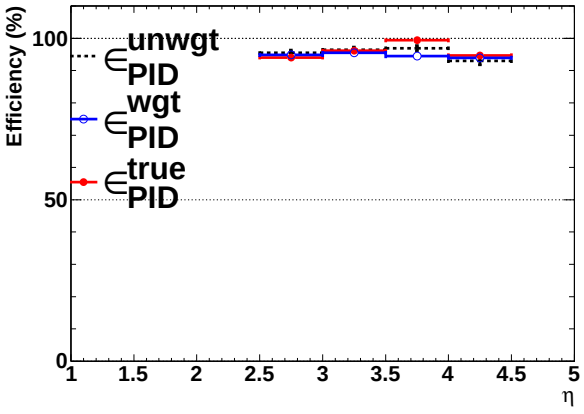


(c) $p_T > 1.2\,\mathrm{GeV}/c$

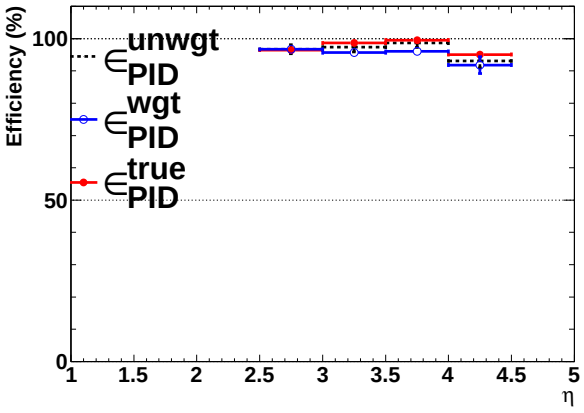
Figure 4.19: Comparison of unweighted (black) and weighted efficiencies (empty marker) from the MC calibration sample with MC truth values (solid marker). Plots are for an average of positive and negative kaons at $\sqrt{s} = 0.9\,\mathrm{TeV}$.



(a) $p_T < 0.8\,\mathrm{GeV}/c$

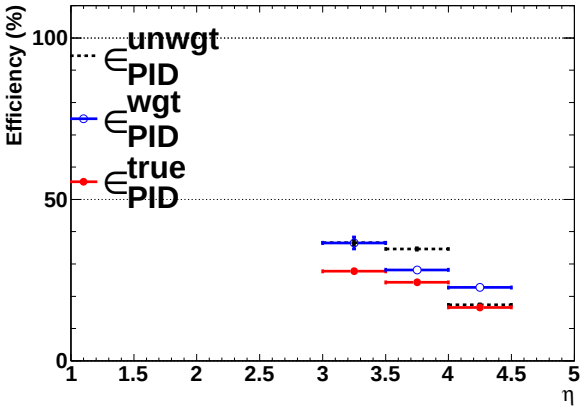


(b) $0.8\,\mathrm{GeV}/c \leq p_T < 1.2\,\mathrm{GeV}/c$

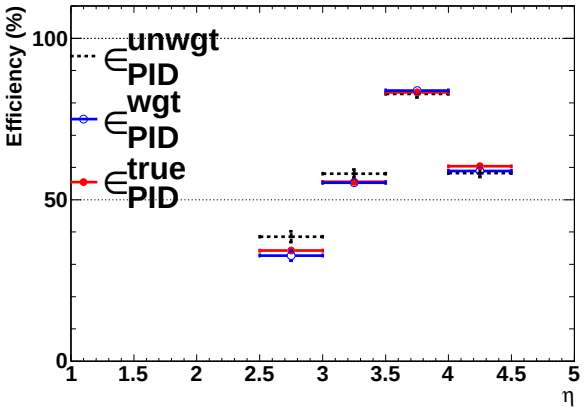


(c) $p_T > 1.2\,\mathrm{GeV}/c$

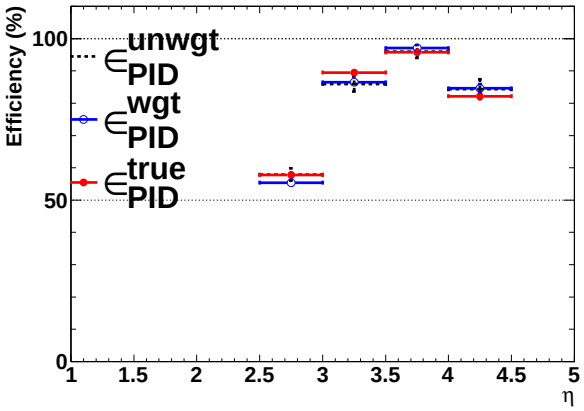
Figure 4.20: Comparison of unweighted (black) and weighted efficiencies (empty marker) from the MC calibration sample with MC truth values (solid marker). Plots are for an average of positive and negative pions at $\sqrt{\mathbf{s}} = 0.9\,\mathrm{TeV}$.



(a) $p_T < 0.8\,\mathrm{GeV}/c$

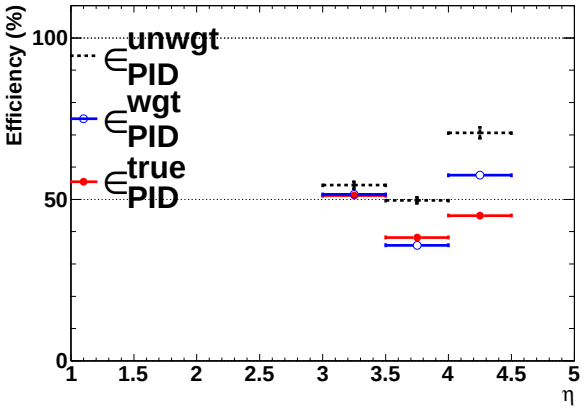


(b) $0.8\,\mathrm{GeV}/c \leq p_T < 1.2\,\mathrm{GeV}/c$

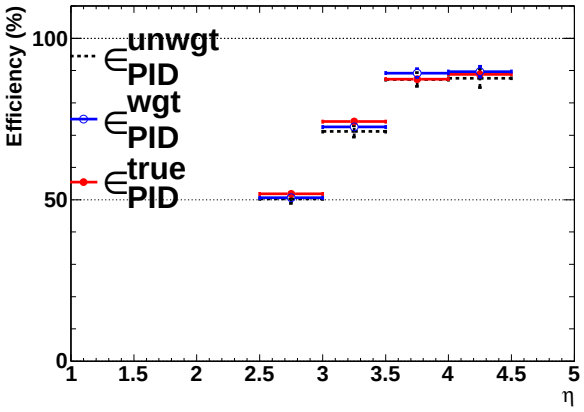


(c) $p_T > 1.2\,\mathrm{GeV}/c$

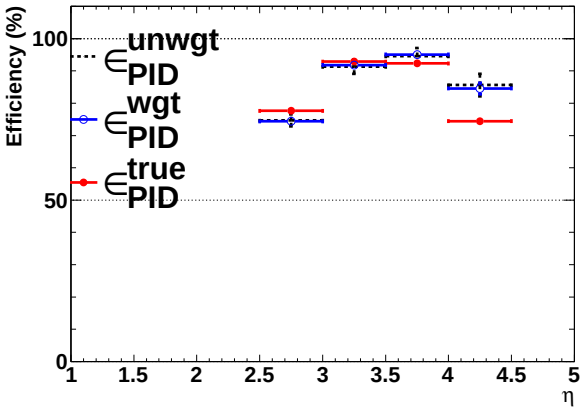
Figure 4.21: Comparison of unweighted (black) and weighted efficiencies (empty marker) from the MC calibration sample with MC Truth values (solid marker). Plots are for an average of protons and antiprotons at $\sqrt{\mathrm{s}} = 7\,\mathrm{TeV}$.



(a) $p_T < 0.8\,\mathrm{GeV}/c$

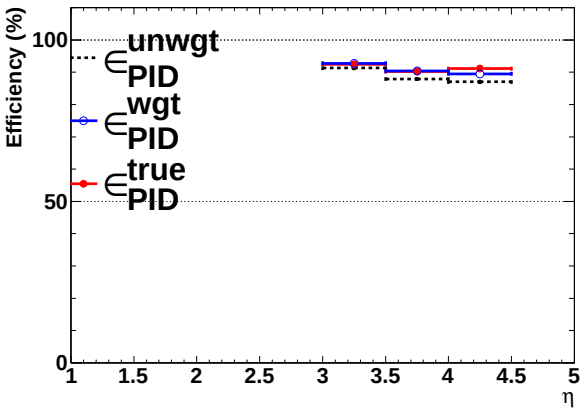


(b) $0.8\,\mathrm{GeV}/c \leq p_T < 1.2\,\mathrm{GeV}/c$

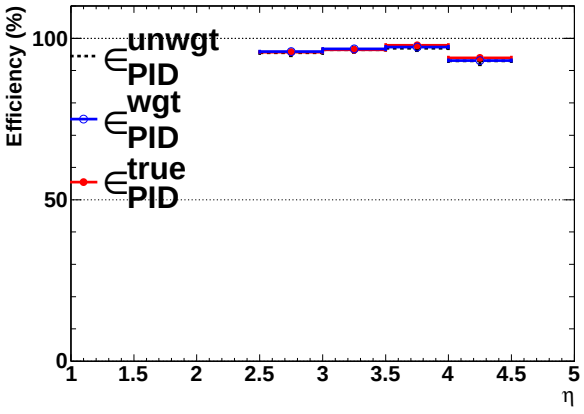


(c) $p_T > 1.2\,\mathrm{GeV}/c$

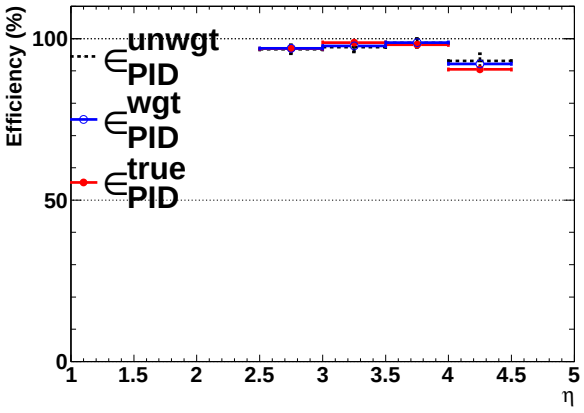
Figure 4.22: Comparison of unweighted (black) and weighted efficiencies (empty marker) from the MC calibration sample with MC truth values (solid marker). Plots are for an average of positive and negative kaons at $\sqrt{\mathrm{s}} = 7\,\mathrm{TeV}$.



(a) $p_T < 0.8\,\mathrm{GeV}/c$



(b) $0.8\,\mathrm{GeV}/c \leq p_T < 1.2\,\mathrm{GeV}/c$



(c) $p_T > 1.2\,\mathrm{GeV}/c$

Figure 4.23: Comparison of unweighted (black) and weighted efficiencies (empty marker) from the MC calibration sample with MC truth values (solid marker). Plots are for an average of positive and negative pions at $\sqrt{\mathrm{s}} = 7\,\mathrm{TeV}$.

4.6.5 Contamination Corrections

The DLL cuts in the track selection are quantified by a set of ID and *mis*ID efficiencies. Through these efficiencies it is possible to calculate the content of each particle species from the selected candidates in the analysis samples. Due to non-zero *mis*ID rates, all the three samples contaminate each other, therefore the relationship between the selected candidates and the true particle content is represented by a matrix equation,

$$\underbrace{\begin{bmatrix} p_{Sel} \\ K_{Sel} \\ \pi_{Sel} \end{bmatrix}}_{V_{Sel}} = \underbrace{\begin{bmatrix} \epsilon_{\mathbf{p}\to\mathbf{p}} & \epsilon_{K\to p} & \epsilon_{\pi\to p} \\ \epsilon_{p\to K} & \epsilon_{\mathbf{K}\to\mathbf{K}} & \epsilon_{\pi\to K} \\ \epsilon_{p\to\pi} & \epsilon_{K\to\pi} & \epsilon_{\boldsymbol{\pi}\to\boldsymbol{\pi}} \end{bmatrix}}_{M_{ID}} \underbrace{\begin{bmatrix} p_{True} \\ K_{True} \\ \pi_{True} \end{bmatrix}}_{V_{True}} . \tag{4.10}$$

This gives the explicit mathematical relationship between the selected proton, kaon or pion candidates in the analysis sample, V_{Sel}, and the initial true content before DLL cuts are applied, V_{True}.

The 3×3 matrix, M_{ID}, contains ID efficiencies as diagonal terms and *mis*ID rates as off-diagonal terms. The vector V_{Sel} can be expressed as a function of the selected candidates through a simple matrix inversion:

$$V_{True} = M_{ID}^{-1} V_{Sel}. \tag{4.11}$$

Each element of M_{ID} has an associated error that has to be propagated correctly to the inverse matrix. The error on each M_{ID}^{-1} element is calculated by random Gaussian smearing to each element of M_{ID} (according to its error) and inverting it 100000 times to get a population of inverse matrices. In this way it is possible to get a distribution for each element of M_{ID}^{-1} and extract the uncertainty as the RMS. The values of the ID and *mis*ID fractions can be found in Appendix A.

In principle the analysis should account for the presence of other particle types, in particular muons and electrons. However, due to the tight PID requirements, electrons are easily discarded. Moreover muons, which appear very similar to pions in the RICH, are not statistically significant in number; according to MC, muons account for less

than 1‰ in the pion-enriched samples and therefore can be neglected.

4.6.6 Results and Purities

The performance of the PID is significantly worse in data than in MC at low η and low p_T. In order to avoid systematic effects due to extremely low PID efficiencies, we have chosen to exclude bins with insufficient statistics in the calibration samples. From the

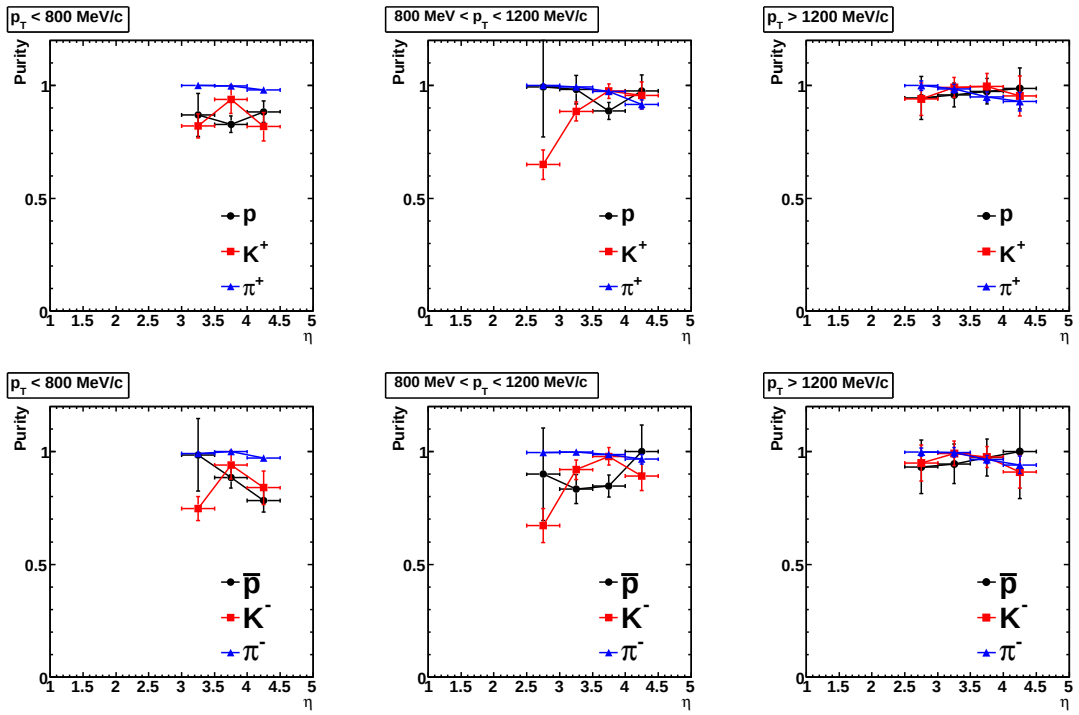


Figure 4.24: Purity of selected samples at $\sqrt{s} = 0.9\,\text{TeV}$ (magnet polarity up).

ID and *mis*ID rates it is also possible to estimate the purity of the analysis samples. According to Eq. 4.10, these purities can be written as:

$$p_{purity} = \frac{\epsilon_{\mathbf{p}\to\mathbf{p}} \times p_{True}}{p_{Sel}} \quad K_{purity} = \frac{\epsilon_{\mathbf{K}\to\mathbf{K}} \times K_{True}}{K_{Sel}} \quad \pi_{purity} = \frac{\epsilon_{\boldsymbol{\pi}\to\boldsymbol{\pi}} \times \pi_{True}}{\pi_{Sel}}. \tag{4.12}$$

The purities of all samples, shown in Figures 4.24-4.25, are in generally above 70%, as expected from the optimisation procedure.

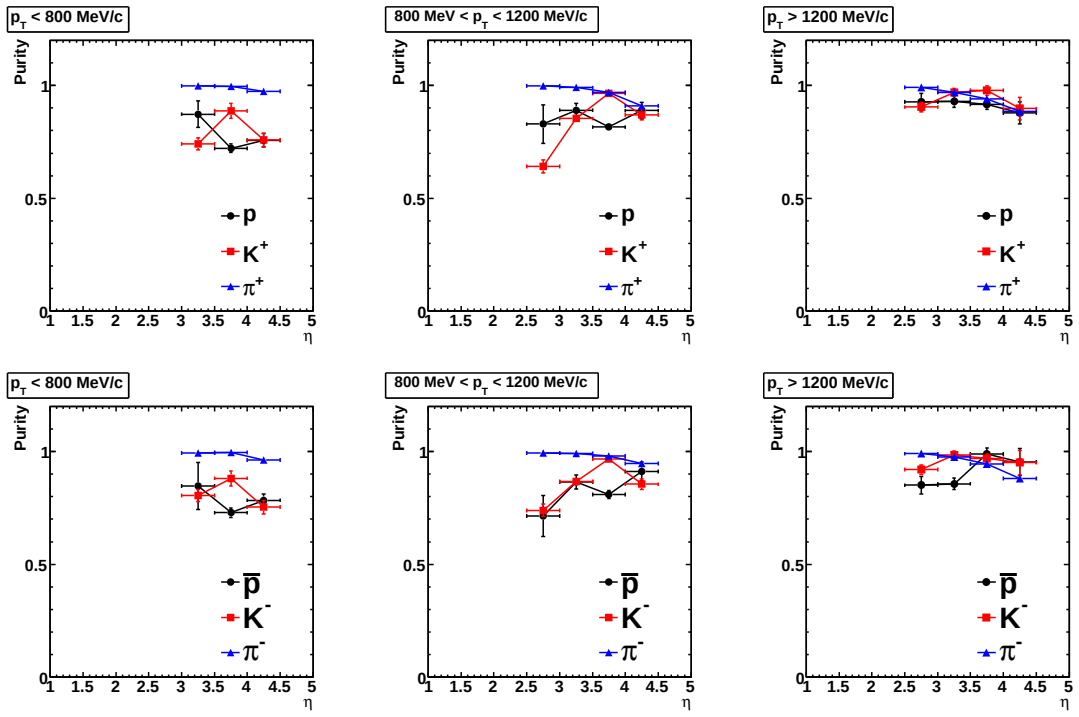


Figure 4.25: Purity of selected samples at $\sqrt{s} = 7\,\text{TeV}$ (magnet polarity up).

4.7 Material Interactions and Reconstruction Efficiency

Interaction of particles with the detector material is the main cause of charged particles, produced within the LHCb geometrical acceptance, not being reconstructed by the tracking algorithms. In order to estimate the magnitude of this effect, MC simulations of the detector response have been used.

The probability of interaction is dependent on two factors: the interaction cross section and the thickness of material traversed by the particle. The cross section is dependent on the particle momentum while the material traversed in the LHCb detector is dependent on η. In this analysis the reconstruction efficiency is calculated in MC separately in bins of η and p_T. In this way the reconstruction efficiency correction from the MC is used on particles with similar kinematics in data. The p_T in a given bin of η is highly correlated to the momentum and the choice of variable is valid, even though the binning is not explicitly in momentum. An example of this correlation is shown in Figure 4.26, where p_T is plotted against p for protons in the range $3 < |\eta| <$

3.5.

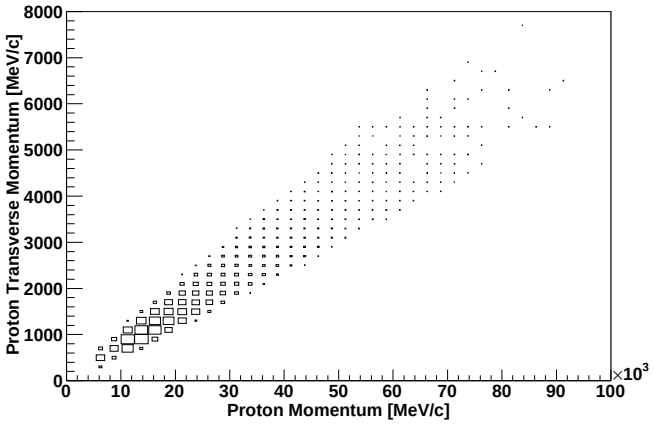


Figure 4.26: Correlation between p_T and p for protons with $3 < |\eta| < 3.5$. The relationship between p, p_T and η is demonstrated by the limits within which the data lie.

Interaction cross sections differ between protons, kaons and pions due to the different processes occurring during the interaction. The production of resonances such as Λ's in proton-aluminum interactions means that the probability of protons interacting in the detector is greater than for pions or kaons. Moreover, the interaction cross section is not symmetric between p and $\bar{p}$ and varies as a function of momentum, as shown in Figure 4.27. These effects must be reproduced correctly in the simulation so as not to introduce biases in the estimation of the reconstruction efficiencies that can affect the final measurement. The LHCb MC simulation framework uses the interaction cross sections of the so-called LHEP physics lists as part of the GEANT4 package [62]. Several cross-checks have been performed within the LHCb collaboration to test the reliability of the simulation; only a summary of the results is presented here. The study involved the use of a simplified geometry and the simulation of particle beams of momenta 1, 5, 10, 100 GeV/c. These simulated particles were incident on blocks of aluminum of thicknesses 1 mm, 1 cm, 5 cm and 10 cm. Further tests were carried out on simulated blocks of silicon and beryllium. The fractions of particles that interacted in the simulation were recorded and compared to the expectations given by the cross sections in the LHEP physics list. It was found that there is good agreement between the implementation of material interaction cross sections observed and the input cross

sections.

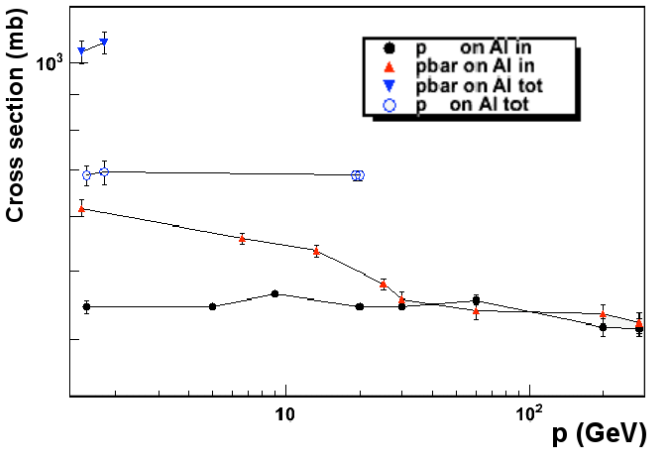
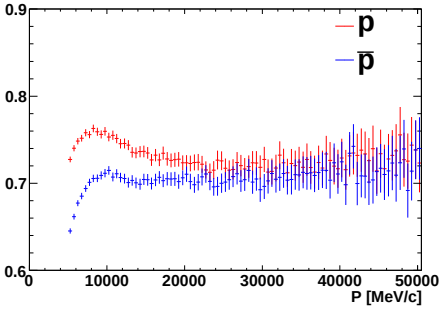


Figure 4.27: Measurement of the inelastic and total cross sections in aluminium for proton and antiprotons as a function of momentum [2].

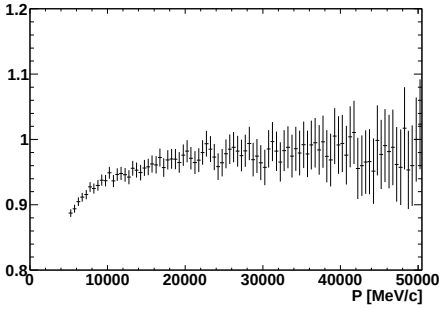
Hadronic interactions introduce the most important correction in the reconstruction efficiency, defined as $(\#long\,reconstructed)/(\#generated)$, between negative and positive particles or different hadron species. These corrections are significant at low momenta, as demonstrated in Figure 4.28 as a function of momentum. Material interactions have a significant impact on the reconstruction efficiencies as a function of η, demonstrated by MC in (Figures 4.29-4.30) and shown over the region $1 < \eta < 5$, within the phase-space acceptance of η, p_T and $p > 5\,\mathrm{GeV}/c$. Systematic uncertainties associated to the amount of material traversed by the particles, and residual discrepancies between the cross section in data and LHEP are discussed in Sections 5.2.2 and 5.2.3 respectively.

4.8 Monte Carlo Validation Study

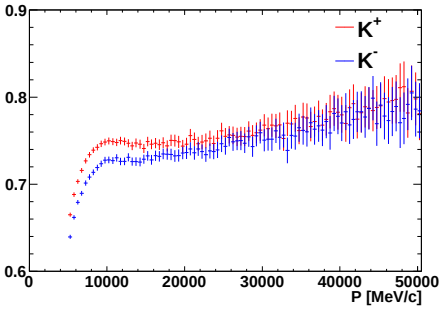
As well as for data, the full analysis was carried out on MC samples, both at $\sqrt{\mathbf{s}} = 0.9\,\mathrm{TeV}$ and $7\,\mathrm{TeV}$. The analysis procedure is the same as for the data but the PID calibration is performed on the MC. As noted in Section 4.6.4.3, the most biased efficiencies are those of protons and kaons, particularly in the lowest p_T bin for which a correction factor for the PID efficiency has been estimated. In this section we describe an estimation of the same factor but using a different approach, as described below.



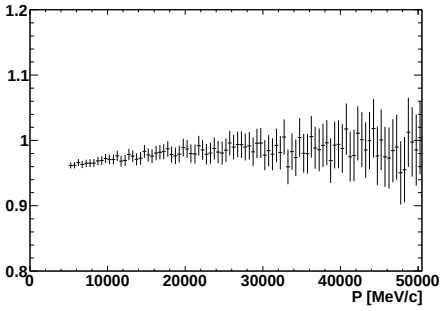
(a) Reconstruction efficiency for p and $\bar{p}$



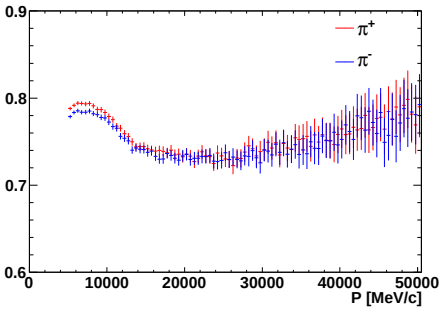
(b) $\bar{p}/p$ reconstruction efficiency ratio



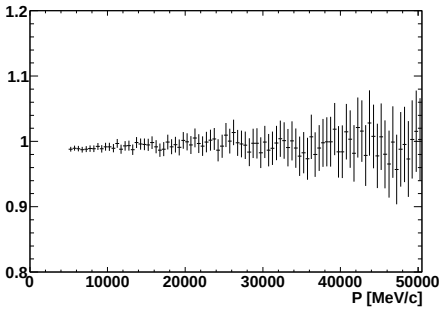
(c) Reconstruction efficiency for K^+ and K^-



(d) K^-/K^+ reconstruction efficiency ratio



(e) Reconstruction efficiency for π^+ and π^-

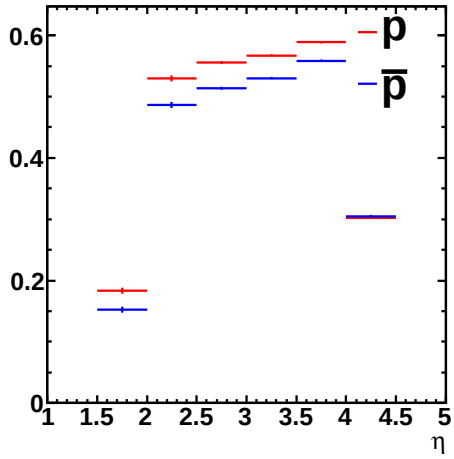


(f) π^-/π^+ reconstruction efficiency ratio

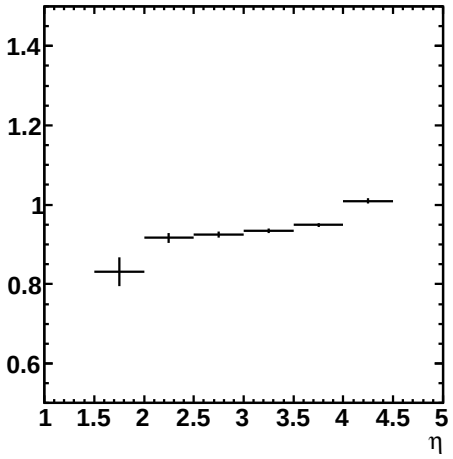
Figure 4.28: Reconstruction efficiencies for reconstructed long tracks as a function of momentum at $\sqrt{s} = 7\,\text{TeV}$, as determined from MC.

The PID efficiencies for opposite sign charged tracks of the same hadron species (e.g. p and $\bar{p}$) are very similar and almost completely correlated. On the other hand, PID efficiencies of different particle species are in general uncorrelated. As a consequence, the biases in the estimation of the PID efficiencies mostly affect the production ratios between different particle species (e.g. $(p+\bar{p})/(K^+ + K^-)$) whilst the biases cancel in the antiparticle/particle ratios.

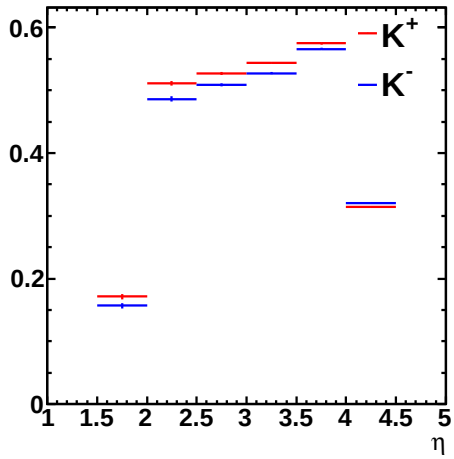
Therefore, the gradients in Eq. 4.9 for the proton and kaon PID efficiencies in



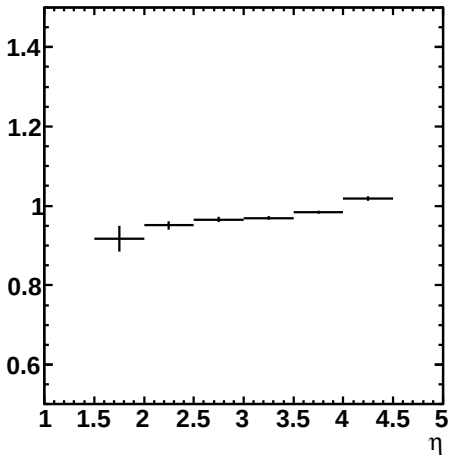
(a) Reconstruction efficiency for p and $\bar{p}$



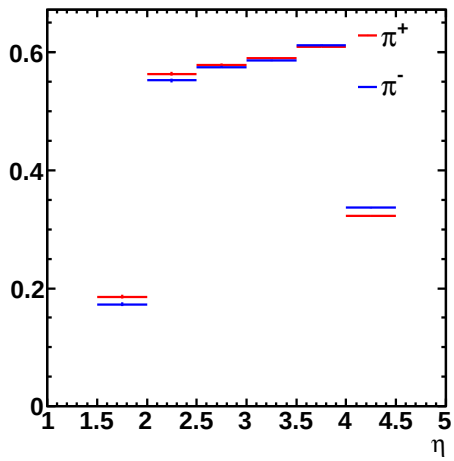
(b) $\bar{p}/p$ reconstruction efficiency ratio vs



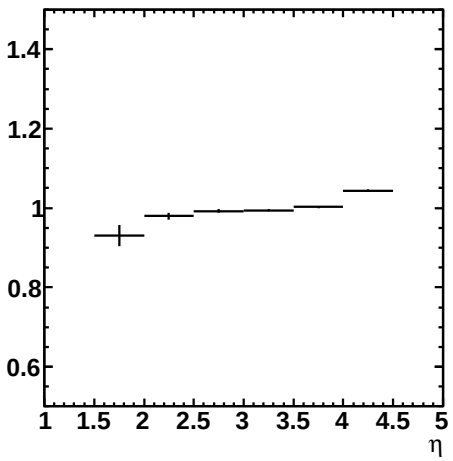
(c) Reconstruction efficiency for K^+ and K^-



(d) K^-/K^+ reconstruction efficiency ratio

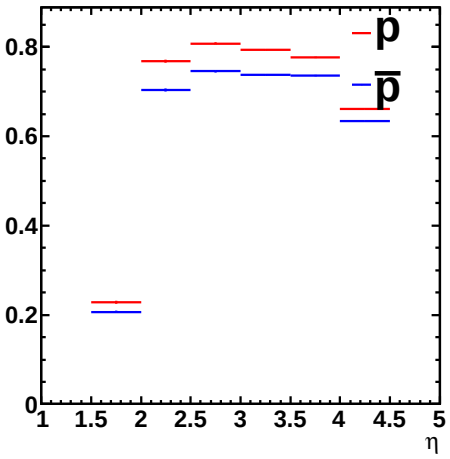


(e) Reconstruction efficiency for π^+ and π^-

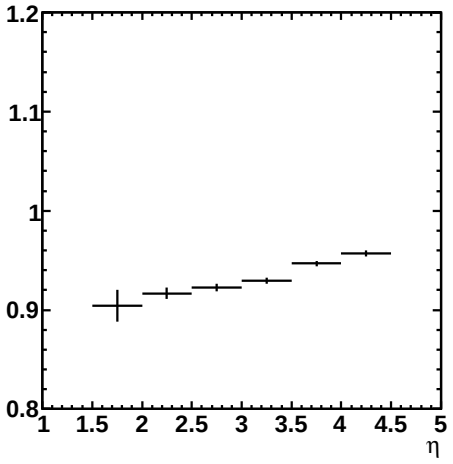


(f) π^-/π^+ reconstruction efficiency ratio

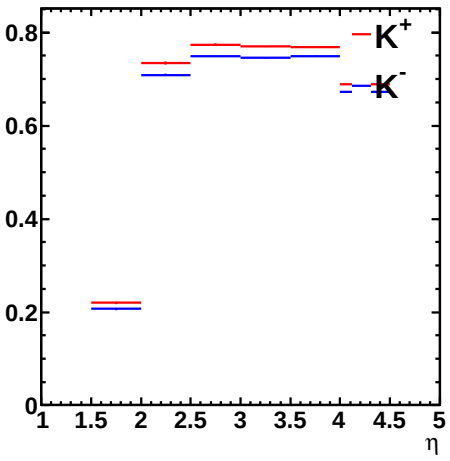
Figure 4.29: Reconstruction efficiencies for reconstructed long tracks as a function of η at $\sqrt{s} = 0.9\,\text{TeV}$, integrated over the full p_T range as determined from MC.



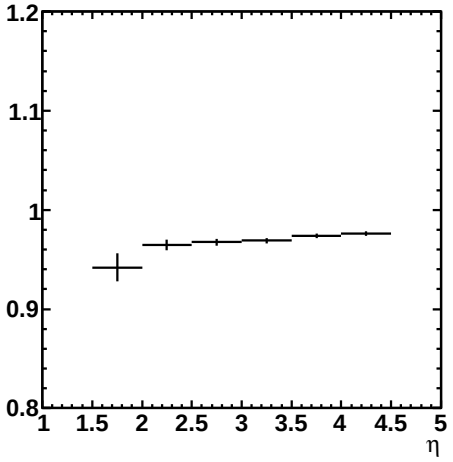
(a) Reconstruction efficiency for p and $\bar{p}$



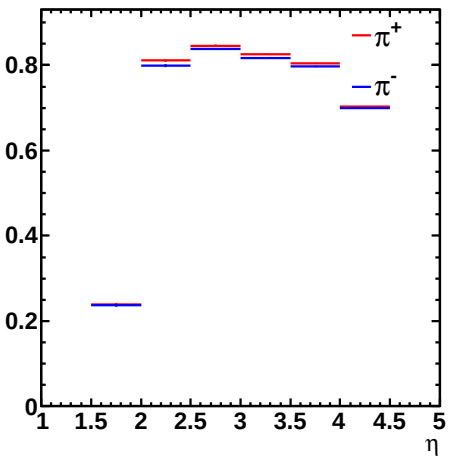
(b) $\bar{p}/p$ reconstruction efficiency ratio



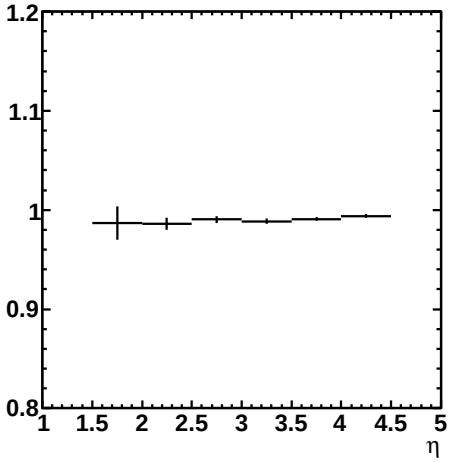
(c) Reconstruction efficiency for K^+ and K^-



(d) K^-/K^+ reconstruction efficiency ratio



(e) Reconstruction efficiency for π^+ and π^-



(f) π^-/π^+ reconstruction efficiency ratio

Figure 4.30: Reconstruction efficiency for reconstructed long tracks as a function of η at $\sqrt{s} = 7\,\text{TeV}$, integrated over the full p_T range as determined from MC.

the lowest p_T bin at each centre of mass energy have been re-tuned in order to minimise the $\chi^2/\#DOF$ between the ratio obtained through the MC validation procedure, $R^{\text{MC validation}}$, and the prediction of the LHCb MC, $R^{\text{LHCb MC}}$. The χ^2 value is calculated by summing over all the η bins (considered independent) and including only the ratios $(p+\bar{p})/(K^+ + K^-)$, $(p+\bar{p})/(\pi^+ + \pi^-)$ and $(K^+ + K^-)/(\pi^+ + \pi^-)$. The details of the procedure are given below.

If $R_{A,B} = A/B$ represents a generic production ratio between particle A and particle B, considering Eq. 4.10 and neglecting *mis*ID fractions (non-diagonal terms in M_{ID}), it can be derived that

$$\frac{A_{True}}{B_{True}} \simeq \frac{A_{Sel}}{B_{Sel}} \times \frac{\epsilon_{B\to B}}{\epsilon_{A\to A}} \tag{4.13}$$

where $\epsilon_{A\to A(B\to B)}$ is the charge-averaged PID identification efficiency for the particle $A(B)$.

Since

$$R_{A,B} = \frac{\epsilon_B^{Rec}}{\epsilon_A^{Rec}} \times \frac{A_{True}}{B_{True}}, \tag{4.14}$$

where $\epsilon^{Rec}_{A(B)}$ is the reconstruction efficiency for the particle $A(B)$, then, to a good approximation

$$R_{A,B} \propto \frac{\epsilon_{B\to B}}{\epsilon_{A\to A}}. \tag{4.15}$$

The multiplication of the proton(kaon) PID efficiency by the correction factor, $\alpha_{proton(kaon)}$, modifies the dependence of the ratios on the PID efficiencies in the following way

$$R'_{p,K} \propto \frac{\epsilon_{K\to K} \times \alpha_{kaon}}{\epsilon_{p\to p} \times \alpha_{proton}}, \quad R'_{p,\pi} \propto \frac{\epsilon_{\pi\to\pi}}{\epsilon_{p\to p} \times \alpha_{proton}}, \quad R'_{K,\pi} \propto \frac{\epsilon_{\pi\to\pi}}{\epsilon_{K\to K} \times \alpha_{kaon}}. \tag{4.16}$$

Finally, α_{proton} and α_{kaon} are tuned on MC in order to minimise the quantity

$$\frac{\chi^2}{\#DOF} = \sum_i \sum_{A\neq B} \left(\frac{R'^{\text{MC validation}}_{A,B} - R^{\text{LHCb MC}}_{A,B}}{\sqrt{\sigma^2_{\text{MCvalidation}} + \sigma^2_{\text{LHCbMC}}}} \right)^2, \tag{4.17}$$

where the indices A and B run over the particle species (p, K and π), the index i runs

over the η bins and $\sigma_{\text{MCvalidation}}$ and σ_{LHCbMC} are the statistical uncertainties. The values for the correction factors found with the above procedure are

	α_{proton}	α_{kaon}
$\sqrt{\mathbf{s}} = 0.9\,\text{TeV}$	1.33	0.90
$\sqrt{\mathbf{s}} = 7\,\text{TeV}$	1.1	0.86 .

The values are similar to those in Section 4.6.4.3 with the exception of protons at low energy, for which the new gradient is approximately 20% smaller. As anticipated in Section 4.6.4.3, this alternative method allows a test of the full analysis chain so that other potential biases associated with the calibration of the *mis*ID efficiencies can be accounted for. The errors on the correction factors are not considered here. However, a related systematic uncertainty, to be assigned to the ratios, is determined as follows.

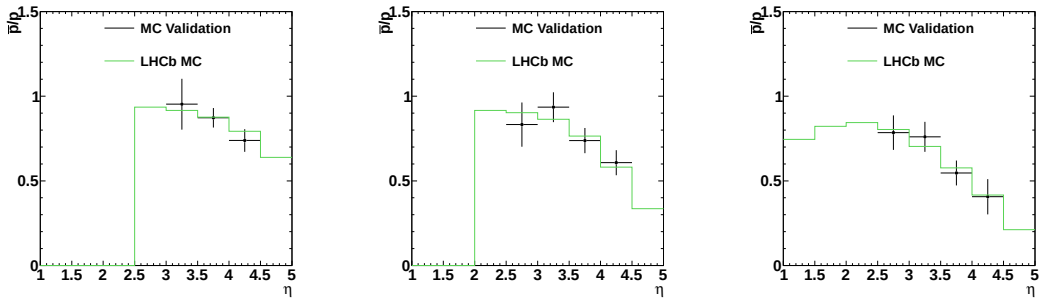
Once the corrections calculated above are applied, a systematic fractional uncertainty, to be assigned to proton and kaon PID efficiencies, can be estimated. As is the case for the bias in the PID efficiency, the uncertainty is completely correlated between negative and positive particles. Moreover, the uncertainty is forced to be the same for proton and kaon identification efficiencies. This latter constraint has been applied only for simplicity; in fact, when calculated separately, the uncertainties obtained are very similar for the two particle species. The uncertainty has been tuned so that, by adding it in quadrature to the denominator in Eq. 4.17, the $\chi^2/\#DOF$ is equal to unity. Separate uncertainties are calculated for the lowest p_T bin and the two higher p_T bins while $\sqrt{\mathbf{s}} = 0.9\,\text{TeV}$ and $\sqrt{\mathbf{s}} = 7\,\text{TeV}$ η bins have been merged in the $\chi^2/\#DOF$ calculation. Therefore, a common value is given for both centre of mass energies. The need for a separate uncertainty for the lowest p_T bin is dictated by a more pronounced bias in the PID efficiency estimation (the cause of this effect is explained in Section 4.6.4.1). In the case of the $(p+\bar{p})/(K^+ + K^-)$ ratio, the additional uncertainty is

$$\left(\frac{\Delta R_{p,K}^{\text{MC validation}}}{R_{p,K}^{\text{MC validation}}}\right)_{extra} \simeq \sqrt{\left(\frac{\Delta\epsilon_p}{\epsilon_p}\right)^2 + \left(\frac{\Delta\epsilon_K}{\epsilon_K}\right)^2}, \tag{4.18}$$

where $\Delta\epsilon_{PID} = \Delta\epsilon_p/\epsilon_p = \Delta\epsilon_K/\epsilon_K$ is the quantity being tuned. Suitable values for $\Delta\epsilon_{PID}$ have been found to be 3% and 11% respectively at $p_T < 0.8\,\text{GeV}/c$ and $p_T \geq$

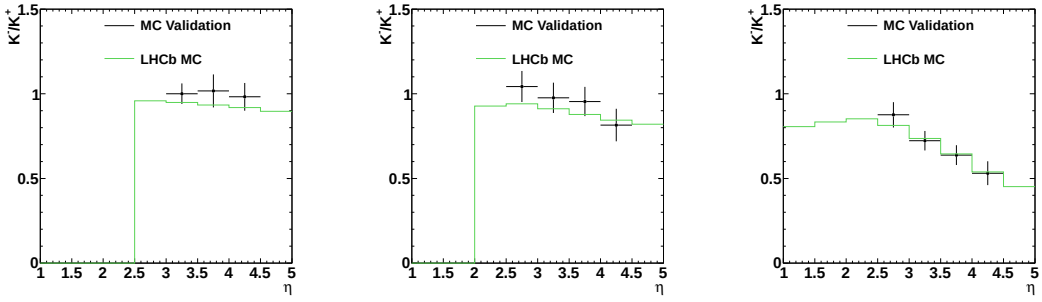
0.8 GeV/c. The scaling factors and uncertainties from these studies are adopted for the analysis of the data.

The fully corrected ratios in Figures 4.31-4.42, which include additional systematic uncertainties of the type described in Eq. 4.18, show good consistency between the measurement performed on MC and the generator-level predictions, validating the analysis procedure.



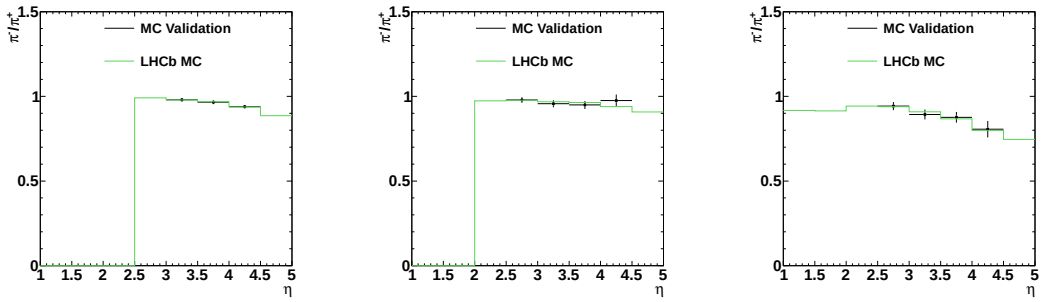
(a) $p_T < 0.8\,\text{GeV}/c$ (b) $0.8\,\text{GeV}/c \leq p_T < 1.2\,\text{GeV}/c$ (c) $p_T \geq 1.2\,\text{GeV}/c$

Figure 4.31: Comparison of the fully corrected $\bar{p}/p$ ratio in MC and the generator level prediction at $\sqrt{s} = 0.9\,\text{TeV}$.



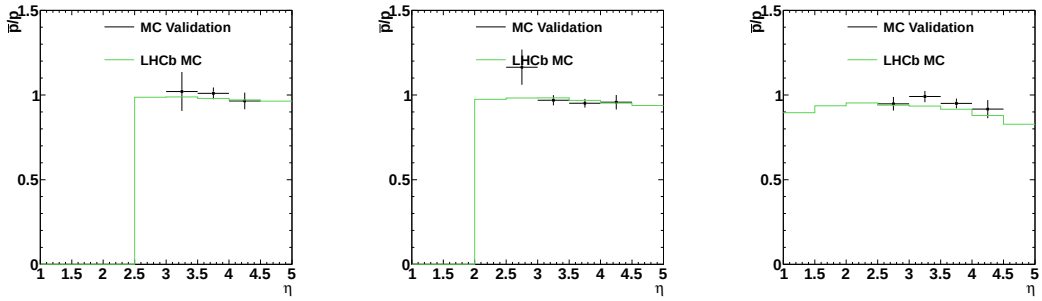
(a) $p_T < 0.8\,\text{GeV}/c$ (b) $0.8\,\text{GeV}/c \leq p_T < 1.2\,\text{GeV}/c$ (c) $p_T \geq 1.2\,\text{GeV}/c$

Figure 4.32: Comparison of the fully corrected K^-/K^+ ratio in MC and the generator level prediction at $\sqrt{s} = 0.9\,\text{TeV}$.



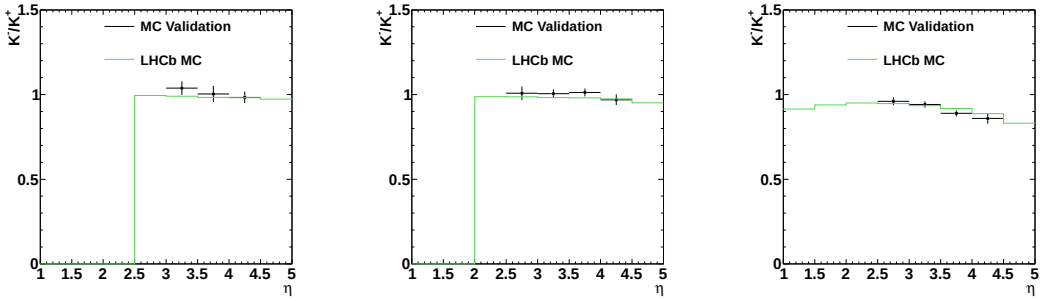
(a) $p_T < 0.8\,\mathrm{GeV}/c$ (b) $0.8\,\mathrm{GeV}/c \leq p_T < 1.2\,\mathrm{GeV}/c$ (c) $p_T \geq 1.2\,\mathrm{GeV}/c$

Figure 4.33: Comparison of the fully corrected π^-/π^+ ratio in MC and the generator level prediction at $\sqrt{\mathbf{s}} = 0.9\,\mathrm{TeV}$.



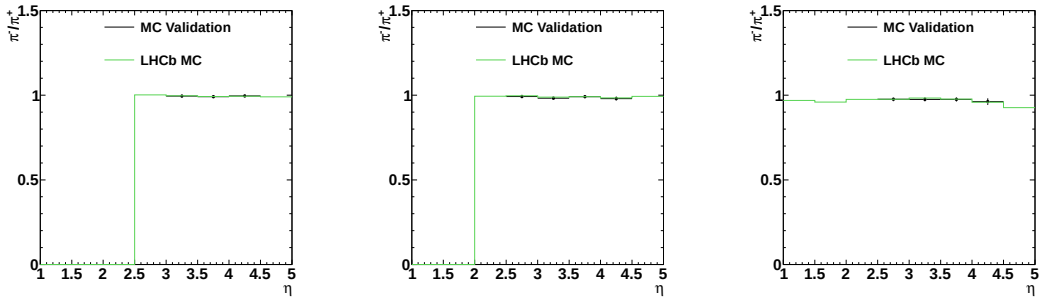
(a) $p_T < 0.8\,\mathrm{GeV}/c$ (b) $0.8\,\mathrm{GeV}/c \leq p_T < 1.2\,\mathrm{GeV}/c$ (c) $p_T \geq 1.2\,\mathrm{GeV}/c$

Figure 4.34: Comparison of the fully corrected $\bar{p}/p$ ratio in MC and the generator level prediction at $\sqrt{\mathbf{s}} = 7\,\mathrm{TeV}$.



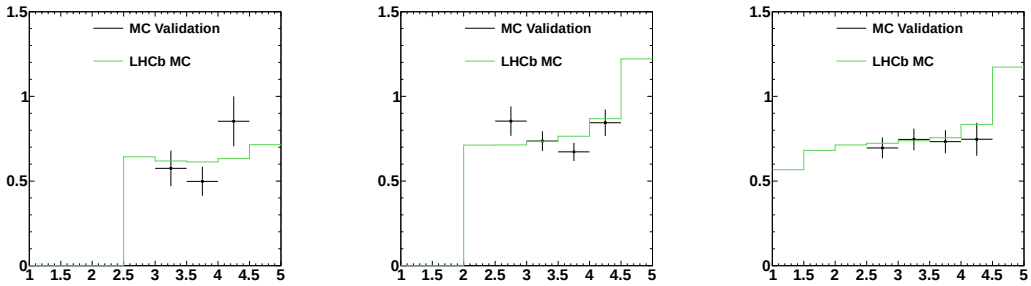
(a) $p_T < 0.8\,\mathrm{GeV}/c$ (b) $0.8\,\mathrm{GeV}/c \leq p_T < 1.2\,\mathrm{GeV}/c$ (c) $p_T \geq 1.2\,\mathrm{GeV}/c$

Figure 4.35: Comparison of the fully corrected K^-/K^+ ratio in MC and the generator level prediction at $\sqrt{\mathbf{s}} = 7\,\mathrm{TeV}$.



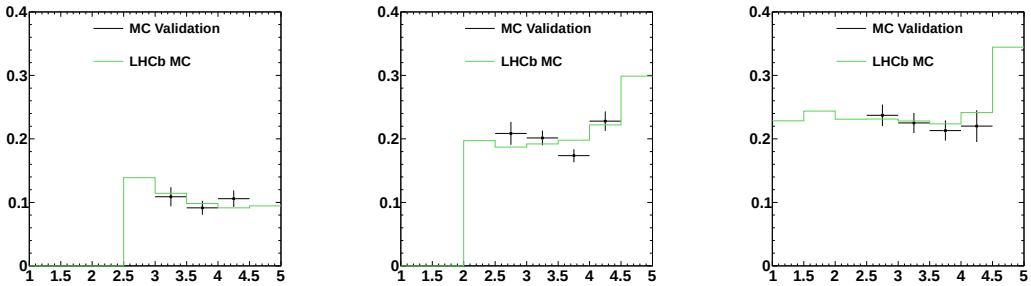
(a) $p_T < 0.8\,\mathrm{GeV}/c$ (b) $0.8\,\mathrm{GeV}/c \leq p_T < 1.2\,\mathrm{GeV}/c$ (c) $p_T \geq 1.2\,\mathrm{GeV}/c$

Figure 4.36: Comparison of the fully corrected π^-/π^+ ratio in MC and the generator level prediction at $\sqrt{\mathbf{s}} = 7\,\mathrm{TeV}$.



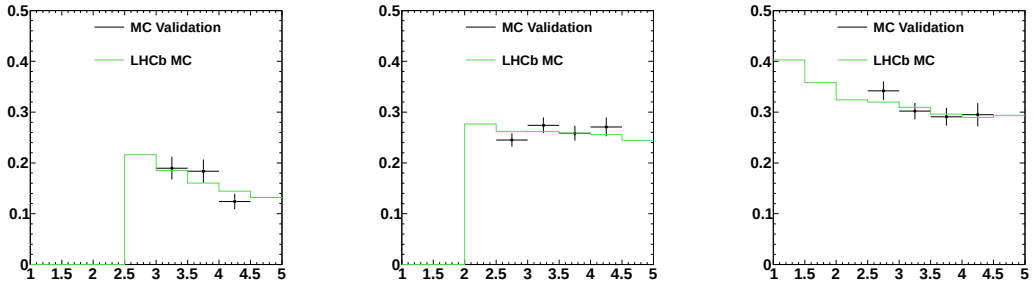
(a) $p_T < 0.8\,\mathrm{GeV}/c$ (b) $0.8\,\mathrm{GeV}/c \leq p_T < 1.2\,\mathrm{GeV}/c$ (c) $p_T \geq 1.2\,\mathrm{GeV}/c$

Figure 4.37: Comparison of the fully corrected $(p + \bar{p})/(K^+ + K^-)$ ratio in MC and the generator level prediction at $\sqrt{\mathbf{s}} = 0.9\,\mathrm{TeV}$.



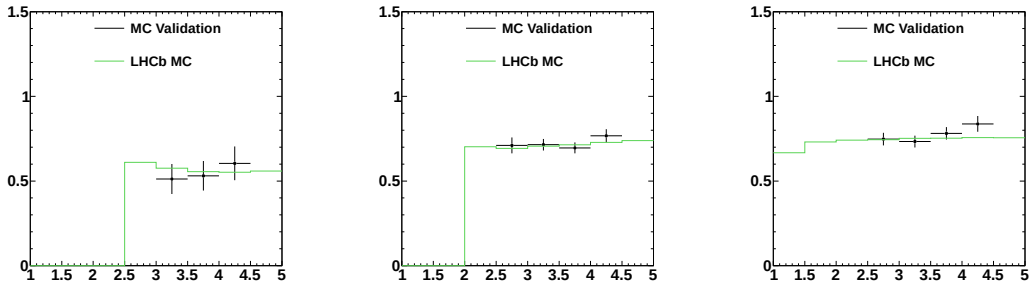
(a) $p_T < 0.8\,\mathrm{GeV}/c$ (b) $0.8\,\mathrm{GeV}/c \leq p_T < 1.2\,\mathrm{GeV}/c$ (c) $p_T \geq 1.2\,\mathrm{GeV}/c$

Figure 4.38: Comparison of the fully corrected $(p + \bar{p})/(\pi^+ + \pi^-)$ ratio in MC and the generator level prediction at $\sqrt{\mathbf{s}} = 0.9\,\mathrm{TeV}$.



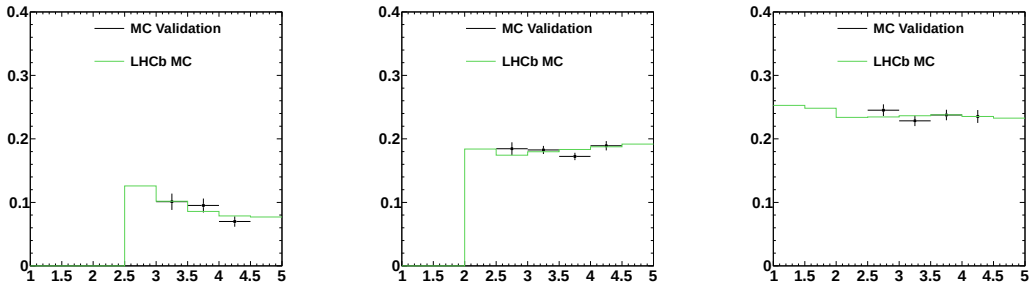
(a) $p_T < 0.8\,\mathrm{GeV}/c$ (b) $0.8\,\mathrm{GeV}/c \leq p_T < 1.2\,\mathrm{GeV}/c$ (c) $p_T \geq 1.2\,\mathrm{GeV}/c$

Figure 4.39: Comparison of the fully corrected $(K^+ + K^-)/(\pi^+ + \pi^-)$ ratio in MC and the generator level prediction at $\sqrt{\mathbf{s}} = 0.9\,\mathrm{TeV}$.



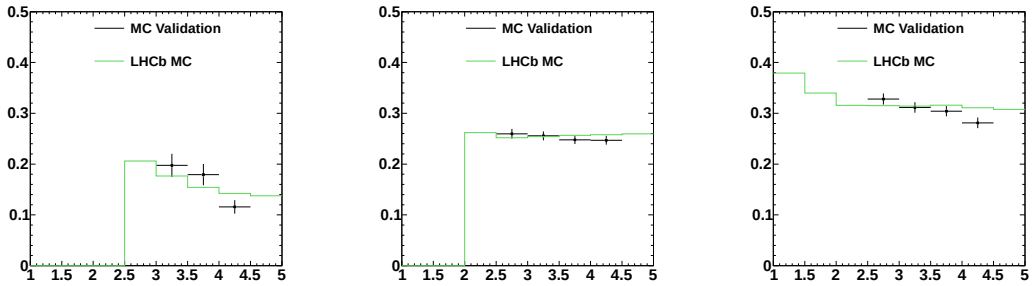
(a) $p_T < 0.8\,\mathrm{GeV}/c$ (b) $0.8\,\mathrm{GeV}/c \leq p_T < 1.2\,\mathrm{GeV}/c$ (c) $p_T \geq 1.2\,\mathrm{GeV}/c$

Figure 4.40: Comparison of the fully corrected $(p + \bar{p})/(K^+ + K^-)$ ratio in MC and the generator level prediction at $\sqrt{\mathbf{s}} = 7\,\mathrm{TeV}$.



(a) $p_T < 0.8\,\mathrm{GeV}/c$ (b) $0.8\,\mathrm{GeV}/c \leq p_T < 1.2\,\mathrm{GeV}/c$ (c) $p_T \geq 1.2\,\mathrm{GeV}/c$

Figure 4.41: Comparison of the fully corrected $(p + \bar{p})/(\pi^+ + \pi^-)$ ratio in MC and the generator level prediction at $\sqrt{\mathbf{s}} = 7\,\mathrm{TeV}$.



(a) $p_T < 0.8\,\mathrm{GeV}/c$ (b) $0.8\,\mathrm{GeV}/c \leq p_T < 1.2\,\mathrm{GeV}/c$ (c) $p_T \geq 1.2\,\mathrm{GeV}/c$

Figure 4.42: Comparison of the fully corrected $(K^+ + K^-)/(\pi^+ + \pi^-)$ ratio in MC and the generator level prediction at $\sqrt{\mathbf{s}} = 7\,\mathrm{TeV}$.

The study of the full analysis procedure in MC shows that it possible to recover the generator level ratios within the uncertainties of the method. In the next chapter, the sources of systematic uncertainties are investigated and the final measurements are presented.

Chapter 5

Hadron Ratios - Systematic Uncertainties and Results

5.1 Introduction

This chapter presents the sources of systematic uncertainty for the hadron ratio measurements, with robustness checks of the analysis procedure. The results for all the production ratios are also given.

5.2 Systematic Uncertainties

In this section, an overview of the systematic uncertainties affecting the production ratio measurements is given.

5.2.1 PID

The PID corrections carry the uncertainty of the identification efficiencies derived from the calibration samples. The uncertainties due to the statistics of the observed particles in data and those that come from the PID efficiencies are considered separately. Additional PID systematic uncertainties are assigned to the proton and kaon identification efficiencies to take into account residual biases in the analysis validation, as outlined in Section 4.8. The estimation of the PID efficiencies are the dominant contribution of

uncertainties in the ratios.

5.2.2 Detector Description in MC

Differences in the amount of material present in the simulation and in the real detector can bias the determination of the reconstruction efficiency, having a direct impact on the final result. Particles of different species and charge interact with the detector in different ways (e.g. through unequal interaction cross sections in the detector material). Hence any bias introduced by a non-optimal detector description in the MC may not completely cancel in the final production ratio. Conservatively, when estimating the systematic uncertainty, it is assumed that the material is uniformly under (over) estimated by 10%. To translate this increase (decrease) into an uncertainty on a ratio, A/B, a determination of an alternative reconstruction efficiency is performed under the assumption that the difference in the reconstruction efficiency between particle A and particle B, in a given (p_T, η) bin, is due to the effect of material interactions. For each given bin, it is useful to define the quantity

$$\mathcal{A}_d = \left|\epsilon^A_{Rec} - \epsilon^B_{Rec}\right|, \tag{5.1}$$

where $\epsilon^{A(B)}_{Rec}$ is the reconstruction efficiency for particle A (B) as measured in the MC.

In order to determine the systematic uncertainty, the reconstruction efficiencies for A and B are varied by subtracting or adding the 10% uncertainty assigned to the detector description, Δ_{MC}, multiplied by $\mathcal{A}_d$. Four alternative efficiencies, two for each particle, are obtained

$$\epsilon^{A\pm}_{Rec} = \epsilon^A_{Rec} \pm \Delta_{MC}\mathcal{A}_d \tag{5.2}$$

$$\epsilon^{B\pm}_{Rec} = \epsilon^B_{Rec} \pm \Delta_{MC}\mathcal{A}_d. \tag{5.3}$$

By combining each of the efficiencies in Eq. 5.2 with one of those in Eq. 5.3 it is possible to calculate four alternative ratios. The maximum shift between these four alternative ratios from the ratio calculated using the unmodified efficiencies, ϵ^A_{Rec} and ϵ^B_{Rec}, is taken

as the systematic uncertainty. It is noted that if the reconstruction efficiency for A and B is the same, the systematic uncertainty is identically zero. In fact, in that case any bias would cancel exactly in the ratio. The partial or total cancellation of systematic uncertainties in the ratios is the main reason for the introduction of the factor $\mathcal{A}_d$. The systematic uncertainty assigned to the ratio is small, typically $\lesssim 1\%$.

5.2.3 Material Interaction Cross Sections

In addition to the detector description, there is an uncertainty in the agreement between the interaction cross sections implemented in the MC and the true cross sections. Proton and anti-proton interaction cross section data are limited in the momentum range of interest. For example, for a 20 GeV proton interacting with aluminium there is a 10% difference between the cross section implemented in the MC and the measured cross section (see Figure 4.27). Furthermore, for protons above $p > 5\,\mathrm{GeV}/c$ to which this analysis is restricted, there are differences at the 20% level between various extrapolations of the cross sections from the lower momentum range where data exist to higher momenta (see Figure 5.1). The conservative assumption of a $\pm 20\%$

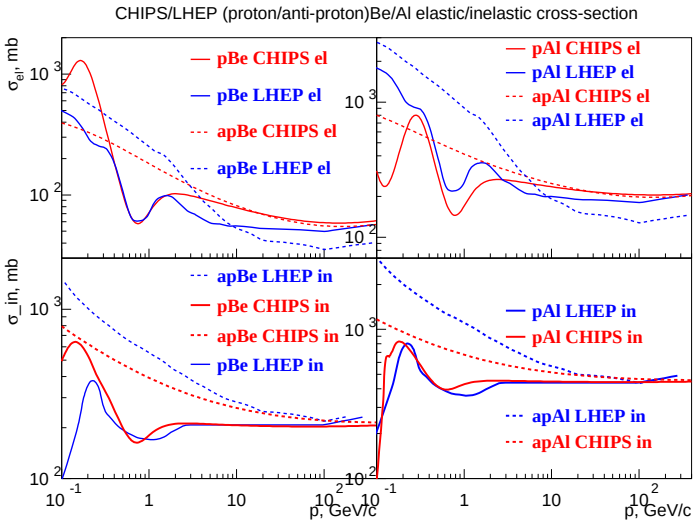


Figure 5.1: LHEP and CHIPS predictions for the inelastic and elastic cross sections of protons (antiprotons) on aluminium and beryllium as a function of momentum. Predictions for protons with a momentum above $5\,\mathrm{GeV}/c$ differ at the $\sim 20\%$ level.

uncertainty in the proton interaction cross sections implemented in the MC, $\Delta_{\sigma_{Int}}$, is

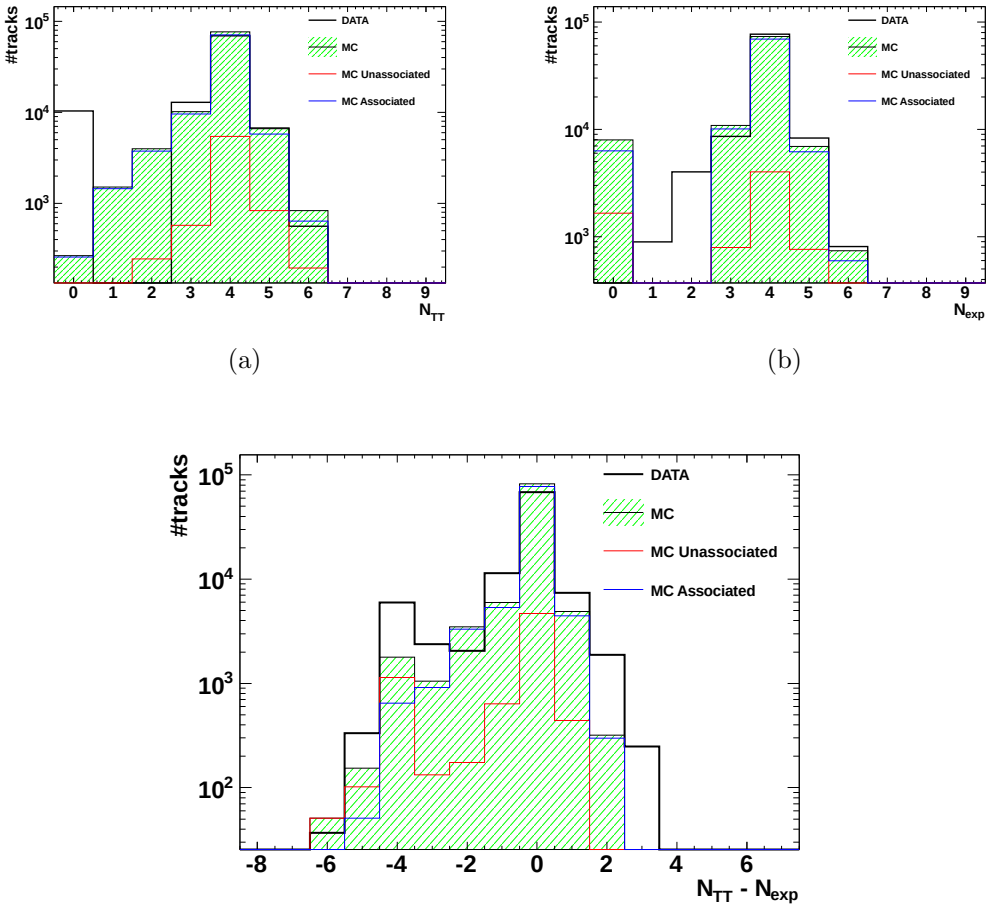
made. This is translated into an uncertainty on the ratio by calculating alternative reconstruction efficiencies using the $\mathcal{A}_d$ method, as described in the previous section, with the substitution $\Delta_{MC} \rightarrow \Delta_{\sigma_{Int}}$. The same uncertainty, $\pm 20\%$ is conservatively assigned to kaons. The data for the cross sections for $\pi^{\pm}$ exist at the momentum range of interest and show better agreement with MC, therefore the uncertainty for pions is reduced to 5%. The same method is used for ratios of different particle species, but the relevant uncertainties are combined in quadrature. The resulting systematic uncertainty on the final ratio is of order 1% (on average) for the antiparticle/particle ratios. The uncertainty for the production ratios of different particle species, which may differ significantly in the reconstruction efficiency, particularly at low momentum, is about a factor 2 larger.

5.2.4 Ghost Tracks

Track reconstruction algorithms in LHCb associate hits in the various tracking sub-detectors to form tracks. This procedure is normally very efficient but leads to a fraction of tracks being "fakes" or "ghosts" originating from wrongly associated hits that were not produced by one single particle. Ghosts are indistinguishable from true tracks on a track-by-track basis so that their statistical contribution must be estimated. In general, the ghost rate depends on the detector performance and design.

A method based on information from the TT which does not rely completely on the MC has been developed. The TT information is not used in the long track reconstruction and provides an independent check against fakes since ghost tracks should not produce any hits in the TT. The relevant quantity considered is the difference between the number of associated TT hits and the expected number of TT hits (estimated from the track properties and position within the detector), $N_{diff} = N_{TT} - N_{exp}$. For an example (η, p_T) bin, Figure 5.2 shows the distribution of N_{diff} for the pion analysis sample in data, and in MC for reconstructed tracks that may or may not be associated to a particle at the generator level. It is noted that N_{TT} and N_{exp} peak at 4 hits, which is the number of TT layers traversed by long tracks. Therefore, a genuine long track is

expected to hit four TT silicon pads on average. Conversely, fake long tracks, should leave no hits in the TT, and peak at $N_{diff} = -4$. In order to quantify the ghost-track contribution, two regions in N_{diff} are identified: the region $N_{diff} < -2$, where a clear peak from ghosts for unassociated tracks is visible, and the region $N_{diff} > -2$, where most of the genuine tracks lie (unassociated tracks in this region are not to be considered ghosts, but simple inefficiencies in the MC association algorithm). The fraction



(a) (b)

(c)

Figure 5.2: Distributions of (a) N_{TT}, (b) N_{exp} and (c) $N_{diff} = N_{TT} - N_{exp}$ for tracks in the pion analysis with a measured momentum below the Cherenkov threshold for pions with $3.5 < \eta < 4.0$ and $0.8 < p_T < 1.2\,\text{GeV}$.

of ghost tracks is estimated in MC as

$$f_g^{MC} = \frac{\#(tracks|N_{diff} < -2)_{NA}^{MC}}{\#tracks^{MC}}, \tag{5.4}$$

where $\#(tracks|N_{diff} < -2)^{MC}_{NA}$ is the number of unassociated tracks with $N_{diff} < -2$ and $\#tracks^{MC}$ the total number of tracks. The ghost fraction in data is calculated by scaling f_g^{MC} according to the relative numbers of tracks with $N_{diff} < -2$ in the two samples, so that

$$f_g^{data} = f_g^{MC} \times \frac{\left(\frac{\#(tracks|N_{diff}<-2)^{data}}{\#tracks^{data}}\right)}{\left(\frac{\#(tracks|N_{diff}<-2)^{MC}}{\#tracks^{MC}}\right)}. \tag{5.5}$$

where $\#(tracks|N_{diff} < -2)^{data}$ is the number of tracks with $N_{diff} < -2$ in data.

The ghost rate has an additional dependence on the fraction of tracks produced by particles travelling above or below the Cherenkov threshold. Photon hits in the RICH can be associated to a track using simple geometrical arguments. Therefore, samples of tracks above the threshold can benefit from a ghost suppression thanks to the additional requirement of associated photon hits in the RICH. In order to achieve a better estimation of the ghost rate in data, each of the analysis samples is divided into two sub-samples consisting of tracks above or below the threshold. Two separate ghost rates are then calculated for the two sub-samples and combined into a single rate, according to their relative contribution in the analysis sample:

$$F_g = f^{data}_{g,below} \times \left(\frac{\#tracks^{data}_{below}}{\#tracks^{data}}\right) + f^{data}_{g,above} \times \left(\frac{\#tracks^{data}_{above}}{\#tracks^{data}}\right), \tag{5.6}$$

where $f_{g,below(above)}$ is the ghost rate for tracks below (above) Cherenkov momentum threshold calculated using Eq. 5.5 and $\#tracks^{data}_{below(above)}$ is the fraction of tracks below (above) the Cherenkov threshold in data. The ghost rate defined above is determined separately for protons, kaons and pions of each charge and in each (p_T, η) bin.

A summary of ghost fractions in MC, the fractions of tracks above and below threshold, and ghost fractions in data are given in Appendix B for each bin at the two beam energies. The ghosts fractions are found to be $\lesssim 2\%$.

On average, ghost fractions in data are higher than in MC by a factor ~ 2. A similar conclusion can be inferred by a visual inspection of the relative peak height in the regions $N_{diff} < 2$ and $N_{diff} > 2$ in Figure 5.2. A systematic uncertainty is assigned to the final ratio by varying the reconstruction efficiency by $\mathcal{A}_d \times F_g$, as described in

Section 5.2.2. Typical values for this uncertainty are of the order of 1‰.

In order to perform a cross-check of the small magnitude of this uncertainty, different track $\chi^2/\#NDOF$ cuts have been considered. No significant difference is observed in the final ratios (Section 5.5), which confirms that systematic uncertainties due to ghosts are negligible.

5.2.5 Tracking Asymmetries

Several studies performed within the LHCb collaboration indicate no track reconstruction asymmetry between positive and negative particles. However, there is statistical limitation of these studies; the uncertainty on the asymmetry is estimated at 1% for the $\sqrt{\mathbf{s}} = 0.9\,\text{TeV}$ data and 0.5% for the $\sqrt{\mathbf{s}} = 7\,\text{TeV}$ data. If such an asymmetry did exist it would affect the relative acceptance between particles and antiparticles, for which a $\pm 1\%$ or $\pm 0.5\%$ systematic uncertainty is conservatively assigned to the $\sqrt{\mathbf{s}} = 0.9\,\text{TeV}$ and $\sqrt{\mathbf{s}} = 7\,\text{TeV}$ particle-antiparticle ratios respectively[1]. This uncertainty becomes negligible for the ratios of different hadron species, where particles of opposite charge are averaged.

5.2.6 Non-Prompt Contamination

As anticipated in Section 4.2, MC is used to correct the final ratios for the residual non-prompt particle contamination in the analysis samples. In a similar way as for other systematic uncertainties, the effect on the ratio cancels to first order. The same non-prompt fraction observed in the MC is considered for the data. Non-prompt fractions in MC, for each bin, are tabulated in Appendix C. The fractions are very similar for positive and negative tracks and hence the effect of contamination is usually negligible in the ratio. The systematic uncertainty in the final ratio is determined by varying the reconstruction efficiency by $\mathcal{A}_d$ multiplied by the non-prompt fraction determined from the MC, as described in Section 5.2.2. Typical values for this uncertainty are of the order of 1‰.

[1] LHCb tracking group, private communication Oct 2011.

Similarly, the impact on the analysis of different cut values for the $IP\chi^2/\#NDOF$ of the tracks have been investigated and has confirmed this conclusion.

5.2.7 Summary

A summary of the contributions from each source of uncertainty is given in Tables 5.1-5.2 for the $\sqrt{\mathbf{s}} = 0.9\,\text{TeV}$ data and Tables 5.3- 5.4 for the $\sqrt{\mathbf{s}} = 7\,\text{TeV}$ data. Expanded tables for each bin can be found in Appendix E. In all cases, the dominant source of systematic uncertainty is the PID.

Table 5.1: The range of systematic uncertainties for the $\bar{p}/p$, K^-/K^+ and π^-/π^+ ratios at $\sqrt{\mathbf{s}} = 0.90\,\text{TeV}$. All values given in %.

Source of uncertainty	$\bar{p}/p$	K^-/K^+	π^-/π^+
PID	7.48 - 46.66	4.86 - 42.42	0.77 - 5.95
Material interactions	0.18 - 1.58	0.13 - 1.45	0.02 - 0.39
MC detector description	0.09 - 0.79	0.06 - 0.73	0.04 - 0.78
Ghost tracks	0.01 - 0.11	0.01 - 0.06	0.00 - 0.08
Non-prompt contamination	0.02 - 0.23	0.01 - 0.06	0.01 - 0.14
Tracking asymmetry	1.00 - 1.00	1.00 - 1.00	1.00 - 1.00
Total systematic uncertainty	7.68 - 46.71	4.98 - 42.44	1.27 - 6.04

Table 5.2: The range of systematic uncertainties for the $(p+\bar{p})/(K^+ + K^-)$, $(p+\bar{p})/(\pi^+ + \pi^-)$ and $(K^+ + K^-)/(\pi^+ + \pi^-)$ ratios at $\sqrt{\mathbf{s}} = 0.9\,\text{TeV}$. Values are given in %.

Source of uncertainty	$(p+\bar{p})/(K^+ + K^-)$	$(p+\bar{p})/(\pi^+ + \pi^-)$	$(K^+ + K^-)/(\pi^+ + \pi^-)$
PID	10.23 - 63.68	8.14 - 46.80	5.94 - 42.56
Material interactions	0.11 - 2.23	0.46 - 1.36	0.21 - 2.48
MC detector description	0.04 - 0.79	0.22 - 0.66	0.10 - 1.20
Ghost tracks	0.00 - 0.12	0.02 - 0.08	0.01 - 0.08
Non-prompt contamination	0.01 - 0.20	0.05 - 0.12	0.01 - 0.13
Total systematic uncertainty	10.24 - 63.70	8.62 - 46.82	5.95 - 42.63

Table 5.3: The range of systematic uncertainties for the $\bar{p}/p$, K^-/K^+ and π^-/π^+ ratios at $\sqrt{\mathbf{s}} = 7.00\,\text{TeV}$. All values given in %.

Source of uncertainty	$\bar{p}/p$	K^-/K^+	π^-/π^+
PID	3.40 - 26.44	2.03 - 15.77	0.55 - 2.69
Material interactions	0.29 - 1.77	0.25 - 0.71	0.02 - 0.11
MC detector description	0.15 - 0.89	0.12 - 0.35	0.04 - 0.22
Ghost tracks	0.02 - 0.35	0.01 - 0.07	0.00 - 0.02
Non-prompt contamination	0.02 - 0.19	0.04 - 0.07	0.01 - 0.05
Tracking asymmetry	0.50 - 0.50	0.50 - 0.50	0.50 - 0.50
Total systematic uncertainty	3.48 - 26.52	2.14 - 15.80	0.75 - 2.75

Table 5.4: The range of systematic uncertainties for the $(p+\bar{p})/(K^+ + K^-)$, $(p+\bar{p})/(\pi^+ + \pi^-)$ and $(K^+ + K^-)/(\pi^+ + \pi^-)$ ratios at $\sqrt{\mathbf{s}} = 7.0\,\text{TeV}$. Values are given in %.

Source of uncertainty	$(p+\bar{p})/(K^+ + K^-)$	$(p+\bar{p})/(\pi^+ + \pi^-)$	$(K^+ + K^-)/(\pi^+ + \pi^-)$
PID	5.89 - 31.11	4.62 - 26.63	3.74 - 16.09
Material interactions	0.44 - 3.13	1.24 - 1.58	0.20 - 2.14
MC detector description	0.16 - 1.11	0.60 - 0.77	0.10 - 1.04
Ghost tracks	0.03 - 0.28	0.06 - 0.33	0.01 - 0.22
Non-prompt contamination	0.03 - 0.27	0.10 - 0.21	0.02 - 0.21
Total systematic uncertainty	6.08 - 31.11	4.84 - 26.70	3.74 - 16.25

5.3 Robustness Tests

5.3.1 Magnet Polarity

Differences between the ratio measurements performed with opposite polarities of the LHCb dipole magnet may lead to an additional systematic uncertainty in the ratios. The quantity that may reveal potential biases is the *pull*, defined as

$$pull = \frac{R_{\uparrow} - R_{\downarrow}}{\sqrt{\sigma_{\uparrow}^2 + \sigma_{\downarrow}^2}}, \tag{5.7}$$

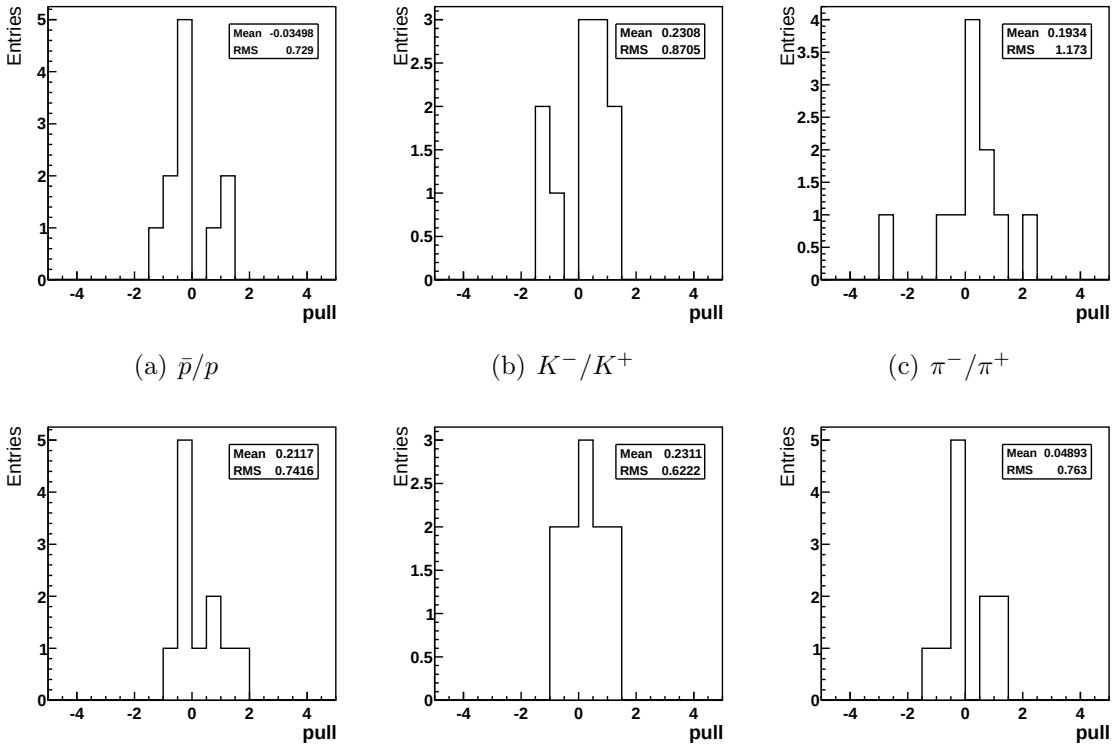
where $R_{\uparrow(\downarrow)}$ is a ratio measurement in a given (p_T, η) bin with magnet polarity up (down) and $\sigma_{\uparrow(\downarrow)}$ is its statistical uncertainty. A pull distributed as a Gaussian with mean zero and unit is index of good consistency between the two datasets. The pull distributions obtained for each p_T bin and a particular ratio are shown in Figures 5.3-5.4. It can be seen that the two datasets are broadly consistent and differences are not statistically significant. Therefore, we do not assign an associated systematic error.

5.3.2 Clone Tracks

The full analysis has been repeated using different requirements on the clone veto. It has been verified that reducing the cut to $d < 0.01$ (see Section 4.4.2) or removing completely the clone veto has a negligible impact on the final result. This is to be expected, since the clone rates for different particle species and charge are almost completely correlated. Therefore we do not assign a corresponding systematic uncertainty.

5.3.3 Diffractive Events Contribution

Experimentally it is not possible to distinguish between diffractive and non-diffractive events in LHCb. Therefore, in this analysis, no assumption is made on the nature of the initial pp collision. However, diffractive events are heavily suppressed by the PV requirement. In order to estimate the impact of diffractive events on the final result, the full analysis has been performed twice by explicitly removing or including



(a) $\bar{p}/p$ (b) K^-/K^+ (c) π^-/π^+

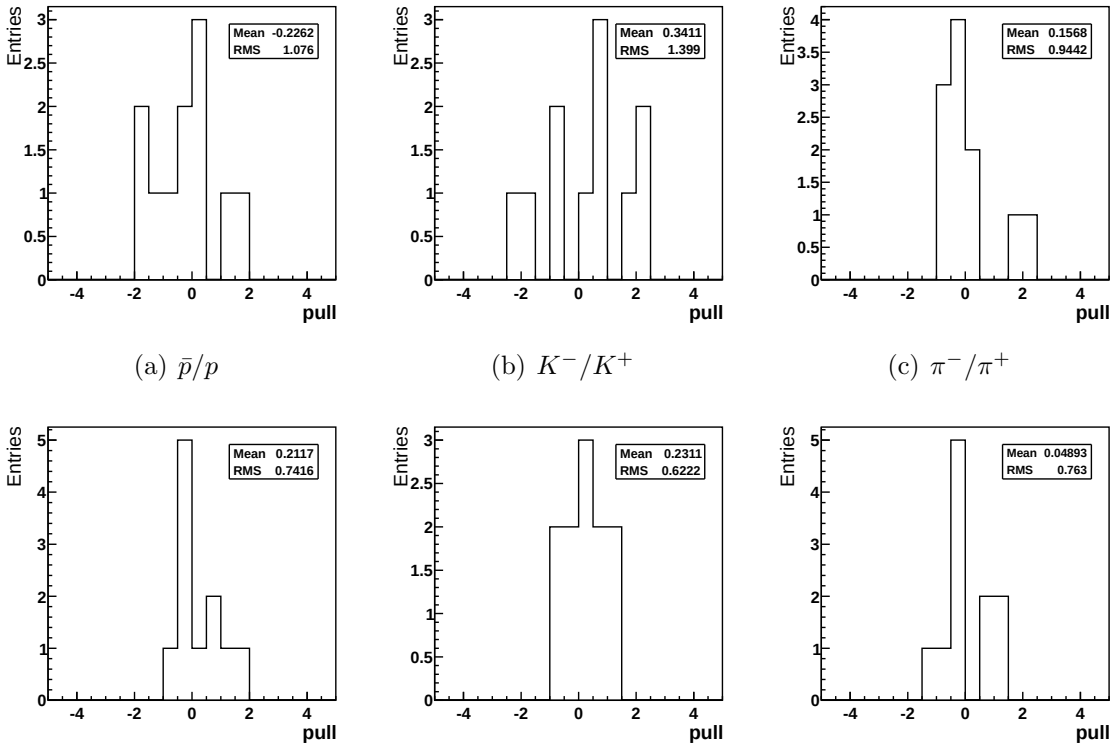
(d) $(p+\bar{p})/(K^+ + K^-)$ (e) $(p+\bar{p})/(\pi^+ + \pi^-)$ (f) $(K^+ + K^-)/(\pi^+ + \pi^-)$

Figure 5.3: Pull distribution at $\sqrt{\mathbf{s}} = 0.9\,\text{TeV}$ for magnet up and down.

diffractive events in the determination of the reconstruction efficiency in MC. The difference between the two ratio measurements is found to be compatible with zero within statistical errors.

5.3.4 Correlations

In the final measurement the results for magnet up and down have to be combined and correlations between uncertainties must be taken into account. Since the two datasets are statistically consistent, a weighted average is performed. The statistical uncertainties on the track sample and on the PID efficiencies are considered as completely uncorrelated whereas all the remaining systematics are treated as 100% correlated.



(a) $\bar{p}/p$ (b) K^-/K^+ (c) π^-/π^+

(d) $(p+\bar{p})/(K^+ + K^-)$ (e) $(p+\bar{p})/(\pi^+ + \pi^-)$ (f) $(K^+ + K^-)/(\pi^+ + \pi^-)$

Figure 5.4: Pull distribution at $\sqrt{\mathbf{s}} = 7\,\text{TeV}$ for magnet up and down.

5.4 Translating the Results from Pseudo-Rapidity to Rapidity

The analysis is performed in bins of pseudo-rapidity, however, it is interesting to interpret the results also in terms of rapidity, y. The results are therefore re-expressed as a function of y using the procedure below.

In each bin of η, for all the selected candidates, the rapidity is calculated. The mean and RMS rapidity is then determined for that η bin. However, for interpreting the final results, it is necessary to know how the mean rapidity is biased by reconstruction effects. Therefore the procedure was repeated on MC events, both for those tracks passing the reconstruction, and for the generated particles satisfying the kinematic requirements prior to reconstruction. The differences between these two sets of results in the MC were applied as corrections to the data values. The results are given in Appendix D. It can be seen that the reconstructed mean y are similar in data and MC and that the

reconstruction biases are small.

It is noted that, whilst η is a purely geometrical variable, y depends on the mass of a particle. In other words, two particles of different species with the same η have a different y. Moreover, for the procedure to be consistent, it is required that the two samples of particles involved in the ratio, within each η bin, have the same average y. Therefore, this procedure can only be applied to the antiparticle/particle ratios.

5.5 Results

The results for the $\bar{p}/p$, K^-/K^+, π^-/π^+, $(p+\bar{p})/(K^+ + K^-)$, $(p+\bar{p})/(\pi^+ + \pi^-)$ and $(K^+ + K^-)/(\pi^+ + \pi^-)$ ratios and associated uncertainties as a function of η are given in Tables 5.5- 5.16.

Table 5.5: The $\bar{p}/p$ ratio and uncertainty (statistical + systematic) for data taken at $\sqrt{\mathbf{s}} = 0.9\,\text{TeV}$ as a function of η.

η	$p_T < 0.8$	$0.8 < p_T < 1.2$	$p_T > 1.2$
$2 < \eta < 2.5$	-	-	-
$2.5 < \eta < 3$	-	$1.107 \pm 0.020 \pm 0.349$	$0.794 \pm 0.015 \pm 0.089$
$3 < \eta < 3.5$	$0.751 \pm 0.011 \pm 0.163$	$0.684 \pm 0.010 \pm 0.049$	$0.614 \pm 0.010 \pm 0.047$
$3.5 < \eta < 4$	$0.729 \pm 0.007 \pm 0.040$	$0.576 \pm 0.007 \pm 0.032$	$0.456 \pm 0.009 \pm 0.033$
$4 < \eta < 4.5$	$0.660 \pm 0.009 \pm 0.046$	$0.451 \pm 0.009 \pm 0.038$	$0.328 \pm 0.010 \pm 0.049$
$4.5 < \eta < 5$	-	-	-

Table 5.6: The K^-/K^+ ratio and uncertainty (statistical + systematic) for data taken at $\sqrt{\mathbf{s}} = 0.9\,\text{TeV}$ as a function of η.

η	$p_T < 0.8$	$0.8 < p_T < 1.2$	$p_T > 1.2$
$2 < \eta < 2.5$	-	-	-
$2.5 < \eta < 3$	-	$0.870 \pm 0.010 \pm 0.267$	$0.936 \pm 0.013 \pm 0.069$
$3 < \eta < 3.5$	$0.834 \pm 0.007 \pm 0.069$	$0.847 \pm 0.009 \pm 0.040$	$0.783 \pm 0.011 \pm 0.037$
$3.5 < \eta < 4$	$1.001 \pm 0.007 \pm 0.064$	$0.792 \pm 0.009 \pm 0.028$	$0.723 \pm 0.012 \pm 0.031$
$4 < \eta < 4.5$	$1.002 \pm 0.007 \pm 0.093$	$0.680 \pm 0.010 \pm 0.041$	$0.506 \pm 0.014 \pm 0.050$
$4.5 < \eta < 5$	-	-	-

Table 5.7: The π^-/π^+ ratio and uncertainty (statistical + systematic) for data taken at $\sqrt{\mathbf{s}} = 0.9\,\text{TeV}$ as a function of η.

η	$p_T < 0.8$	$0.8 < p_T < 1.2$	$p_T > 1.2$
$2 < \eta < 2.5$	-	-	-
$2.5 < \eta < 3$	-	$0.987 \pm 0.010 \pm 0.013$	$0.970 \pm 0.016 \pm 0.014$
$3 < \eta < 3.5$	$0.979 \pm 0.005 \pm 0.010$	$0.971 \pm 0.011 \pm 0.010$	$0.926 \pm 0.017 \pm 0.014$
$3.5 < \eta < 4$	$0.968 \pm 0.004 \pm 0.011$	$0.951 \pm 0.012 \pm 0.010$	$0.871 \pm 0.019 \pm 0.012$
$4 < \eta < 4.5$	$0.928 \pm 0.004 \pm 0.015$	$0.971 \pm 0.016 \pm 0.018$	$0.816 \pm 0.025 \pm 0.029$
$4.5 < \eta < 5$	-	-	-

For the majority of the bins there is a total uncertainty of around 5%. In some bins the uncertainty is larger due to low statistics being available either in the analysis

Table 5.8: The $\bar{p}/p$ ratio and uncertainty (statistical + systematic) for data taken at $\sqrt{\mathbf{s}} = 7.0\,\text{TeV}$ as a function of η.

η	$p_T < 0.8$	$0.8 < p_T < 1.2$	$p_T > 1.2$
$2 < \eta < 2.5$	-	-	-
$2.5 < \eta < 3$	-	$1.181 \pm 0.020 \pm 0.195$	$0.880 \pm 0.009 \pm 0.039$
$3 < \eta < 3.5$	$0.734 \pm 0.011 \pm 0.124$	$0.942 \pm 0.011 \pm 0.036$	$0.905 \pm 0.008 \pm 0.026$
$3.5 < \eta < 4$	$1.015 \pm 0.009 \pm 0.037$	$0.916 \pm 0.007 \pm 0.022$	$0.903 \pm 0.008 \pm 0.023$
$4 < \eta < 4.5$	$0.957 \pm 0.010 \pm 0.051$	$0.906 \pm 0.010 \pm 0.039$	$0.831 \pm 0.010 \pm 0.050$
$4.5 < \eta < 5$	-	-	-

Table 5.9: The K^-/K^+ ratio and uncertainty (statistical + systematic) for data taken at $\sqrt{\mathbf{s}} = 7.0\,\text{TeV}$ as a function of η.

η	$p_T < 0.8$	$0.8 < p_T < 1.2$	$p_T > 1.2$
$2 < \eta < 2.5$	-	-	-
$2.5 < \eta < 3$	-	$0.995 \pm 0.008 \pm 0.101$	$0.991 \pm 0.007 \pm 0.021$
$3 < \eta < 3.5$	$0.992 \pm 0.006 \pm 0.063$	$0.966 \pm 0.006 \pm 0.019$	$0.999 \pm 0.006 \pm 0.016$
$3.5 < \eta < 4$	$1.062 \pm 0.005 \pm 0.040$	$0.948 \pm 0.006 \pm 0.014$	$0.930 \pm 0.006 \pm 0.017$
$4 < \eta < 4.5$	$1.161 \pm 0.005 \pm 0.055$	$0.898 \pm 0.006 \pm 0.025$	$0.958 \pm 0.009 \pm 0.049$
$4.5 < \eta < 5$	-	-	-

Table 5.10: The π^-/π^+ ratio and uncertainty (statistical + systematic) for data taken at $\sqrt{\mathbf{s}} = 7.0\,\text{TeV}$ as a function of η.

η	$p_T < 0.8$	$0.8 < p_T < 1.2$	$p_T > 1.2$
$2 < \eta < 2.5$	-	-	-
$2.5 < \eta < 3$	-	$1.002 \pm 0.007 \pm 0.006$	$1.015 \pm 0.010 \pm 0.005$
$3 < \eta < 3.5$	$1.011 \pm 0.004 \pm 0.006$	$0.998 \pm 0.007 \pm 0.004$	$0.998 \pm 0.010 \pm 0.004$
$3.5 < \eta < 4$	$1.002 \pm 0.003 \pm 0.006$	$1.003 \pm 0.008 \pm 0.003$	$1.000 \pm 0.011 \pm 0.005$
$4 < \eta < 4.5$	$0.976 \pm 0.003 \pm 0.006$	$0.998 \pm 0.009 \pm 0.008$	$0.974 \pm 0.012 \pm 0.017$
$4.5 < \eta < 5$	-	-	-

Table 5.11: The $(p+\bar{p})/(K^+ + K^-)$ ratio and uncertainty (statistical + systematic) for data taken at $\sqrt{\mathbf{s}} = 0.9\,\text{TeV}$ as a function of η.

η	$p_T < 0.8$	$0.8 < p_T < 1.2$	$p_T > 1.2$
$2 < \eta < 2.5$	-	-	-
$2.5 < \eta < 3$	-	$1.831 \pm 0.039 \pm 0.822$	$0.855 \pm 0.020 \pm 0.119$
$3 < \eta < 3.5$	$0.481 \pm 0.008 \pm 0.139$	$0.779 \pm 0.014 \pm 0.073$	$0.851 \pm 0.019 \pm 0.084$
$3.5 < \eta < 4$	$0.363 \pm 0.004 \pm 0.066$	$0.709 \pm 0.012 \pm 0.055$	$0.799 \pm 0.021 \pm 0.076$
$4 < \eta < 4.5$	$0.433 \pm 0.007 \pm 0.086$	$0.865 \pm 0.021 \pm 0.098$	$1.067 \pm 0.045 \pm 0.200$
$4.5 < \eta < 5$	-	-	-

Table 5.12: The $(p+\bar{p})/(\pi^+ + \pi^-)$ ratio and uncertainty (statistical + systematic) for data taken at $\sqrt{\mathbf{s}} = 0.9\,\text{TeV}$ as a function of η.

η	$p_T < 0.8$	$0.8 < p_T < 1.2$	$p_T > 1.2$
$2 < \eta < 2.5$	-	-	-
$2.5 < \eta < 3$	-	$0.328 \pm 0.007 \pm 0.104$	$0.300 \pm 0.008 \pm 0.035$
$3 < \eta < 3.5$	$0.086 \pm 0.001 \pm 0.021$	$0.208 \pm 0.004 \pm 0.016$	$0.272 \pm 0.007 \pm 0.023$
$3.5 < \eta < 4$	$0.062 \pm 0.001 \pm 0.008$	$0.175 \pm 0.003 \pm 0.011$	$0.252 \pm 0.007 \pm 0.020$
$4 < \eta < 4.5$	$0.076 \pm 0.001 \pm 0.010$	$0.233 \pm 0.006 \pm 0.022$	$0.301 \pm 0.013 \pm 0.047$
$4.5 < \eta < 5$	-	-	-

Table 5.13: The $(K^+ + K^-)/(\pi^+ + \pi^-)$ ratio and uncertainty (statistical + systematic) for data taken at $\sqrt{\mathbf{s}} = 0.9\,\text{TeV}$ as a function of η.

η	$p_T < 0.8$	$0.8 < p_T < 1.2$	$p_T > 1.2$
$2 < \eta < 2.5$	-	-	-
$2.5 < \eta < 3$	-	$0.184 \pm 0.003 \pm 0.056$	$0.351 \pm 0.008 \pm 0.028$
$3 < \eta < 3.5$	$0.180 \pm 0.002 \pm 0.026$	$0.267 \pm 0.004 \pm 0.015$	$0.319 \pm 0.008 \pm 0.018$
$3.5 < \eta < 4$	$0.171 \pm 0.001 \pm 0.023$	$0.247 \pm 0.004 \pm 0.011$	$0.314 \pm 0.009 \pm 0.017$
$4 < \eta < 4.5$	$0.173 \pm 0.001 \pm 0.025$	$0.268 \pm 0.006 \pm 0.018$	$0.281 \pm 0.012 \pm 0.031$
$4.5 < \eta < 5$	-	-	-

Table 5.14: The $(p+\bar{p})/(K^+ + K^-)$ ratio and uncertainty (statistical + systematic) for data taken at $\sqrt{\mathbf{s}} = 7.0\,\text{TeV}$ as a function of η.

η	$p_T < 0.8$	$0.8 < p_T < 1.2$	$p_T > 1.2$
$2 < \eta < 2.5$	-	-	-
$2.5 < \eta < 3$	-	$1.051 \pm 0.020 \pm 0.204$	$0.705 \pm 0.009 \pm 0.047$
$3 < \eta < 3.5$	$0.465 \pm 0.008 \pm 0.111$	$0.660 \pm 0.009 \pm 0.039$	$0.682 \pm 0.007 \pm 0.039$
$3.5 < \eta < 4$	$0.398 \pm 0.004 \pm 0.067$	$0.593 \pm 0.006 \pm 0.032$	$0.659 \pm 0.007 \pm 0.039$
$4 < \eta < 4.5$	$0.379 \pm 0.004 \pm 0.068$	$0.670 \pm 0.009 \pm 0.047$	$0.744 \pm 0.011 \pm 0.071$
$4.5 < \eta < 5$	-	-	-

Table 5.15: The $(p+\bar{p})/(\pi^+ + \pi^-)$ ratio and uncertainty (statistical + systematic) for data taken at $\sqrt{\mathbf{s}} = 7.0\,\text{TeV}$ as a function of η.

η	$p_T < 0.8$	$0.8 < p_T < 1.2$	$p_T > 1.2$
$2 < \eta < 2.5$	-	-	-
$2.5 < \eta < 3$	-	$0.235 \pm 0.004 \pm 0.039$	$0.262 \pm 0.004 \pm 0.014$
$3 < \eta < 3.5$	$0.085 \pm 0.001 \pm 0.017$	$0.174 \pm 0.002 \pm 0.009$	$0.245 \pm 0.003 \pm 0.011$
$3.5 < \eta < 4$	$0.069 \pm 0.001 \pm 0.008$	$0.156 \pm 0.002 \pm 0.006$	$0.242 \pm 0.003 \pm 0.010$
$4 < \eta < 4.5$	$0.051 \pm 0.001 \pm 0.007$	$0.184 \pm 0.003 \pm 0.010$	$0.244 \pm 0.004 \pm 0.017$
$4.5 < \eta < 5$	-	-	-

Table 5.16: The $(K^+ + K^-)/(\pi^+ + \pi^-)$ ratio and uncertainty (statistical + systematic) for data taken at $\sqrt{\mathbf{s}} = 7.0\,\text{TeV}$ as a function of η.

η	$p_T < 0.8$	$0.8 < p_T < 1.2$	$p_T > 1.2$
$2 < \eta < 2.5$	-	-	-
$2.5 < \eta < 3$	-	$0.224 \pm 0.002 \pm 0.024$	$0.371 \pm 0.004 \pm 0.014$
$3 < \eta < 3.5$	$0.181 \pm 0.001 \pm 0.024$	$0.263 \pm 0.003 \pm 0.010$	$0.357 \pm 0.004 \pm 0.012$
$3.5 < \eta < 4$	$0.173 \pm 0.001 \pm 0.021$	$0.262 \pm 0.003 \pm 0.009$	$0.367 \pm 0.005 \pm 0.013$
$4 < \eta < 4.5$	$0.131 \pm 0.001 \pm 0.016$	$0.275 \pm 0.003 \pm 0.011$	$0.328 \pm 0.005 \pm 0.020$
$4.5 < \eta < 5$	-	-	-

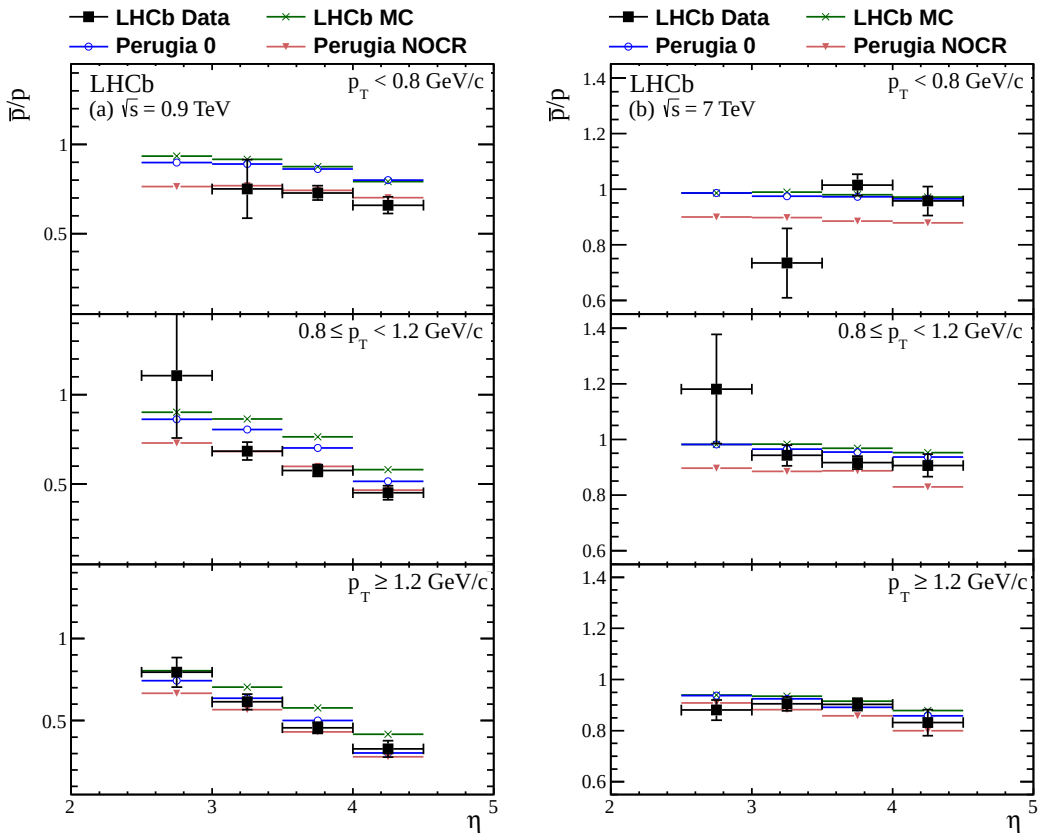
sample itself, or the RICH calibration sample. These ratios are plotted in Figures 5.5-5.10 as a function of η. MC predictions from the LHCb MC [29], comparing the Perugia-0 and Perugia-NOCR (without colour reconnection) PYTHIA tunes [63], are also shown.

The antiparticle/particle ratios at $\sqrt{\mathbf{s}} = 0.9\,\text{TeV}$ show a significant dependence on η, which is particularly pronounced for $\bar{p}/p$. This behaviour is similar to that expected from the MC model predictions, but the quantitative agreement with data is not perfect, particularly for $\bar{p}/p$, where the Perugia-NOCR tune gives the best prediction and the BNT is underestimated by other models. At $\sqrt{\mathbf{s}} = 7\,\text{TeV}$ these ratios are closer to unity, evolve less rapidly with η, and are well predicted by all PYTHIA tunings.

Results for $(p+\bar{p})/(K^+ + K^-)$, $(p+\bar{p})/(\pi^+ + \pi^-)$ and $(K^+ + K^-)/(\pi^+ + \pi^-)$ ratios show in general a slight p_T dependence and are not well described by the tunes except for the LHCb MC.

5.5.1 Baryon Number Transport in the $\bar{p}/p$ Ratio.

As seen in Chapter 1, the study of the $\bar{p}/p$ ratio provides information on the BNT. Several measurements have been performed by other collaborations such as ALICE [27], PHOBOS [64], STAR [65], PHENIX [66] and BRAHMS [67]. It is convenient to interpret the results in terms of the *rapidity loss* (or *rapidity gap*) $\Delta y = y_{beam} - y_{p(\bar{p})}$, where y_{beam} is the rapidity of the colliding protons moving towards the positive z axis in the LHCb reference frame and $y_{p(\bar{p})}$ is the rapidity of the outgoing proton (antiproton). In this way, data points corresponding to different kinematic regimes and experiments

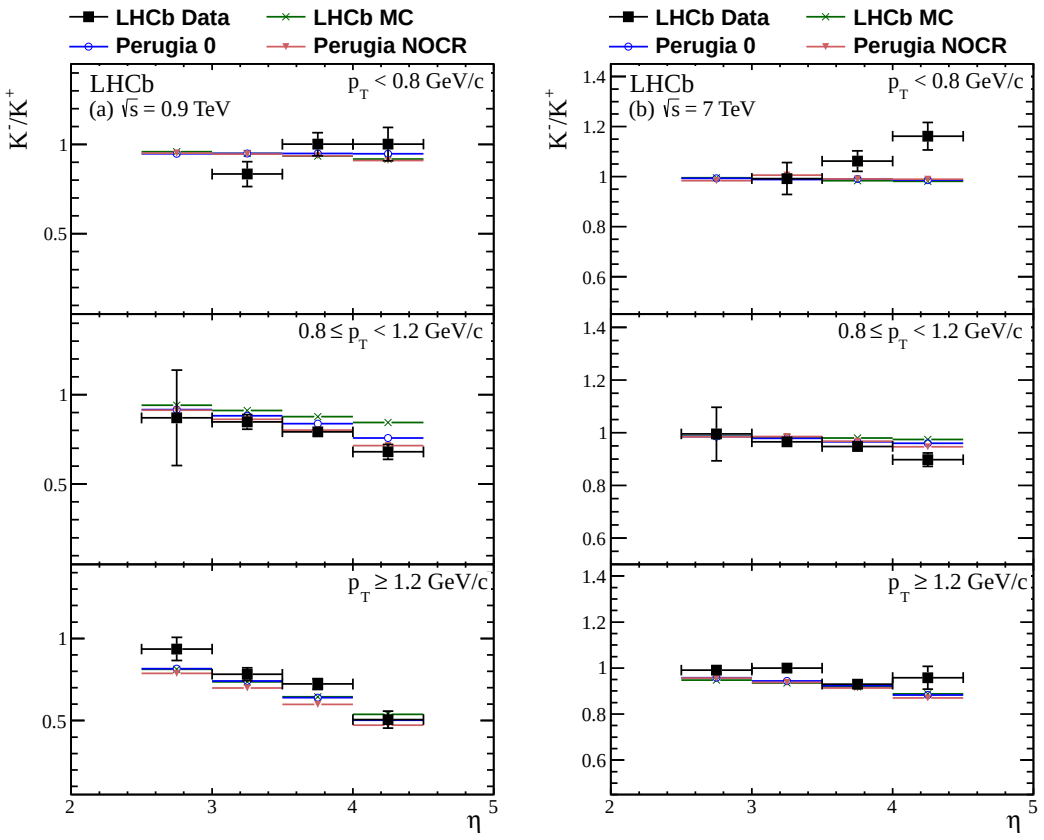


(a) $\sqrt{s} = 0.9\,\text{TeV}$ (b) $\sqrt{s} = 7\,\text{TeV}$

Figure 5.5: $\bar{p}/p$ ratio and total uncertainty as a function of pseudo-rapidity.

can be visualised in the same plot. The $\bar{p}/p$ ratio as a function of Δy is shown in Figure 5.11. The LHCb data are in agreement with other measurements in the same Δy range, although significantly more precise. It is interesting to notice that the ratio tends to ~ 1 towards high Δy. This suggests that the baryon number information of the initial state can be carried over a limited range of rapidity loss. In fact, it is naively expected that the higher the Δy value, the harder (on average) the primary pp interaction, and hence higher the chance that the information on the baryon number is lost.

Furthermore, it is noted that the LHCb data do not indicate any significant dependence on the transverse momentum. Therefore a weighted mean over the transverse momentum for data points in the same bin of pseudo-rapidity has been performed. The p_T-averaged results, shown in Figure 5.12 and summarised in Table 5.17, exhibit



(a) $\sqrt{s} = 0.9$ TeV (b) $\sqrt{s} = 7$ TeV

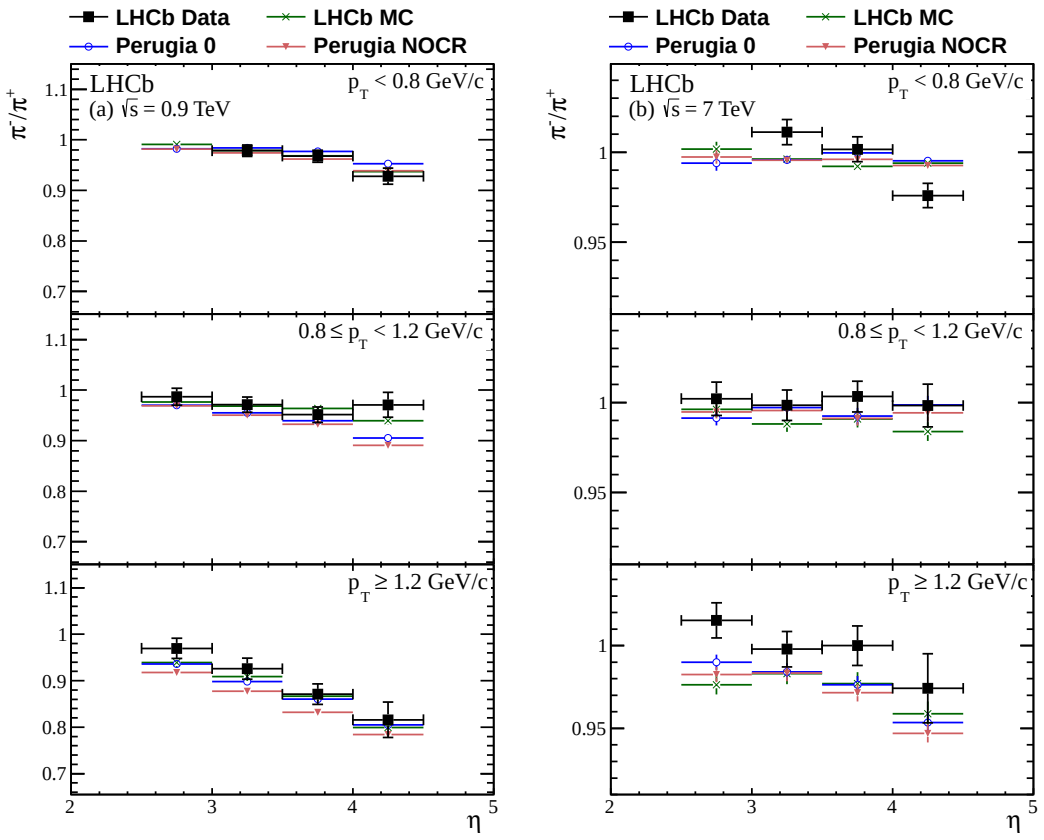
Figure 5.6: K^-/K^+ ratio and total uncertainty as a function of pseudo-rapidity.

more clearly the higher precision of the LHCb measurements with respect to those of the other experiments.

Table 5.17: The $\bar{p}/p$ ratio and uncertainty averaged in p_T as a function of the rapidity loss, Δy.

$\sqrt{s}$	η range	Δy	ratio
0.9 TeV	$4 - 4.5$	3.1 ± 0.2	0.48 ± 0.03
	$3.5 - 4$	3.5 ± 0.2	0.57 ± 0.02
	$3 - 3.5$	3.9 ± 0.2	0.65 ± 0.03
	$2.5 - 3$	4.2 ± 0.1	0.81 ± 0.09
7 TeV	$4 - 4.5$	5.1 ± 0.2	0.90 ± 0.03
	$3.5 - 4$	5.5 ± 0.2	0.92 ± 0.02
	$3 - 3.5$	5.9 ± 0.2	0.91 ± 0.02
	$2.5 - 3$	6.3 ± 0.1	0.89 ± 0.04

Finally, the p_T-averaged data can be exploited to investigate the mechanisms that are responsible for the BNT. As described in [20], the Δy dependence of the $\bar{p}/p$



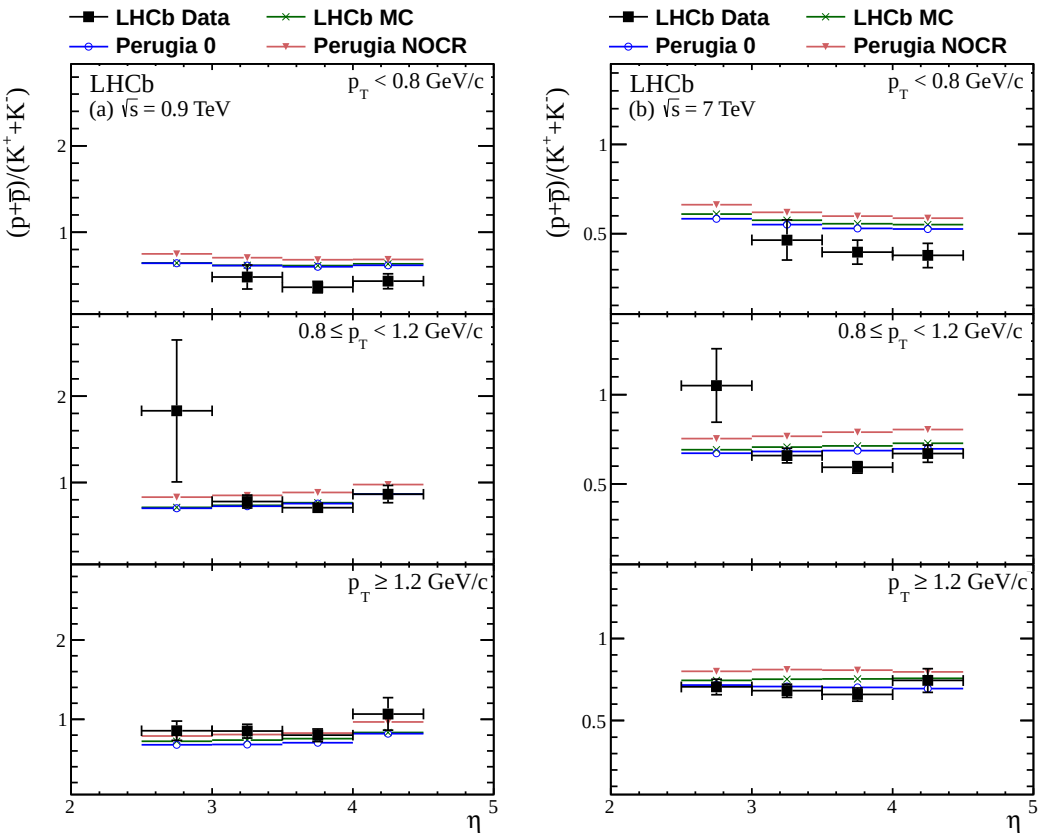
(a) $\sqrt{s} = 0.9\,\text{TeV}$ (b) $\sqrt{s} = 7\,\text{TeV}$

Figure 5.7: π^-/π^+ ratio and total uncertainty as a function of pseudo-rapidity.

ratio within the Regge model, where baryon pair production in governed by Pomeron exchange and the BNT by string-junction exchange, can be parametrised in the form

$$\frac{\bar{p}}{p} \approx \frac{1}{1 + C\exp\left[(\alpha_J - \alpha_P)\,\Delta y\right]}, \tag{5.8}$$

where the parameters α_J (α_P) is the intercept of the string junction (Pomeron) Regge trajectory and C determines the relative contribution of the two. Similarly to the procedure followed in [27], a fit has been performed to the LHCb and ALICE data, where C and $\alpha_J - \alpha_P$ have been set as floating parameters and are determined to be 22.5 ± 6.0 and -0.98 ± 0.07 respectively with a χ^2/NDF of 8.7/8. The fitted curve is shown in Figure 5.13. Taking $\alpha_P = 1.2$ [68] suggests a low value of α_J, significantly below the $\alpha_J \approx 0.5$ expected if the string-junction intercept is associated with that of the standard Reggeon (or meson). The value of $\alpha_J \approx 0.9$ which would be expected if



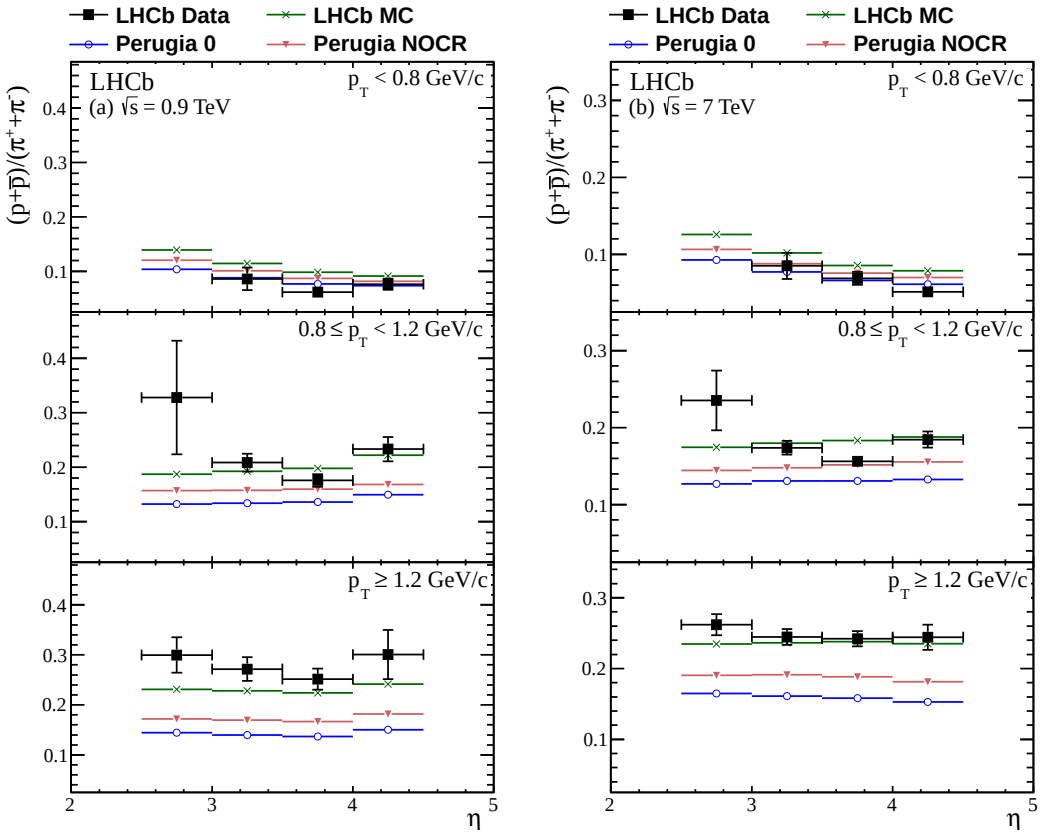
(a) $\sqrt{s} = 0.9\,\text{TeV}$ (b) $\sqrt{s} = 7\,\text{TeV}$

Figure 5.8: $(p + \bar{p})/(K^+ + K^-)$ ratio and total uncertainty as a function of pseudo-rapidity.

the string junction is associated with the Odderon [69] is excluded using this fit model. The same conclusion applies if the LHCb and ALICE $\bar{p}/p$ ratio values are fitted with the alternative parametrisation [70]

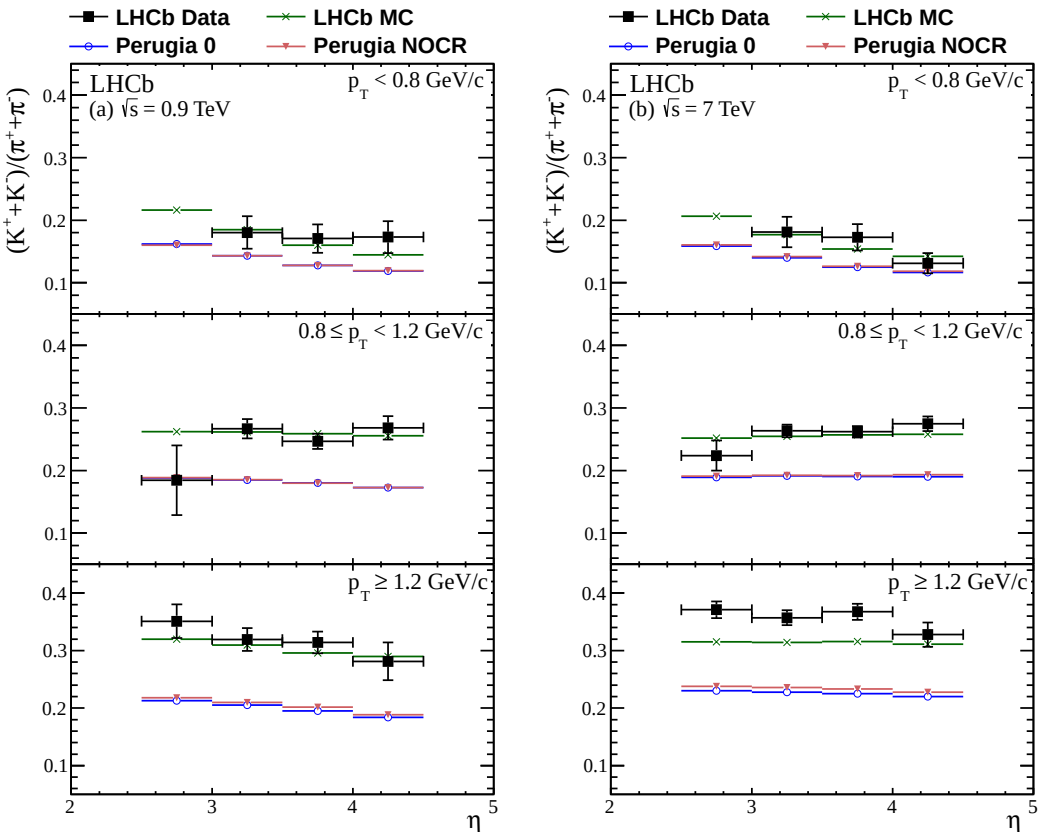
$$C' \cdot (s[\text{GeV}^2])^{(\alpha_J - \alpha_P)/2} \cdot \cosh[y(\alpha_J - \alpha_P)], \tag{5.9}$$

which yields the results $C' = 10.2 \pm 1.8$, $(\alpha_J - \alpha_P) = -0.86 \pm 0.05$ with a χ^2/NDF of 10.2/8.



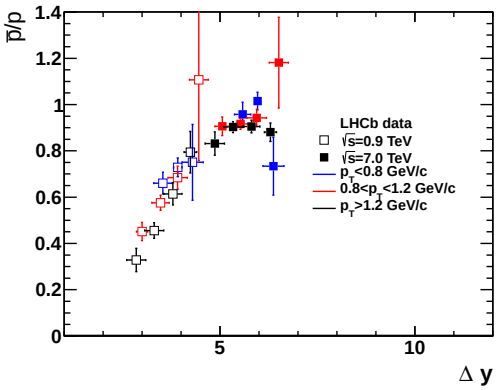
(a) $\sqrt{\mathbf{s}} = 0.9\,\text{TeV}$ (b) $\sqrt{\mathbf{s}} = 7\,\text{TeV}$

Figure 5.9: $(p + \bar{p})/(\pi^+ + \pi^-)$ ratio and total uncertainty as a function of pseudo-rapidity.

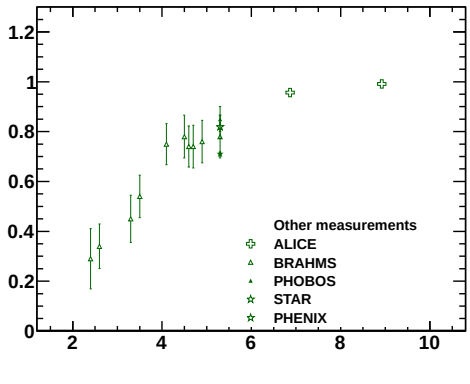


(a) $\sqrt{\mathbf{s}} = 0.9\,\text{TeV}$ (b) $\sqrt{\mathbf{s}} = 7\,\text{TeV}$

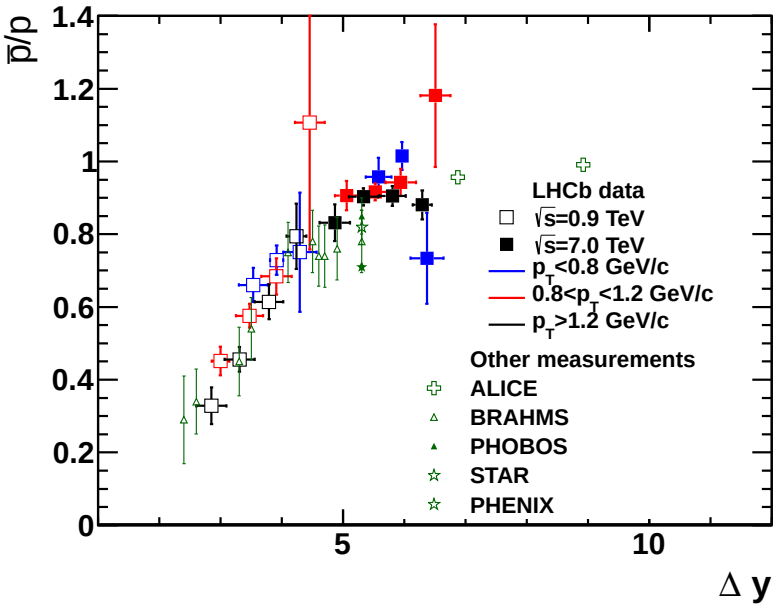
Figure 5.10: $(K^+ + K^-)/(\pi^+ + \pi^-)$ ratio and total uncertainty as a function of pseudo-rapidity.



(a) LHCb data

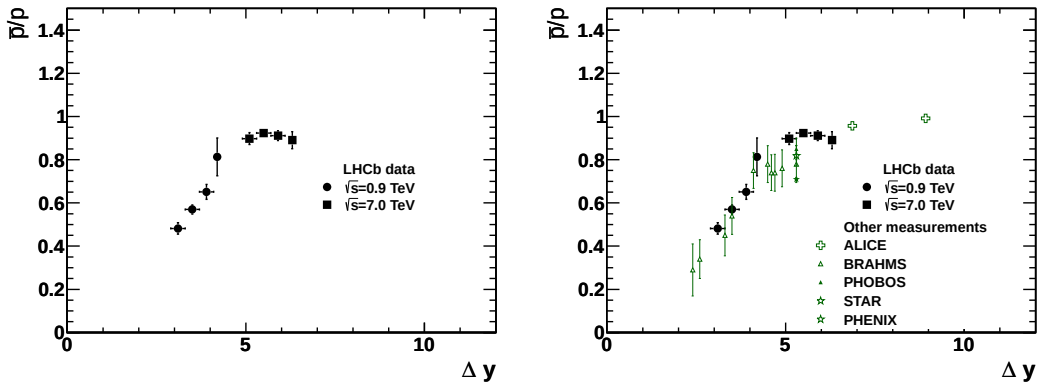


(b) ALICE, PHOBOS, STAR, PHENIX and BRAHMS data



(c) Comparison of the results of LHCb with other experiments.

Figure 5.11: $\bar{p}/p$ ratio as a function of Δy.



(a) (b)

Figure 5.12: $\bar{p}/p$ ratio as a function of Δy averaged in p_T (a) for LHCb data alone and (b) compared with other experiments.

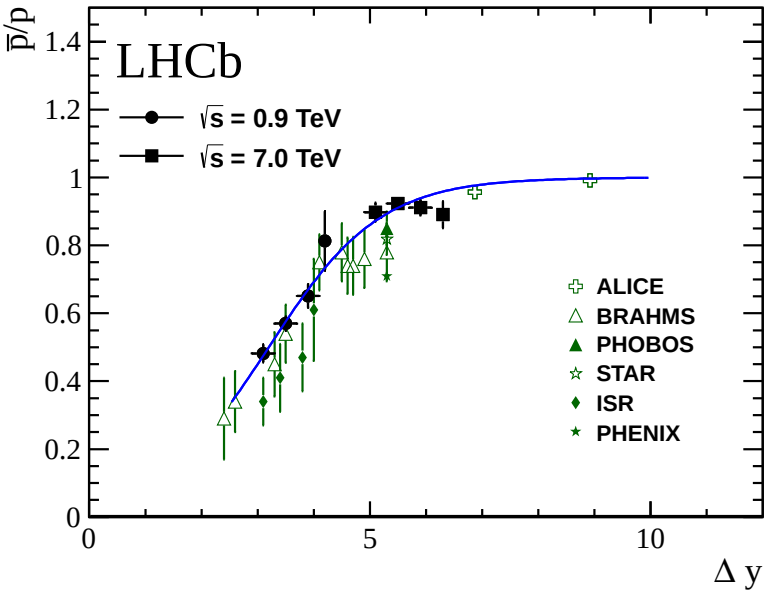


Figure 5.13: Fit to the $\bar{p}/p$ ratio as measured from the LHCb and ALICE experiments (others superimposed).

Chapter 6

Conclusions

A deep understanding of the structure of pp collision events is crucial to perform physics analyses at LHC energies.

In this thesis, the production of prompt charged particles is studied in detail in a completely new kinematic region.

The measurement of the $\bar{p}/p$ ratio shows that, although the compared tunings reproduce the reduction of the ratio at high pseudorapidity, the ratio, and hence the BNT, is globally underestimated by several PYTHIA tunings, especially at $\sqrt{\mathbf{s}} = 0.9\,\text{TeV}$. The dependence of this ratio over the wide Δy range accessible to LHCb confirms the prediction of a BNT suppression towards high Δy. The same analysis provides a full range of measurements of production ratios between different hadron species as an excellent test of the current parametrisation and implementation of the hadronisation mechanism. The comparison with PYTHIA, based on the string fragmentation model, shows that agreement with data is not perfect, indicating that at LHC energies and in the forward region there is a need for a retuning.

The measurement of prompt hadron production ratios at $\sqrt{\mathbf{s}} = 0.9\,\text{TeV}$ and $\sqrt{\mathbf{s}} = 7\,\text{TeV}$ sheds new light on the mechanisms responsible for BNT and hadronisation. Moreover, it provides a valuable input to soft-QCD models and tunings of MC event generators in the forward region, where it is needed most.

The hadron ratio analysis benefits from the powerful particle identification of the LHCb RICH system. In order to achieve optimal RICH performance the reconstruction of the angle of emission of Cherenkov photons from charged tracks has to be optimised. Chapter 3 summarises the current procedure for the calibration of the magnetic distortion in RICH1. The calibration parameters from the MDCS system improve the resolution on the Cherenkov angle in RICH1 by a factor ~ 2. The system also has uniform performance over time and in different regions of RICH1.

The MDCS system described in this thesis is currently being used within LHCb to periodically calibrate the magnetic distortion. The MDCS gives a major contribute to the overall PID performance of the LHCb detector and hence to the precision of all LHCb measurements.

Appendix A

PID Efficiency Tables for Hadron Ratios

Raw (unweighted in momentum and track multiplicity) PID efficiency tables are reported in Tables A.1-A.6 for magnet polarity down data and in Tables A.7-A.12 for magnet up. Tables weighted to low energy data are reported in Tables A.13-A.18,A.19-A.24; tables weighted to high energy data are in Tables A.25-A.30,A.31-A.36.

Table A.1: PID efficiencies for positive tracks with $p_T < 0.8\,\mathrm{GeV}/c$ and magnet polarity down.

	$\mathbf{p} \to \mathbf{p}$	$\mathbf{K}^+ \to \mathbf{p}$	$\boldsymbol{\pi}^+ \to \mathbf{p}$
$\mathbf{2.5 < \eta < 3.0}$	–	–	–
$\mathbf{3.0 < \eta < 3.5}$	0.0960 ± 0.0033	0.0115 ± 0.0014	0.0000 ± 0.0001
$\mathbf{3.5 < \eta < 4.0}$	0.2693 ± 0.0030	0.0081 ± 0.0016	0.0033 ± 0.0001
$\mathbf{4.0 < \eta < 4.5}$	0.1394 ± 0.0021	0.0033 ± 0.0012	0.0016 ± 0.0001

	$\mathbf{p} \to \mathbf{K}^+$	$\mathbf{K}^+ \to \mathbf{K}^+$	$\boldsymbol{\pi}^+ \to \mathbf{K}^+$
$\mathbf{2.5 < \eta < 3.0}$	–	–	–
$\mathbf{3.0 < \eta < 3.5}$	0.1584 ± 0.0043	0.3375 ± 0.0079	0.0016 ± 0.0001
$\mathbf{3.5 < \eta < 4.0}$	0.0657 ± 0.0014	0.5089 ± 0.0104	0.0034 ± 0.0001
$\mathbf{4.0 < \eta < 4.5}$	0.1821 ± 0.0025	0.5825 ± 0.0151	0.0101 ± 0.0002

	$\mathbf{p} \to \boldsymbol{\pi}^+$	$\mathbf{K}^+ \to \boldsymbol{\pi}^+$	$\boldsymbol{\pi}^+ \to \boldsymbol{\pi}^+$
$\mathbf{2.5 < \eta < 3.0}$	–	–	–
$\mathbf{3.0 < \eta < 3.5}$	0.0088 ± 0.0016	0.0264 ± 0.0096	0.8558 ± 0.0029
$\mathbf{3.5 < \eta < 4.0}$	0.0637 ± 0.0019	0.0000 ± 0.0107	0.8519 ± 0.0020
$\mathbf{4.0 < \eta < 4.5}$	0.1949 ± 0.0032	0.1059 ± 0.0164	0.8669 ± 0.0024

Table A.2: PID efficiencies for positive tracks with $0.8\,\mathrm{GeV}/c \leq p_T < 1.2\,\mathrm{GeV}/c$ and magnet polarity down.

	$\mathbf{p} \to \mathbf{p}$	$\mathbf{K}^+ \to \mathbf{p}$	$\boldsymbol{\pi}^+ \to \mathbf{p}$
$\mathbf{2.5 < \eta < 3.0}$	0.0891 ± 0.0050	0.0196 ± 0.0024	0.0000 ± 0.0001
$\mathbf{3.0 < \eta < 3.5}$	0.2577 ± 0.0052	0.0069 ± 0.0022	0.0051 ± 0.0008
$\mathbf{3.5 < \eta < 4.0}$	0.6776 ± 0.0071	0.0148 ± 0.0040	0.0239 ± 0.0015
$\mathbf{4.0 < \eta < 4.5}$	0.4598 ± 0.0078	0.0098 ± 0.0044	0.0060 ± 0.0021

	$\mathbf{p} \to \mathbf{K}^+$	$\mathbf{K}^+ \to \mathbf{K}^+$	$\boldsymbol{\pi}^+ \to \mathbf{K}^+$
$\mathbf{2.5 < \eta < 3.0}$	0.1582 ± 0.0068	0.3370 ± 0.0104	0.0012 ± 0.0002
$\mathbf{3.0 < \eta < 3.5}$	0.1333 ± 0.0035	0.6920 ± 0.0156	0.0102 ± 0.0007
$\mathbf{3.5 < \eta < 4.0}$	0.0259 ± 0.0011	0.8029 ± 0.0182	0.0044 ± 0.0004
$\mathbf{4.0 < \eta < 4.5}$	0.0546 ± 0.0024	0.8016 ± 0.0277	0.0316 ± 0.0016

	$\mathbf{p} \to \boldsymbol{\pi}^+$	$\mathbf{K}^+ \to \boldsymbol{\pi}^+$	$\boldsymbol{\pi}^+ \to \boldsymbol{\pi}^+$
$\mathbf{2.5 < \eta < 3.0}$	0.0082 ± 0.0020	0.0047 ± 0.0098	0.8544 ± 0.0070
$\mathbf{3.0 < \eta < 3.5}$	0.0255 ± 0.0023	0.0166 ± 0.0090	0.8951 ± 0.0069
$\mathbf{3.5 < \eta < 4.0}$	0.1514 ± 0.0034	0.0206 ± 0.0096	0.9327 ± 0.0068
$\mathbf{4.0 < \eta < 4.5}$	0.2795 ± 0.0064	0.0690 ± 0.0145	0.8904 ± 0.0103

.

Table A.3: PID efficiencies for positive tracks with $p_T \geq 1.2\,\mathrm{GeV}/c$ and magnet polarity down.

	$\mathbf{p} \to \mathbf{p}$	$\mathbf{K}^+ \to \mathbf{p}$	$\boldsymbol{\pi}^+ \to \mathbf{p}$
$\mathbf{2.5 < \eta < 3.0}$	0.3031 ± 0.0080	0.0032 ± 0.0025	0.0090 ± 0.0016
$\mathbf{3.0 < \eta < 3.5}$	0.6505 ± 0.0115	0.0044 ± 0.0040	0.0182 ± 0.0027
$\mathbf{3.5 < \eta < 4.0}$	0.8620 ± 0.0115	0.0028 ± 0.0052	0.0181 ± 0.0033
$\mathbf{4.0 < \eta < 4.5}$	0.6339 ± 0.0154	0.0141 ± 0.0076	0.0078 ± 0.0050

	$\mathbf{p} \to \mathbf{K}^+$	$\mathbf{K}^+ \to \mathbf{K}^+$	$\boldsymbol{\pi}^+ \to \mathbf{K}^+$
$\mathbf{2.5 < \eta < 3.0}$	0.0715 ± 0.0035	0.6023 ± 0.0160	0.0057 ± 0.0008
$\mathbf{3.0 < \eta < 3.5}$	0.0267 ± 0.0018	0.8209 ± 0.0210	0.0011 ± 0.0006
$\mathbf{3.5 < \eta < 4.0}$	0.0080 ± 0.0009	0.8396 ± 0.0250	0.0069 ± 0.0008
$\mathbf{4.0 < \eta < 4.5}$	0.0175 ± 0.0021	0.6479 ± 0.0363	0.0109 ± 0.0016

	$\mathbf{p} \to \boldsymbol{\pi}^+$	$\mathbf{K}^+ \to \boldsymbol{\pi}^+$	$\boldsymbol{\pi}^+ \to \boldsymbol{\pi}^+$
$\mathbf{2.5 < \eta < 3.0}$	0.0444 ± 0.0037	0.0114 ± 0.0081	0.9017 ± 0.0112
$\mathbf{3.0 < \eta < 3.5}$	0.1033 ± 0.0048	0.0000 ± 0.0087	0.9370 ± 0.0117
$\mathbf{3.5 < \eta < 4.0}$	0.2094 ± 0.0052	0.0360 ± 0.0109	0.9464 ± 0.0115
$\mathbf{4.0 < \eta < 4.5}$	0.2585 ± 0.0099	0.0729 ± 0.0197	0.8710 ± 0.0177

Table A.4: PID efficiencies for negative tracks with $p_T < 0.8\,\mathrm{GeV}/c$ and magnet polarity down.

	$\bar{\mathbf{p}} \to \bar{\mathbf{p}}$	$\mathbf{K}^- \to \bar{\mathbf{p}}$	$\boldsymbol{\pi}^- \to \bar{\mathbf{p}}$
$\mathbf{2.5 < \eta < 3.0}$	–	–	–
$\mathbf{3.0 < \eta < 3.5}$	0.0911 ± 0.0032	0.0093 ± 0.0014	0.0000 ± 0.0001
$\mathbf{3.5 < \eta < 4.0}$	0.2605 ± 0.0031	0.0052 ± 0.0015	0.0029 ± 0.0001
$\mathbf{4.0 < \eta < 4.5}$	0.1271 ± 0.0021	0.0036 ± 0.0012	0.0016 ± 0.0001

	$\bar{\mathbf{p}} \to \mathbf{K}^-$	$\mathbf{K}^- \to \mathbf{K}^-$	$\boldsymbol{\pi}^- \to \mathbf{K}^-$
$\mathbf{2.5 < \eta < 3.0}$	–	–	–
$\mathbf{3.0 < \eta < 3.5}$	0.1601 ± 0.0044	0.3343 ± 0.0078	0.0016 ± 0.0001
$\mathbf{3.5 < \eta < 4.0}$	0.0680 ± 0.0015	0.4782 ± 0.0094	0.0035 ± 0.0001
$\mathbf{4.0 < \eta < 4.5}$	0.1709 ± 0.0025	0.5918 ± 0.0158	0.0097 ± 0.0002

	$\bar{\mathbf{p}} \to \boldsymbol{\pi}^-$	$\mathbf{K}^- \to \boldsymbol{\pi}^-$	$\boldsymbol{\pi}^- \to \boldsymbol{\pi}^-$
$\mathbf{2.5 < \eta < 3.0}$	–	–	–
$\mathbf{3.0 < \eta < 3.5}$	0.0141 ± 0.0020	0.0151 ± 0.0097	0.8536 ± 0.0029
$\mathbf{3.5 < \eta < 4.0}$	0.0711 ± 0.0020	0.0360 ± 0.0102	0.8509 ± 0.0020
$\mathbf{4.0 < \eta < 4.5}$	0.2050 ± 0.0034	0.1176 ± 0.0172	0.8731 ± 0.0024

Table A.5: PID efficiencies for negative tracks with $0.8\,\mathrm{GeV}/c \leq p_T < 1.2\,\mathrm{GeV}/c$ and magnet polarity down.

	$\bar{\mathrm{p}} \to \bar{\mathrm{p}}$	$\mathrm{K}^- \to \bar{\mathrm{p}}$	$\pi^- \to \bar{\mathrm{p}}$
$\mathbf{2.5 < \eta < 3.0}$	0.0806 ± 0.0049	0.0153 ± 0.0022	0.0000 ± 0.0001
$\mathbf{3.0 < \eta < 3.5}$	0.2520 ± 0.0053	0.0015 ± 0.0021	0.0061 ± 0.0007
$\mathbf{3.5 < \eta < 4.0}$	0.6677 ± 0.0074	0.0211 ± 0.0039	0.0212 ± 0.0015
$\mathbf{4.0 < \eta < 4.5}$	0.4452 ± 0.0081	0.0000 ± 0.0042	0.0038 ± 0.0020

	$\bar{\mathrm{p}} \to \mathrm{K}^-$	$\mathrm{K}^- \to \mathrm{K}^-$	$\pi^- \to \mathrm{K}^-$
$\mathbf{2.5 < \eta < 3.0}$	0.1540 ± 0.0069	0.3333 ± 0.0103	0.0006 ± 0.0002
$\mathbf{3.0 < \eta < 3.5}$	0.1418 ± 0.0038	0.7077 ± 0.0159	0.0111 ± 0.0007
$\mathbf{3.5 < \eta < 4.0}$	0.0264 ± 0.0012	0.7998 ± 0.0179	0.0048 ± 0.0004
$\mathbf{4.0 < \eta < 4.5}$	0.0547 ± 0.0025	0.8240 ± 0.0298	0.0297 ± 0.0015

	$\bar{\mathrm{p}} \to \pi^-$	$\mathrm{K}^- \to \pi^-$	$\pi^- \to \pi^-$
$\mathbf{2.5 < \eta < 3.0}$	0.0100 ± 0.0022	0.0093 ± 0.0102	0.8576 ± 0.0070
$\mathbf{3.0 < \eta < 3.5}$	0.0258 ± 0.0025	0.0152 ± 0.0092	0.8904 ± 0.0069
$\mathbf{3.5 < \eta < 4.0}$	0.1488 ± 0.0036	0.0189 ± 0.0096	0.9372 ± 0.0068
$\mathbf{4.0 < \eta < 4.5}$	0.2882 ± 0.0070	0.0400 ± 0.0161	0.9047 ± 0.0104

Table A.6: PID efficiencies for negative tracks with $p_T \geq 1.2\,\mathrm{GeV}/c$ and magnet polarity down.

	$\bar{\mathrm{p}} \to \bar{\mathrm{p}}$	$\mathrm{K}^- \to \bar{\mathrm{p}}$	$\pi^- \to \bar{\mathrm{p}}$
$\mathbf{2.5 < \eta < 3.0}$	0.2906 ± 0.0082	0.0079 ± 0.0027	0.0082 ± 0.0015
$\mathbf{3.0 < \eta < 3.5}$	0.6288 ± 0.0117	0.0080 ± 0.0037	0.0126 ± 0.0025
$\mathbf{3.5 < \eta < 4.0}$	0.8570 ± 0.0122	0.0086 ± 0.0053	0.0151 ± 0.0031
$\mathbf{4.0 < \eta < 4.5}$	0.6127 ± 0.0160	0.0000 ± 0.0065	0.0150 ± 0.0047

	$\bar{\mathrm{p}} \to \mathrm{K}^-$	$\mathrm{K}^- \to \mathrm{K}^-$	$\pi^- \to \mathrm{K}^-$
$\mathbf{2.5 < \eta < 3.0}$	0.0700 ± 0.0037	0.6146 ± 0.0166	0.0057 ± 0.0008
$\mathbf{3.0 < \eta < 3.5}$	0.0295 ± 0.0020	0.8035 ± 0.0203	0.0034 ± 0.0007
$\mathbf{3.5 < \eta < 4.0}$	0.0073 ± 0.0009	0.8438 ± 0.0257	0.0075 ± 0.0008
$\mathbf{4.0 < \eta < 4.5}$	0.0153 ± 0.0022	0.6536 ± 0.0363	0.0135 ± 0.0018

	$\bar{\mathrm{p}} \to \pi^-$	$\mathrm{K}^- \to \pi^-$	$\pi^- \to \pi^-$
$\mathbf{2.5 < \eta < 3.0}$	0.0393 ± 0.0039	0.0171 ± 0.0086	0.9040 ± 0.0111
$\mathbf{3.0 < \eta < 3.5}$	0.1122 ± 0.0052	0.0002 ± 0.0090	0.9405 ± 0.0116
$\mathbf{3.5 < \eta < 4.0}$	0.2183 ± 0.0057	0.0165 ± 0.0111	0.9385 ± 0.0114
$\mathbf{4.0 < \eta < 4.5}$	0.2735 ± 0.0107	0.0875 ± 0.0202	0.8250 ± 0.0172

Table A.7: PID efficiencies for positive tracks with $p_T < 0.8\,\mathrm{GeV}/c$ and magnet polarity up.

	$\mathbf{p} \to \mathbf{p}$	$\mathbf{K}^+ \to \mathbf{p}$	$\boldsymbol{\pi}^+ \to \mathbf{p}$
$\mathbf{2.5 < \eta < 3.0}$	–	–	–
$\mathbf{3.0 < \eta < 3.5}$	0.0961 ± 0.0042	0.0071 ± 0.0018	0.0000 ± 0.0001
$\mathbf{3.5 < \eta < 4.0}$	0.2611 ± 0.0039	0.0057 ± 0.0021	0.0032 ± 0.0002
$\mathbf{4.0 < \eta < 4.5}$	0.1281 ± 0.0026	0.0013 ± 0.0016	0.0017 ± 0.0002

	$\mathbf{p} \to \mathbf{K}^+$	$\mathbf{K}^+ \to \mathbf{K}^+$	$\boldsymbol{\pi}^+ \to \mathbf{K}^+$
$\mathbf{2.5 < \eta < 3.0}$	–	–	–
$\mathbf{3.0 < \eta < 3.5}$	0.1597 ± 0.0056	0.3470 ± 0.0110	0.0015 ± 0.0001
$\mathbf{3.5 < \eta < 4.0}$	0.0663 ± 0.0018	0.5084 ± 0.0136	0.0035 ± 0.0001
$\mathbf{4.0 < \eta < 4.5}$	0.1656 ± 0.0031	0.5673 ± 0.0198	0.0097 ± 0.0003

	$\mathbf{p} \to \boldsymbol{\pi}^+$	$\mathbf{K}^+ \to \boldsymbol{\pi}^+$	$\boldsymbol{\pi}^+ \to \boldsymbol{\pi}^+$
$\mathbf{2.5 < \eta < 3.0}$	–	–	–
$\mathbf{3.0 < \eta < 3.5}$	0.0145 ± 0.0025	0.0125 ± 0.0133	0.8432 ± 0.0038
$\mathbf{3.5 < \eta < 4.0}$	0.0729 ± 0.0026	0.0000 ± 0.0139	0.8509 ± 0.0027
$\mathbf{4.0 < \eta < 4.5}$	0.2038 ± 0.0042	0.1104 ± 0.0221	0.8717 ± 0.0032

Table A.8: PID efficiencies for positive tracks with $0.8\,\mathrm{GeV}/c \leq p_T < 1.2\,\mathrm{GeV}/c$ and magnet polarity up.

	$\mathbf{p} \to \mathbf{p}$	$\mathbf{K}^+ \to \mathbf{p}$	$\boldsymbol{\pi}^+ \to \mathbf{p}$
$\mathbf{2.5 < \eta < 3.0}$	0.0800 ± 0.0062	0.0199 ± 0.0034	0.0000 ± 0.0002
$\mathbf{3.0 < \eta < 3.5}$	0.2558 ± 0.0067	0.0041 ± 0.0030	0.0053 ± 0.0010
$\mathbf{3.5 < \eta < 4.0}$	0.6560 ± 0.0093	0.0152 ± 0.0052	0.0210 ± 0.0020
$\mathbf{4.0 < \eta < 4.5}$	0.4267 ± 0.0098	0.0126 ± 0.0061	0.0071 ± 0.0027

	$\mathbf{p} \to \mathbf{K}^+$	$\mathbf{K}^+ \to \mathbf{K}^+$	$\boldsymbol{\pi}^+ \to \mathbf{K}^+$
$\mathbf{2.5 < \eta < 3.0}$	0.1576 ± 0.0090	0.3014 ± 0.0137	0.0014 ± 0.0004
$\mathbf{3.0 < \eta < 3.5}$	0.1329 ± 0.0046	0.7048 ± 0.0214	0.0114 ± 0.0009
$\mathbf{3.5 < \eta < 4.0}$	0.0286 ± 0.0015	0.7845 ± 0.0231	0.0050 ± 0.0006
$\mathbf{4.0 < \eta < 4.5}$	0.0621 ± 0.0032	0.7316 ± 0.0346	0.0289 ± 0.0020

	$\mathbf{p} \to \boldsymbol{\pi}^+$	$\mathbf{K}^+ \to \boldsymbol{\pi}^+$	$\boldsymbol{\pi}^+ \to \boldsymbol{\pi}^+$
$\mathbf{2.5 < \eta < 3.0}$	0.0099 ± 0.0027	0.0000 ± 0.0139	0.8379 ± 0.0093
$\mathbf{3.0 < \eta < 3.5}$	0.0278 ± 0.0032	0.0208 ± 0.0123	0.8830 ± 0.0092
$\mathbf{3.5 < \eta < 4.0}$	0.1553 ± 0.0045	0.0398 ± 0.0127	0.9335 ± 0.0090
$\mathbf{4.0 < \eta < 4.5}$	0.3013 ± 0.0087	0.1147 ± 0.0205	0.8990 ± 0.0138

Table A.9: PID efficiencies for positive tracks with $p_T \geq 1.2\,\mathrm{GeV}/c$ and magnet polarity up.

	$\mathbf{p} \to \mathbf{p}$	$\mathbf{K}^+ \to \mathbf{p}$	$\boldsymbol{\pi}^+ \to \mathbf{p}$
$\mathbf{2.5 < \eta < 3.0}$	0.2858 ± 0.0105	0.0000 ± 0.0036	0.0043 ± 0.0020
$\mathbf{3.0 < \eta < 3.5}$	0.6246 ± 0.0149	0.0030 ± 0.0049	0.0164 ± 0.0036
$\mathbf{3.5 < \eta < 4.0}$	0.8570 ± 0.0154	0.0052 ± 0.0074	0.0208 ± 0.0044
$\mathbf{4.0 < \eta < 4.5}$	0.5958 ± 0.0192	0.0000 ± 0.0100	0.0177 ± 0.0069

	$\mathbf{p} \to \mathbf{K}^+$	$\mathbf{K}^+ \to \mathbf{K}^+$	$\boldsymbol{\pi}^+ \to \mathbf{K}^+$
$\mathbf{2.5 < \eta < 3.0}$	0.0752 ± 0.0049	0.6160 ± 0.0237	0.0066 ± 0.0011
$\mathbf{3.0 < \eta < 3.5}$	0.0311 ± 0.0026	0.7877 ± 0.0265	0.0039 ± 0.0009
$\mathbf{3.5 < \eta < 4.0}$	0.0080 ± 0.0012	0.8252 ± 0.0335	0.0065 ± 0.0010
$\mathbf{4.0 < \eta < 4.5}$	0.0223 ± 0.0031	0.6500 ± 0.0506	0.0170 ± 0.0027

	$\mathbf{p} \to \boldsymbol{\pi}^+$	$\mathbf{K}^+ \to \boldsymbol{\pi}^+$	$\boldsymbol{\pi}^+ \to \boldsymbol{\pi}^+$
$\mathbf{2.5 < \eta < 3.0}$	0.0346 ± 0.0046	0.0000 ± 0.0118	0.9030 ± 0.0149
$\mathbf{3.0 < \eta < 3.5}$	0.1027 ± 0.0063	0.0221 ± 0.0119	0.9326 ± 0.0156
$\mathbf{3.5 < \eta < 4.0}$	0.2226 ± 0.0072	0.0187 ± 0.0148	0.9384 ± 0.0152
$\mathbf{4.0 < \eta < 4.5}$	0.2581 ± 0.0126	0.1245 ± 0.0296	0.8240 ± 0.0230

Table A.10: PID efficiencies for negative tracks with $p_T < 0.8\,\mathrm{GeV}/c$ and magnet polarity up.

	$\bar{\mathbf{p}} \to \bar{\mathbf{p}}$	$\mathbf{K}^- \to \bar{\mathbf{p}}$	$\boldsymbol{\pi}^- \to \bar{\mathbf{p}}$
$\mathbf{2.5 < \eta < 3.0}$	–	–	–
$\mathbf{3.0 < \eta < 3.5}$	0.1056 ± 0.0048	0.0073 ± 0.0017	0.0001 ± 0.0001
$\mathbf{3.5 < \eta < 4.0}$	0.2630 ± 0.0042	0.0076 ± 0.0021	0.0030 ± 0.0002
$\mathbf{4.0 < \eta < 4.5}$	0.1307 ± 0.0028	0.0009 ± 0.0014	0.0016 ± 0.0002

	$\bar{\mathbf{p}} \to \mathbf{K}^-$	$\mathbf{K}^- \to \mathbf{K}^-$	$\boldsymbol{\pi}^- \to \mathbf{K}^-$
$\mathbf{2.5 < \eta < 3.0}$	–	–	–
$\mathbf{3.0 < \eta < 3.5}$	0.1609 ± 0.0061	0.3309 ± 0.0102	0.0018 ± 0.0002
$\mathbf{3.5 < \eta < 4.0}$	0.0658 ± 0.0019	0.4840 ± 0.0130	0.0036 ± 0.0001
$\mathbf{4.0 < \eta < 4.5}$	0.1750 ± 0.0034	0.5385 ± 0.0185	0.0091 ± 0.0003

	$\bar{\mathbf{p}} \to \boldsymbol{\pi}^-$	$\mathbf{K}^- \to \boldsymbol{\pi}^-$	$\boldsymbol{\pi}^- \to \boldsymbol{\pi}^-$
$\mathbf{2.5 < \eta < 3.0}$	–	–	–
$\mathbf{3.0 < \eta < 3.5}$	0.0080 ± 0.0024	0.0335 ± 0.0129	0.8446 ± 0.0038
$\mathbf{3.5 < \eta < 4.0}$	0.0791 ± 0.0028	0.0128 ± 0.0139	0.8515 ± 0.0027
$\mathbf{4.0 < \eta < 4.5}$	0.2029 ± 0.0046	0.1852 ± 0.0223	0.8711 ± 0.0032

Table A.11: PID efficiencies for negative tracks with $0.8\,\mathrm{GeV}/c \leq p_T < 1.2\,\mathrm{GeV}/c$ and magnet polarity up.

	$\bar{\mathrm{p}} \to \bar{\mathrm{p}}$	$\mathrm{K}^- \to \bar{\mathrm{p}}$	$\pi^- \to \bar{\mathrm{p}}$
$\mathbf{2.5 < \eta < 3.0}$	0.0794 ± 0.0066	0.0256 ± 0.0034	0.0000 ± 0.0002
$\mathbf{3.0 < \eta < 3.5}$	0.2531 ± 0.0070	0.0024 ± 0.0028	0.0056 ± 0.0010
$\mathbf{3.5 < \eta < 4.0}$	0.6607 ± 0.0099	0.0114 ± 0.0055	0.0223 ± 0.0020
$\mathbf{4.0 < \eta < 4.5}$	0.4423 ± 0.0111	0.0000 ± 0.0091	0.0060 ± 0.0026

	$\bar{\mathrm{p}} \to \mathrm{K}^-$	$\mathrm{K}^- \to \mathrm{K}^-$	$\pi^- \to \mathrm{K}^-$
$\mathbf{2.5 < \eta < 3.0}$	0.1563 ± 0.0096	0.3094 ± 0.0128	0.0010 ± 0.0003
$\mathbf{3.0 < \eta < 3.5}$	0.1268 ± 0.0047	0.6904 ± 0.0210	0.0106 ± 0.0009
$\mathbf{3.5 < \eta < 4.0}$	0.0252 ± 0.0015	0.8401 ± 0.0262	0.0055 ± 0.0006
$\mathbf{4.0 < \eta < 4.5}$	0.0610 ± 0.0036	1.0000 ± 0.0628	0.0337 ± 0.0022

	$\bar{\mathrm{p}} \to \pi^-$	$\mathrm{K}^- \to \pi^-$	$\pi^- \to \pi^-$
$\mathbf{2.5 < \eta < 3.0}$	0.0128 ± 0.0032	0.0198 ± 0.0129	0.8364 ± 0.0093
$\mathbf{3.0 < \eta < 3.5}$	0.0231 ± 0.0035	0.0190 ± 0.0121	0.8942 ± 0.0093
$\mathbf{3.5 < \eta < 4.0}$	0.1491 ± 0.0048	0.0000 ± 0.0136	0.9315 ± 0.0091
$\mathbf{4.0 < \eta < 4.5}$	0.2801 ± 0.0095	0.0000 ± 0.0323	0.8859 ± 0.0138

Table A.12: PID efficiencies for negative tracks with $p_T \geq 1.2\,\mathrm{GeV}/c$ and magnet polarity up.

	$\bar{\mathrm{p}} \to \bar{\mathrm{p}}$	$\mathrm{K}^- \to \bar{\mathrm{p}}$	$\pi^- \to \bar{\mathrm{p}}$
$\mathbf{2.5 < \eta < 3.0}$	0.2974 ± 0.0111	0.0000 ± 0.0033	0.0097 ± 0.0020
$\mathbf{3.0 < \eta < 3.5}$	0.6348 ± 0.0158	0.0244 ± 0.0053	0.0175 ± 0.0035
$\mathbf{3.5 < \eta < 4.0}$	0.8616 ± 0.0163	0.0007 ± 0.0073	0.0068 ± 0.0042
$\mathbf{4.0 < \eta < 4.5}$	0.6337 ± 0.0231	0.0000 ± 0.0092	0.0012 ± 0.0063

	$\bar{\mathrm{p}} \to \mathrm{K}^-$	$\mathrm{K}^- \to \mathrm{K}^-$	$\pi^- \to \mathrm{K}^-$
$\mathbf{2.5 < \eta < 3.0}$	0.0675 ± 0.0048	0.5868 ± 0.0219	0.0059 ± 0.0010
$\mathbf{3.0 < \eta < 3.5}$	0.0254 ± 0.0025	0.7662 ± 0.0261	0.0004 ± 0.0007
$\mathbf{3.5 < \eta < 4.0}$	0.0077 ± 0.0012	0.8504 ± 0.0346	0.0086 ± 0.0012
$\mathbf{4.0 < \eta < 4.5}$	0.0202 ± 0.0035	0.6336 ± 0.0492	0.0081 ± 0.0020

	$\bar{\mathrm{p}} \to \pi^-$	$\mathrm{K}^- \to \pi^-$	$\pi^- \to \pi^-$
$\mathbf{2.5 < \eta < 3.0}$	0.0413 ± 0.0050	0.0049 ± 0.0115	0.8851 ± 0.0146
$\mathbf{3.0 < \eta < 3.5}$	0.1034 ± 0.0067	0.0202 ± 0.0122	0.9386 ± 0.0157
$\mathbf{3.5 < \eta < 4.0}$	0.2029 ± 0.0074	0.0361 ± 0.0151	0.9592 ± 0.0157
$\mathbf{4.0 < \eta < 4.5}$	0.2650 ± 0.0152	0.1344 ± 0.0298	0.8775 ± 0.0243

Table A.13: PID efficiencies weighted at $\sqrt{s} = 0.9\,\text{TeV}$ for positive tracks with $p_T < 0.8\,\text{GeV}/c$ and magnet polarity down.

	$\mathbf{p} \to \mathbf{p}$	$\mathbf{K}^+ \to \mathbf{p}$	$\boldsymbol{\pi}^+ \to \mathbf{p}$
$\mathbf{2.5 < \eta < 3.0}$	–	–	–
$\mathbf{3.0 < \eta < 3.5}$	0.1279 ± 0.0338	0.0267 ± 0.0050	0.0000 ± 0.0002
$\mathbf{3.5 < \eta < 4.0}$	0.2338 ± 0.0075	0.0013 ± 0.0026	0.0029 ± 0.0005
$\mathbf{4.0 < \eta < 4.5}$	0.1599 ± 0.0049	0.0019 ± 0.0021	0.0022 ± 0.0005

	$\mathbf{p} \to \mathbf{K}^+$	$\mathbf{K}^+ \to \mathbf{K}^+$	$\boldsymbol{\pi}^+ \to \mathbf{K}^+$
$\mathbf{2.5 < \eta < 3.0}$	–	–	–
$\mathbf{3.0 < \eta < 3.5}$	0.0735 ± 0.0100	0.3597 ± 0.0142	0.0011 ± 0.0002
$\mathbf{3.5 < \eta < 4.0}$	0.0361 ± 0.0032	0.3571 ± 0.0167	0.0013 ± 0.0001
$\mathbf{4.0 < \eta < 4.5}$	0.0911 ± 0.0033	0.4070 ± 0.0227	0.0043 ± 0.0003

	$\mathbf{p} \to \boldsymbol{\pi}^+$	$\mathbf{K}^+ \to \boldsymbol{\pi}^+$	$\boldsymbol{\pi}^+ \to \boldsymbol{\pi}^+$
$\mathbf{2.5 < \eta < 3.0}$	–	–	–
$\mathbf{3.0 < \eta < 3.5}$	0.0000 ± 0.0042	0.0093 ± 0.0179	0.9289 ± 0.0015
$\mathbf{3.5 < \eta < 4.0}$	0.0181 ± 0.0032	0.0084 ± 0.0298	0.9084 ± 0.0013
$\mathbf{4.0 < \eta < 4.5}$	0.0880 ± 0.0043	0.0201 ± 0.0378	0.8745 ± 0.0018

Table A.14: PID efficiencies weighted at $\sqrt{s} = 0.9\,\text{TeV}$ for positive tracks with $0.8\,\text{GeV}/c \leq p_T < 1.2\,\text{GeV}/c$ and magnet polarity down.

	$\mathbf{p} \to \mathbf{p}$	$\mathbf{K}^+ \to \mathbf{p}$	$\boldsymbol{\pi}^+ \to \mathbf{p}$
$\mathbf{2.5 < \eta < 3.0}$	0.1573 ± 0.0297	0.0254 ± 0.0118	0.0000 ± 0.0006
$\mathbf{3.0 < \eta < 3.5}$	0.4260 ± 0.0172	0.0178 ± 0.0101	0.0000 ± 0.0027
$\mathbf{3.5 < \eta < 4.0}$	0.8686 ± 0.0085	0.0126 ± 0.0132	0.0345 ± 0.0060
$\mathbf{4.0 < \eta < 4.5}$	0.7588 ± 0.0155	0.0000 ± 0.0128	0.0092 ± 0.0093

	$\mathbf{p} \to \mathbf{K}^+$	$\mathbf{K}^+ \to \mathbf{K}^+$	$\boldsymbol{\pi}^+ \to \mathbf{K}^+$
$\mathbf{2.5 < \eta < 3.0}$	0.1647 ± 0.0217	0.4547 ± 0.0299	0.0015 ± 0.0005
$\mathbf{3.0 < \eta < 3.5}$	0.0847 ± 0.0079	0.7386 ± 0.0277	0.0063 ± 0.0012
$\mathbf{3.5 < \eta < 4.0}$	0.0100 ± 0.0014	0.8884 ± 0.0282	0.0027 ± 0.0007
$\mathbf{4.0 < \eta < 4.5}$	0.0250 ± 0.0028	0.9048 ± 0.0308	0.0257 ± 0.0051

	$\mathbf{p} \to \boldsymbol{\pi}^+$	$\mathbf{K}^+ \to \boldsymbol{\pi}^+$	$\boldsymbol{\pi}^+ \to \boldsymbol{\pi}^+$
$\mathbf{2.5 < \eta < 3.0}$	0.0000 ± 0.0016	0.0000 ± 0.0272	0.9211 ± 0.0055
$\mathbf{3.0 < \eta < 3.5}$	0.0020 ± 0.0072	0.0109 ± 0.0227	0.9600 ± 0.0048
$\mathbf{3.5 < \eta < 4.0}$	0.0897 ± 0.0078	0.0229 ± 0.0244	0.9548 ± 0.0061
$\mathbf{4.0 < \eta < 4.5}$	0.2132 ± 0.0165	0.0421 ± 0.0267	0.9281 ± 0.0115

Table A.15: PID efficiencies weighted at $\sqrt{s} = 0.9\,\text{TeV}$ for positive tracks with $p_T \geq 1.2\,\text{GeV}/c$ and magnet polarity down.

	$\mathbf{p} \to \mathbf{p}$	$\mathbf{K}^+ \to \mathbf{p}$	$\boldsymbol{\pi}^+ \to \mathbf{p}$
$\mathbf{2.5 < \eta < 3.0}$	0.3952 ± 0.0276	0.0000 ± 0.0104	0.0093 ± 0.0048
$\mathbf{3.0 < \eta < 3.5}$	0.8403 ± 0.0180	0.0000 ± 0.0200	0.0268 ± 0.0127
$\mathbf{3.5 < \eta < 4.0}$	0.9750 ± 0.0134	0.0000 ± 0.0181	0.0326 ± 0.0137
$\mathbf{4.0 < \eta < 4.5}$	0.8611 ± 0.0337	0.0560 ± 0.0299	0.0093 ± 0.0188

	$\mathbf{p} \to \mathbf{K}^+$	$\mathbf{K}^+ \to \mathbf{K}^+$	$\boldsymbol{\pi}^+ \to \mathbf{K}^+$
$\mathbf{2.5 < \eta < 3.0}$	0.0681 ± 0.0115	0.6910 ± 0.0390	0.0035 ± 0.0014
$\mathbf{3.0 < \eta < 3.5}$	0.0152 ± 0.0044	0.9600 ± 0.0370	0.0000 ± 0.0013
$\mathbf{3.5 < \eta < 4.0}$	0.0013 ± 0.0002	0.9386 ± 0.0345	0.0031 ± 0.0009
$\mathbf{4.0 < \eta < 4.5}$	0.0027 ± 0.0004	0.7256 ± 0.0780	0.0117 ± 0.0038

	$\mathbf{p} \to \boldsymbol{\pi}^+$	$\mathbf{K}^+ \to \boldsymbol{\pi}^+$	$\boldsymbol{\pi}^+ \to \boldsymbol{\pi}^+$
$\mathbf{2.5 < \eta < 3.0}$	0.0057 ± 0.0110	0.0035 ± 0.0276	0.9530 ± 0.0073
$\mathbf{3.0 < \eta < 3.5}$	0.0524 ± 0.0151	0.0000 ± 0.0305	0.9530 ± 0.0129
$\mathbf{3.5 < \eta < 4.0}$	0.1312 ± 0.0162	0.0126 ± 0.0286	0.9422 ± 0.0135
$\mathbf{4.0 < \eta < 4.5}$	0.1244 ± 0.0318	0.0000 ± 0.0687	0.9202 ± 0.0214

Table A.16: PID efficiencies weighted at $\sqrt{s} = 0.9\,\text{TeV}$ for negative tracks with $p_T < 0.8\,\text{GeV}/c$ and magnet polarity down.

	$\bar{\mathbf{p}} \to \bar{\mathbf{p}}$	$\mathbf{K}^- \to \bar{\mathbf{p}}$	$\boldsymbol{\pi}^- \to \bar{\mathbf{p}}$
$\mathbf{2.5 < \eta < 3.0}$	–	–	–
$\mathbf{3.0 < \eta < 3.5}$	0.1017 ± 0.0128	0.0060 ± 0.0035	0.0000 ± 0.0002
$\mathbf{3.5 < \eta < 4.0}$	0.2222 ± 0.0079	0.0061 ± 0.0026	0.0031 ± 0.0005
$\mathbf{4.0 < \eta < 4.5}$	0.1467 ± 0.0053	0.0075 ± 0.0020	0.0029 ± 0.0005

	$\bar{\mathbf{p}} \to \mathbf{K}^-$	$\mathbf{K}^- \to \mathbf{K}^-$	$\boldsymbol{\pi}^- \to \mathbf{K}^-$
$\mathbf{2.5 < \eta < 3.0}$	–	–	–
$\mathbf{3.0 < \eta < 3.5}$	0.0961 ± 0.0127	0.3561 ± 0.0146	0.0010 ± 0.0002
$\mathbf{3.5 < \eta < 4.0}$	0.0252 ± 0.0018	0.3377 ± 0.0161	0.0015 ± 0.0001
$\mathbf{4.0 < \eta < 4.5}$	0.0857 ± 0.0037	0.3410 ± 0.0209	0.0046 ± 0.0003

	$\bar{\mathbf{p}} \to \boldsymbol{\pi}^-$	$\mathbf{K}^- \to \boldsymbol{\pi}^-$	$\boldsymbol{\pi}^- \to \boldsymbol{\pi}^-$
$\mathbf{2.5 < \eta < 3.0}$	–	–	–
$\mathbf{3.0 < \eta < 3.5}$	0.0000 ± 0.0056	0.0040 ± 0.0199	0.9248 ± 0.0016
$\mathbf{3.5 < \eta < 4.0}$	0.0166 ± 0.0036	0.0132 ± 0.0302	0.9077 ± 0.0013
$\mathbf{4.0 < \eta < 4.5}$	0.0968 ± 0.0055	0.2237 ± 0.0374	0.8854 ± 0.0018

Table A.17: PID efficiencies weighted at $\sqrt{s} = 0.9\,\text{TeV}$ for negative tracks with $0.8\,\text{GeV}/c \leq p_T < 1.2\,\text{GeV}/c$ and magnet polarity down.

	$\bar{\mathbf{p}} \to \bar{\mathbf{p}}$	$\mathbf{K}^- \to \bar{\mathbf{p}}$	$\boldsymbol{\pi}^- \to \bar{\mathbf{p}}$
$\mathbf{2.5 < \eta < 3.0}$	0.1202 ± 0.0177	0.0278 ± 0.0100	0.0000 ± 0.0002
$\mathbf{3.0 < \eta < 3.5}$	0.4429 ± 0.0186	0.0000 ± 0.0078	0.0049 ± 0.0032
$\mathbf{3.5 < \eta < 4.0}$	0.8750 ± 0.0103	0.0122 ± 0.0134	0.0268 ± 0.0055
$\mathbf{4.0 < \eta < 4.5}$	0.7914 ± 0.0148	0.0000 ± 0.0129	0.0046 ± 0.0093

	$\bar{\mathbf{p}} \to \mathbf{K}^-$	$\mathbf{K}^- \to \mathbf{K}^-$	$\boldsymbol{\pi}^- \to \mathbf{K}^-$
$\mathbf{2.5 < \eta < 3.0}$	0.1939 ± 0.0256	0.4328 ± 0.0257	0.0004 ± 0.0003
$\mathbf{3.0 < \eta < 3.5}$	0.0965 ± 0.0086	0.8208 ± 0.0273	0.0056 ± 0.0010
$\mathbf{3.5 < \eta < 4.0}$	0.0062 ± 0.0007	0.8942 ± 0.0285	0.0017 ± 0.0003
$\mathbf{4.0 < \eta < 4.5}$	0.0144 ± 0.0026	0.9195 ± 0.0433	0.0204 ± 0.0028

	$\bar{\mathbf{p}} \to \boldsymbol{\pi}^-$	$\mathbf{K}^- \to \boldsymbol{\pi}^-$	$\boldsymbol{\pi}^- \to \boldsymbol{\pi}^-$
$\mathbf{2.5 < \eta < 3.0}$	0.0000 ± 0.0013	0.0000 ± 0.0244	0.9230 ± 0.0049
$\mathbf{3.0 < \eta < 3.5}$	0.0000 ± 0.0058	0.0000 ± 0.0235	0.9510 ± 0.0048
$\mathbf{3.5 < \eta < 4.0}$	0.0638 ± 0.0092	0.0034 ± 0.0249	0.9641 ± 0.0054
$\mathbf{4.0 < \eta < 4.5}$	0.1544 ± 0.0145	0.0247 ± 0.0396	0.9398 ± 0.0105

Table A.18: PID efficiencies weighted at $\sqrt{s} = 0.9\,\text{TeV}$ for negative tracks with $p_T \geq 1.2\,\text{GeV}/c$ and magnet polarity down.

	$\bar{\mathbf{p}} \to \bar{\mathbf{p}}$	$\mathbf{K}^- \to \bar{\mathbf{p}}$	$\boldsymbol{\pi}^- \to \bar{\mathbf{p}}$
$\mathbf{2.5 < \eta < 3.0}$	0.3944 ± 0.0298	0.0000 ± 0.0138	0.0050 ± 0.0046
$\mathbf{3.0 < \eta < 3.5}$	0.8227 ± 0.0232	0.0000 ± 0.0186	0.0202 ± 0.0108
$\mathbf{3.5 < \eta < 4.0}$	0.9701 ± 0.0164	0.0158 ± 0.0172	0.0000 ± 0.0112
$\mathbf{4.0 < \eta < 4.5}$	0.8217 ± 0.0316	0.0000 ± 0.0235	0.0000 ± 0.0200

	$\bar{\mathbf{p}} \to \mathbf{K}^-$	$\mathbf{K}^- \to \mathbf{K}^-$	$\boldsymbol{\pi}^- \to \mathbf{K}^-$
$\mathbf{2.5 < \eta < 3.0}$	0.0506 ± 0.0089	0.6947 ± 0.0418	0.0017 ± 0.0005
$\mathbf{3.0 < \eta < 3.5}$	0.0103 ± 0.0020	0.9959 ± 0.0485	0.0004 ± 0.0002
$\mathbf{3.5 < \eta < 4.0}$	0.0008 ± 0.0002	0.9157 ± 0.0342	0.0023 ± 0.0006
$\mathbf{4.0 < \eta < 4.5}$	0.0036 ± 0.0007	0.8834 ± 0.0710	0.0081 ± 0.0030

	$\bar{\mathbf{p}} \to \boldsymbol{\pi}^-$	$\mathbf{K}^- \to \boldsymbol{\pi}^-$	$\boldsymbol{\pi}^- \to \boldsymbol{\pi}^-$
$\mathbf{2.5 < \eta < 3.0}$	0.0000 ± 0.0090	0.0423 ± 0.0338	0.9537 ± 0.0089
$\mathbf{3.0 < \eta < 3.5}$	0.0475 ± 0.0192	0.0000 ± 0.0384	0.9639 ± 0.0112
$\mathbf{3.5 < \eta < 4.0}$	0.1298 ± 0.0188	0.0000 ± 0.0297	0.9826 ± 0.0113
$\mathbf{4.0 < \eta < 4.5}$	0.1648 ± 0.0296	0.0000 ± 0.0603	0.8737 ± 0.0246

Table A.19: PID efficiencies weighted at $\sqrt{s} = 0.9\,\text{TeV}$ for positive tracks with $p_T < 0.8\,\text{GeV}/c$ and magnet polarity up.

	$\mathbf{p} \to \mathbf{p}$	$\mathbf{K}^+ \to \mathbf{p}$	$\boldsymbol{\pi}^+ \to \mathbf{p}$
$\mathbf{2.5 < \eta < 3.0}$	–	–	–
$\mathbf{3.0 < \eta < 3.5}$	0.1178 ± 0.0147	0.0133 ± 0.0056	0.0000 ± 0.0003
$\mathbf{3.5 < \eta < 4.0}$	0.2457 ± 0.0102	0.0066 ± 0.0035	0.0035 ± 0.0007
$\mathbf{4.0 < \eta < 4.5}$	0.1414 ± 0.0063	0.0000 ± 0.0022	0.0022 ± 0.0007

	$\mathbf{p} \to \mathbf{K}^+$	$\mathbf{K}^+ \to \mathbf{K}^+$	$\boldsymbol{\pi}^+ \to \mathbf{K}^+$
$\mathbf{2.5 < \eta < 3.0}$	–	–	–
$\mathbf{3.0 < \eta < 3.5}$	0.1100 ± 0.0141	0.3402 ± 0.0189	0.0007 ± 0.0002
$\mathbf{3.5 < \eta < 4.0}$	0.0322 ± 0.0033	0.3940 ± 0.0239	0.0013 ± 0.0002
$\mathbf{4.0 < \eta < 4.5}$	0.0842 ± 0.0045	0.3813 ± 0.0262	0.0051 ± 0.0005

	$\mathbf{p} \to \boldsymbol{\pi}^+$	$\mathbf{K}^+ \to \boldsymbol{\pi}^+$	$\boldsymbol{\pi}^+ \to \boldsymbol{\pi}^+$
$\mathbf{2.5 < \eta < 3.0}$	–	–	–
$\mathbf{3.0 < \eta < 3.5}$	0.0004 ± 0.0039	0.0014 ± 0.0263	0.9185 ± 0.0022
$\mathbf{3.5 < \eta < 4.0}$	0.0099 ± 0.0028	0.0000 ± 0.0397	0.9103 ± 0.0017
$\mathbf{4.0 < \eta < 4.5}$	0.0927 ± 0.0063	0.0532 ± 0.0450	0.8777 ± 0.0025

Table A.20: PID efficiencies weighted at $\sqrt{s} = 0.9\,\text{TeV}$ for positive tracks with $0.8\,\text{GeV}/c \leq p_T < 1.2\,\text{GeV}/c$ and magnet polarity up.

	$\mathbf{p} \to \mathbf{p}$	$\mathbf{K}^+ \to \mathbf{p}$	$\boldsymbol{\pi}^+ \to \mathbf{p}$
$\mathbf{2.5 < \eta < 3.0}$	0.1554 ± 0.0353	0.0017 ± 0.0124	0.0000 ± 0.0005
$\mathbf{3.0 < \eta < 3.5}$	0.4526 ± 0.0228	0.0000 ± 0.0127	0.0020 ± 0.0034
$\mathbf{3.5 < \eta < 4.0}$	0.8861 ± 0.0117	0.0095 ± 0.0152	0.0224 ± 0.0082
$\mathbf{4.0 < \eta < 4.5}$	0.7409 ± 0.0196	0.0174 ± 0.0183	0.0000 ± 0.0136

	$\mathbf{p} \to \mathbf{K}^+$	$\mathbf{K}^+ \to \mathbf{K}^+$	$\boldsymbol{\pi}^+ \to \mathbf{K}^+$
$\mathbf{2.5 < \eta < 3.0}$	0.1355 ± 0.0236	0.4875 ± 0.0391	0.0000 ± 0.0013
$\mathbf{3.0 < \eta < 3.5}$	0.0861 ± 0.0112	0.7512 ± 0.0349	0.0064 ± 0.0014
$\mathbf{3.5 < \eta < 4.0}$	0.0118 ± 0.0020	0.8878 ± 0.0294	0.0035 ± 0.0010
$\mathbf{4.0 < \eta < 4.5}$	0.0172 ± 0.0031	0.8153 ± 0.0513	0.0064 ± 0.0016

	$\mathbf{p} \to \boldsymbol{\pi}^+$	$\mathbf{K}^+ \to \boldsymbol{\pi}^+$	$\boldsymbol{\pi}^+ \to \boldsymbol{\pi}^+$
$\mathbf{2.5 < \eta < 3.0}$	0.0000 ± 0.0012	0.0000 ± 0.0336	0.9197 ± 0.0066
$\mathbf{3.0 < \eta < 3.5}$	0.0000 ± 0.0064	0.0253 ± 0.0280	0.9517 ± 0.0063
$\mathbf{3.5 < \eta < 4.0}$	0.0818 ± 0.0120	0.0349 ± 0.0256	0.9647 ± 0.0081
$\mathbf{4.0 < \eta < 4.5}$	0.2484 ± 0.0208	0.0534 ± 0.0467	0.9451 ± 0.0144

Table A.21: PID efficiencies weighted at $\sqrt{s} = 0.9\,\text{TeV}$ for positive tracks with $p_T \geq 1.2\,\text{GeV}/c$ and magnet polarity up.

	$\mathbf{p} \to \mathbf{p}$	$\mathbf{K}^+ \to \mathbf{p}$	$\boldsymbol{\pi}^+ \to \mathbf{p}$
$\mathbf{2.5 < \eta < 3.0}$	0.4723 ± 0.0389	0.0000 ± 0.0126	0.0075 ± 0.0071
$\mathbf{3.0 < \eta < 3.5}$	0.8494 ± 0.0248	0.0000 ± 0.0150	0.0121 ± 0.0124
$\mathbf{3.5 < \eta < 4.0}$	0.9517 ± 0.0178	0.0018 ± 0.0283	0.0078 ± 0.0152
$\mathbf{4.0 < \eta < 4.5}$	0.8140 ± 0.0379	0.0127 ± 0.0278	0.0000 ± 0.0253

	$\mathbf{p} \to \mathbf{K}^+$	$\mathbf{K}^+ \to \mathbf{K}^+$	$\boldsymbol{\pi}^+ \to \mathbf{K}^+$
$\mathbf{2.5 < \eta < 3.0}$	0.0352 ± 0.0092	0.7287 ± 0.0565	0.0059 ± 0.0012
$\mathbf{3.0 < \eta < 3.5}$	0.0084 ± 0.0016	0.9003 ± 0.0412	0.0003 ± 0.0003
$\mathbf{3.5 < \eta < 4.0}$	0.0013 ± 0.0002	0.9941 ± 0.0595	0.0012 ± 0.0002
$\mathbf{4.0 < \eta < 4.5}$	0.0094 ± 0.0041	0.7954 ± 0.0746	0.0096 ± 0.0037

	$\mathbf{p} \to \boldsymbol{\pi}^+$	$\mathbf{K}^+ \to \boldsymbol{\pi}^+$	$\boldsymbol{\pi}^+ \to \boldsymbol{\pi}^+$
$\mathbf{2.5 < \eta < 3.0}$	0.0010 ± 0.0169	0.0000 ± 0.0454	0.9446 ± 0.0120
$\mathbf{3.0 < \eta < 3.5}$	0.0423 ± 0.0195	0.0000 ± 0.0330	0.9776 ± 0.0123
$\mathbf{3.5 < \eta < 4.0}$	0.1517 ± 0.0223	0.0000 ± 0.0495	0.9790 ± 0.0149
$\mathbf{4.0 < \eta < 4.5}$	0.1245 ± 0.0364	0.0499 ± 0.0594	0.8940 ± 0.0322

Table A.22: PID efficiencies weighted at $\sqrt{s} = 0.9\,\text{TeV}$ for negative tracks with $p_T < 0.8\,\text{GeV}/c$ and magnet polarity up.

	$\bar{\mathbf{p}} \to \bar{\mathbf{p}}$	$\mathbf{K}^- \to \bar{\mathbf{p}}$	$\boldsymbol{\pi}^- \to \bar{\mathbf{p}}$
$\mathbf{2.5 < \eta < 3.0}$	–	–	–
$\mathbf{3.0 < \eta < 3.5}$	0.1716 ± 0.0356	0.0015 ± 0.0045	0.0000 ± 0.0004
$\mathbf{3.5 < \eta < 4.0}$	0.2387 ± 0.0107	0.0043 ± 0.0032	0.0014 ± 0.0005
$\mathbf{4.0 < \eta < 4.5}$	0.1500 ± 0.0071	0.0000 ± 0.0024	0.0033 ± 0.0007

	$\bar{\mathbf{p}} \to \mathbf{K}^-$	$\mathbf{K}^- \to \mathbf{K}^-$	$\boldsymbol{\pi}^- \to \mathbf{K}^-$
$\mathbf{2.5 < \eta < 3.0}$	–	–	–
$\mathbf{3.0 < \eta < 3.5}$	0.2077 ± 0.0315	0.3333 ± 0.0185	0.0014 ± 0.0003
$\mathbf{3.5 < \eta < 4.0}$	0.0310 ± 0.0032	0.3281 ± 0.0198	0.0013 ± 0.0002
$\mathbf{4.0 < \eta < 4.5}$	0.0992 ± 0.0056	0.3871 ± 0.0305	0.0040 ± 0.0004

	$\bar{\mathbf{p}} \to \boldsymbol{\pi}^-$	$\mathbf{K}^- \to \boldsymbol{\pi}^-$	$\boldsymbol{\pi}^- \to \boldsymbol{\pi}^-$
$\mathbf{2.5 < \eta < 3.0}$	–	–	–
$\mathbf{3.0 < \eta < 3.5}$	0.0000 ± 0.0099	0.0526 ± 0.0255	0.9242 ± 0.0021
$\mathbf{3.5 < \eta < 4.0}$	0.0087 ± 0.0038	0.0000 ± 0.0382	0.9073 ± 0.0017
$\mathbf{4.0 < \eta < 4.5}$	0.0900 ± 0.0066	0.1312 ± 0.0498	0.8787 ± 0.0024

Table A.23: PID efficiencies weighted at $\sqrt{s} = 0.9\,\text{TeV}$ for negative tracks with $0.8\,\text{GeV}/c \leq p_T < 1.2\,\text{GeV}/c$ and magnet polarity up.

	$\bar{\mathbf{p}} \to \bar{\mathbf{p}}$	$\mathbf{K}^- \to \bar{\mathbf{p}}$	$\boldsymbol{\pi}^- \to \bar{\mathbf{p}}$
$\mathbf{2.5 < \eta < 3.0}$	0.1132 ± 0.0258	0.0227 ± 0.0133	0.0000 ± 0.0006
$\mathbf{3.0 < \eta < 3.5}$	0.4425 ± 0.0250	0.0036 ± 0.0119	0.0130 ± 0.0033
$\mathbf{3.5 < \eta < 4.0}$	0.8614 ± 0.0142	0.0000 ± 0.0164	0.0217 ± 0.0072
$\mathbf{4.0 < \eta < 4.5}$	0.8041 ± 0.0222	0.0000 ± 0.0206	0.0000 ± 0.0132

	$\bar{\mathbf{p}} \to \mathbf{K}^-$	$\mathbf{K}^- \to \mathbf{K}^-$	$\boldsymbol{\pi}^- \to \mathbf{K}^-$
$\mathbf{2.5 < \eta < 3.0}$	0.1137 ± 0.0283	0.4059 ± 0.0316	0.0006 ± 0.0004
$\mathbf{3.0 < \eta < 3.5}$	0.0865 ± 0.0105	0.7437 ± 0.0350	0.0036 ± 0.0009
$\mathbf{3.5 < \eta < 4.0}$	0.0060 ± 0.0007	0.9805 ± 0.0384	0.0036 ± 0.0009
$\mathbf{4.0 < \eta < 4.5}$	0.0180 ± 0.0029	0.9011 ± 0.0648	0.0261 ± 0.0048

	$\bar{\mathbf{p}} \to \boldsymbol{\pi}^-$	$\mathbf{K}^- \to \boldsymbol{\pi}^-$	$\boldsymbol{\pi}^- \to \boldsymbol{\pi}^-$
$\mathbf{2.5 < \eta < 3.0}$	0.0000 ± 0.0029	0.0198 ± 0.0291	0.9231 ± 0.0073
$\mathbf{3.0 < \eta < 3.5}$	0.0000 ± 0.0097	0.0087 ± 0.0290	0.9517 ± 0.0051
$\mathbf{3.5 < \eta < 4.0}$	0.0875 ± 0.0125	0.0000 ± 0.0327	0.9606 ± 0.0076
$\mathbf{4.0 < \eta < 4.5}$	0.2042 ± 0.0252	0.0089 ± 0.0589	0.9323 ± 0.0139

Table A.24: PID efficiencies weighted at $\sqrt{s} = 0.9\,\text{TeV}$ for negative tracks with $p_T \geq 1.2\,\text{GeV}/c$ and magnet polarity up.

	$\bar{\mathbf{p}} \to \bar{\mathbf{p}}$	$\mathbf{K}^- \to \bar{\mathbf{p}}$	$\boldsymbol{\pi}^- \to \bar{\mathbf{p}}$
$\mathbf{2.5 < \eta < 3.0}$	0.3623 ± 0.0376	0.0000 ± 0.0156	0.0071 ± 0.0057
$\mathbf{3.0 < \eta < 3.5}$	0.8275 ± 0.0281	0.0337 ± 0.0246	0.0000 ± 0.0143
$\mathbf{3.5 < \eta < 4.0}$	1.0000 ± 0.0255	0.0000 ± 0.0161	0.0045 ± 0.0129
$\mathbf{4.0 < \eta < 4.5}$	0.7680 ± 0.0425	0.0000 ± 0.0069	0.0000 ± 0.0260

	$\bar{\mathbf{p}} \to \mathbf{K}^-$	$\mathbf{K}^- \to \mathbf{K}^-$	$\boldsymbol{\pi}^- \to \mathbf{K}^-$
$\mathbf{2.5 < \eta < 3.0}$	0.0341 ± 0.0066	0.6346 ± 0.0538	0.0026 ± 0.0010
$\mathbf{3.0 < \eta < 3.5}$	0.0100 ± 0.0030	0.9334 ± 0.0524	0.0001 ± 0.0001
$\mathbf{3.5 < \eta < 4.0}$	0.0025 ± 0.0007	0.9355 ± 0.0450	0.0063 ± 0.0022
$\mathbf{4.0 < \eta < 4.5}$	0.0069 ± 0.0020	0.8038 ± 0.0604	0.0163 ± 0.0058

	$\bar{\mathbf{p}} \to \boldsymbol{\pi}^-$	$\mathbf{K}^- \to \boldsymbol{\pi}^-$	$\boldsymbol{\pi}^- \to \boldsymbol{\pi}^-$
$\mathbf{2.5 < \eta < 3.0}$	0.0093 ± 0.0149	0.0000 ± 0.0365	0.9438 ± 0.0106
$\mathbf{3.0 < \eta < 3.5}$	0.0141 ± 0.0162	0.0000 ± 0.0460	0.9845 ± 0.0157
$\mathbf{3.5 < \eta < 4.0}$	0.1449 ± 0.0307	0.0391 ± 0.0375	0.9717 ± 0.0132
$\mathbf{4.0 < \eta < 4.5}$	0.2337 ± 0.0434	0.0722 ± 0.0465	0.8762 ± 0.0338

Table A.25: PID efficiencies weighted at $\sqrt{s} = 7\,\text{TeV}$ for positive tracks with $p_T < 0.8\,\text{GeV}/c$ and magnet polarity down.

	$\mathbf{p} \to \mathbf{p}$	$\mathbf{K}^+ \to \mathbf{p}$	$\boldsymbol{\pi}^+ \to \mathbf{p}$
$\mathbf{2.5 < \eta < 3.0}$	–	–	–
$\mathbf{3.0 < \eta < 3.5}$	0.0977 ± 0.0121	0.0139 ± 0.0016	0.0000 ± 0.0001
$\mathbf{3.5 < \eta < 4.0}$	0.1682 ± 0.0023	0.0044 ± 0.0011	0.0041 ± 0.0002
$\mathbf{4.0 < \eta < 4.5}$	0.1381 ± 0.0020	0.0027 ± 0.0012	0.0020 ± 0.0002

	$\mathbf{p} \to \mathbf{K}^+$	$\mathbf{K}^+ \to \mathbf{K}^+$	$\boldsymbol{\pi}^+ \to \mathbf{K}^+$
$\mathbf{2.5 < \eta < 3.0}$	–	–	–
$\mathbf{3.0 < \eta < 3.5}$	0.1206 ± 0.0133	0.3217 ± 0.0062	0.0016 ± 0.0001
$\mathbf{3.5 < \eta < 4.0}$	0.0518 ± 0.0018	0.3724 ± 0.0095	0.0029 ± 0.0001
$\mathbf{4.0 < \eta < 4.5}$	0.1617 ± 0.0021	0.5237 ± 0.0128	0.0093 ± 0.0002

	$\mathbf{p} \to \boldsymbol{\pi}^+$	$\mathbf{K}^+ \to \boldsymbol{\pi}^+$	$\boldsymbol{\pi}^+ \to \boldsymbol{\pi}^+$
$\mathbf{2.5 < \eta < 3.0}$	–	–	–
$\mathbf{3.0 < \eta < 3.5}$	0.0000 ± 0.0159	0.0314 ± 0.0100	0.8790 ± 0.0008
$\mathbf{3.5 < \eta < 4.0}$	0.0442 ± 0.0029	0.0000 ± 0.0187	0.8738 ± 0.0006
$\mathbf{4.0 < \eta < 4.5}$	0.1634 ± 0.0026	0.0997 ± 0.0178	0.8716 ± 0.0007

Table A.26: PID efficiencies weighted at $\sqrt{s} = 7\,\text{TeV}$ for positive tracks with $0.8\,\text{GeV}/c \leq p_T < 1.2\,\text{GeV}/c$ and magnet polarity down.

	$\mathbf{p} \to \mathbf{p}$	$\mathbf{K}^+ \to \mathbf{p}$	$\boldsymbol{\pi}^+ \to \mathbf{p}$
$\mathbf{2.5 < \eta < 3.0}$	0.1022 ± 0.0078	0.0219 ± 0.0028	0.0000 ± 0.0002
$\mathbf{3.0 < \eta < 3.5}$	0.2673 ± 0.0043	0.0083 ± 0.0024	0.0041 ± 0.0009
$\mathbf{3.5 < \eta < 4.0}$	0.7270 ± 0.0034	0.0144 ± 0.0043	0.0251 ± 0.0018
$\mathbf{4.0 < \eta < 4.5}$	0.5193 ± 0.0055	0.0076 ± 0.0046	0.0061 ± 0.0026

	$\mathbf{p} \to \mathbf{K}^+$	$\mathbf{K}^+ \to \mathbf{K}^+$	$\boldsymbol{\pi}^+ \to \mathbf{K}^+$
$\mathbf{2.5 < \eta < 3.0}$	0.1629 ± 0.0099	0.3612 ± 0.0083	0.0014 ± 0.0003
$\mathbf{3.0 < \eta < 3.5}$	0.1332 ± 0.0033	0.6869 ± 0.0088	0.0094 ± 0.0007
$\mathbf{3.5 < \eta < 4.0}$	0.0217 ± 0.0010	0.8321 ± 0.0101	0.0036 ± 0.0004
$\mathbf{4.0 < \eta < 4.5}$	0.0433 ± 0.0020	0.8073 ± 0.0147	0.0277 ± 0.0015

	$\mathbf{p} \to \boldsymbol{\pi}^+$	$\mathbf{K}^+ \to \boldsymbol{\pi}^+$	$\boldsymbol{\pi}^+ \to \boldsymbol{\pi}^+$
$\mathbf{2.5 < \eta < 3.0}$	0.0078 ± 0.0030	0.0000 ± 0.0096	0.8741 ± 0.0019
$\mathbf{3.0 < \eta < 3.5}$	0.0198 ± 0.0022	0.0343 ± 0.0082	0.9129 ± 0.0019
$\mathbf{3.5 < \eta < 4.0}$	0.1269 ± 0.0028	0.0186 ± 0.0094	0.9432 ± 0.0020
$\mathbf{4.0 < \eta < 4.5}$	0.2659 ± 0.0051	0.0651 ± 0.0134	0.8977 ± 0.0037

Table A.27: PID efficiencies weighted at $\sqrt{s} = 7\,\text{TeV}$ for positive tracks with $p_T \geq 1.2\,\text{GeV}/c$ and magnet polarity down.

	$\mathbf{p} \to \mathbf{p}$	$\mathbf{K}^+ \to \mathbf{p}$	$\boldsymbol{\pi}^+ \to \mathbf{p}$
$\mathbf{2.5 < \eta < 3.0}$	0.3348 ± 0.0066	0.0045 ± 0.0029	0.0112 ± 0.0020
$\mathbf{3.0 < \eta < 3.5}$	0.6964 ± 0.0056	0.0040 ± 0.0044	0.0162 ± 0.0033
$\mathbf{3.5 < \eta < 4.0}$	0.8936 ± 0.0038	0.0042 ± 0.0055	0.0174 ± 0.0038
$\mathbf{4.0 < \eta < 4.5}$	0.6536 ± 0.0094	0.0161 ± 0.0083	0.0027 ± 0.0061

	$\mathbf{p} \to \mathbf{K}^+$	$\mathbf{K}^+ \to \mathbf{K}^+$	$\boldsymbol{\pi}^+ \to \mathbf{K}^+$
$\mathbf{2.5 < \eta < 3.0}$	0.0657 ± 0.0033	0.6317 ± 0.0096	0.0043 ± 0.0007
$\mathbf{3.0 < \eta < 3.5}$	0.0229 ± 0.0016	0.8528 ± 0.0106	0.0009 ± 0.0005
$\mathbf{3.5 < \eta < 4.0}$	0.0061 ± 0.0008	0.8479 ± 0.0126	0.0074 ± 0.0009
$\mathbf{4.0 < \eta < 4.5}$	0.0142 ± 0.0019	0.6060 ± 0.0233	0.0112 ± 0.0018

	$\mathbf{p} \to \boldsymbol{\pi}^+$	$\mathbf{K}^+ \to \boldsymbol{\pi}^+$	$\boldsymbol{\pi}^+ \to \boldsymbol{\pi}^+$
$\mathbf{2.5 < \eta < 3.0}$	0.0396 ± 0.0036	0.0072 ± 0.0078	0.9145 ± 0.0032
$\mathbf{3.0 < \eta < 3.5}$	0.0943 ± 0.0044	0.0000 ± 0.0089	0.9477 ± 0.0036
$\mathbf{3.5 < \eta < 4.0}$	0.1893 ± 0.0043	0.0366 ± 0.0108	0.9475 ± 0.0039
$\mathbf{4.0 < \eta < 4.5}$	0.2528 ± 0.0088	0.0733 ± 0.0206	0.8611 ± 0.0080

Table A.28: PID efficiencies weighted at $\sqrt{s} = 7\,\text{TeV}$ for negative tracks with $p_T < 0.8\,\text{GeV}/c$ and magnet polarity down.

	$\bar{\mathbf{p}} \to \bar{\mathbf{p}}$	$\mathbf{K}^- \to \bar{\mathbf{p}}$	$\boldsymbol{\pi}^- \to \bar{\mathbf{p}}$
$\mathbf{2.5 < \eta < 3.0}$	–	–	–
$\mathbf{3.0 < \eta < 3.5}$	0.0766 ± 0.0101	0.0095 ± 0.0015	0.0000 ± 0.0001
$\mathbf{3.5 < \eta < 4.0}$	0.1676 ± 0.0023	0.0034 ± 0.0010	0.0036 ± 0.0002
$\mathbf{4.0 < \eta < 4.5}$	0.1244 ± 0.0020	0.0053 ± 0.0010	0.0021 ± 0.0002

	$\bar{\mathbf{p}} \to \mathbf{K}^-$	$\mathbf{K}^- \to \mathbf{K}^-$	$\boldsymbol{\pi}^- \to \mathbf{K}^-$
$\mathbf{2.5 < \eta < 3.0}$	–	–	–
$\mathbf{3.0 < \eta < 3.5}$	0.1404 ± 0.0147	0.3186 ± 0.0062	0.0015 ± 0.0001
$\mathbf{3.5 < \eta < 4.0}$	0.0492 ± 0.0015	0.3418 ± 0.0080	0.0030 ± 0.0001
$\mathbf{4.0 < \eta < 4.5}$	0.1513 ± 0.0021	0.4164 ± 0.0108	0.0089 ± 0.0002

	$\bar{\mathbf{p}} \to \boldsymbol{\pi}^-$	$\mathbf{K}^- \to \boldsymbol{\pi}^-$	$\boldsymbol{\pi}^- \to \boldsymbol{\pi}^-$
$\mathbf{2.5 < \eta < 3.0}$	–	–	–
$\mathbf{3.0 < \eta < 3.5}$	0.0000 ± 0.0221	0.0189 ± 0.0103	0.8762 ± 0.0008
$\mathbf{3.5 < \eta < 4.0}$	0.0412 ± 0.0029	0.0289 ± 0.0158	0.8726 ± 0.0006
$\mathbf{4.0 < \eta < 4.5}$	0.1757 ± 0.0028	0.2948 ± 0.0156	0.8773 ± 0.0007

Table A.29: PID efficiencies weighted at $\sqrt{s} = 7\,\text{TeV}$ for negative tracks with $0.8\,\text{GeV}/c \leq p_T < 1.2\,\text{GeV}/c$ and magnet polarity down.

	$\bar{\mathbf{p}} \to \bar{\mathbf{p}}$	$\mathbf{K}^- \to \bar{\mathbf{p}}$	$\boldsymbol{\pi}^- \to \bar{\mathbf{p}}$
$\mathbf{2.5 < \eta < 3.0}$	0.0743 ± 0.0054	0.0183 ± 0.0027	0.0000 ± 0.0002
$\mathbf{3.0 < \eta < 3.5}$	0.2635 ± 0.0045	0.0002 ± 0.0024	0.0063 ± 0.0009
$\mathbf{3.5 < \eta < 4.0}$	0.7216 ± 0.0036	0.0193 ± 0.0042	0.0213 ± 0.0017
$\mathbf{4.0 < \eta < 4.5}$	0.5130 ± 0.0058	0.0000 ± 0.0045	0.0043 ± 0.0025

	$\bar{\mathbf{p}} \to \mathbf{K}^-$	$\mathbf{K}^- \to \mathbf{K}^-$	$\boldsymbol{\pi}^- \to \mathbf{K}^-$
$\mathbf{2.5 < \eta < 3.0}$	0.1423 ± 0.0092	0.3513 ± 0.0083	0.0006 ± 0.0002
$\mathbf{3.0 < \eta < 3.5}$	0.1407 ± 0.0035	0.7308 ± 0.0098	0.0094 ± 0.0006
$\mathbf{3.5 < \eta < 4.0}$	0.0214 ± 0.0010	0.8371 ± 0.0100	0.0037 ± 0.0004
$\mathbf{4.0 < \eta < 4.5}$	0.0422 ± 0.0021	0.8225 ± 0.0161	0.0271 ± 0.0015

	$\bar{\mathbf{p}} \to \boldsymbol{\pi}^-$	$\mathbf{K}^- \to \boldsymbol{\pi}^-$	$\boldsymbol{\pi}^- \to \boldsymbol{\pi}^-$
$\mathbf{2.5 < \eta < 3.0}$	0.0091 ± 0.0034	0.0063 ± 0.0100	0.8769 ± 0.0019
$\mathbf{3.0 < \eta < 3.5}$	0.0218 ± 0.0023	0.0098 ± 0.0092	0.9088 ± 0.0018
$\mathbf{3.5 < \eta < 4.0}$	0.1233 ± 0.0030	0.0118 ± 0.0094	0.9481 ± 0.0019
$\mathbf{4.0 < \eta < 4.5}$	0.2680 ± 0.0054	0.0434 ± 0.0151	0.9100 ± 0.0035

Table A.30: PID efficiencies weighted at $\sqrt{s} = 7\,\text{TeV}$ for negative tracks with $p_T \geq 1.2\,\text{GeV}/c$ and magnet polarity down.

	$\bar{\text{p}} \to \bar{\text{p}}$	$\text{K}^- \to \bar{\text{p}}$	$\pi^- \to \bar{\text{p}}$
$\mathbf{2.5 < \eta < 3.0}$	0.3333 ± 0.0070	0.0101 ± 0.0032	0.0110 ± 0.0020
$\mathbf{3.0 < \eta < 3.5}$	0.6713 ± 0.0060	0.0053 ± 0.0040	0.0128 ± 0.0031
$\mathbf{3.5 < \eta < 4.0}$	0.8907 ± 0.0041	0.0053 ± 0.0054	0.0096 ± 0.0035
$\mathbf{4.0 < \eta < 4.5}$	0.6345 ± 0.0099	0.0000 ± 0.0080	0.0082 ± 0.0058

	$\bar{\text{p}} \to \text{K}^-$	$\text{K}^- \to \text{K}^-$	$\pi^- \to \text{K}^-$
$\mathbf{2.5 < \eta < 3.0}$	0.0648 ± 0.0035	0.6446 ± 0.0100	0.0046 ± 0.0007
$\mathbf{3.0 < \eta < 3.5}$	0.0273 ± 0.0019	0.8413 ± 0.0104	0.0028 ± 0.0006
$\mathbf{3.5 < \eta < 4.0}$	0.0058 ± 0.0008	0.8491 ± 0.0132	0.0078 ± 0.0009
$\mathbf{4.0 < \eta < 4.5}$	0.0099 ± 0.0019	0.6241 ± 0.0241	0.0158 ± 0.0022

	$\bar{\text{p}} \to \pi^-$	$\text{K}^- \to \pi^-$	$\pi^- \to \pi^-$
$\mathbf{2.5 < \eta < 3.0}$	0.0339 ± 0.0038	0.0099 ± 0.0085	0.9160 ± 0.0031
$\mathbf{3.0 < \eta < 3.5}$	0.1001 ± 0.0046	0.0000 ± 0.0091	0.9504 ± 0.0035
$\mathbf{3.5 < \eta < 4.0}$	0.1993 ± 0.0047	0.0101 ± 0.0112	0.9438 ± 0.0037
$\mathbf{4.0 < \eta < 4.5}$	0.2579 ± 0.0092	0.1017 ± 0.0213	0.7752 ± 0.0088

Table A.31: PID efficiencies weighted at $\sqrt{s} = 7\,\text{TeV}$ for positive tracks with $p_T < 0.8\,\text{GeV}/c$ and magnet polarity up.

	$\text{p} \to \text{p}$	$\text{K}^+ \to \text{p}$	$\pi^+ \to \text{p}$
$\mathbf{2.5 < \eta < 3.0}$	–	–	–
$\mathbf{3.0 < \eta < 3.5}$	0.0674 ± 0.0042	0.0073 ± 0.0019	0.0000 ± 0.0001
$\mathbf{3.5 < \eta < 4.0}$	0.1687 ± 0.0029	0.0035 ± 0.0014	0.0042 ± 0.0003
$\mathbf{4.0 < \eta < 4.5}$	0.1234 ± 0.0024	0.0012 ± 0.0015	0.0021 ± 0.0003

	$\text{p} \to \text{K}^+$	$\text{K}^+ \to \text{K}^+$	$\pi^+ \to \text{K}^+$
$\mathbf{2.5 < \eta < 3.0}$	–	–	–
$\mathbf{3.0 < \eta < 3.5}$	0.1319 ± 0.0099	0.3256 ± 0.0089	0.0013 ± 0.0001
$\mathbf{3.5 < \eta < 4.0}$	0.0514 ± 0.0020	0.3711 ± 0.0120	0.0030 ± 0.0001
$\mathbf{4.0 < \eta < 4.5}$	0.1480 ± 0.0026	0.5049 ± 0.0166	0.0092 ± 0.0003

	$\text{p} \to \pi^+$	$\text{K}^+ \to \pi^+$	$\pi^+ \to \pi^+$
$\mathbf{2.5 < \eta < 3.0}$	–	–	–
$\mathbf{3.0 < \eta < 3.5}$	0.0045 ± 0.0117	0.0079 ± 0.0142	0.8652 ± 0.0011
$\mathbf{3.5 < \eta < 4.0}$	0.0460 ± 0.0035	0.0000 ± 0.0231	0.8717 ± 0.0008
$\mathbf{4.0 < \eta < 4.5}$	0.1782 ± 0.0035	0.1130 ± 0.0236	0.8758 ± 0.0010

Table A.32: PID efficiencies weighted at $\sqrt{s} = 7\,\text{TeV}$ for positive tracks with $0.8\,\text{GeV}/c \leq p_T < 1.2\,\text{GeV}/c$ and magnet polarity up.

	$\mathbf{p} \to \mathbf{p}$	$\mathbf{K}^+ \to \mathbf{p}$	$\boldsymbol{\pi}^+ \to \mathbf{p}$
$\mathbf{2.5 < \eta < 3.0}$	0.0788 ± 0.0079	0.0198 ± 0.0037	0.0000 ± 0.0003
$\mathbf{3.0 < \eta < 3.5}$	0.2683 ± 0.0057	0.0042 ± 0.0034	0.0045 ± 0.0012
$\mathbf{3.5 < \eta < 4.0}$	0.7069 ± 0.0045	0.0163 ± 0.0055	0.0217 ± 0.0023
$\mathbf{4.0 < \eta < 4.5}$	0.4877 ± 0.0072	0.0114 ± 0.0065	0.0080 ± 0.0036

	$\mathbf{p} \to \mathbf{K}^+$	$\mathbf{K}^+ \to \mathbf{K}^+$	$\boldsymbol{\pi}^+ \to \mathbf{K}^+$
$\mathbf{2.5 < \eta < 3.0}$	0.1563 ± 0.0128	0.3327 ± 0.0118	0.0011 ± 0.0004
$\mathbf{3.0 < \eta < 3.5}$	0.1355 ± 0.0045	0.7166 ± 0.0129	0.0096 ± 0.0009
$\mathbf{3.5 < \eta < 4.0}$	0.0243 ± 0.0014	0.8191 ± 0.0129	0.0043 ± 0.0005
$\mathbf{4.0 < \eta < 4.5}$	0.0474 ± 0.0026	0.7238 ± 0.0197	0.0256 ± 0.0019

	$\mathbf{p} \to \boldsymbol{\pi}^+$	$\mathbf{K}^+ \to \boldsymbol{\pi}^+$	$\boldsymbol{\pi}^+ \to \boldsymbol{\pi}^+$
$\mathbf{2.5 < \eta < 3.0}$	0.0054 ± 0.0042	0.0000 ± 0.0140	0.8560 ± 0.0028
$\mathbf{3.0 < \eta < 3.5}$	0.0169 ± 0.0027	0.0221 ± 0.0118	0.9000 ± 0.0026
$\mathbf{3.5 < \eta < 4.0}$	0.1333 ± 0.0038	0.0334 ± 0.0120	0.9448 ± 0.0026
$\mathbf{4.0 < \eta < 4.5}$	0.2880 ± 0.0068	0.1160 ± 0.0185	0.9029 ± 0.0048

Table A.33: PID efficiencies weighted at $\sqrt{s} = 7\,\text{TeV}$ for positive tracks with $p_T \geq 1.2\,\text{GeV}/c$ and magnet polarity up.

	$\mathbf{p} \to \mathbf{p}$	$\mathbf{K}^+ \to \mathbf{p}$	$\boldsymbol{\pi}^+ \to \mathbf{p}$
$\mathbf{2.5 < \eta < 3.0}$	0.3237 ± 0.0089	0.0000 ± 0.0042	0.0072 ± 0.0027
$\mathbf{3.0 < \eta < 3.5}$	0.6792 ± 0.0075	0.0000 ± 0.0052	0.0133 ± 0.0042
$\mathbf{3.5 < \eta < 4.0}$	0.8873 ± 0.0052	0.0064 ± 0.0075	0.0172 ± 0.0049
$\mathbf{4.0 < \eta < 4.5}$	0.6083 ± 0.0120	0.0000 ± 0.0107	0.0206 ± 0.0082

	$\mathbf{p} \to \mathbf{K}^+$	$\mathbf{K}^+ \to \mathbf{K}^+$	$\boldsymbol{\pi}^+ \to \mathbf{K}^+$
$\mathbf{2.5 < \eta < 3.0}$	0.0682 ± 0.0045	0.6548 ± 0.0148	0.0053 ± 0.0010
$\mathbf{3.0 < \eta < 3.5}$	0.0255 ± 0.0022	0.8143 ± 0.0139	0.0028 ± 0.0009
$\mathbf{3.5 < \eta < 4.0}$	0.0069 ± 0.0011	0.8292 ± 0.0173	0.0056 ± 0.0010
$\mathbf{4.0 < \eta < 4.5}$	0.0168 ± 0.0027	0.6041 ± 0.0319	0.0196 ± 0.0033

	$\mathbf{p} \to \boldsymbol{\pi}^+$	$\mathbf{K}^+ \to \boldsymbol{\pi}^+$	$\boldsymbol{\pi}^+ \to \boldsymbol{\pi}^+$
$\mathbf{2.5 < \eta < 3.0}$	0.0272 ± 0.0047	0.0000 ± 0.0123	0.9169 ± 0.0042
$\mathbf{3.0 < \eta < 3.5}$	0.0933 ± 0.0058	0.0183 ± 0.0116	0.9465 ± 0.0047
$\mathbf{3.5 < \eta < 4.0}$	0.2034 ± 0.0059	0.0268 ± 0.0152	0.9424 ± 0.0052
$\mathbf{4.0 < \eta < 4.5}$	0.2471 ± 0.0109	0.1188 ± 0.0279	0.7866 ± 0.0114

Table A.34: PID efficiencies weighted at $\sqrt{s} = 7\,\text{TeV}$ for negative tracks with $p_T < 0.8\,\text{GeV}/c$ and magnet polarity up.

	$\bar{\text{p}} \to \bar{\text{p}}$	$\text{K}^- \to \bar{\text{p}}$	$\pi^- \to \bar{\text{p}}$
$2.5 < \eta < 3.0$	–	–	–
$3.0 < \eta < 3.5$	0.1019 ± 0.0129	0.0077 ± 0.0019	0.0000 ± 0.0001
$3.5 < \eta < 4.0$	0.1642 ± 0.0032	0.0053 ± 0.0014	0.0034 ± 0.0003
$4.0 < \eta < 4.5$	0.1323 ± 0.0027	0.0002 ± 0.0012	0.0021 ± 0.0003

	$\bar{\text{p}} \to \text{K}^-$	$\text{K}^- \to \text{K}^-$	$\pi^- \to \text{K}^-$
$2.5 < \eta < 3.0$	–	–	–
$3.0 < \eta < 3.5$	0.1442 ± 0.0116	0.3157 ± 0.0083	0.0018 ± 0.0002
$3.5 < \eta < 4.0$	0.0519 ± 0.0023	0.3528 ± 0.0114	0.0032 ± 0.0001
$4.0 < \eta < 4.5$	0.1582 ± 0.0028	0.4721 ± 0.0159	0.0083 ± 0.0003

	$\bar{\text{p}} \to \pi^-$	$\text{K}^- \to \pi^-$	$\pi^- \to \pi^-$
$2.5 < \eta < 3.0$	–	–	–
$3.0 < \eta < 3.5$	0.0000 ± 0.0168	0.0337 ± 0.0132	0.8680 ± 0.0011
$3.5 < \eta < 4.0$	0.0517 ± 0.0045	0.0000 ± 0.0226	0.8722 ± 0.0008
$4.0 < \eta < 4.5$	0.1749 ± 0.0037	0.1999 ± 0.0221	0.8757 ± 0.0009

Table A.35: PID efficiencies weighted at $\sqrt{s} = 7\,\text{TeV}$ for negative tracks with $0.8\,\text{GeV}/c \leq p_T < 1.2\,\text{GeV}/c$ and magnet polarity up.

	$\bar{\text{p}} \to \bar{\text{p}}$	$\text{K}^- \to \bar{\text{p}}$	$\pi^- \to \bar{\text{p}}$
$2.5 < \eta < 3.0$	0.0781 ± 0.0097	0.0283 ± 0.0038	0.0000 ± 0.0002
$3.0 < \eta < 3.5$	0.2653 ± 0.0060	0.0012 ± 0.0030	0.0060 ± 0.0011
$3.5 < \eta < 4.0$	0.7105 ± 0.0048	0.0087 ± 0.0058	0.0223 ± 0.0023
$4.0 < \eta < 4.5$	0.4987 ± 0.0078	0.0058 ± 0.0068	0.0064 ± 0.0035

	$\bar{\text{p}} \to \text{K}^-$	$\text{K}^- \to \text{K}^-$	$\pi^- \to \text{K}^-$
$2.5 < \eta < 3.0$	0.1351 ± 0.0111	0.3401 ± 0.0107	0.0009 ± 0.0003
$3.0 < \eta < 3.5$	0.1294 ± 0.0047	0.6987 ± 0.0125	0.0086 ± 0.0008
$3.5 < \eta < 4.0$	0.0199 ± 0.0012	0.8764 ± 0.0146	0.0046 ± 0.0005
$4.0 < \eta < 4.5$	0.0501 ± 0.0031	0.8547 ± 0.0230	0.0320 ± 0.0022

	$\bar{\text{p}} \to \pi^-$	$\text{K}^- \to \pi^-$	$\pi^- \to \pi^-$
$2.5 < \eta < 3.0$	0.0065 ± 0.0048	0.0205 ± 0.0126	0.8566 ± 0.0028
$3.0 < \eta < 3.5$	0.0138 ± 0.0030	0.0191 ± 0.0116	0.9086 ± 0.0025
$3.5 < \eta < 4.0$	0.1279 ± 0.0040	0.0000 ± 0.0138	0.9424 ± 0.0026
$4.0 < \eta < 4.5$	0.2636 ± 0.0074	0.0248 ± 0.0214	0.8886 ± 0.0050

Table A.36: PID efficiencies weighted at $\sqrt{s} = 7\,\text{TeV}$ for negative tracks with $p_T \geq 1.2\,\text{GeV}/c$ and magnet polarity up.

	$\bar{\mathbf{p}} \to \bar{\mathbf{p}}$	$\mathbf{K}^- \to \bar{\mathbf{p}}$	$\boldsymbol{\pi}^- \to \bar{\mathbf{p}}$
$\mathbf{2.5 < \eta < 3.0}$	0.3300 ± 0.0093	0.0006 ± 0.0039	0.0130 ± 0.0028
$\mathbf{3.0 < \eta < 3.5}$	0.6807 ± 0.0081	0.0245 ± 0.0057	0.0150 ± 0.0040
$\mathbf{3.5 < \eta < 4.0}$	0.8910 ± 0.0055	0.0000 ± 0.0070	0.0023 ± 0.0046
$\mathbf{4.0 < \eta < 4.5}$	0.6396 ± 0.0140	0.0000 ± 0.0082	0.0068 ± 0.0081

	$\bar{\mathbf{p}} \to \mathbf{K}^-$	$\mathbf{K}^- \to \mathbf{K}^-$	$\boldsymbol{\pi}^- \to \mathbf{K}^-$
$\mathbf{2.5 < \eta < 3.0}$	0.0634 ± 0.0045	0.6114 ± 0.0137	0.0050 ± 0.0009
$\mathbf{3.0 < \eta < 3.5}$	0.0203 ± 0.0021	0.7968 ± 0.0142	0.0003 ± 0.0006
$\mathbf{3.5 < \eta < 4.0}$	0.0059 ± 0.0010	0.8533 ± 0.0172	0.0084 ± 0.0012
$\mathbf{4.0 < \eta < 4.5}$	0.0131 ± 0.0026	0.5781 ± 0.0322	0.0079 ± 0.0020

	$\bar{\mathbf{p}} \to \boldsymbol{\pi}^-$	$\mathbf{K}^- \to \boldsymbol{\pi}^-$	$\boldsymbol{\pi}^- \to \boldsymbol{\pi}^-$
$\mathbf{2.5 < \eta < 3.0}$	0.0376 ± 0.0049	0.0000 ± 0.0117	0.8989 ± 0.0044
$\mathbf{3.0 < \eta < 3.5}$	0.0912 ± 0.0061	0.0106 ± 0.0121	0.9491 ± 0.0045
$\mathbf{3.5 < \eta < 4.0}$	0.1878 ± 0.0062	0.0358 ± 0.0145	0.9644 ± 0.0049
$\mathbf{4.0 < \eta < 4.5}$	0.2643 ± 0.0132	0.1613 ± 0.0305	0.8515 ± 0.0109

Appendix B

Fake Track Rates Tables

Tables of ghost rates in MC and data.

Table B.1: Ghost track information for protons, magnet down, $p_T < 0.8$ and $\sqrt{\mathbf{s}} = 0.9\,\text{TeV}$.

η	2-2.5	2.5-3	3-3.5	3.5-4	4-4.5	4.5-5.0
p:						
MC: Ghost fraction above threshold	-	-	0.0020	0.0022	0.0039	-
MC: Ghost fraction below threshold	-	-	0.0015	0.0044	0.0059	-
Data: Fraction of tracks above threshold	-	-	0.0113	0.0593	0.5819	-
Data: Fraction of tracks below threshold	-	-	0.9887	0.9407	0.4181	-
Data: Ghost Fraction	-	-	0.0046	0.0156	0.0091	-
$\bar{p}$:						
MC: Ghost fraction above threshold	-	-	0.0029	0.0025	0.0042	-
MC: Ghost fraction below threshold	-	-	0.0016	0.0046	0.0057	-
Data: Fraction of tracks above threshold	-	-	0.0106	0.0486	0.5234	-
Data: Fraction of tracks below threshold	-	-	0.9894	0.9514	0.4766	-
Data: Ghost Fraction	-	-	0.0057	0.0178	0.0133	-

Table B.2: Ghost track information for protons, magnet down, $0.8 < p_T < 1.2$ and $\sqrt{\mathbf{s}} = 0.9\,\text{TeV}$.

η	2-2.5	2.5-3	3-3.5	3.5-4	4-4.5	4.5-5.0
p:						
MC: Ghost fraction above threshold	-	0.0031	0.0033	0.0018	0.0014	-
MC: Ghost fraction below threshold	-	0.0028	0.0027	0.0049	0.0054	-
Data: Fraction of tracks above threshold	-	0.0034	0.0135	0.5563	0.9404	-
Data: Fraction of tracks below threshold	-	0.9966	0.9865	0.4437	0.0596	-
Data: Ghost Fraction	-	0.0063	0.0091	0.0154	0.0058	-
$\bar{p}$:						
MC: Ghost fraction above threshold	-	0.0016	0.0028	0.0021	0.0022	-
MC: Ghost fraction below threshold	-	0.0026	0.0028	0.0051	0.0079	-
Data: Fraction of tracks above threshold	-	0.0033	0.0122	0.5296	0.9169	-
Data: Fraction of tracks below threshold	-	0.9967	0.9878	0.4704	0.0831	-
Data: Ghost Fraction	-	0.0061	0.0096	0.0180	0.0092	-

Table B.3: Ghost track information for protons, magnet down, $p_T > 1.2$ and $\sqrt{\mathbf{s}} = 0.9\,\text{TeV}$.

η	2-2.5	2.5-3	3-3.5	3.5-4	4-4.5	4.5-5.0
p:						
MC: Ghost fraction above threshold	-	0.0046	0.0028	0.0022	0.0020	-
MC: Ghost fraction below threshold	-	0.0063	0.0063	0.0177	0.0149	-
Data: Fraction of tracks above threshold	-	0.0444	0.2562	0.8533	0.9334	-
Data: Fraction of tracks below threshold	-	0.9556	0.7438	0.1467	0.0666	-
Data: Ghost Fraction	-	0.0143	0.0137	0.0221	0.0096	-
$\bar{p}$:						
MC: Ghost fraction above threshold	-	0.0062	0.0027	0.0027	0.0028	-
MC: Ghost fraction below threshold	-	0.0070	0.0073	0.0254	0.0213	-
Data: Fraction of tracks above threshold	-	0.0347	0.2154	0.8396	0.9353	-
Data: Fraction of tracks below threshold	-	0.9653	0.7846	0.1604	0.0647	-
Data: Ghost Fraction	-	0.0170	0.0169	0.0271	0.0123	-

Table B.4: Ghost track information for kaons, magnet down, $p_T < 0.8$ and $\sqrt{\mathbf{s}} = 0.9\,\text{TeV}$.

η	2-2.5	2.5-3	3-3.5	3.5-4	4-4.5	4.5-5.0
K^+ :						
MC: Ghost fraction above threshold	-	-	0.0022	0.0015	0.0045	-
MC: Ghost fraction below threshold	-	-	0.0023	0.0032	0.0054	-
Data: Fraction of tracks above threshold	-	-	0.1220	0.9305	0.9894	-
Data: Fraction of tracks below threshold	-	-	0.8780	0.0695	0.0106	-
Data: Ghost Fraction	-	-	0.0068	0.0055	0.0096	-
K^- :						
MC: Ghost fraction above threshold	-	-	0.0023	0.0015	0.0044	-
MC: Ghost fraction below threshold	-	-	0.0022	0.0029	0.0054	-
Data: Fraction of tracks above threshold	-	-	0.1232	0.9114	0.9898	-
Data: Fraction of tracks below threshold	-	-	0.8768	0.0886	0.0102	-
Data: Ghost Fraction	-	-	0.0066	0.0055	0.0114	-

Table B.5: Ghost track information for kaons, magnet down, $0.8 < p_T < 1.2$ and $\sqrt{\mathbf{s}} = 0.9\,\text{TeV}$.

η	2-2.5	2.5-3	3-3.5	3.5-4	4-4.5	4.5-5.0
K^+ :						
MC: Ghost fraction above threshold	-	0.0037	0.0016	0.0015	0.0016	-
MC: Ghost fraction below threshold	-	0.0031	0.0025	0.0037	0.0046	-
Data: Fraction of tracks above threshold	-	0.0174	0.4366	0.9356	0.9415	-
Data: Fraction of tracks below threshold	-	0.9826	0.5634	0.0644	0.0585	-
Data: Ghost Fraction	-	0.0077	0.0063	0.0100	0.0068	-
K^- :						
MC: Ghost fraction above threshold	-	0.0036	0.0014	0.0017	0.0016	-
MC: Ghost fraction below threshold	-	0.0030	0.0023	0.0034	0.0051	-
Data: Fraction of tracks above threshold	-	0.0188	0.4357	0.9392	0.9558	-
Data: Fraction of tracks below threshold	-	0.9812	0.5643	0.0608	0.0442	-
Data: Ghost Fraction	-	0.0077	0.0054	0.0111	0.0071	-

Table B.6: Ghost track information for kaons, magnet down, $p_T > 1.2$ and $\sqrt{\mathbf{s}} = 0.9\,\text{TeV}$.

η	2-2.5	2.5-3	3-3.5	3.5-4	4-4.5	4.5-5.0
K^+ :						
MC: Ghost fraction above threshold	-	0.0030	0.0019	0.0019	0.0016	-
MC: Ghost fraction below threshold	-	0.0037	0.0031	0.0111	0.0075	-
Data: Fraction of tracks above threshold	-	0.4347	0.7827	0.9322	0.9698	-
Data: Fraction of tracks below threshold	-	0.5653	0.2173	0.0678	0.0302	-
Data: Ghost Fraction	-	0.0082	0.0061	0.0162	0.0055	-
K^- :						
MC: Ghost fraction above threshold	-	0.0033	0.0019	0.0019	0.0019	-
MC: Ghost fraction below threshold	-	0.0041	0.0036	0.0087	0.0053	-
Data: Fraction of tracks above threshold	-	0.4346	0.7628	0.9250	0.9682	-
Data: Fraction of tracks below threshold	-	0.5654	0.2372	0.0750	0.0318	-
Data: Ghost Fraction	-	0.0086	0.0075	0.0171	0.0077	-

Table B.7: Ghost track information for pions, magnet down, $p_T < 0.8$ and $\sqrt{\mathbf{s}} = 0.9\,\text{TeV}$.

η	2-2.5	2.5-3	3-3.5	3.5-4	4-4.5	4.5-5.0
π^+:						
MC: Ghost fraction above threshold	-	-	0.0013	0.0018	0.0053	-
MC: Ghost fraction below threshold	-	-	0.0025	0.0035	0.0089	-
Data: Fraction of tracks above threshold	-	-	0.8584	0.9705	0.9877	-
Data: Fraction of tracks below threshold	-	-	0.1416	0.0295	0.0123	-
Data: Ghost Fraction	-	-	0.0033	0.0050	0.0105	-
π^-:						
MC: Ghost fraction above threshold	-	-	0.0014	0.0018	0.0052	-
MC: Ghost fraction below threshold	-	-	0.0029	0.0047	0.0095	-
Data: Fraction of tracks above threshold	-	-	0.8627	0.9719	0.9865	-
Data: Fraction of tracks below threshold	-	-	0.1373	0.0281	0.0135	-
Data: Ghost Fraction	-	-	0.0032	0.0048	0.0107	-

Table B.8: Ghost track information for pions, magnet down, $0.8 < p_T < 1.2$ and $\sqrt{\mathbf{s}} = 0.9\,\text{TeV}$.

η	2-2.5	2.5-3	3-3.5	3.5-4	4-4.5	4.5-5.0
π^+:						
MC: Ghost fraction above threshold	-	0.0025	0.0018	0.0019	0.0020	-
MC: Ghost fraction below threshold	-	0.0042	0.0028	0.0040	0.0071	-
Data: Fraction of tracks above threshold	-	0.8568	0.8652	0.9153	0.9438	-
Data: Fraction of tracks below threshold	-	0.1432	0.1348	0.0847	0.0562	-
Data: Ghost Fraction	-	0.0053	0.0055	0.0096	0.0066	-
π^-:						
MC: Ghost fraction above threshold	-	0.0027	0.0019	0.0018	0.0022	-
MC: Ghost fraction below threshold	-	0.0039	0.0023	0.0046	0.0093	-
Data: Fraction of tracks above threshold	-	0.8607	0.8614	0.9223	0.9581	-
Data: Fraction of tracks below threshold	-	0.1393	0.1386	0.0777	0.0419	-
Data: Ghost Fraction	-	0.0052	0.0054	0.0110	0.0068	-

Table B.9: Ghost track information for pions, magnet down, $p_T > 1.2$ and $\sqrt{\mathbf{s}} = 0.9\,\text{TeV}$.

η	2-2.5	2.5-3	3-3.5	3.5-4	4-4.5	4.5-5.0
π^+:						
MC: Ghost fraction above threshold	-	0.0033	0.0021	0.0022	0.0021	-
MC: Ghost fraction below threshold	-	0.0073	0.0083	0.0166	0.0277	-
Data: Fraction of tracks above threshold	-	0.8403	0.8748	0.9313	0.9454	-
Data: Fraction of tracks below threshold	-	0.1597	0.1252	0.0687	0.0546	-
Data: Ghost Fraction	-	0.0088	0.0086	0.0183	0.0087	-
π^-:						
MC: Ghost fraction above threshold	-	0.0033	0.0025	0.0020	0.0025	-
MC: Ghost fraction below threshold	-	0.0065	0.0053	0.0152	0.0280	-
Data: Fraction of tracks above threshold	-	0.8372	0.8575	0.9293	0.9502	-
Data: Fraction of tracks below threshold	-	0.1628	0.1425	0.0707	0.0498	-
Data: Ghost Fraction	-	0.0083	0.0084	0.0168	0.0114	-

Table B.10: Ghost track information for protons, magnet down, $p_T < 0.8$ and $\sqrt{\mathbf{s}} = 7.0\,\text{TeV}$.

η	2-2.5	2.5-3	3-3.5	3.5-4	4-4.5	4.5-5.0
p:						
MC: Ghost fraction above threshold	-	-	0.0067	0.0107	0.0143	-
MC: Ghost fraction below threshold	-	-	0.0082	0.0211	0.0139	-
Data: Fraction of tracks above threshold	-	-	0.0383	0.0594	0.6333	-
Data: Fraction of tracks below threshold	-	-	0.9617	0.9406	0.3667	-
Data: Ghost Fraction	-	-	0.0175	0.0507	0.0221	-
$\bar{p}$:						
MC: Ghost fraction above threshold	-	-	0.0064	0.0101	0.0146	-
MC: Ghost fraction below threshold	-	-	0.0095	0.0214	0.0124	-
Data: Fraction of tracks above threshold	-	-	0.0374	0.0561	0.6120	-
Data: Fraction of tracks below threshold	-	-	0.9626	0.9439	0.3880	-
Data: Ghost Fraction	-	-	0.0191	0.0494	0.0214	-

Table B.11: Ghost track information for protons, magnet down, $0.8 < p_T < 1.2$ and $\sqrt{\mathbf{s}} = 7.0\,\text{TeV}$.

η	2-2.5	2.5-3	3-3.5	3.5-4	4-4.5	4.5-5.0
p:						
MC: Ghost fraction above threshold	-	0.0037	0.0045	0.0052	0.0048	-
MC: Ghost fraction below threshold	-	0.0066	0.0124	0.0200	0.0091	-
Data: Fraction of tracks above threshold	-	0.0173	0.0216	0.5367	0.9578	-
Data: Fraction of tracks below threshold	-	0.9827	0.9784	0.4633	0.0422	-
Data: Ghost Fraction	-	0.0120	0.0261	0.0362	0.0086	-
$\bar{p}$:						
MC: Ghost fraction above threshold	-	0.0069	0.0057	0.0053	0.0057	-
MC: Ghost fraction below threshold	-	0.0081	0.0142	0.0213	0.0127	-
Data: Fraction of tracks above threshold	-	0.0149	0.0205	0.5318	0.9602	-
Data: Fraction of tracks below threshold	-	0.9851	0.9795	0.4682	0.0398	-
Data: Ghost Fraction	-	0.0152	0.0287	0.0394	0.0106	-

Table B.12: Ghost track information for protons, magnet down, $p_T > 1.2$ and $\sqrt{\mathbf{s}} = 7.0\,\text{TeV}$.

η	2-2.5	2.5-3	3-3.5	3.5-4	4-4.5	4.5-5.0
p:						
MC: Ghost fraction above threshold	-	0.0032	0.0022	0.0034	0.0033	-
MC: Ghost fraction below threshold	-	0.0368	0.0284	0.0392	0.0152	-
Data: Fraction of tracks above threshold	-	0.0909	0.2834	0.7827	0.9633	-
Data: Fraction of tracks below threshold	-	0.9091	0.7166	0.2173	0.0367	-
Data: Ghost Fraction	-	0.0440	0.0275	0.0303	0.0070	-
$\bar{p}$:						
MC: Ghost fraction above threshold	-	0.0040	0.0033	0.0034	0.0031	-
MC: Ghost fraction below threshold	-	0.0355	0.0318	0.0436	0.0256	-
Data: Fraction of tracks above threshold	-	0.0930	0.2836	0.7808	0.9653	-
Data: Fraction of tracks below threshold	-	0.9070	0.7164	0.2192	0.0347	-
Data: Ghost Fraction	-	0.0425	0.0305	0.0342	0.0075	-

Table B.13: Ghost track information for kaons, magnet down, $p_T < 0.8$ and $\sqrt{\mathbf{s}} = 7.0\,\text{TeV}$.

η	2-2.5	2.5-3	3-3.5	3.5-4	4-4.5	4.5-5.0
K^+ :						
MC: Ghost fraction above threshold	-	-	0.0066	0.0055	0.0184	-
MC: Ghost fraction below threshold	-	-	0.0114	0.0177	0.0158	-
Data: Fraction of tracks above threshold	-	-	0.1169	0.9083	0.9946	-
Data: Fraction of tracks below threshold	-	-	0.8831	0.0917	0.0054	-
Data: Ghost Fraction	-	-	0.0218	0.0171	0.0246	-
K^- :						
MC: Ghost fraction above threshold	-	-	0.0071	0.0062	0.0193	-
MC: Ghost fraction below threshold	-	-	0.0115	0.0178	0.0148	-
Data: Fraction of tracks above threshold	-	-	0.1194	0.9038	0.9945	-
Data: Fraction of tracks below threshold	-	-	0.8806	0.0962	0.0055	-
Data: Ghost Fraction	-	-	0.0198	0.0181	0.0243	-

Table B.14: Ghost track information for kaons, magnet down, $0.8 < p_T < 1.2$ and $\sqrt{\mathbf{s}} = 7.0\,\text{TeV}$.

η	2-2.5	2.5-3	3-3.5	3.5-4	4-4.5	4.5-5.0
K^+ :						
MC: Ghost fraction above threshold	-	0.0029	0.0013	0.0017	0.0034	-
MC: Ghost fraction below threshold	-	0.0105	0.0069	0.0101	0.0147	-
Data: Fraction of tracks above threshold	-	0.0305	0.3854	0.9114	0.9589	-
Data: Fraction of tracks below threshold	-	0.9695	0.6146	0.0886	0.0411	-
Data: Ghost Fraction	-	0.0176	0.0109	0.0107	0.0077	-
K^- :						
MC: Ghost fraction above threshold	-	0.0052	0.0011	0.0018	0.0034	-
MC: Ghost fraction below threshold	-	0.0103	0.0066	0.0128	0.0135	-
Data: Fraction of tracks above threshold	-	0.0319	0.3911	0.9114	0.9622	-
Data: Fraction of tracks below threshold	-	0.9681	0.6089	0.0886	0.0378	-
Data: Ghost Fraction	-	0.0182	0.0104	0.0118	0.0079	-

Table B.15: Ghost track information for kaons, magnet down, $p_T > 1.2$ and $\sqrt{\mathbf{s}} = 7.0\,\text{TeV}$.

η	2-2.5	2.5-3	3-3.5	3.5-4	4-4.5	4.5-5.0
K^+ :						
MC: Ghost fraction above threshold	-	0.0013	0.0011	0.0012	0.0015	-
MC: Ghost fraction below threshold	-	0.0105	0.0104	0.0177	0.0134	-
Data: Fraction of tracks above threshold	-	0.4728	0.6896	0.8882	0.9725	-
Data: Fraction of tracks below threshold	-	0.5272	0.3104	0.1118	0.0275	-
Data: Ghost Fraction	-	0.0105	0.0069	0.0137	0.0036	-
K^- :						
MC: Ghost fraction above threshold	-	0.0012	0.0009	0.0015	0.0018	-
MC: Ghost fraction below threshold	-	0.0106	0.0097	0.0170	0.0107	-
Data: Fraction of tracks above threshold	-	0.4815	0.6894	0.8825	0.9720	-
Data: Fraction of tracks below threshold	-	0.5185	0.3106	0.1175	0.0280	-
Data: Ghost Fraction	-	0.0102	0.0071	0.0147	0.0045	-

Table B.16: Ghost track information for pions, magnet down, $p_T < 0.8$ and $\sqrt{\mathbf{s}} = 7.0\,\text{TeV}$.

η	2-2.5	2.5-3	3-3.5	3.5-4	4-4.5	4.5-5.0
π^+:						
MC: Ghost fraction above threshold	-	-	0.0015	0.0034	0.0129	-
MC: Ghost fraction below threshold	-	-	0.0050	0.0118	0.0217	-
Data: Fraction of tracks above threshold	-	-	0.7865	0.9562	0.9881	-
Data: Fraction of tracks below threshold	-	-	0.2135	0.0438	0.0119	-
Data: Ghost Fraction	-	-	0.0040	0.0091	0.0206	-
π^-:						
MC: Ghost fraction above threshold	-	-	0.0016	0.0035	0.0130	-
MC: Ghost fraction below threshold	-	-	0.0051	0.0121	0.0222	-
Data: Fraction of tracks above threshold	-	-	0.7895	0.9574	0.9875	-
Data: Fraction of tracks below threshold	-	-	0.2105	0.0426	0.0125	-
Data: Ghost Fraction	-	-	0.0039	0.0085	0.0196	-

Table B.17: Ghost track information for pions, magnet down, $0.8 < p_T < 1.2$ and $\sqrt{\mathbf{s}} = 7.0\,\text{TeV}$.

η	2-2.5	2.5-3	3-3.5	3.5-4	4-4.5	4.5-5.0
π^+:						
MC: Ghost fraction above threshold	-	0.0012	0.0013	0.0014	0.0031	-
MC: Ghost fraction below threshold	-	0.0044	0.0046	0.0143	0.0164	-
Data: Fraction of tracks above threshold	-	0.8229	0.7848	0.8756	0.9431	-
Data: Fraction of tracks below threshold	-	0.1771	0.2152	0.1244	0.0569	-
Data: Ghost Fraction	-	0.0029	0.0039	0.0106	0.0074	-
π^-:						
MC: Ghost fraction above threshold	-	0.0012	0.0012	0.0015	0.0031	-
MC: Ghost fraction below threshold	-	0.0050	0.0056	0.0105	0.0153	-
Data: Fraction of tracks above threshold	-	0.8206	0.7799	0.8769	0.9462	-
Data: Fraction of tracks below threshold	-	0.1794	0.2201	0.1231	0.0538	-
Data: Ghost Fraction	-	0.0029	0.0039	0.0105	0.0066	-

Table B.18: Ghost track information for pions, magnet down, $p_T > 1.2$ and $\sqrt{\mathbf{s}} = 7.0\,\mathrm{TeV}$.

η	2-2.5	2.5-3	3-3.5	3.5-4	4-4.5	4.5-5.0
π^+:						
MC: Ghost fraction above threshold	-	0.0010	0.0011	0.0014	0.0029	-
MC: Ghost fraction below threshold	-	0.0110	0.0214	0.0330	0.0346	-
Data: Fraction of tracks above threshold	-	0.7591	0.7651	0.8652	0.9184	-
Data: Fraction of tracks below threshold	-	0.2409	0.2349	0.1348	0.0816	-
Data: Ghost Fraction	-	0.0055	0.0082	0.0164	0.0078	-
π^-:						
MC: Ghost fraction above threshold	-	0.0011	0.0009	0.0011	0.0033	-
MC: Ghost fraction below threshold	-	0.0085	0.0220	0.0292	0.0335	-
Data: Fraction of tracks above threshold	-	0.7537	0.7577	0.8563	0.9262	-
Data: Fraction of tracks below threshold	-	0.2463	0.2423	0.1437	0.0738	-
Data: Ghost Fraction	-	0.0048	0.0087	0.0167	0.0088	-

Appendix C

Non-Prompt Rates Tables

Table C.1: Non-prompt contamination information from MC for protons, magnet down, $p_T < 0.8$ and $\sqrt{\mathbf{s}} = 0.9\,\text{TeV}$.

η	2-2.5	2.5-3	3-3.5	3.5-4	4-4.5	4.5-5.0
p non prompt contamination fraction	-	-	0.0282	0.0243	0.0247	-
$\bar{p}$ non prompt contamination fraction	-	-	0.0295	0.0265	0.0279	-

Table C.2: Non-prompt contamination information from MC for protons, magnet down, $0.8 < p_T < 1.2$ and $\sqrt{\mathbf{s}} = 0.9\,\text{TeV}$.

η	2-2.5	2.5-3	3-3.5	3.5-4	4-4.5	4.5-5.0
p non prompt contamination fraction	-	0.0197	0.0176	0.0187	0.0172	-
$\bar{p}$ non prompt contamination fraction	-	0.0203	0.0191	0.0197	0.0205	-

Table C.3: Non-prompt contamination information from MC for protons, magnet down, $p_T > 1.2$ and $\sqrt{\mathbf{s}} = 0.9\,\text{TeV}$.

η	2-2.5	2.5-3	3-3.5	3.5-4	4-4.5	4.5-5.0
p non prompt contamination fraction	-	0.0142	0.0147	0.0145	0.0120	-
$\bar{p}$ non prompt contamination fraction	-	0.0168	0.0162	0.0168	0.0176	-

Table C.4: Non-prompt contamination information from MC for kaons, magnet down, $p_T < 0.8$ and $\sqrt{\mathbf{s}} = 0.9\,\text{TeV}$.

η	2-2.5	2.5-3	3-3.5	3.5-4	4-4.5	4.5-5.0
K^+ non prompt contamination fraction	-	-	0.0092	0.0077	0.0089	-
K^- non prompt contamination fraction	-	-	0.0091	0.0076	0.0090	-

Table C.5: Non-prompt contamination information from MC for kaons, magnet down, $0.8 < p_T < 1.2$ and $\sqrt{\mathbf{s}} = 0.9\,\text{TeV}$.

η	2-2.5	2.5-3	3-3.5	3.5-4	4-4.5	4.5-5.0
K^+ non prompt contamination fraction	-	0.0120	0.0102	0.0080	0.0062	-
K^- non prompt contamination fraction	-	0.0123	0.0110	0.0085	0.0066	-

Table C.6: Non-prompt contamination information from MC for kaons, magnet down, $p_T > 1.2$ and $\sqrt{\mathbf{s}} = 0.9\,\text{TeV}$.

η	2-2.5	2.5-3	3-3.5	3.5-4	4-4.5	4.5-5.0
K^+ non prompt contamination fraction	-	0.0193	0.0148	0.0101	0.0057	-
K^- non prompt contamination fraction	-	0.0224	0.0181	0.0138	0.0117	-

Table C.7: Non-prompt contamination information from MC for pions, magnet down, $p_T < 0.8$ and $\sqrt{\mathbf{s}} = 0.9\,\text{TeV}$.

η	2-2.5	2.5-3	3-3.5	3.5-4	4-4.5	4.5-5.0
π^+ non prompt contamination fraction	-	-	0.0096	0.0128	0.0175	-
π^- non prompt contamination fraction	-	-	0.0099	0.0135	0.0192	-

Table C.8: Non-prompt contamination information from MC for pions, magnet down, $0.8 < p_T < 1.2$ and $\sqrt{\mathbf{s}} = 0.9\,\text{TeV}$.

η	2-2.5	2.5-3	3-3.5	3.5-4	4-4.5	4.5-5.0
π^+ non prompt contamination fraction	-	0.0094	0.0099	0.0097	0.0083	-
π^- non prompt contamination fraction	-	0.0096	0.0099	0.0098	0.0088	-

Table C.9: Non-prompt contamination information from MC for pions, magnet down, $p_T > 1.2$ and $\sqrt{\mathbf{s}} = 0.9\,\text{TeV}$.

η	2-2.5	2.5-3	3-3.5	3.5-4	4-4.5	4.5-5.0
π^+ non prompt contamination fraction	-	0.0126	0.0104	0.0104	0.0070	-
π^- non prompt contamination fraction	-	0.0134	0.0121	0.0117	0.0085	-

Table C.10: Non-prompt contamination information from MC for protons, magnet down, $p_T < 0.8$ and $\sqrt{\mathbf{s}} = 7.0\,\text{TeV}$.

η	2-2.5	2.5-3	3-3.5	3.5-4	4-4.5	4.5-5.0
p non prompt contamination fraction	-	-	0.0214	0.0252	0.0237	-
$\bar{p}$ non prompt contamination fraction	-	-	0.0224	0.0250	0.0241	-

Table C.11: Non-prompt contamination information from MC for protons, magnet down, $0.8 < p_T < 1.2$ and $\sqrt{\mathbf{s}} = 7.0\,\text{TeV}$.

η	2-2.5	2.5-3	3-3.5	3.5-4	4-4.5	4.5-5.0
p non prompt contamination fraction	-	0.0131	0.0131	0.0169	0.0177	-
$\bar{p}$ non prompt contamination fraction	-	0.0130	0.0126	0.0176	0.0171	-

Table C.12: Non-prompt contamination information from MC for protons, magnet down, $p_T > 1.2$ and $\sqrt{\mathbf{s}} = 7.0\,\text{TeV}$.

η	2-2.5	2.5-3	3-3.5	3.5-4	4-4.5	4.5-5.0
p non prompt contamination fraction	-	0.0129	0.0132	0.0150	0.0139	-
$\bar{p}$ non prompt contamination fraction	-	0.0128	0.0129	0.0143	0.0162	-

Table C.13: Non-prompt contamination information from MC for kaons, magnet down, $p_T < 0.8$ and $\sqrt{\mathbf{s}} = 7.0\,\text{TeV}$.

η	2-2.5	2.5-3	3-3.5	3.5-4	4-4.5	4.5-5.0
K^+ non prompt contamination fraction	-	-	0.0205	0.0185	0.0221	-
K^- non prompt contamination fraction	-	-	0.0204	0.0190	0.0228	-

Table C.14: Non-prompt contamination information from MC for kaons, magnet down, $0.8 < p_T < 1.2$ and $\sqrt{\mathbf{s}} = 7.0\,\text{TeV}$.

η	2-2.5	2.5-3	3-3.5	3.5-4	4-4.5	4.5-5.0
K^+ non prompt contamination fraction	-	0.0208	0.0201	0.0185	0.0167	-
K^- non prompt contamination fraction	-	0.0197	0.0198	0.0181	0.0172	-

Table C.15: Non-prompt contamination information from MC for kaons, magnet down, $p_T > 1.2$ and $\sqrt{\mathbf{s}} = 7.0\,\text{TeV}$.

η	2-2.5	2.5-3	3-3.5	3.5-4	4-4.5	4.5-5.0
K^+ non prompt contamination fraction	-	0.0343	0.0333	0.0297	0.0255	-
K^- non prompt contamination fraction	-	0.0383	0.0342	0.0323	0.0281	-

Table C.16: Non-prompt contamination information from MC for pions, magnet down, $p_T < 0.8$ and $\sqrt{\mathbf{s}} = 7.0\,\text{TeV}$.

η	2-2.5	2.5-3	3-3.5	3.5-4	4-4.5	4.5-5.0
π^+ non prompt contamination fraction	-	-	0.0127	0.0189	0.0338	-
π^- non prompt contamination fraction	-	-	0.0128	0.0191	0.0346	-

Table C.17: Non-prompt contamination information from MC for pions, magnet down, $0.8 < p_T < 1.2$ and $\sqrt{\mathbf{s}} = 7.0\,\text{TeV}$.

η	2-2.5	2.5-3	3-3.5	3.5-4	4-4.5	4.5-5.0
π^+ non prompt contamination fraction	-	0.0136	0.0168	0.0189	0.0183	-
π^- non prompt contamination fraction	-	0.0137	0.0164	0.0192	0.0181	-

Table C.18: Non-prompt contamination information from MC for pions, magnet down, $p_T > 1.2$ and $\sqrt{\mathbf{s}} = 7.0\,\text{TeV}$.

η	2-2.5	2.5-3	3-3.5	3.5-4	4-4.5	4.5-5.0
π^+ non prompt contamination fraction	-	0.0216	0.0217	0.0232	0.0214	-
π^- non prompt contamination fraction	-	0.0225	0.0224	0.0229	0.0238	-

Appendix D

Pseudorapidity to Rapidity Translation Tables

Table D.1: Mean rapidity values for protons in MC and Data for $p_T < 0.8$ GeV and $\sqrt{\mathbf{s}} = 0.9\,\text{TeV}$.

η range	2.5-3	3-3.5	3.5-4	4-4.5
Mean reconstructed rapidity in data (RMS)	-	2.62(0.27)	3.24(0.11)	3.59(0.24)
Mean reconstructed rapidity in MC (RMS)	-	2.62(0.20)	3.19(0.15)	3.52(0.20)
Mean generated rapidity in MC (RMS)	-	2.58(0.18)	2.90(0.29)	3.27(0.39)
Corrected mean rapidity in data (RMS)	-	2.58(0.27)	2.96(0.11)	3.34(0.24)

Table D.2: Mean rapidity values for protons in MC and Data for $0.8 < p_T < 1.2$ GeV and $\sqrt{\mathbf{s}} = 0.9\,\text{TeV}$.

η range	2.5-3	3-3.5	3.5-4	4-4.5
Mean reconstructed rapidity in data (RMS)	2.44(0.24)	3.01(0.25)	3.39(0.22)	3.80(0.14)
Mean reconstructed rapidity in MC (RMS)	2.42(0.16)	2.95(0.14)	3.38(0.15)	3.82(0.13)
Mean generated rapidity in MC (RMS)	2.40(0.15)	2.90(0.15)	3.39(0.15)	3.89(0.15)
Corrected mean rapidity in data (RMS)	2.42(0.24)	2.96(0.25)	3.40(0.22)	3.87(0.14)

Table D.3: Mean rapidity values for protons in MC and Data for $p_T > 1.2$ GeV and $\sqrt{\mathbf{s}} = 0.9$ TeV.

η range	2.5-3	3-3.5	3.5-4	4-4.5
Mean reconstructed rapidity in data (RMS)	2.69(0.16)	3.09(0.23)	3.55(0.24)	3.96(0.25)
Mean reconstructed rapidity in MC (RMS)	2.64(0.13)	3.08(0.15)	3.56(0.15)	3.99(0.12)
Mean generated rapidity in MC (RMS)	2.58(0.15)	3.07(0.15)	3.56(0.15)	4.05(0.15)
Corrected mean rapidity in data (RMS)	2.63(0.16)	3.08(0.23)	3.56(0.24)	4.02(0.25)

Table D.4: Mean rapidity values for kaons in MC and Data for $p_T < 0.8$ GeV and $\sqrt{\mathbf{s}} = 0.9$ TeV.

η range	2.5-3	3-3.5	3.5-4	4-4.5
Mean reconstructed rapidity in data (RMS)	-	3.01(0.25)	3.47(0.25)	3.82(0.18)
Mean reconstructed rapidity in MC (RMS)	-	2.98(0.15)	3.46(0.17)	3.84(0.16)
Mean generated rapidity in MC (RMS)	-	2.96(0.14)	3.31(0.22)	3.69(0.31)
Corrected mean rapidity in data (RMS)	-	2.99(0.25)	3.32(0.25)	3.67(0.18)

Table D.5: Mean rapidity values for kaons in MC and Data for $0.8 < p_T < 1.2$ GeV and $\sqrt{\mathbf{s}} = 0.9$ TeV.

η range	2.5-3	3-3.5	3.5-4	4-4.5
Mean reconstructed rapidity in data (RMS)	2.66(0.19)	3.13(0.21)	3.61(0.22)	4.04(0.25)
Mean reconstructed rapidity in MC (RMS)	2.63(0.15)	3.13(0.15)	3.61(0.14)	4.05(0.12)
Mean generated rapidity in MC (RMS)	2.62(0.15)	3.12(0.15)	3.61(0.14)	4.11(0.14)
Corrected mean rapidity in data (RMS)	2.65(0.19)	3.12(0.21)	3.62(0.22)	4.11(0.25)

Table D.6: Mean rapidity values for kaons in MC and Data for $p_T > 1.2$ GeV and $\sqrt{\mathbf{s}} = 0.9$ TeV.

η range	2.5-3	3-3.5	3.5-4	4-4.5
Mean reconstructed rapidity in data (RMS)	2.71(0.14)	3.20(0.15)	3.69(0.17)	4.14(0.21)
Mean reconstructed rapidity in MC (RMS)	2.70(0.14)	3.20(0.15)	3.67(0.14)	4.10(0.11)
Mean generated rapidity in MC (RMS)	2.69(0.14)	3.18(0.14)	3.68(0.14)	4.17(0.14)
Corrected mean rapidity in data (RMS)	2.69(0.14)	3.18(0.15)	3.70(0.17)	4.20(0.21)

Table D.7: Mean rapidity values for pions in MC and Data for $p_T < 0.8$ GeV and $\sqrt{\mathbf{s}} = 0.9$ TeV.

η range	2.5-3	3-3.5	3.5-4	4-4.5
Mean reconstructed rapidity in data (RMS)	-	3.23(0.09)	3.70(0.15)	4.08(0.24)
Mean reconstructed rapidity in MC (RMS)	-	3.25(0.14)	3.68(0.14)	4.08(0.13)
Mean generated rapidity in MC (RMS)	-	3.24(0.13)	3.69(0.14)	4.14(0.16)
Corrected mean rapidity in data (RMS)	-	3.23(0.09)	3.71(0.15)	4.15(0.24)

Table D.8: Mean rapidity values for pions in MC and Data for $0.8 < p_T < 1.2$ GeV and $\sqrt{\mathbf{s}} = 0.9\,\text{TeV}$.

η range	2.5-3	3-3.5	3.5-4	4-4.5
Mean reconstructed rapidity in data (RMS)	2.74(0.07)	3.24(0.07)	3.74(0.08)	4.23(0.10)
Mean reconstructed rapidity in MC (RMS)	2.73(0.14)	3.24(0.15)	3.72(0.14)	4.15(0.12)
Mean generated rapidity in MC (RMS)	2.73(0.14)	3.23(0.14)	3.73(0.14)	4.22(0.14)
Corrected mean rapidity in data (RMS)	2.74(0.07)	3.23(0.07)	3.75(0.08)	4.30(0.10)

Table D.9: Mean rapidity values for pions in MC and Data for $p_T > 1.2$ GeV and $\sqrt{\mathbf{s}} = 0.9\,\text{TeV}$.

η range	2.5-3	3-3.5	3.5-4	4-4.5
Mean reconstructed rapidity in data (RMS)	2.75(0.05)	3.25(0.05)	3.74(0.05)	4.24(0.07)
Mean reconstructed rapidity in MC (RMS)	2.73(0.14)	3.24(0.15)	3.72(0.14)	4.16(0.12)
Mean generated rapidity in MC (RMS)	2.73(0.14)	3.23(0.14)	3.73(0.14)	4.22(0.14)
Corrected mean rapidity in data (RMS)	2.75(0.05)	3.24(0.05)	3.75(0.05)	4.30(0.07)

Table D.10: Mean rapidity values for protons in MC and Data for $p_T < 0.8$ GeV and $\sqrt{\mathbf{s}} = 7.0\,\text{TeV}$.

η range	2.5-3	3-3.5	3.5-4	4-4.5
Mean reconstructed rapidity in data (RMS)	-	2.64(0.27)	3.25(0.09)	3.66(0.21)
Mean reconstructed rapidity in MC (RMS)	-	2.68(0.20)	3.21(0.14)	3.63(0.21)
Mean generated rapidity in MC (RMS)	-	2.59(0.18)	2.93(0.29)	3.31(0.39)
Corrected mean rapidity in data (RMS)	-	2.55(0.27)	2.96(0.09)	3.34(0.21)

Table D.11: Mean rapidity values for protons in MC and Data for $0.8 < p_T < 1.2$ GeV and $\sqrt{\mathbf{s}} = 7.0\,\text{TeV}$.

η range	2.5-3	3-3.5	3.5-4	4-4.5
Mean reconstructed rapidity in data (RMS)	2.46(0.25)	3.04(0.25)	3.39(0.23)	3.84(0.19)
Mean reconstructed rapidity in MC (RMS)	2.46(0.16)	2.96(0.14)	3.40(0.15)	3.87(0.15)
Mean generated rapidity in MC (RMS)	2.41(0.15)	2.91(0.15)	3.41(0.15)	3.90(0.15)
Corrected mean rapidity in data (RMS)	2.41(0.25)	2.98(0.25)	3.40(0.23)	3.86(0.19)

Table D.12: Mean rapidity values for protons in MC and Data for $p_T > 1.2$ GeV and $\sqrt{\mathbf{s}} = 7.0\,\text{TeV}$.

η range	2.5-3	3-3.5	3.5-4	4-4.5
Mean reconstructed rapidity in data (RMS)	2.70(0.16)	3.13(0.22)	3.58(0.24)	4.03(0.25)
Mean reconstructed rapidity in MC (RMS)	2.67(0.14)	3.11(0.15)	3.59(0.15)	4.06(0.15)
Mean generated rapidity in MC (RMS)	2.60(0.15)	3.10(0.16)	3.59(0.16)	4.09(0.15)
Corrected mean rapidity in data (RMS)	2.63(0.16)	3.12(0.22)	3.59(0.24)	4.06(0.25)

Table D.13: Mean rapidity values for kaons in MC and Data for $p_T < 0.8$ GeV and $\sqrt{\mathbf{s}} = 7.0\,\text{TeV}$.

η range	2.5-3	3-3.5	3.5-4	4-4.5
Mean reconstructed rapidity in data (RMS)	-	3.03(0.25)	3.48(0.25)	3.87(0.22)
Mean reconstructed rapidity in MC (RMS)	-	2.97(0.15)	3.47(0.18)	3.87(0.18)
Mean generated rapidity in MC (RMS)	-	2.96(0.15)	3.33(0.22)	3.72(0.31)
Corrected mean rapidity in data (RMS)	-	3.02(0.25)	3.34(0.25)	3.72(0.22)

Table D.14: Mean rapidity values for kaons in MC and Data for $0.8 < p_T < 1.2$ GeV and $\sqrt{\mathbf{s}} = 7.0\,\text{TeV}$.

η range	2.5-3	3-3.5	3.5-4	4-4.5
Mean reconstructed rapidity in data (RMS)	2.66(0.19)	3.14(0.21)	3.63(0.21)	4.09(0.23)
Mean reconstructed rapidity in MC (RMS)	2.63(0.15)	3.14(0.14)	3.63(0.15)	4.10(0.14)
Mean generated rapidity in MC (RMS)	2.63(0.15)	3.13(0.15)	3.62(0.15)	4.12(0.15)
Corrected mean rapidity in data (RMS)	2.65(0.19)	3.12(0.21)	3.62(0.21)	4.11(0.23)

Table D.15: Mean rapidity values for kaons in MC and Data for $p_T > 1.2$ GeV and $\sqrt{\mathbf{s}} = 7.0\,\text{TeV}$.

η range	2.5-3	3-3.5	3.5-4	4-4.5
Mean reconstructed rapidity in data (RMS)	2.71(0.13)	3.20(0.14)	3.70(0.15)	4.17(0.18)
Mean reconstructed rapidity in MC (RMS)	2.72(0.14)	3.20(0.14)	3.69(0.14)	4.15(0.14)
Mean generated rapidity in MC (RMS)	2.70(0.15)	3.20(0.14)	3.70(0.15)	4.19(0.14)
Corrected mean rapidity in data (RMS)	2.70(0.13)	3.20(0.14)	3.70(0.15)	4.21(0.18)

Table D.16: Mean rapidity values for pions in MC and Data for $p_T < 0.8$ GeV and $\sqrt{\mathbf{s}} = 7.0\,\text{TeV}$.

η range	2.5-3	3-3.5	3.5-4	4-4.5
Mean reconstructed rapidity in data (RMS)	-	3.23(0.09)	3.70(0.14)	4.12(0.22)
Mean reconstructed rapidity in MC (RMS)	-	3.24(0.14)	3.70(0.14)	4.13(0.16)
Mean generated rapidity in MC (RMS)	-	3.24(0.14)	3.70(0.14)	4.15(0.16)
Corrected mean rapidity in data (RMS)	-	3.23(0.09)	3.70(0.14)	4.14(0.22)

Table D.17: Mean rapidity values for pions in MC and Data for $0.8 < p_T < 1.2$ GeV and $\sqrt{\mathbf{s}} = 7.0\,\text{TeV}$.

η range	2.5-3	3-3.5	3.5-4	4-4.5
Mean reconstructed rapidity in data (RMS)	2.74(0.07)	3.24(0.07)	3.74(0.07)	4.24(0.08)
Mean reconstructed rapidity in MC (RMS)	2.74(0.14)	3.24(0.14)	3.73(0.14)	4.21(0.14)
Mean generated rapidity in MC (RMS)	2.73(0.14)	3.24(0.14)	3.74(0.14)	4.23(0.14)
Corrected mean rapidity in data (RMS)	2.74(0.07)	3.24(0.07)	3.74(0.07)	4.26(0.08)

Table D.18: Mean rapidity values for pions in MC and Data for $p_T > 1.2$ GeV and $\sqrt{\mathbf{s}} = 7.0$ TeV.

η range	2.5-3	3-3.5	3.5-4	4-4.5
Mean reconstructed rapidity in data (RMS)	2.75(0.04)	3.25(0.04)	3.75(0.05)	4.24(0.05)
Mean reconstructed rapidity in MC (RMS)	2.74(0.14)	3.24(0.14)	3.74(0.14)	4.22(0.14)
Mean generated rapidity in MC (RMS)	2.74(0.14)	3.24(0.14)	3.74(0.14)	4.23(0.14)
Corrected mean rapidity in data (RMS)	2.74(0.04)	3.24(0.04)	3.75(0.05)	4.26(0.05)

Appendix E

Uncertainties Tables for the Hadron Ratios

Uncertainty contributions (in %) for the prompt hadron ratio results.

Table E.1: Relative statistical and systematic uncertainties in for the ratio $\bar{p}/p$ in the range $p_T < 0.8$ for each bin of η at $\sqrt{\mathbf{s}} = 0.9\,\text{TeV}$.

Source of uncertainty	$2.5 < \eta < 3$	$3 < \eta < 3.5$	$3.5 < \eta < 4$	$4 < \eta < 4.5$
PID Statistical	-	0.3299	0.0748	0.0970
Ghost Tracks	-	0.0004	0.0011	0.0009
MC Detector Description	-	0.0079	0.0061	0.0070
Material Interaction X Section	-	0.0158	0.0122	0.0142
Tracking Asymmetries	-	0.0100	0.0100	0.0100
Non-prompt Contamination	-	0.0023	0.0016	0.0018
Total Systematic Uncertainty	-	0.3305	0.0768	0.0988
Total Statistical Uncertainty	-	0.0150	0.0099	0.0137
Total Uncertainty	-	0.2182	0.0556	0.0710

Table E.2: Relative statistical and systematic uncertainties in for the ratio $\bar{p}/p$ in the range $0.8 < p_T < 1.2$ for each bin of η at $\sqrt{\mathbf{s}} = 0.9\,\text{TeV}$.

Source of uncertainty	$2.5 < \eta < 3$	$3 < \eta < 3.5$	$3.5 < \eta < 4$	$4 < \eta < 4.5$
PID Statistical	0.4666	0.1031	0.0788	0.1262
Ghost Tracks	0.0005	0.0005	0.0002	0.0001
MC Detector Description	0.0074	0.0051	0.0013	0.0009
Material Interaction X Section	0.0147	0.0102	0.0027	0.0018
Tracking Asymmetries	0.0100	0.0100	0.0100	0.0100
Non-prompt Contamination	0.0015	0.0010	0.0003	0.0002
Total Systematic Uncertainty	0.4671	0.1042	0.0795	0.1267
Total Statistical Uncertainty	0.0180	0.0144	0.0125	0.0191
Total Uncertainty	0.3159	0.0731	0.0567	0.0874

Table E.3: Relative statistical and systematic uncertainties in for the ratio $\bar{p}/p$ in the range $p_T > 1.2$ for each bin of η at $\sqrt{\mathbf{s}} = 0.9\,\text{TeV}$.

Source of uncertainty	$2.5 < \eta < 3$	$3 < \eta < 3.5$	$3.5 < \eta < 4$	$4 < \eta < 4.5$
PID Statistical	0.1601	0.1082	0.1029	0.2193
Ghost Tracks	0.0008	0.0003	0.0003	0.0003
MC Detector Description	0.0049	0.0016	0.0013	0.0032
Material Interaction X Section	0.0099	0.0032	0.0025	0.0064
Tracking Asymmetries	0.0100	0.0100	0.0100	0.0100
Non-prompt Contamination	0.0008	0.0003	0.0002	0.0005
Total Systematic Uncertainty	0.1608	0.1087	0.1035	0.2196
Total Statistical Uncertainty	0.0187	0.0169	0.0198	0.0315
Total Uncertainty	0.1132	0.0777	0.0746	0.1538

Table E.4: Relative statistical and systematic uncertainties in for the ratio K^-/K^+ in the range $p_T < 0.8$ for each bin of η at $\sqrt{\mathbf{s}} = 0.9\,\text{TeV}$.

Source of uncertainty	$2.5 < \eta < 3$	$3 < \eta < 3.5$	$3.5 < \eta < 4$	$4 < \eta < 4.5$
PID Statistical	-	0.1243	0.0919	0.1305
Ghost Tracks	-	0.0002	0.0001	0.0006
MC Detector Description	-	0.0028	0.0023	0.0063
Material Interaction X Section	-	0.0057	0.0047	0.0127
Tracking Asymmetries	-	0.0100	0.0100	0.0100
Non-prompt Contamination	-	0.0003	0.0002	0.0006
Total Systematic Uncertainty	-	0.1249	0.0926	0.1318
Total Statistical Uncertainty	-	0.0080	0.0065	0.0073
Total Uncertainty	-	0.0835	0.0647	0.0928

Table E.5: Relative statistical and systematic uncertainties in for the ratio K^-/K^+ in the range $0.8 < p_T < 1.2$ for each bin of η at $\sqrt{\mathbf{s}} = 0.9\,\text{TeV}$.

Source of uncertainty	$2.5 < \eta < 3$	$3 < \eta < 3.5$	$3.5 < \eta < 4$	$4 < \eta < 4.5$
PID Statistical	0.4242	0.0674	0.0486	0.0876
Ghost Tracks	0.0003	0.0001	0.0002	0.0006
MC Detector Description	0.0039	0.0022	0.0019	0.0073
Material Interaction X Section	0.0078	0.0044	0.0037	0.0145
Tracking Asymmetries	0.0100	0.0100	0.0100	0.0100
Non-prompt Contamination	0.0005	0.0002	0.0002	0.0005
Total Systematic Uncertainty	0.4244	0.0684	0.0498	0.0897
Total Statistical Uncertainty	0.0118	0.0101	0.0109	0.0154
Total Uncertainty	0.3069	0.0484	0.0366	0.0615

Table E.6: Relative statistical and systematic uncertainties in for the ratio K^-/K^+ in the range $p_T > 1.2$ for each bin of η at $\sqrt{\mathbf{s}} = 0.9\,\text{TeV}$.

Source of uncertainty	$2.5 < \eta < 3$	$3 < \eta < 3.5$	$3.5 < \eta < 4$	$4 < \eta < 4.5$
PID Statistical	0.1079	0.0681	0.0655	0.1412
Ghost Tracks	0.0002	0.0001	0.0002	0.0001
MC Detector Description	0.0017	0.0006	0.0011	0.0019
Material Interaction X Section	0.0034	0.0013	0.0022	0.0039
Tracking Asymmetries	0.0100	0.0100	0.0100	0.0100
Non-prompt Contamination	0.0004	0.0001	0.0001	0.0002
Total Systematic Uncertainty	0.1084	0.0689	0.0664	0.1416
Total Statistical Uncertainty	0.0138	0.0145	0.0168	0.0276
Total Uncertainty	0.0753	0.0499	0.0462	0.1023

Table E.7: Relative statistical and systematic uncertainties in for the ratio π^-/π^+ in the range $p_T < 0.8$ for each bin of η at $\sqrt{\mathbf{s}} = 0.9\,\text{TeV}$.

Source of uncertainty	$2.5 < \eta < 3$	$3 < \eta < 3.5$	$3.5 < \eta < 4$	$4 < \eta < 4.5$
PID Statistical	-	0.0077	0.0093	0.0146
Ghost Tracks	-	0.0000	0.0000	0.0008
MC Detector Description	-	0.0006	0.0004	0.0078
Material Interaction X Section	-	0.0003	0.0002	0.0039
Tracking Asymmetries	-	0.0100	0.0100	0.0100
Non-prompt Contamination	-	0.0001	0.0001	0.0014
Total Systematic Uncertainty	-	0.0127	0.0137	0.0199
Total Statistical Uncertainty	-	0.0050	0.0039	0.0044
Total Uncertainty	-	0.0117	0.0122	0.0172

Table E.8: Relative statistical and systematic uncertainties in for the ratio π^-/π^+ in the range $0.8 < p_T < 1.2$ for each bin of η at $\sqrt{\mathbf{s}} = 0.9\,\text{TeV}$.

Source of uncertainty	$2.5 < \eta < 3$	$3 < \eta < 3.5$	$3.5 < \eta < 4$	$4 < \eta < 4.5$
PID Statistical	0.0171	0.0137	0.0145	0.0292
Ghost Tracks	0.0000	0.0000	0.0002	0.0004
MC Detector Description	0.0008	0.0007	0.0015	0.0057
Material Interaction X Section	0.0004	0.0004	0.0007	0.0029
Tracking Asymmetries	0.0100	0.0100	0.0100	0.0100
Non-prompt Contamination	0.0001	0.0001	0.0001	0.0005
Total Systematic Uncertainty	0.0198	0.0170	0.0177	0.0316
Total Statistical Uncertainty	0.0105	0.0113	0.0124	0.0169
Total Uncertainty	0.0170	0.0155	0.0162	0.0253

Table E.9: Relative statistical and systematic uncertainties in for the ratio π^-/π^+ in the range $p_T > 1.2$ for each bin of η at $\sqrt{\mathbf{s}} = 0.9\,\text{TeV}$.

Source of uncertainty	$2.5 < \eta < 3$	$3 < \eta < 3.5$	$3.5 < \eta < 4$	$4 < \eta < 4.5$
PID Statistical	0.0250	0.0268	0.0282	0.0595
Ghost Tracks	0.0001	0.0001	0.0003	0.0002
MC Detector Description	0.0012	0.0008	0.0016	0.0015
Material Interaction X Section	0.0006	0.0004	0.0008	0.0007
Tracking Asymmetries	0.0100	0.0100	0.0100	0.0100
Non-prompt Contamination	0.0002	0.0001	0.0002	0.0001
Total Systematic Uncertainty	0.0270	0.0287	0.0300	0.0604
Total Statistical Uncertainty	0.0170	0.0189	0.0218	0.0312
Total Uncertainty	0.0224	0.0244	0.0256	0.0468

Table E.10: Relative statistical and systematic uncertainties in for the ratio $(p+\bar{p})/(K^+ + K^-)$ in the range $p_T < 0.8$ for each bin of η at $\sqrt{\mathbf{s}} = 0.9\,\text{TeV}$.

Source of uncertainty	$2.5 < \eta < 3$	$3 < \eta < 3.5$	$3.5 < \eta < 4$	$4 < \eta < 4.5$
PID Statistical	-	0.3568	0.1185	0.1626
PID Systematic	-	0.1618	0.1618	0.1618
Ghost Tracks	-	0.0005	0.0009	0.0001
MC Detector Description	-	0.0077	0.0060	0.0005
Material Interaction X Section	-	0.0220	0.0170	0.0014
Non-prompt Contamination	-	0.0020	0.0014	0.0001
Total Systematic Uncertainty	-	0.3925	0.2014	0.2294
Total Statistical Uncertainty	-	0.0169	0.0119	0.0155
Total Uncertainty	-	0.2892	0.1826	0.1985

Table E.11: Relative statistical and systematic uncertainties in for the ratio $(p+\bar{p})/(K^+ + K^-)$ in the range $0.8 < p_T < 1.2$ for each bin of η at $\sqrt{\mathbf{s}} = 0.9\,\text{TeV}$.

Source of uncertainty	$2.5 < \eta < 3$	$3 < \eta < 3.5$	$3.5 < \eta < 4$	$4 < \eta < 4.5$
PID Statistical	0.6354	0.1232	0.0926	0.1537
PID Systematic	0.0436	0.0436	0.0436	0.0436
Ghost Tracks	0.0003	0.0000	0.0002	0.0005
MC Detector Description	0.0045	0.0004	0.0016	0.0066
Material Interaction X Section	0.0129	0.0011	0.0044	0.0186
Non-prompt Contamination	0.0009	0.0001	0.0003	0.0012
Total Systematic Uncertainty	0.6370	0.1307	0.1024	0.1611
Total Statistical Uncertainty	0.0215	0.0176	0.0166	0.0245
Total Uncertainty	0.4493	0.0960	0.0792	0.1155

Table E.12: Relative statistical and systematic uncertainties in for the ratio $(p+\bar{p})/(K^+ + K^-)$ in the range $p_T > 1.2$ for each bin of η at $\sqrt{\mathbf{s}} = 0.9\,\text{TeV}$.

Source of uncertainty	$2.5 < \eta < 3$	$3 < \eta < 3.5$	$3.5 < \eta < 4$	$4 < \eta < 4.5$
PID Statistical	0.1930	0.1278	0.1223	0.2614
PID Systematic	0.0436	0.0436	0.0436	0.0436
Ghost Tracks	0.0002	0.0006	0.0012	0.0007
MC Detector Description	0.0013	0.0042	0.0053	0.0079
Material Interaction X Section	0.0037	0.0119	0.0151	0.0223
Non-prompt Contamination	0.0003	0.0007	0.0008	0.0011
Total Systematic Uncertainty	0.1979	0.1357	0.1308	0.2661
Total Statistical Uncertainty	0.0233	0.0223	0.0260	0.0419
Total Uncertainty	0.1408	0.1018	0.0988	0.1926

Table E.13: Relative statistical and systematic uncertainties in for the ratio $(p+\bar{p})/(\pi^+ + \pi^-)$ in the range $p_T < 0.8$ for each bin of η at $\sqrt{\mathbf{s}} = 0.9\,\text{TeV}$.

Source of uncertainty	$2.5 < \eta < 3$	$3 < \eta < 3.5$	$3.5 < \eta < 4$	$4 < \eta < 4.5$
PID Statistical	-	0.3300	0.0754	0.0980
PID Systematic	-	0.1144	0.1144	0.1144
Ghost Tracks	-	0.0002	0.0004	0.0005
MC Detector Description	-	0.0041	0.0022	0.0044
Material Interaction X Section	-	0.0085	0.0046	0.0091
Non-prompt Contamination	-	0.0012	0.0006	0.0012
Total Systematic Uncertainty	-	0.3494	0.1371	0.1510
Total Statistical Uncertainty	-	0.0158	0.0107	0.0144
Total Uncertainty	-	0.2404	0.1265	0.1341

Table E.14: Relative statistical and systematic uncertainties in for the ratio $(p+\bar{p})/(\pi^+ + \pi^-)$ in the range $0.8 < p_T < 1.2$ for each bin of η at $\sqrt{\mathbf{s}} = 0.9\,\text{TeV}$.

Source of uncertainty	$2.5 < \eta < 3$	$3 < \eta < 3.5$	$3.5 < \eta < 4$	$4 < \eta < 4.5$
PID Statistical	0.4670	0.1040	0.0801	0.1296
PID Systematic	0.0308	0.0308	0.0308	0.0308
Ghost Tracks	0.0004	0.0004	0.0005	0.0004
MC Detector Description	0.0056	0.0044	0.0034	0.0066
Material Interaction X Section	0.0116	0.0090	0.0070	0.0136
Non-prompt Contamination	0.0011	0.0008	0.0006	0.0012
Total Systematic Uncertainty	0.4682	0.1089	0.0862	0.1341
Total Statistical Uncertainty	0.0209	0.0183	0.0176	0.0255
Total Uncertainty	0.3177	0.0793	0.0655	0.0960

Table E.15: Relative statistical and systematic uncertainties in for the ratio $(p+\bar{p})/(\pi^+ + \pi^-)$ in the range $p_T > 1.2$ for each bin of η at $\sqrt{\mathbf{s}} = 0.9\,\text{TeV}$.

Source of uncertainty	$2.5 < \eta < 3$	$3 < \eta < 3.5$	$3.5 < \eta < 4$	$4 < \eta < 4.5$
PID Statistical	0.1620	0.1114	0.1067	0.2272
PID Systematic	0.0308	0.0308	0.0308	0.0308
Ghost Tracks	0.0008	0.0008	0.0008	0.0006
MC Detector Description	0.0055	0.0055	0.0035	0.0061
Material Interaction X Section	0.0114	0.0113	0.0073	0.0126
Non-prompt Contamination	0.0009	0.0008	0.0005	0.0008
Total Systematic Uncertainty	0.1654	0.1163	0.1114	0.2297
Total Statistical Uncertainty	0.0253	0.0254	0.0295	0.0443
Total Uncertainty	0.1179	0.0869	0.0840	0.1638

Table E.16: Relative statistical and systematic uncertainties in for the ratio $(K^+ + K^-)/(\pi^+ + \pi^-)$ in the range $p_T < 0.8$ for each bin of η at $\sqrt{\mathbf{s}} = 0.9\,\text{TeV}$.

Source of uncertainty	$2.5 < \eta < 3$	$3 < \eta < 3.5$	$3.5 < \eta < 4$	$4 < \eta < 4.5$
PID Statistical	-	0.1245	0.0924	0.1313
PID Systematic	-	0.1144	0.1144	0.1144
Ghost Tracks	-	0.0008	0.0005	0.0005
MC Detector Description	-	0.0120	0.0083	0.0048
Material Interaction X Section	-	0.0248	0.0171	0.0100
Non-prompt Contamination	-	0.0011	0.0010	0.0008
Total Systematic Uncertainty	-	0.1715	0.1483	0.1745
Total Statistical Uncertainty	-	0.0094	0.0076	0.0085
Total Uncertainty	-	0.1440	0.1326	0.1470

Table E.17: Relative statistical and systematic uncertainties in for the ratio $(K^+ + K^-)/(\pi^+ + \pi^-)$ in the range $0.8 < p_T < 1.2$ for each bin of η at $\sqrt{\mathbf{s}} = 0.9\,\text{TeV}$.

Source of uncertainty	$2.5 < \eta < 3$	$3 < \eta < 3.5$	$3.5 < \eta < 4$	$4 < \eta < 4.5$
PID Statistical	0.4245	0.0688	0.0507	0.0923
PID Systematic	0.0308	0.0308	0.0308	0.0308
Ghost Tracks	0.0008	0.0003	0.0002	0.0001
MC Detector Description	0.0104	0.0048	0.0018	0.0010
Material Interaction X Section	0.0214	0.0099	0.0038	0.0021
Non-prompt Contamination	0.0013	0.0005	0.0002	0.0001
Total Systematic Uncertainty	0.4263	0.0762	0.0595	0.0974
Total Statistical Uncertainty	0.0158	0.0152	0.0165	0.0228
Total Uncertainty	0.3019	0.0585	0.0485	0.0700

Table E.18: Relative statistical and systematic uncertainties in for the ratio $(K^+ + K^-)/(\pi^+ + \pi^-)$ in the range $p_T > 1.2$ for each bin of η at $\sqrt{\mathbf{s}} = 0.9\,\text{TeV}$.

Source of uncertainty	$2.5 < \eta < 3$	$3 < \eta < 3.5$	$3.5 < \eta < 4$	$4 < \eta < 4.5$
PID Statistical	0.1107	0.0732	0.0714	0.1535
PID Systematic	0.0308	0.0308	0.0308	0.0308
Ghost Tracks	0.0004	0.0001	0.0003	0.0001
MC Detector Description	0.0042	0.0012	0.0017	0.0017
Material Interaction X Section	0.0086	0.0026	0.0036	0.0034
Non-prompt Contamination	0.0009	0.0002	0.0002	0.0001
Total Systematic Uncertainty	0.1154	0.0795	0.0778	0.1566
Total Statistical Uncertainty	0.0219	0.0238	0.0275	0.0417
Total Uncertainty	0.0835	0.0621	0.0595	0.1167

Table E.19: Relative statistical and systematic uncertainties in for the ratio $\bar{p}/p$ in the range $p_T < 0.8$ for each bin of η at $\sqrt{\mathbf{s}} = 7.0\,\text{TeV}$.

Source of uncertainty	$2.5 < \eta < 3$	$3 < \eta < 3.5$	$3.5 < \eta < 4$	$4 < \eta < 4.5$
PID Statistical	-	0.2385	0.0486	0.0740
Ghost Tracks	-	0.0017	0.0035	0.0012
MC Detector Description	-	0.0089	0.0067	0.0055
Material Interaction X Section	-	0.0177	0.0134	0.0109
Tracking Asymmetries	-	0.0050	0.0050	0.0050
Non-prompt Contamination	-	0.0019	0.0017	0.0013
Total Systematic Uncertainty	-	0.2394	0.0514	0.0752
Total Statistical Uncertainty	-	0.0150	0.0086	0.0108
Total Uncertainty	-	0.1699	0.0378	0.0546

Table E.20: Relative statistical and systematic uncertainties in for the ratio $\bar{p}/p$ in the range $0.8 < p_T < 1.2$ for each bin of η at $\sqrt{\mathbf{s}} = 7.0\,\text{TeV}$.

Source of uncertainty	$2.5 < \eta < 3$	$3 < \eta < 3.5$	$3.5 < \eta < 4$	$4 < \eta < 4.5$
PID Statistical	0.2644	0.0528	0.0340	0.0641
Ghost Tracks	0.0012	0.0015	0.0009	0.0004
MC Detector Description	0.0079	0.0054	0.0024	0.0035
Material Interaction X Section	0.0159	0.0107	0.0047	0.0070
Tracking Asymmetries	0.0050	0.0050	0.0050	0.0050
Non-prompt Contamination	0.0011	0.0007	0.0004	0.0006
Total Systematic Uncertainty	0.2652	0.0546	0.0348	0.0648
Total Statistical Uncertainty	0.0170	0.0120	0.0080	0.0113
Total Uncertainty	0.1661	0.0398	0.0254	0.0447

Table E.21: Relative statistical and systematic uncertainties in for the ratio $\bar{p}/p$ in the range $p_T > 1.2$ for each bin of η at $\sqrt{\mathbf{s}} = 7.0\,\text{TeV}$.

Source of uncertainty	$2.5 < \eta < 3$	$3 < \eta < 3.5$	$3.5 < \eta < 4$	$4 < \eta < 4.5$
PID Statistical	0.0624	0.0404	0.0359	0.0886
Ghost Tracks	0.0021	0.0008	0.0005	0.0002
MC Detector Description	0.0046	0.0027	0.0015	0.0022
Material Interaction X Section	0.0093	0.0053	0.0029	0.0044
Tracking Asymmetries	0.0050	0.0050	0.0050	0.0050
Non-prompt Contamination	0.0006	0.0004	0.0002	0.0004
Total Systematic Uncertainty	0.0635	0.0413	0.0364	0.0889
Total Statistical Uncertainty	0.0108	0.0086	0.0086	0.0118
Total Uncertainty	0.0454	0.0298	0.0265	0.0611

Table E.22: Relative statistical and systematic uncertainties in for the ratio K^-/K^+ in the range $p_T < 0.8$ for each bin of η at $\sqrt{\mathbf{s}} = 7.0\,\text{TeV}$.

Source of uncertainty	$2.5 < \eta < 3$	$3 < \eta < 3.5$	$3.5 < \eta < 4$	$4 < \eta < 4.5$
PID Statistical	-	0.0893	0.0540	0.0673
Ghost Tracks	-	0.0007	0.0005	0.0007
MC Detector Description	-	0.0033	0.0029	0.0029
Material Interaction X Section	-	0.0067	0.0058	0.0057
Tracking Asymmetries	-	0.0050	0.0050	0.0050
Non-prompt Contamination	-	0.0007	0.0006	0.0007
Total Systematic Uncertainty	-	0.0897	0.0547	0.0678
Total Statistical Uncertainty	-	0.0060	0.0047	0.0042
Total Uncertainty	-	0.0642	0.0383	0.0475

Table E.23: Relative statistical and systematic uncertainties in for the ratio K^-/K^+ in the range $0.8 < p_T < 1.2$ for each bin of η at $\sqrt{\mathbf{s}} = 7.0\,\text{TeV}$.

Source of uncertainty	$2.5 < \eta < 3$	$3 < \eta < 3.5$	$3.5 < \eta < 4$	$4 < \eta < 4.5$
PID Statistical	0.1577	0.0270	0.0203	0.0390
Ghost Tracks	0.0006	0.0003	0.0002	0.0003
MC Detector Description	0.0031	0.0026	0.0019	0.0035
Material Interaction X Section	0.0062	0.0052	0.0038	0.0071
Tracking Asymmetries	0.0050	0.0050	0.0050	0.0050
Non-prompt Contamination	0.0006	0.0005	0.0004	0.0006
Total Systematic Uncertainty	0.1580	0.0281	0.0214	0.0402
Total Statistical Uncertainty	0.0081	0.0060	0.0061	0.0070
Total Uncertainty	0.1020	0.0207	0.0162	0.0284

Table E.24: Relative statistical and systematic uncertainties in for the ratio K^-/K^+ in the range $p_T > 1.2$ for each bin of η at $\sqrt{\mathbf{s}} = 7.0\,\text{TeV}$.

Source of uncertainty	$2.5 < \eta < 3$	$3 < \eta < 3.5$	$3.5 < \eta < 4$	$4 < \eta < 4.5$
PID Statistical	0.0311	0.0222	0.0265	0.0750
Ghost Tracks	0.0002	0.0001	0.0002	0.0001
MC Detector Description	0.0017	0.0018	0.0012	0.0019
Material Interaction X Section	0.0034	0.0036	0.0025	0.0037
Tracking Asymmetries	0.0050	0.0050	0.0050	0.0050
Non-prompt Contamination	0.0006	0.0006	0.0004	0.0005
Total Systematic Uncertainty	0.0318	0.0232	0.0271	0.0753
Total Statistical Uncertainty	0.0067	0.0064	0.0069	0.0097
Total Uncertainty	0.0226	0.0173	0.0198	0.0518

Table E.25: Relative statistical and systematic uncertainties in for the ratio π^-/π^+ in the range $p_T < 0.8$ for each bin of η at $\sqrt{\mathbf{s}} = 7.0\,\text{TeV}$.

Source of uncertainty	$2.5 < \eta < 3$	$3 < \eta < 3.5$	$3.5 < \eta < 4$	$4 < \eta < 4.5$
PID Statistical	-	0.0055	0.0060	0.0060
Ghost Tracks	-	0.0000	0.0001	0.0001
MC Detector Description	-	0.0007	0.0006	0.0007
Material Interaction X Section	-	0.0003	0.0003	0.0003
Tracking Asymmetries	-	0.0050	0.0050	0.0050
Non-prompt Contamination	-	0.0001	0.0001	0.0002
Total Systematic Uncertainty	-	0.0075	0.0079	0.0079
Total Statistical Uncertainty	-	0.0038	0.0029	0.0028
Total Uncertainty	-	0.0069	0.0069	0.0069

Table E.26: Relative statistical and systematic uncertainties in for the ratio π^-/π^+ in the range $0.8 < p_T < 1.2$ for each bin of η at $\sqrt{\mathbf{s}} = 7.0\,\text{TeV}$.

Source of uncertainty	$2.5 < \eta < 3$	$3 < \eta < 3.5$	$3.5 < \eta < 4$	$4 < \eta < 4.5$
PID Statistical	0.0082	0.0059	0.0058	0.0122
Ghost Tracks	0.0000	0.0000	0.0001	0.0001
MC Detector Description	0.0007	0.0004	0.0006	0.0014
Material Interaction X Section	0.0003	0.0002	0.0003	0.0007
Tracking Asymmetries	0.0050	0.0050	0.0050	0.0050
Non-prompt Contamination	0.0001	0.0001	0.0001	0.0002
Total Systematic Uncertainty	0.0097	0.0078	0.0077	0.0133
Total Statistical Uncertainty	0.0072	0.0075	0.0078	0.0091
Total Uncertainty	0.0092	0.0084	0.0085	0.0119

Table E.27: Relative statistical and systematic uncertainties in for the ratio π^-/π^+ in the range $p_T > 1.2$ for each bin of η at $\sqrt{\mathbf{s}} = 7.0\,\text{TeV}$.

Source of uncertainty	$2.5 < \eta < 3$	$3 < \eta < 3.5$	$3.5 < \eta < 4$	$4 < \eta < 4.5$
PID Statistical	0.0088	0.0088	0.0106	0.0269
Ghost Tracks	0.0001	0.0001	0.0002	0.0002
MC Detector Description	0.0009	0.0009	0.0014	0.0022
Material Interaction X Section	0.0004	0.0004	0.0007	0.0011
Tracking Asymmetries	0.0050	0.0050	0.0050	0.0050
Non-prompt Contamination	0.0002	0.0002	0.0003	0.0005
Total Systematic Uncertainty	0.0102	0.0102	0.0119	0.0275
Total Statistical Uncertainty	0.0095	0.0100	0.0109	0.0127
Total Uncertainty	0.0105	0.0107	0.0120	0.0214

Table E.28: Relative statistical and systematic uncertainties in for the ratio $(p+\bar{p})/(K^+ + K^-)$ in the range $p_T < 0.8$ for each bin of η at $\sqrt{\mathbf{s}} = 7.0\,\text{TeV}$.

Source of uncertainty	$2.5 < \eta < 3$	$3 < \eta < 3.5$	$3.5 < \eta < 4$	$4 < \eta < 4.5$
PID Statistical	-	0.2550	0.0727	0.1001
PID Systematic	-	0.1618	0.1618	0.1618
Ghost Tracks	-	0.0007	0.0008	0.0007
MC Detector Description	-	0.0035	0.0016	0.0030
Material Interaction X Section	-	0.0099	0.0044	0.0084
Non-prompt Contamination	-	0.0007	0.0004	0.0007
Total Systematic Uncertainty	-	0.3022	0.1774	0.1905
Total Statistical Uncertainty	-	0.0162	0.0098	0.0116
Total Uncertainty	-	0.2395	0.1696	0.1803

Table E.29: Relative statistical and systematic uncertainties in for the ratio $(p+\bar{p})/(K^+ + K^-)$ in the range $0.8 < p_T < 1.2$ for each bin of η at $\sqrt{\mathbf{s}} = 7.0\,\text{TeV}$.

Source of uncertainty	$2.5 < \eta < 3$	$3 < \eta < 3.5$	$3.5 < \eta < 4$	$4 < \eta < 4.5$
PID Statistical	0.3080	0.0593	0.0396	0.0750
PID Systematic	0.0436	0.0436	0.0436	0.0436
Ghost Tracks	0.0003	0.0008	0.0019	0.0008
MC Detector Description	0.0016	0.0028	0.0050	0.0085
Material Interaction X Section	0.0044	0.0080	0.0142	0.0240
Non-prompt Contamination	0.0003	0.0005	0.0009	0.0014
Total Systematic Uncertainty	0.3111	0.0741	0.0608	0.0906
Total Statistical Uncertainty	0.0189	0.0135	0.0101	0.0133
Total Uncertainty	0.1954	0.0612	0.0543	0.0720

Table E.30: Relative statistical and systematic uncertainties in for the ratio $(p+\bar{p})/(K^+ + K^-)$ in the range $p_T > 1.2$ for each bin of η at $\sqrt{\mathbf{s}} = 7.0\,\text{TeV}$.

Source of uncertainty	$2.5 < \eta < 3$	$3 < \eta < 3.5$	$3.5 < \eta < 4$	$4 < \eta < 4.5$
PID Statistical	0.0698	0.0461	0.0446	0.1161
PID Systematic	0.0436	0.0436	0.0436	0.0436
Ghost Tracks	0.0023	0.0021	0.0028	0.0009
MC Detector Description	0.0051	0.0073	0.0088	0.0111
Material Interaction X Section	0.0144	0.0208	0.0249	0.0313
Non-prompt Contamination	0.0018	0.0024	0.0025	0.0027
Total Systematic Uncertainty	0.0838	0.0672	0.0679	0.1285
Total Statistical Uncertainty	0.0127	0.0107	0.0111	0.0153
Total Uncertainty	0.0674	0.0588	0.0603	0.0966

Table E.31: Relative statistical and systematic uncertainties in for the ratio $(p+\bar{p})/(\pi^+ + \pi^-)$ in the range $p_T < 0.8$ for each bin of η at $\sqrt{\mathbf{s}} = 7.0\,\text{TeV}$.

Source of uncertainty	$2.5 < \eta < 3$	$3 < \eta < 3.5$	$3.5 < \eta < 4$	$4 < \eta < 4.5$
PID Statistical	-	0.2386	0.0490	0.0743
PID Systematic	-	0.1144	0.1144	0.1144
Ghost Tracks	-	0.0013	0.0030	0.0014
MC Detector Description	-	0.0067	0.0060	0.0065
Material Interaction X Section	-	0.0138	0.0124	0.0133
Non-prompt Contamination	-	0.0014	0.0015	0.0021
Total Systematic Uncertainty	-	0.2650	0.1253	0.1372
Total Statistical Uncertainty	-	0.0155	0.0090	0.0112
Total Uncertainty	-	0.1989	0.1202	0.1280

Table E.32: Relative statistical and systematic uncertainties in for the ratio $(p+\bar{p})/(\pi^+ + \pi^-)$ in the range $0.8 < p_T < 1.2$ for each bin of η at $\sqrt{\mathbf{s}} = 7.0\,\text{TeV}$.

Source of uncertainty	$2.5 < \eta < 3$	$3 < \eta < 3.5$	$3.5 < \eta < 4$	$4 < \eta < 4.5$
PID Statistical	0.2645	0.0531	0.0345	0.0652
PID Systematic	0.0308	0.0308	0.0308	0.0308
Ghost Tracks	0.0011	0.0019	0.0024	0.0006
MC Detector Description	0.0077	0.0071	0.0061	0.0062
Material Interaction X Section	0.0158	0.0147	0.0127	0.0128
Non-prompt Contamination	0.0010	0.0011	0.0011	0.0011
Total Systematic Uncertainty	0.2670	0.0636	0.0484	0.0736
Total Statistical Uncertainty	0.0185	0.0142	0.0112	0.0145
Total Uncertainty	0.1651	0.0516	0.0423	0.0565

Table E.33: Relative statistical and systematic uncertainties in for the ratio $(p+\bar{p})/(\pi^+ + \pi^-)$ in the range $p_T > 1.2$ for each bin of η at $\sqrt{\mathbf{s}} = 7.0\,\text{TeV}$.

Source of uncertainty	$2.5 < \eta < 3$	$3 < \eta < 3.5$	$3.5 < \eta < 4$	$4 < \eta < 4.5$
PID Statistical	0.0630	0.0413	0.0374	0.0926
PID Systematic	0.0308	0.0308	0.0308	0.0308
Ghost Tracks	0.0033	0.0018	0.0022	0.0006
MC Detector Description	0.0073	0.0063	0.0067	0.0068
Material Interaction X Section	0.0151	0.0131	0.0138	0.0139
Non-prompt Contamination	0.0015	0.0013	0.0014	0.0014
Total Systematic Uncertainty	0.0723	0.0536	0.0509	0.0988
Total Statistical Uncertainty	0.0144	0.0131	0.0139	0.0174
Total Uncertainty	0.0571	0.0454	0.0445	0.0728

Table E.34: Relative statistical and systematic uncertainties in for the ratio $(K^+ + K^-)/(\pi^+ + \pi^-)$ in the range $p_T < 0.8$ for each bin of η at $\sqrt{\mathbf{s}} = 7.0\,\text{TeV}$.

Source of uncertainty	$2.5 < \eta < 3$	$3 < \eta < 3.5$	$3.5 < \eta < 4$	$4 < \eta < 4.5$
PID Statistical	-	0.0894	0.0544	0.0675
PID Systematic	-	0.1144	0.1144	0.1144
Ghost Tracks	-	0.0022	0.0013	0.0008
MC Detector Description	-	0.0104	0.0076	0.0034
Material Interaction X Section	-	0.0214	0.0158	0.0070
Non-prompt Contamination	-	0.0021	0.0014	0.0011
Total Systematic Uncertainty	-	0.1472	0.1279	0.1331
Total Statistical Uncertainty	-	0.0071	0.0055	0.0050
Total Uncertainty	-	0.1333	0.1218	0.1242

Table E.35: Relative statistical and systematic uncertainties in for the ratio $(K^+ + K^-)/(\pi^+ + \pi^-)$ in the range $0.8 < p_T < 1.2$ for each bin of η at $\sqrt{\mathbf{s}} = 7.0\,\text{TeV}$.

Source of uncertainty	$2.5 < \eta < 3$	$3 < \eta < 3.5$	$3.5 < \eta < 4$	$4 < \eta < 4.5$
PID Statistical	0.1580	0.0276	0.0211	0.0409
PID Systematic	0.0308	0.0308	0.0308	0.0308
Ghost Tracks	0.0017	0.0004	0.0001	0.0002
MC Detector Description	0.0094	0.0042	0.0011	0.0022
Material Interaction X Section	0.0193	0.0086	0.0022	0.0045
Non-prompt Contamination	0.0019	0.0008	0.0002	0.0004
Total Systematic Uncertainty	0.1625	0.0425	0.0374	0.0514
Total Statistical Uncertainty	0.0109	0.0096	0.0099	0.0115
Total Uncertainty	0.1084	0.0381	0.0350	0.0426

Table E.36: Relative statistical and systematic uncertainties in for the ratio $(K^+ + K^-)/(\pi^+ + \pi^-)$ in the range $p_T > 1.2$ for each bin of η at $\sqrt{\mathbf{s}} = 7.0\,\text{TeV}$.

Source of uncertainty	$2.5 < \eta < 3$	$3 < \eta < 3.5$	$3.5 < \eta < 4$	$4 < \eta < 4.5$
PID Statistical	0.0324	0.0239	0.0285	0.0797
PID Systematic	0.0308	0.0308	0.0308	0.0308
Ghost Tracks	0.0002	0.0001	0.0003	0.0003
MC Detector Description	0.0021	0.0010	0.0020	0.0041
Material Interaction X Section	0.0044	0.0020	0.0040	0.0084
Non-prompt Contamination	0.0008	0.0003	0.0006	0.0011
Total Systematic Uncertainty	0.0449	0.0391	0.0422	0.0860
Total Statistical Uncertainty	0.0116	0.0119	0.0129	0.0160
Total Uncertainty	0.0391	0.0361	0.0380	0.0641

Bibliography

[1] G. Chew and S. C. Frautschi, Phys.Rev.Lett. **7**, 394 (1961). xi, 4, 5

[2] I. C. database. xx, 132

[3] P. Skands, 1104.2863. 2

[4] T. Regge, Nuovo Cim. **14**, 951 (1959). 4

[5] R. Blankenbecler and M. Goldberger, Phys.Rev. **126**, 766 (1962). 4

[6] S. Mandelstam, Phys. Rev. **112**, 1344 (1958). 5

[7] R. Eden, Rept.Prog.Phys. **34**, 995 (1971). 5, 6

[8] L. Lukaszuk and B. Nicolescu, Lett.Nuovo Cim. **8**, 405 (1973). 6

[9] B. Andersson *et al.*, Physics Reports **97**, 31 (1983). 9, 10

[10] B.R. and Webber, Nuclear Physics B **238**, 492 (1984). 9, 13

[11] X. Artru and G. Mennessier, Nucl.Phys. **B70**, 93 (1974). 10

[12] B. Andersson *et al.*, Nuclear Physics B **197**, 45 (1982). 11

[13] B. Andersson *et al.*, Physica Scripta **32**, 574 (1985). 11

[14] G. C. Rossi and G. Veneziano, Nucl. Phys. **B123**, 507 (1977). 14, 15

[15] A. Capella *et al.*, Phys. Rept. **236**, 225 (1994). 14

[16] X. Artru, Nucl. Phys. **B85**, 442 (1975). 14

[17] B. Z. Kopeliovich, Sov. J. Nucl. Phys. **45**, 1078 (1987). 14

[18] B. Kopeliovich and B. Povh, Z. Phys. **C75**, 693 (1997), [hep-ph/9607486]. 14

[19] B. Kopeliovich and B. Povh, Phys. Lett. **B446**, 321 (1999), [hep-ph/9810530]. 14

[20] D. Kharzeev, Phys. Lett. **B378**, 238 (1996), [nucl-th/9602027]. 14, 15, 163

[21] C. Merino *et al.*, 0906.2659. 14

[22] S. E. Vance and M. Gyulassy, Phys. Rev. Lett. **83**, 1735 (1999), [nucl-th/9901009]. 14

[23] G. H. Arakelyan *et al.*, Eur. Phys. J. **C54**, 577 (2008), [0709.3174]. 14

[24] P. Koch, Zeitschrift fr Physik C Particles and Fields **38**, 269 (1988), 10.1007/BF01574548. 14

[25] R. G. Roberts, *The Structure of the Proton* (Cambridge University Press, 1994). 16

[26] F. W. Bopp and Y. Shabelski, Phys.Atom.Nucl. **68**, 2093 (2005), [hep-ph/0406158]. 16

[27] ALICE Collaboration, A. K. Aamodt *et al.*, Phys.Rev.Lett. **105**, 072002 (2010), [1006.5432]. 16, 161, 164

[28] T. Sjostrand, 0911.5286. 17

[29] T. Sjostrand *et al.*, JHEP **05**, 026 (2006), [hep-ph/0603175]. 17, 161

[30] ALICE Collaboration, K. Aamodt *et al.*, Eur.Phys.J. **C71**, 1655 (2011), [1101.4110]. 18

[31] ALICE Collaboration, M. Chojnacki, J.Phys.G **G38**, 124074 (2011), [1109.6744]. 18

[32] T. A. Collaboration, Journal of Instrumentation **3**, S08002 (2008). 19

[33] T. A. Collaboration, Journal of Instrumentation **3**, S08003 (2008). 19

[34] T. C. Collaboration, Journal of Instrumentation **3**, S08004 (2008). 19

[35] T. L. Collaboration, Journal of Instrumentation **3**, S08005 (2008). 19, 21

[36] T. L. Collaboration, *LHCb : Technical Proposal*, Tech. Proposal No. CERN-LHCC-98-004 (CERN, Geneva, 1998). 21

[37] T. L. Collaboration, *LHCb reoptimized detector design and performance: Technical Design Report*, Technical Design Report LHCb No. CERN-LHCC-2003-030 (CERN, Geneva, 2003). 21

[38] T. L. Collaboration, *LHCb VELO (VErtex LOcator): Technical Design Report*, Technical Design Report LHCb No. CERN-LHCC-2001-011 (CERN, Geneva, 2001). 21, 23

[39] T. L. Collaboration, *LHCb magnet: Technical Design Report*, Technical Design Report LHCb No. CERN-LHCC-2000-007 (CERN, Geneva, 2000). 21

[40] T. L. Collaboration, *LHCb inner tracker: Technical Design Report*, Technical Design Report LHCb No. CERN-LHCC-2002-029 (CERN, Geneva, 2002). 21

[41] T. L. Collaboration, *LHCb outer tracker: Technical Design Report*, Technical Design Report LHCb No. CERN-LHCC-2001-024 (CERN, Geneva, 2001). 21

[42] T. L. Collaboration, *LHCb RICH: Technical Design Report*, Technical Design Report LHCb No. CERN-LHCC-2000-037 (CERN, Geneva, 2000). 21

[43] T. L. Collaboration, *LHCb calorimeters: Technical Design Report*, Technical Design Report LHCb No. CERN-LHCC-2000-036 (CERN, Geneva, 2000). 21

[44] T. L. Collaboration, *LHCb muon system: Technical Design Report*, Technical Design Report LHCb No. CERN-LHCC-2001-010 (CERN, Geneva, 2001). 21

[45] T. L. Collaboration, *LHCb online system, data acquisition and experiment control: Technical Design Report*, Technical Design Report LHCb No. CERN-LHCC-2001-040 (CERN, Geneva, 2001). 21

[46] T. L. Collaboration, *LHCb trigger system: Technical Design Report*, Technical Design Report LHCb No. CERN-LHCC-2003-031 (CERN, Geneva, 2003). 21

[47] T. L. Collaboration, *LHCb computing: Technical Design Report*, Technical Design Report LHCb No. CERN-LHCC-2005-019 (CERN, Geneva, 2005). 21

[48] P. A. Čerenkov, Phys. Rev. **52**, 378 (1937). 40

[49] J. Rademacker and N. Harnew, *Evaluation of the LHCb RICH detectors and a measurement of the CKM angle γ. oai:cds.cern.ch:518861*, PhD thesis, Oxford Univ., Geneva, 2001, Presented on 21 Sep 2001. 41

[50] T. Ypsilantis and J. Seguinot, Nuclear Instruments and Methods in Physics Research Section A: Accelerators, Spectrometers, Detectors and Associated Equipment **343**, 30 (1994). 42

[51] N. Kanaya *et al.*, Nuclear Instruments and Methods in Physics Research Section A: Accelerators, Spectrometers, Detectors and Associated Equipment **553**, 41 (2005), ¡ce:title¿Proceedings of the fifth International Workshop on Ring Imaging Detectors¡/ce:title¿ ¡xocs:full-name¿Fifth International Workshop on Ring Imaging Detectors¡/xocs:full-name¿. 46

[52] M. Adinolfi *et al.*, Nuclear Instruments and Methods in Physics Research Section A: Accelerators, Spectrometers, Detectors and Associated Equipment **572**, 689 (2007). 48

[53] R. Forty, Nuclear Instruments and Methods in Physics Research Section A: Accelerators, Spectrometers, Detectors and Associated Equipment **433**, 257 (1999). 49

[54] M. Patel *et al.*, CERN Report No. LHCb-2005-055. CERN-LHCb-2005-055, 2006 (unpublished). 56

[55] S. Amato *et al.*, *LHCb RICH: Technical Design Report*Technical Design Report LHCb (CERN, Geneva, 2000). 57

[56] N. Brook *et al.*, CERN Report No. LHCb-2004-121. CERN-LHCb-2004-121, 2005 (unpublished). 57

[57] S. Eisenhardt, Nuclear Instruments and Methods in Physics Research Section A: Accelerators, Spectrometers, Detectors and Associated Equipment **617**, 391 (2010), 11th Pisa Meeting on Advanced Detectors - Proceedings of the 11th Pisa Meeting on Advanced Detectors. 68

[58] T. Gys, Nuclear Instruments and Methods in Physics Research Section A: Accelerators, Spectrometers, Detectors and Associated Equipment **465**, 240 (2001). 78

[59] M. Needham, CERN Report No. LHCb-2008-002. CERN-LHCb-2008-002. LPHE-2008-002, 2008 (unpublished). 103

[60] M. Pivk and F. R. Le Diberder, Nucl. Instrum. Meth. **A555**, 356 (2005), [physics/0402083]. 107

[61] D. K. Wouter Verkerke, Roofit. 109

[62] S. Agostinelli *et al.*, Nuclear Instruments and Methods in Physics Research Section A: Accelerators, Spectrometers, Detectors and Associated Equipment **506**, 250 (2003). 131

[63] P. Z. Skands, Phys. Rev. D **82**, 074018 (2010). 161

[64] B. B. B. et al. (PHOBOS Collaboration), Phys. Rev. C **71**, 021901 (2005). 161

[65] B. I. A. *et al.* (STAR Collaboration), Phys. Rev. C **79**, 034909 (2009). 161

[66] PHENIX, S. S. Adler *et al.*, Phys. Rev. **C74**, 024904 (2006), [nucl-ex/0603010]. 161

[67] I. B. *et al.* (BRAHMS Collaboration), Physics Letters B **607**, 42 (2005). 161

[68] A. Kaidalov *et al.*, Sov.J.Nucl.Phys. **44**, 468 (1986). 164

[69] C. Merino *et al.*, 1007.3206. 165

[70] C. Merino *et al.*, 0906.2659. 165